Doctoral Dissertation
博士論文

Comprehensive study of magma flow style based on deformed bubble structure of pumice

(軽石の変形気泡組織に基づくマグマ流動様式の総合的研究)

A Dissertation Submitted for the Degree of Doctor of Philosophy
December, 2019

令和元年12月 博士(理学)申請

Department of Earth and Planetary Science, Graduate School of Science,
The University of Tokyo

東京大学大学院理学系研究科地球惑星科学専攻

Masatoshi Ohashi

大橋 正俊

Acknowledgements

I finished up writing this doctoral dissertation with support from many people. I am sincerely grateful for all of the supports during my Ph.D. work.

The person whom I am most grateful for is Mie Ichihara, who supervised my master and doctor works with patience and kindness. Although my research topic was a little different from what she has studied, she kindly accepted my proposal and gave me a lot of invaluable advice. I am sure I would not have completed the massive project, without her support, to connect bubble textures to the eruption dynamics from the physical viewpoint.

The study about bubble textures was stimulated by Atsushi Toramaru at Kyushu University, who showed me tube pumice in the filed trip at Toya Caldera. He gave me precious advice from geological and petrological points. My Ph.D. work was greatly improved by his strong belief that bubble textures in pyroclast record the eruption dynamics in a conduit.

Analogue experiment with polyurethane foam was joint research with Kameda laboratory, Tokyo University of Agriculture and Technology. I appreciate Masaharu Kameda for giving me an opportunity for the joint research. Measurement of the rheology of polyurethane foam was performed with the rheometer of Osamu Kuwano. I thank him for lending it and giving me fruitful advice. The technical part of the experiments was performed by the members of the Kameda laboratory. I thank Shiori Takeda, Shu Sato, and Kazuya Hirota. In particular, Shiori Takeda joined the joint research for three years. Her outstanding technical skill and admirable research attitude were of help to my Ph. D. work. I am also grateful to TOHO Chemical Industry Co., Ltd. for providing the polyol and polyisocyanate that were used in the experiments.

During my internship at the University of Canterbury in New Zealand, I have spent a great time thanks to people there, especially Darren Gravley and Ben Kennedy. I acknowledge them for accepting me warmly and guiding me to the Taupo volcano. I also thank Takeshi Hasegawa at Ibaraki University for allowing me an opportunity to study in New Zealand.

Many members of the Earthquake Research Institute have contributed their expertise through formal and informal discussions. I thank, in particular, Fukashi Maeno for precious advice throughout the geological part of this thesis. He taught me some fundamental techniques to analyze pyroclasts. I am also grateful for Minoru Takeo, Takao Ohminato, Yosuke Aoki, Yujiro Suzuki, Jun Oikawa, and graduated students for insightful discussion in the physical volcanology seminar. Much of the experimental apparatus used in this project was crafted in the laboratory for technical support by Masayuki Uchida. Taking SEM image of pumice was supported by Natsumi Hokanishi and Atsushi Yasuda. I thank them. Discussion with my colleagues was a great motivation to continue this project. I feel grateful for, especially, Yo Kanno and Kazuya Yamakawa, who spent four years with me in the same laboratory and worked hard together.

Finally, I would like to convey great thankfulness to my family and friends who have always supported me and cheered me up. Thank you.

This project was supported by JSPS KAKENHI Grant Number 16H04039, Grant-in-Aid for JSPS Research Fellowship 17J05094, and the Joint Usage Program of the Earthquake Research Institute, University of Tokyo (2017B01).

Abstract

Bubble textures in pumice have been thought to reflect the history of magma ascent. Thus, it is valuable to create a new analysis method based on the morphological variables, such as bubble size, bubble number density, and bubble shape. The purpose of this thesis is to study the shape of deformed bubbles in various ways and develop a new scheme to connect bubble textures with the dynamics of explosive eruptions. Pumice containing highly deformed bubbles like tubes is called as tube pumice, and it is thought to record the flow history of magma up to fragmentation surface. In order to extract magma flow style, especially the velocity profile, from such a deformed bubble structure, it is necessary to solve the following three problems. (1) Calculate transient bubble deformation. (2) Evaluate the effect of bubble interaction on its shape. and (3) Calculate bubble deformation in an arbitrary velocity field.

First, using the droplet deformation model of Jackson and Tucker (2003), I developed a model that can calculate the transient deformation of a single bubble in an arbitrary velocity field. Next, to evaluate the interaction between bubbles, I performed tensile experiments with a solidifying foam. By comparing the experimental results of bubble shape with the numerical simulations, I confirmed that the average shape of bubbles coincided with the theoretical deformation model of a single bubble. This result suggests that the average of bubbles in pumice can be compared with the numerical simulation of a bubble in a conduit flow.

Next, the bubble deformation model and the quasi-two-dimensional steady conduit flow model were combined to solve the bubble deformation in the conduit. I adapt three rheological models to reproduce various velocity profiles. In the Newtonian isothermal fluid, the velocity profile across the conduit became parabolic. On the other hand, in the fluid with viscous heating, the temperature near the conduit wall rose up sharply, leading to a strong reduction in viscosity. The velocity profile changes from a parabolic shape to a plug-like shape just above the conduit inlet. The bubble shape at the fragmentation surface depends significantly on the velocity profile. The parabolic velocity profile produced highly elongated bubbles deformed mainly by simple shear, but the plug-like velocity profile produced less elongated bubbles deformed primarily by pure shear.

Finally, I conducted a bubble structure analysis of pumice erupted at Taupo Volcano in order to discuss which velocity profile was reasonable. As a result of the analysis, it was found that the plinian eruption had a single peak in the bubble shape distribution, while the ignimbrite eruption had a broad distribution and contained highly elongated bubbles. The comparison of the natural bubble textures with the simulation results suggested that the velocity profile of the plinian eruption was close to a plug-like shape. The reason why the ignimbrite eruption produced a number of tube pumice was explained by shallowing the transition depth at which the velocity profile changed from parabolic to plug-like.

The velocity profile in a conduit flow is closely related to several essential eruption processes, such as degassing and brittle fragmentation. It is of great significance to give constraints to the velocity profile from the natural quantitative observation of pyroclasts.

Contents

Chapter 1

Introduction

The vesiculation of magma is essential in the eruption dynamics of volcanoes, but it is difficult to observe it directly. Textural analysis of pyroclasts can reveal some information, because bubbles in pyroclasts records the vesiculation processes that occurred in the magma (e.g., *Klug et al.*, 2002; *Moitra et al.*, 2013). Many researchers have sought to infer the eruption dynamics of volcanoes by analyzing bubble textures, including number density (*Klug and Cashman*, 1994; *Toramaru*, 2006), size distribution (*Gaonac'h et al.*, 1996; *Giachetti et al.*, 2011), orientation (*Coward*, 1980; *Rust et al.*, 2003), and permeability (*Wright et al.*, 2006, 2009).

Contrary to these morphological variables which reflect the vesiculation processes in a conduit, bubble shape is thought to record the deformation field during magma ascent. Deformation field in magma, which is described by a function of strain and strain rate, has a significant meaning in the dynamics of explosive eruptions. Fragmentation of vesicular magma, which is characterized by a rheological transition from ductile to brittle behavior, is controlled by strain rate as well as viscosity (*Dingwell*, 1996; *Papale*, 1999). The development of permeable porous networks in magma ascending in a conduit, which controls the explosive to non-explosive transition through degassing, is controlled by strain and strain rate (*Okumura et al.*, 2008; *Caricchi et al.*, 2011; *Shields et al.*, 2014).

In this thesis, I focus on the shape of bubbles preserved in pyroclasts. On the basis of the dynamics of bubble deformation, I try to infer the magma flow style during magma ascent. The information of the shear field estimated from natural pyroclasts will be helpful to connect the experimental and theoretical studies to natural eruptions.

The rest of this chapter introduces several notable previous studies about bubble shapes and discusses some problems which should be taken into account. Section 1.1 describes theoretical studies about bubble deformation in a viscous fluid and applications of those studies into bubble shapes in pyroclasts. Section 1.2 introduces tube pumice, which is our research target, from the geological, experimental, and tomographic viewpoints. Section 1.3 discusses the problems of analyzing bubble shapes in tube pumice. Finally, section 1.4 describes the aim and framework of this thesis.

1.1 Bubble deformation

1.1.1 Theoretical studies

In geology and mechanics, a deformation field is frequently expressed by the combination of simple and pure shear deformation. Simple shear is a two-dimensional deformation in which parallel planes in a material remain parallel and maintain a constant distance while translating relative to each other (Fig. 1.1b). Pure shear is a homogeneous axisymetric elongation (Fig. 1.1c). Both shear deformations keep a constant volume during deformation. Deformation of a bubble in these representative shear flows have been experimentally and theoretically studied.

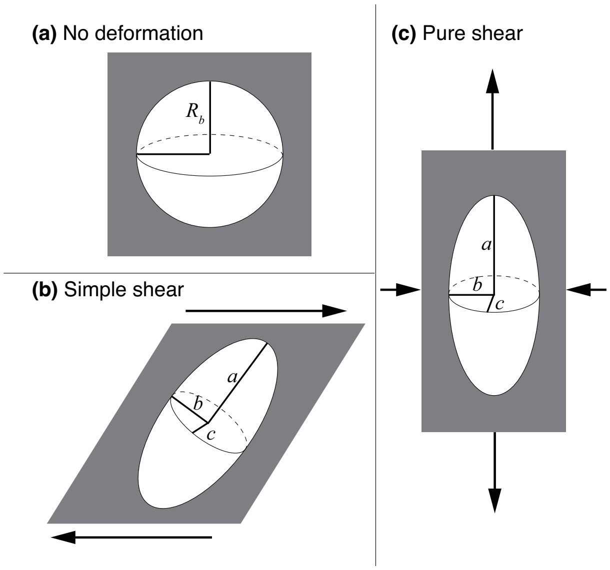

Figure 1.1: Shapes of (a) a non-deformed bubble, (b) a bubble deformed by simple shear, and (c) a bubble deformed by pure shear.

Bubble deformation is controlled by two stresses: viscous and surface tension. Viscous stress causes a spherical bubble to become elongated, whereas surface tension stress returns an elongate bubble to a spherical shape. The competition between these two stresses is expressed by a capillary number, Ca, which is defined as

$$Ca = \frac{R_b \dot{\gamma} \eta}{\Gamma}, \tag{1.1}$$

where R_b is the radius of a spherical bubble, $\dot{\gamma}$ is the shear rate, η is the viscosity of the fluid phase, and Γ is the surface tension. In pure shear deformation, $\dot{\gamma}$ is replaced by the pure shear rate $\dot{\epsilon}$ (see section 3.2.6).

The steady shape of a bubble emplaced in a low Reynolds number flow depends on the capillary number and the viscosity ratio λ of the fluid in the bubble to matrix fluid. The theoretical relationships between Ca and bubble shape for simple shear and pure shear are summarized in Table 1.1. The shape of a bubble is quantified with a deformation degree D given by

$$D = \frac{a-c}{a+c}, \tag{1.2}$$

where a and c represent the long and short axes of the bubble, respectively. The dependence of λ on bubble shapes in magma is negligible because the viscosity ratio is extremely small ($10^{-17} < \lambda < 10^{-6}$). It is known that the theoretical predictions of the shape of a deformed bubble agree well with the experimental data (*Taylor*, 1934; *Rust and Manga*, 2002). Fig. 1.2 shows the steady shape of a deformed bubble in simple shear flow as a function of the capillary number (*Rust and Manga*, 2002). The analytical equation for the small deformation is applicable to $Ca < 0.5$, and that for the large deformation is applicable to $Ca > 0.5$.

Table 1.1: Theoretical equations of a steady bubble shape in simple and pure shear flow

	Simple shear	Pure shear	Reference
Small deformation ($Ca \ll 1$)	$D = Ca$	$D = 2Ca$	*Taylor* (1934)
Large deformation ($Ca \gg 1$)	$a/R_b = 3.45Ca^{1/2}$	$a/R_b = 20Ca^2$	*Hinch and Acrivos* (1980) *Acrivos and Lo* (1978)

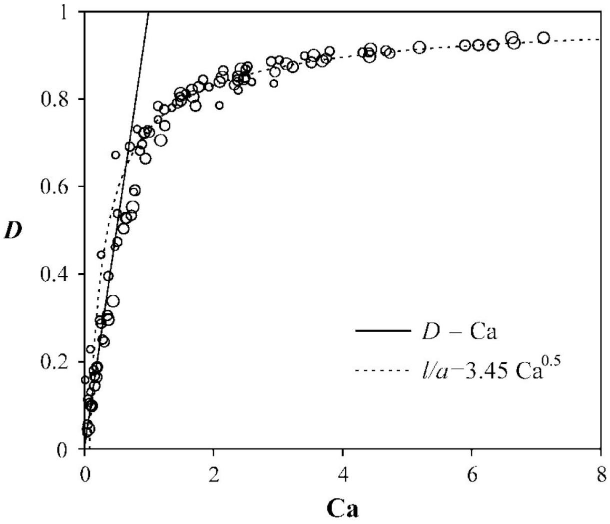

Figure 1.2: Experimental data of bubble deformation degree in simple shear flow with $\lambda \ll 1$ and $Re \ll 1$ (*Rust and Manga*, 2002, Fig. 3). Steady bubble shape depends on the capillary number. The solid line is the analytical solution of the steady bubble shape based on the small deformation theory, $D = Ca$ (*Taylor*, 1934), and the dashed curve is based on the large deformation theory, $a/R_b = 3.45Ca^{1/2}$, (*Hinch and Acrivos*, 1980).

The bubble deformation degree D has two advantages in analyzing deformed bubbles within pumice.

First, it characterizes the elongation, which is the essential factor of the shear fields (*Rust and Manga*, 2002; *Rust et al.*, 2003; *Rust and Cashman*, 2007). Some shear fields, such as simple shear, change not only the long and short axes of a bubble but the median axis. However, it will be challenging to deal with the information about the median axis, because of the complexity of the shear field in a conduit. As shown in chapter 5, a bubble within pumice is far from an ideal ellipsoid. I think that the information about the median axis is easily affected by the additional effect, such as bubble interaction and crystal.

Second, the bubble deformation degree can be measured by a two-dimensional approach and be applicable to a large number of pumice. The measurement of the median axis needs a three-dimensional analysis, such as X-ray computed tomography. However, this method is difficult to analyze a statistically sufficient number of pumice, because of the long measurement time. The purpose of this thesis is to connect to bubble texture with the dynamics of a conduit flow. Therefore, it is required to analyze the large number of pumice (at least 100 clasts).

Following the above reasons, I characterize the bubble texture within pumice by the bubble deformation degree.

1.1.2 Application of the dynamics of bubble deformation to natural volcanic rocks

Based on the theory of steady bubble shape, previous studies inferred the shear environments which produced deformed bubbles preserved in volcanic rocks.

Rust et al. (2003) analyzed bubble shapes within obsidian, trying to distinguish the flow types (simple shear vs. pure shear) and to calculate shear rates and shear stresses. Fig. 1.3 shows deformed bubbles within obsidian from a pyroclastic fall deposit (Rock Mesa). The bubble deformation degrees increase with the equivalent radius, which the theory explains as the viscous stress ($\eta\dot{\gamma}$) overcomes the surface tension stress (Γ/R_b). Assuming that the bubbles were deformed in simple shear and applying the theoretical relation as shown in Table 1.1, *Rust et al.* (2003) estimated $1.5 \times 10^5 \leq Ca/R_b \leq 3.0 \times 10^5\ \mathrm{m}^{-1}$. Using $\eta = 10^{6.7}\ \mathrm{Pa} \cdot \mathrm{s}$ and $\Gamma = 0.3\ \mathrm{N/m}$, they calculated the shear rate, $\dot{\gamma} = 1 \times 10^{-2}\ \mathrm{s}^{-1}$, and the shear stress, $\sigma = 60\ \mathrm{kPa}$. The calculated shear rate for the obsidian pyroclast was much higher than that for the effusive obsidian flow. For example, the obsidian flow sample from Big Glass Mountain recorded the low shear rate ($10^{-6.9} - 10^{-6.6}\ \mathrm{s}^{-1}$). The different shear rates between explosive and effusive eruptions were thought to reflect the distinct physical processes.

The technique of analyzing bubble shapes in obsidian was also applied to the explosive eruption in Newberry volcano, and revealed the time scales and mechanisms of pre-fragmentation magma ascent (*Rust and Cashman*, 2007).

1.2 Tube pumice

Tube pumice (Fig. 1.4) is a common product of explosive silicic eruptions forming calderas. It is composed of highly elongated tube-like bubbles. No standard definition of tube pumice exists at present, but *Wright et al.* (2009) defined it as a pumice having bubbles with an aspect ratio greater than 5:1. Such characteristic pumice is thought to record a particular history of pre-fragmentation shear fields in the conduit.

From the viewpoint of magma fragmentation, *Marti et al.* (1999) focused on tube pumice of Ramadas caldera, and proposed a conceptual idea that tube pumice is a well-preserved magmatic 'strain marker' of the stress state immediately before and during fragmentation. The existence of tube-like bubbles and kink bands

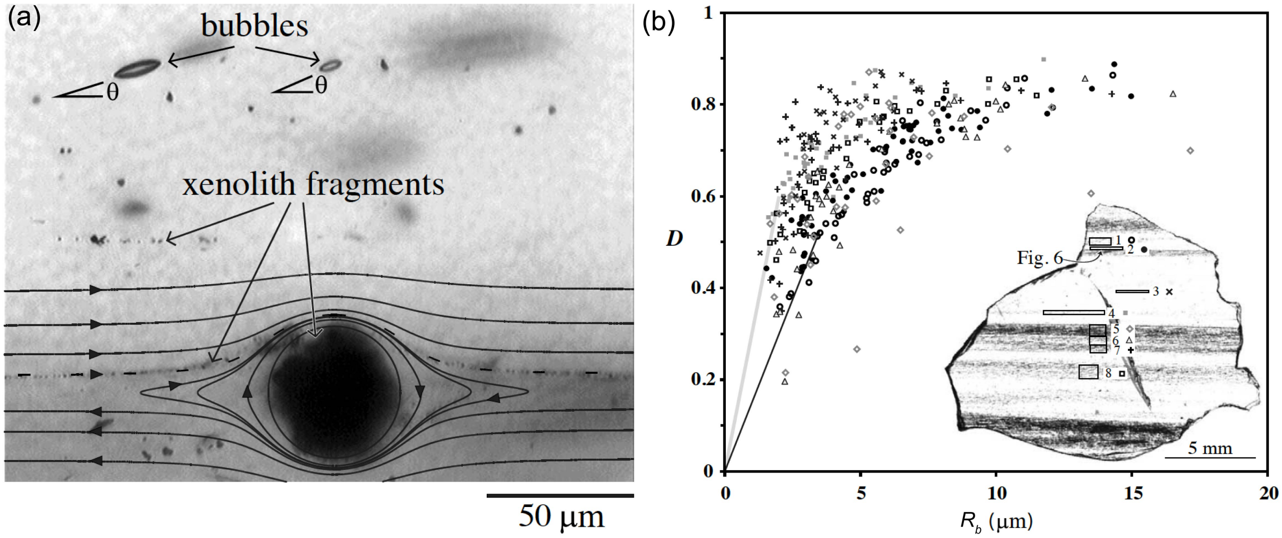

Figure 1.3: Deformed bubbles in a obsidian clast from a pyroclastic fall deposit, Rock Mesa (*Rust et al.*, 2003, (a) Fig. 6, (b) Fig. 7). (a) A thin section of a sample. (b) Bubble deformation degrees as a function of spherical bubble radius measured in two-dimensional images. The thick gray line is $D/R_b = 3.0 \times 10^5\ \mathrm{m}^{-1}$, and the thin black line is $D/R_b = 1.5 \times 10^5\ \mathrm{m}^{-1}$.

in fragments reflects the evolutions of the magma's mechanical response from viscous behaviour through the plastic or viscoelastic stage, and finally to brittle behaviour.

Tube pumice has also been investigated with respect to permeability. Using the measurements of porosity and permeability, *Wright et al.* (2006) showed that bubble deformation increases the permeability parallel to bubble elongation.

Over the past 20 years, tube pumice has been investigated, with linked to the essential processes of eruptions such as magma fragmentation and permeable network formation. The following subsections summarize the geological, experimental, and micro-structural studies about tube pumice.

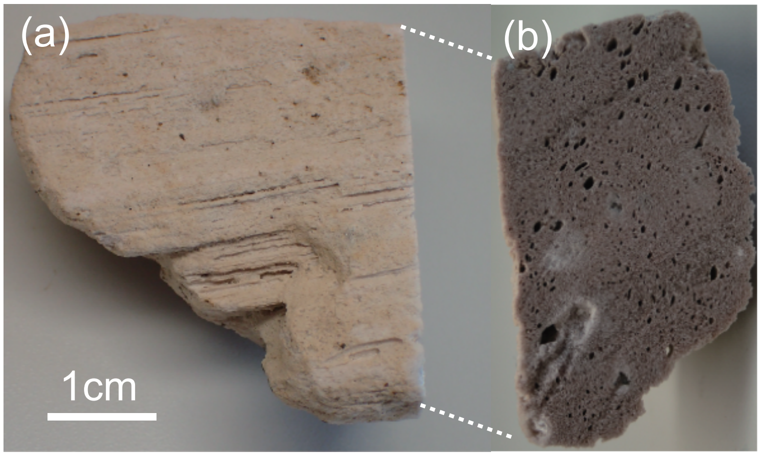

Figure 1.4: Tube pumice from the ignimbrite in Toya caldera. (a) Top view. (b) Side view.

1.2.1 Geological studies

Tube pumice was found in fall and flow deposits of explosive silicic eruptions, especially caldera-forming eruptions. In geology, tube pumice has been considered as a key factor in estimating temporal and spatial variations in a conduit flow.

Taddeucci and Wohletz (2001) analyzed juvenile pyroclasts of a plinian fall deposit and inter-layered ash-flow beds in the Minoan eruption, and showed that bubbles within pumices become more elongated toward the ash flow layer (Fig. 1.5a). This stratigraphic increase in the relative abundance of tube pumice was interpreted as resulting from the increase in shear stress in the flowing magma, which was triggered by the collapse of the conduit walls. Such an increase in the relative abundance of tube pumice toward a flow event was observed in other volcanoes (*Polacci et al.*, 2003; *Houghton et al.*, 2010).

Polacci et al. (2001) performed textural analyses of white and gray pumices of the plinian and pyroclastic flow deposits of the 1991 Pinatubo eruption. White pumice was characterized by higher vesicularity and deformed bubbles, while gray pumice showed lower vesicularity and less deformed bubbles. The coexistence of white and gray pumices with distinct textures was interpreted as the results of the intense shear localization and viscous dissipation at the conduit walls (Fig. 1.5b). Highly deformed bubbles in white pumices were formed in the conduit center where the magma sharply accelerated up to the fragmentation surface (pure shear). The bubbles in gray pumices were deformed around the conduit walls where the melt viscosity is quite small due to intense viscous heating. After fragmentation, the bubbles in the viscous-heating region might have returned to spherical shapes due to surface tension.

Similarly, *Polacci et al.* (2003) presented a textural characterization of pumice clasts from the plinian fall deposit directly underlying the Campanian ignimbrite deposit. Based on the macroscopic texture and clast density, pumice clasts were classified into microvesicular (heterogeneous bubbles), tube (elongated bubbles), and expanded (coalesced/inflated bubbles types). The frequency distribution of pumice types revealed that the proportion of tube pumices increased toward the ignimbrite deposit (Fig. 1.5c), which was interpreted as relating to the change of eruptive regime (convecting/collapsing) and to the onset of caldera collapse. They considered that tube pumice was formed by higher velocity gradients and shear stresses at the conduit walls (Fig. 1.5d). Tube pumice found in the submarine eruption of Havre volcano, Kermadec Arc, was also thought to be elongated around the conduit walls (*Mitchell et al.*, 2019).

Although changes in the relative abundance of tube pumice have been observed and regarded as indicators of temporal and spatial evolutions of conduit flows, the shear field in which bubbles were elongated was not elucidated. In previous studies, two mechanisms have been proposed to deform bubbles in the conduit: simple and pure shear (e.g., *Palladino et al.*, 2008; *Bouvet de Maisonneuve et al.*, 2009; *Dingwell et al.*, 2016). Fig. 1.6 shows the schematic image of bubble deformation in a conduit. Near the conduit wall, bubbles are deformed by simple shear that is the velocity gradient across the conduit. As magma ascends in a conduit, pressure decreases, leading to gas exsolution and bubble inflation. The magma consequently accelerates, driving pure shear deformation, which is intense just below the fragmentation surface. Although the mechanism causing tube pumice is key information to assess the shear field of the conduit flow, this dispute (simple vs. pure shear) has not been elucidated.

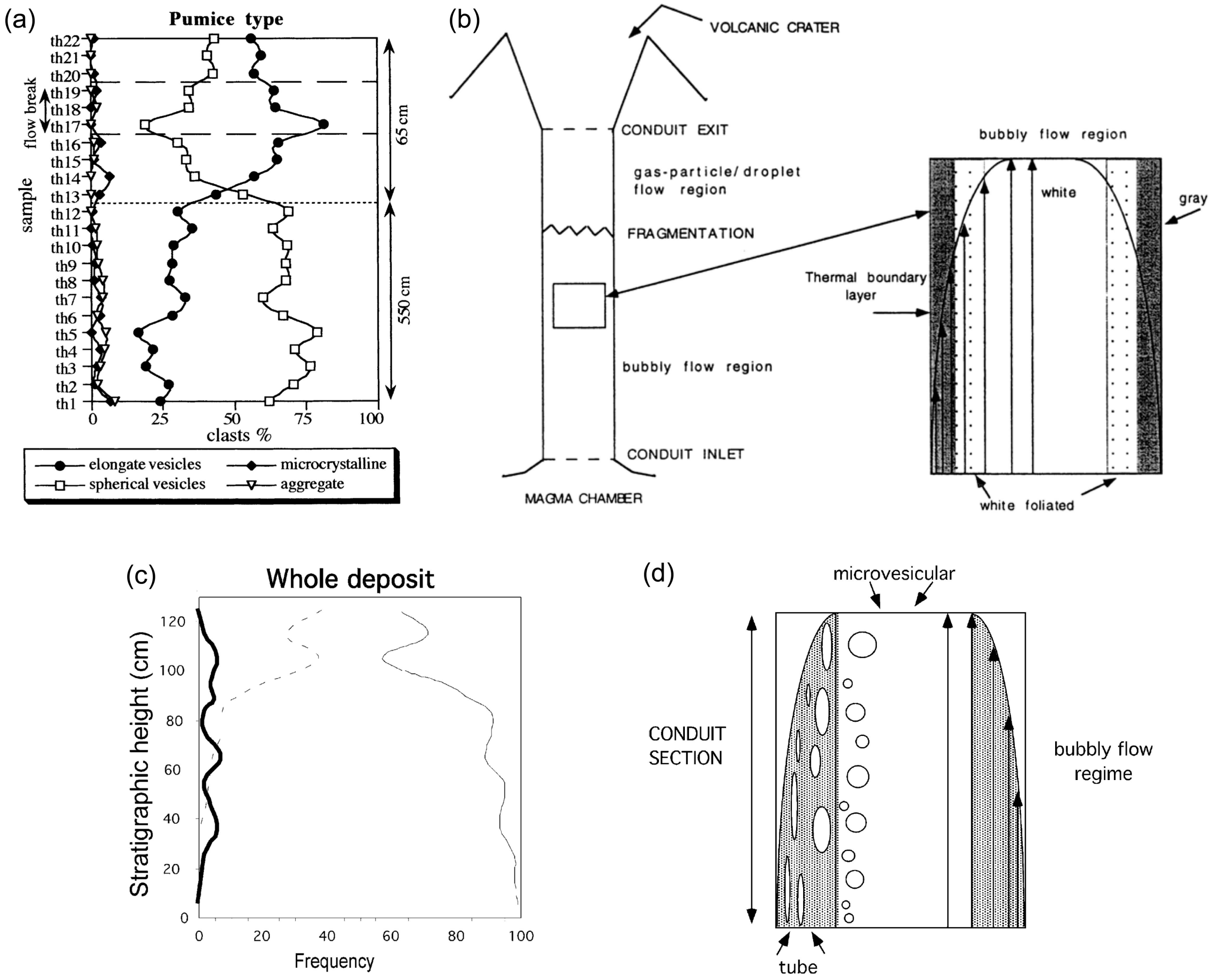

Figure 1.5: (a) Relative abundance of the pumice types in the plinian fall deposit of the Minoan eruption, plotted against the stratigraphic position (*Taddeucci and Wohletz*, 2001, Fig. 11). (b) Schematic conduit image of the 1991 Pinatubo eruption (*Polacci et al.*, 2001, Fig. 6). White pumice (tube pumice) was formed in the conduit center, and gray pumice composed of less elongated bubbles was formed around the conduit walls where viscous heating was intense. (c) The relative abundance of the pumice types in the plinian fall deposit of the Campanian ignimbrite eruption (*Polacci et al.*, 2003, Fig. 4). Dashed, thin, bold lines indicate tube pumice, microvesicular, expanded pumices, respectively. Campanian ignimbrite deposit overlies the fall deposit. (d) Schematic image of the distribution of microvesicular and tube pumices in the conduit of the Campanian ignimbrite eruption (*Polacci et al.*, 2003, Fig. 10). Tube pumice was formed in the region near the conduit walls.

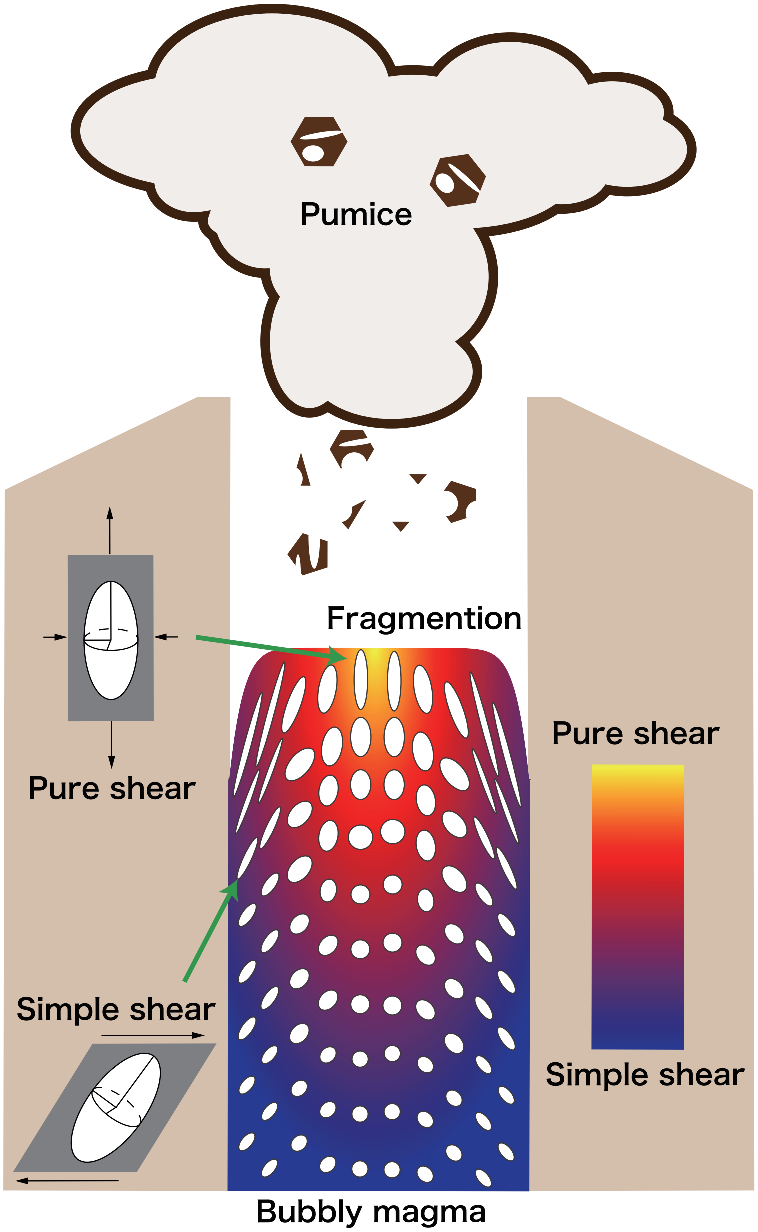

Figure 1.6: Schematic image of bubble deformation in a conduit (modified from *Dingwell et al.* (2016)). Strength of simple and pure shear is qualitatively shown by the gradation from blue to yellow.

1.2.2 Experimental studies

Artificially generating tube pumice in a laboratory is useful in determining the formation mechanism of tube pumice. To our knowledge, products having textures that are similar to tube pumice have been made in fragmentation experiments of gum rosin in acetone (*Phillips et al.*, 1995) and rhyolitic melt (*Martel et al.*, 2000).

Phillips et al. (1995) presented the first experimental investigation of gum rosin-acetone (GRA) solution as an analogue material of bubbly magma. The GRA solution increases its viscosity and solidifies due to evaporation of the solvent at low pressure, so that it is similar to magma that increases its viscosity under decompression due to dehydration. The decompression experiments of GRA solution produced a solid end-product containing tube-like bubbles.

Martel et al. (2000) performed the first fragmentation experiment with two-phase (melt+gas) rhyolitic systems under high temperature and high pressure. Since the melt viscosity increases by degassing of volatile and cooling from air, the fragmented samples quenched and preserved the pre-fragmentation bubble shapes. This fragmentation experiment generated both tube pumice and isotropic pumice which is composed of spherical bubbles (Fig. 1.7). Fragments of which vesicularity is less than 50 vol$\%$ only displayed spherical bubbles, but those above 50 vol$\%$ showed either tube-like or spherical bubbles. The authors did not conclude why isotropic or tube pumices had been generated, but they inferred that the sample holder might have restricted lateral bubble expansion and facilitated the unidirectional deformation.

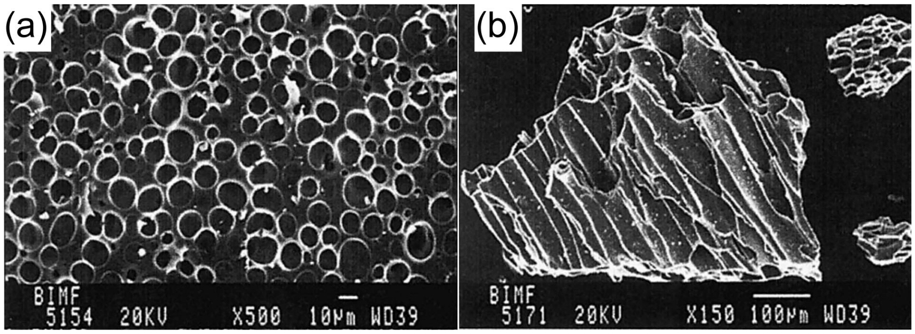

Figure 1.7: SEM images of fragmented samples in the fragmentation experiments by (*Martel et al.*, 2000, Fig. 2). (a) Isotropic pumice. (b) Tube pumice.

1.2.3 Micro-structural studies

X-ray computed tomography of tube pumice has been performed for permeability calculation. High resolution three-dimensional images collected at synchrotron facilities enabled to simulate gas flow within tube pumice by the lattice Boltzman method (*Wright et al.*, 2006; *Degruyter et al.*, 2010a).

One of the remarkable micro-structural studies about tube pumice is *Dingwell et al.* (2016). Using neutron computed tomography, the authors succeeded in resolving thin glass walls and obtaining the detailed three-dimensional images of tube pumice from the Ramadas caldera, Argentina. Fig. 1.8 shows the major axis lengths of bubbles within tube pumice compared with their equivalent radii. Using the theoretical steady shape of a single bubble under simple or pure shear flow (Table. 1.1), the authors estimated the strain rate during bubble deformation. Assuming that shape relaxation after fragmentation made the scatter of bubbles having the same bubble radius, they fitted the steady solution to the upper limit of the scattered distribution (most elongated bubbles) (Fig. 1.8b). They thought the elongated bubbles (upper distribution) might have been quenched and the less elongated bubbles (lower distribution) might have been relaxed. The authors concluded that the bubbles within the tube pumice were deformed by simple shear, because the fitting curve for pure shear required a nonphysical and infinitely fast cooling rate to cover the whole distribution. The estimated strain rate was $10^{-2}\,\mathrm{s}^{-1}$.

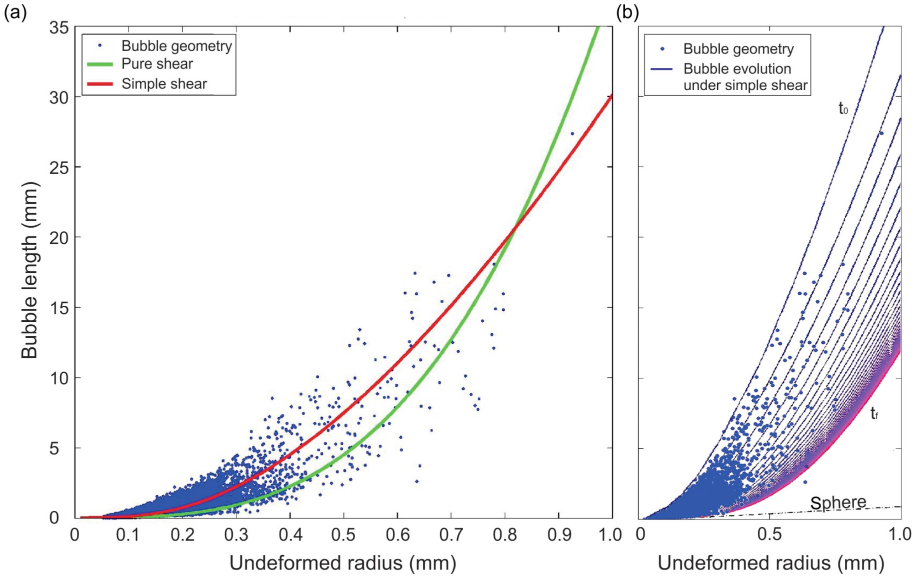

Figure 1.8: The distribution of bubble shapes within tube pumice from the Ramadas caldera (*Dingwell et al.*, 2016, Fig. 8). The major axis length is plotted against the spherical bubble radius. (a) Measured bubbles shapes are compared to the steady bubble shapes for simple (red) and pure shear (green). (b) The authors fitted the analytical solution of the steady bubble shape to the upper limit of the distribution. The scattered distribution of major axis length was explained by shape relaxation after fragmentation.

1.3 Problems of analyzing bubble shapes in tube pumice

Although *Dingwell et al.* (2016) concluded that the bubbles within the tube pumice were deformed by simple shear, there are some important issues that were not taken account of but cannot be ignored. The first issue is transient deformation, whereby bubble deformation stops on the way to reach the steady state because of insufficient strain. The second issue is bubble interaction including both bubble coalescence and the disturbance of the shear field around each bubble. These issues have already been pointed out by *Rust et al.* (2003). In addition to these problems, I proposed third issue: the superposition of simple shear, pure shear, and volumetric shear fields.

1.3.1 Transient deformation

The transient effect of finite strain on bubble deformation has been investigated experimentally. For example, *Okumura et al.* (2008) performed deformation experiments on vesiculated rhyolite melts at high temperatures by twisting columnar specimens, revealing that the degree of bubble elongation increases with increasing shear strain at constant Ca. This result indicates that, in a transient state, a bubble shape is not determined only by Ca as its steady-state form but depends on both Ca and accumulated total strain (defined as time integration of the strain rate that the bubble experiences). Strain-dependent bubble shapes have also been observed in other experiments (*Pistone et al.*, 2012; *Shields et al.*, 2014).

Bubbles in a conduit flow do not always get enough strain to attain the steady shape. In fact, *Rust and Cashman* (2007) reported that bubbles in some obsidian clasts from Newberry volcano recorded transient deformation. Because the existing analysis method for bubble shapes in volcanic rocks was based on the analytical solution for a steady-state, a bubble deformation model which can calculate large transient deformation is required.

1.3.2 Bubble interaction among bubbles

The effects of interactions among bubbles have been examined by numerical simulations. Using a series of three-dimensional boundary integrals and lattice Boltzmann methods, *Manga et al.* (1998) and *Huber et al.* (2013) calculated the deformation of multiple bubbles for a constant Ca. The simulation of *Huber et al.* (2013) showed that the average deformation of many bubbles is slightly smaller than that of a single bubble when $Ca > 0.5$; the opposite result is found for $Ca < 0.5$, because of the shear thinning effect of the effective viscosity. The deviation from a single bubble can be conveniently explained by a mean field approach, whereby the viscous stress acting on a bubble's surface is evaluated by the effective viscosity of a bubbly flow instead of the viscosity of a fluid phase. The mean field approach can be applied to moderately concentrated emulsions ($\phi \leq 0.3$), where ϕ is the dispersed-phase volume fraction (*Loewenberg*, 1998).

The effect of bubble interaction can be negligible when analyzing bubble shapes within an obsidian clast whose vesicularity is quite small. *Manga and Loewenberg* (2001) indicated that even for $\phi = 0.25$, bubble interaction results in a less than 10% overestimation of shear stress and shear rate. To the contrary, the effect of bubble interaction will be significant in pumice with high vesicularity. The validity of the mean-field approach to pumice should be confirmed. *Dingwell et al.* (2016) also mentioned the importance of experimental validation of the deformation model for high vesicularity.

1.3.3 Superposition of simple shear, pure shear, and volumetric fields

If bubbles are deformed by either simple or pure shear, the analytical solutions of a steady bubble shape can be applied to those bubbles. However, the shear field in a conduit is not composed of only either simple or pure shear component but is a mixture of both shear components as shown in Fig. 1.6. The previous idea of exclusively selecting either simple or pure shear is inadequate to depict the shear field in a conduit. In addition, bubble growth in response to decreasing pressure during an eruption has the potential to round a deformed bubble. This volumetric strain rate is assumed to be small in obsidian clasts because obsidians likely forms along conduit walls where the ascent velocity is low (*Rust et al.*, 2003), but will be more significant in pumice.

In order to comprehend the mixture of simple shear, pure shear, and volumetric strain rate fields in a conduit flow, a model which can calculate bubble deformation in arbitrary velocity gradient is required.

1.4 Aim and framework of this thesis

This thesis is written with the aim of getting information on the shear field in a conduit by analyzing bubble shapes in tube pumice. To overcome the three issues mentioned in section 1.3, I combined three different approaches and then analyzed bubble shapes within natural tube pumice found in Taupo volcano. The structure of this thesis is summarized in Fig. 1.9.

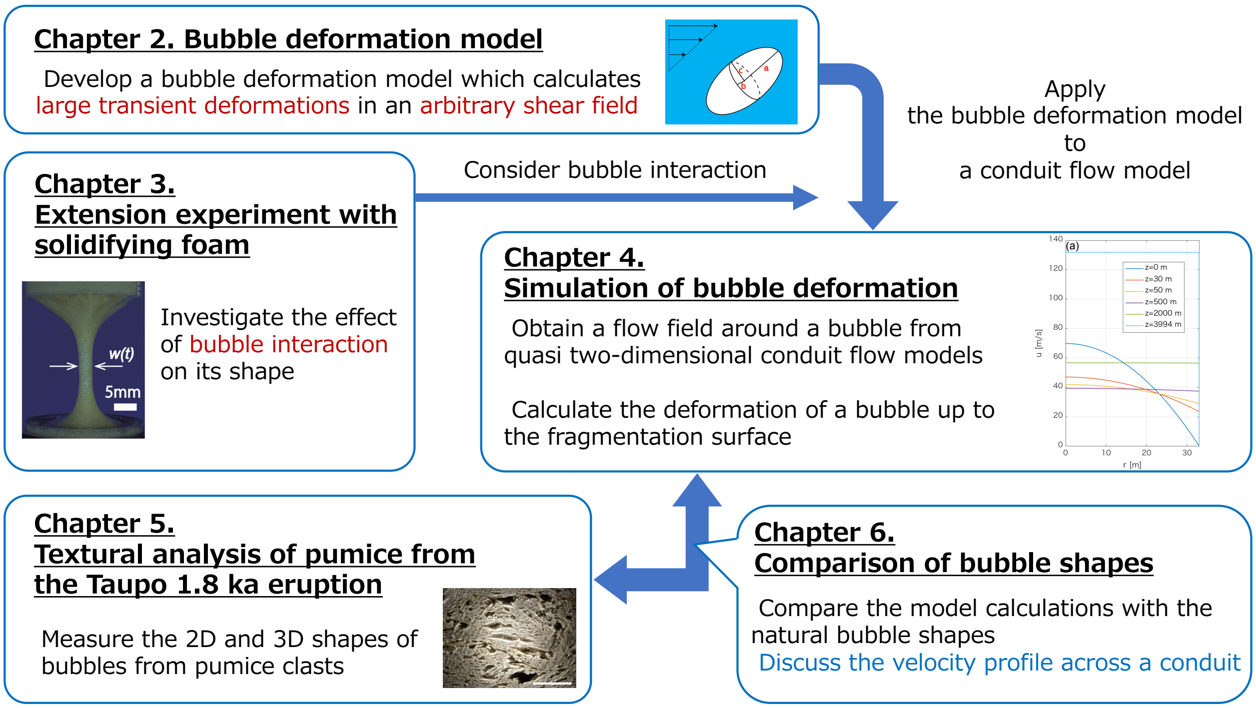

Figure 1.9: Structure of this thesis from chapter 2 to 6.

Firstly, a new bubble deformation model is developed, based on the existing deformation model of a single droplet proposed by *Jackson and Tucker* (2003). The new model can calculate large transient deformations in arbitrary velocity fields including shear and expansion. This model characterizes a bubble shape by a second-order tensor, and then numerically solves a time-development equation that describes the shape evolution of the bubble. The new model is able to simulate the deformation of a single bubble in the superposition of simple shear, pure shear, and volumetric field (bubble growth). The significance of calculating transient deformation is demonstrated through the re-analysis of the published data of bubble shapes in obsidian.

Secondly, I perform extensional experiments with a solidifying foam in order to evaluate bubble interaction. As an analogue material of magma, I use a polyurethane foam. This material undergoes vesiculation, deformation, and solidification at room temperature and atmospheric pressure. I can apply the foam a controlled pure shear deformation during solidification and get deformed bubble textures after solidification, which is similar to tube pumice. Combining the mean field approach with the new bubble deformation model, I analyze bubble shapes preserved in the solidified foam.

Thirdly, I calculate a quasi two-dimensional conduit flow based on the model of *Barmin et al.* (2004) and *Vedeneeva et al.* (2005), and combine it to the new bubble deformation model. The combined model can simulate the entire history of bubble deformation in the conduit flow, which is expected to depend on the velocity profile across a conduit. In this thesis, I consider a parabolic and plug-like velocity profile. The latter profile is produced by a shear-thinning model due to bubble deformation and a viscous-heating model. In order to compare the simulation results with bubble shapes preserved in natural pumice, which I analyzed latter, the input parameters are set assuming the 1.8 ka Taupo eruption.

Finally, I analyze bubble shapes preserved in pumice clasts from the 1.8 ka Taupo eruption, New Zealand. To compare natural bubble textures with numerical simulations, a statistically reasonable number of pumice clasts need to be analyzed. In this thesis, I measure bubble shapes in more than 1000 pumice clasts by a digital microscope with variable illumination function. This device makes a two-dimensional image of bubble texture from a cutting surface of a clast. Some pumice clasts were imaged in three-dimensions by Xray-computed tomography. The comparison of natural bubble textures with the numerical simulations gives valuable insights for the development of velocity profile and the accumulated strain just before fragmentation.

After this introduction, the thesis is organized as follows. Chapter 2 briefly explains the bubble deformation model of *Jackson and Tucker* (2003) ; I then readjust the parameters that they had arbitrarily determined in the model. The modified model agrees well with the results of the previously reported analogue experiments and analytical solutions. As a test of analyzing bubble shapes, I re-analyze the data of obsidian clasts published by *Rust and Cashman* (2007). In Chapter 3, I perform the extensional experiments with polyurethane foam, and measured bubble shapes in the solidified foams by using X-ray computed tomography. I confirm that the mean-field approach is valid even at high vesicularity. Chapter 4 shows the simulation of bubble deformation along and across the conduit. The distribution of bubble shapes at the fragmentation surface is calculated to be compared with the bubble shape distribution found in natural samples. Chapter 5 demonstrates the 2D and 3D analysis of bubbles shapes within pumice clasts from the 1.8 ka Tupo eruption. The developed 2D analysis shows good agreement with the 3D data obtained by the X-ray tomography. I also discuss the validity of data and the transition of eruptive style. In chapter 6, I compare the bubble shapes founded in Taupo volcano with the numerical simulation. I also simulate the conduit flow in an ignimbrite stage in the Taupo eruption. Finally, Chapter 7 discusses the obtained results and their implications for volcanic phenomena.

Chapter 2

Bubble deformation model

2.1 Introduction

The development of a bubble deformation model is essential for investigating large transient deformation of a bubble in a conduit flow. Interest in the model of deformable inclusions is not limited in volcanology. Since the dynamics of a droplet in an imposed flow field control the mechanical properties of polymer blends, several deformation models for a droplet have been developed in polymer science (*Minale*, 2010). In polymer science, the ratio of the viscosities of the droplet (η^*) and polymer matrix (η), $\lambda = \eta^*/\eta$, is close to unity. However, λ is much smaller than unity for a deforming bubble in a viscous magma flow. Therefore, the applicability of models developed in polymer science to the calculation of the shape evolution of a bubble in a magma flow needs to be examined. I expect these polymer-based models to be essentially valid, because the shapes of both a droplet and a bubble are determined by the same physics, with there being competition between viscous stress and surface tension stress on a droplet or bubble.

This chapter begins with a brief explanation of the droplet deformation model proposed by *Jackson and Tucker* (2003). I then modify the parameters that are somewhat arbitrarily determined in the model. The modified model agrees well with previously reported analogue experimental results and analytical solutions. I also improve the model to calculate the deformation induced by bubble expansion. In the last section, the developed model is applied to the published data of bubble shapes within obsidian clasts presented by *Rust and Cashman* (2007). Focusing on the relationship between bubble shape and radius, I am able to better estimate the strain and the deformation duration.

2.2 Brief introduction of Jackson and Tucker model

Jackson and Tucker (2003) developed a model to predict the transient shape evolution of an ellipsoidal Newtonian droplet suspended in a Newtonian matrix under shear flow. I use the term JT when referring to *Jackson and Tucker* (2003) and their droplet model. A single droplet is suspended in a uniform velocity flow which is expressed by the applied velocity gradient tensor $L_{ij}^{\infty} = \partial v_i^{\infty}/\partial x_j$, where v_i^{∞} is the applied velocity and x_i

is the spatial coordinate fixed to the space. This applied velocity gradient tensor also expresses the far-filed velocity field when the fluid does not have a volumetric component. The velocity gradient tensor is simply decomposed into asymmetric and symmetric parts:

$$L^{\infty}_{ij} = W^{\infty}_{ij} + D^{\infty}_{ij}, \tag{2.1}$$

$$W^{\infty}_{ij} = \frac{1}{2}(L^{\infty}_{ij} - L^{\infty}_{ji}), \tag{2.2}$$

$$D^{\infty}_{ij} = \frac{1}{2}(L^{\infty}_{ij} + L^{\infty}_{ji}), \tag{2.3}$$

where W^{∞}_{ij} and D^{∞}_{ij} are the applied vorticity tensor and the rate of deformation tensor, respectively. The JT model assumes negligible inertia and body forces, no translational motion, and no interactions among droplets.

2.2.1 Geometry of a droplet

The morphology of a droplet is expressed by a morphology tensor G_{ij} (*Wetzel and Tucker*, 2001). Positions on the surface of the droplet are described as

$$G_{ij}x_i x_j = 1, \tag{2.4}$$

where G_{ij} is a positive and symmetric second-order tensor and the droplet centroid is fixed at the origin of the spatial coordinate. The repetition of the subscripts indicates summation (Einstein summation convention). The eigenvectors of G_{ij} correspond to the principal axis directions of the droplet, and the eigenvalues of G_{ij} are the inverse squares of the principal semi-axes of the droplet. When the coordinates of semi-axes of the droplet match the principal axes of the ellipsoid, G_{ij} is expressed as

$$\hat{G}_{ij} = \begin{pmatrix} 1/a^2 & 0 & 0 \\ 0 & 1/b^2 & 0 \\ 0 & 0 & 1/c^2 \end{pmatrix}, \tag{2.5}$$

where a, b, and c ($a > b > c$) are the lengths of the three semi-axes of the droplet. A hat over a term means that the bases of a tensor are on the principal axes of the ellipsoid. The radius of an equivalent spherical bubble is given by $R_b = (abc)^{1/3}$. *Jackson and Tucker* (2003) took the material derivative of Eq. (2.4) to obtain the following evolution equation for G_{ij}:

$$\frac{DG_{ij}}{Dt} + L^{*}_{ki}G_{kj} + G_{ik}L^{*}_{kj} = 0, \tag{2.6}$$

where D/Dt represents the material derivative and L^{*}_{ij} is a second-order tensor having the form of a velocity gradient within and on the droplet surface. In fact, the velocity within the droplet must have the form of $L^{*}_{ij}x_j + v'_i$, where v'_i represents a recirculation motion of which the component normal to the surface vanishes at the droplet surface. The recirculation motion may be laminar, as JT considered, or turbulent. In either case, the stress caused by the recirculation is ignored, because I am interested only in cases having small droplet viscosity. Once L^*_{ij} is determined, the history of shape evolution can be obtained by Eq. (2.6). Therefore, constraining the droplet deformation requires L^*_{ij} to be obtained.

2.2.2 Velocity gradient tensor within a droplet

For a droplet with an arbitrary geometry, the solution to the Stokes equations becomes a complex velocity field within the droplet. However, *Eshelby* (1957) and *Bilby et al.* (1975) found that L^*_{ij} is uniform throughout an ellipsoidal droplet. They provided an analytical solution for the velocity field both within and around such a droplet. Using Eshelby's theory, *Wetzel and Tucker* (2001) developed a model for droplet deformation without surface tension. The droplet vorticity tensor $W^{*NoSurf}_{ij}$ and the droplet rate of deformation tensor $D^{*NoSurf}_{ij}$ are given by

$$
\begin{aligned}
W^{*NoSurf}_{ij} &= W^{\infty}_{ij} + C_{ijkl} D^{\infty}_{kl}, &(2.7)\\
D^{*NoSurf}_{ij} &= B_{ijkl} D^{\infty}_{kl}, &(2.8)
\end{aligned}
$$

where C_{ijkl} and B_{ijkl} are the vorticity and strain rate concentration tensors, respectively. These tensors are functions of the ellipsoid geometry and the viscosity ratio, and are calculated using the Eshelby tensor for isotropic incompressible materials (*Wetzel and Tucker*, 2001). When the principal axes match the spatial coordinate axes, C_{ijkl} in Eq. (2.7) vanishes. The JT model assumes that the droplet velocity gradient tensor must be decomposed into two terms due to the linearity of the Stokes equations: Eqs. (2.7) and (2.8) represent droplet deformation due to an external flow, whereas D^{*surf}_{ij} represents shape relaxation due to surface tension (see Appendix A). The JT model then yields the droplet velocity gradient for the ellipsoidal droplet $L^{*Eshelby}_{ij}$, where

$$
L^{*Eshelby}_{ij} = W^{\infty}_{ij} + C_{ijkl} D^{\infty}_{kl} + B_{ijkl} D^{\infty}_{kl} + D^{*surf}_{ij}. \tag{2.9}
$$

The first and second terms represent the vorticity within an ellipsoidal droplet, and the third and fourth terms represent the rate of deformation within the droplet.

A droplet shape with a small λ shows a transition from an ellipsoidal body to a slender body as its length increases (*Taylor*, 1934). The ellipsoidal body is defined as an axisymmetric shape with pointed ends. Following the slender body theory developed by *Khakhar and Ottino* (1986), JT gives the velocity gradient tensor in the slender droplet $L^{*slender}_{ij}$:

$$
L^{*slender}_{ij} = W^{\infty}_{ij} + \xi (D^{\infty}_{ik} m_k m_j - m_i m_k D^{\infty}_{kj}) + D^{*slender}_{ij} + D^{*axi}_{ij}, \tag{2.10}
$$

where $D^{*slender}_{ij}$ is the rate of deformation tensor within a slender droplet, which includes retraction of the longest axis; D^{*axi}_{ij} is the rate of deformation tensor representing cross-sectional relaxation due to surface tension (see Appendix A for more details of both tensors), which takes into account the evolution of a non-axisymmetric droplet into an axisymmetric one as its major length increases; m_i is a unit vector along the longest axis; and ξ

is an orientation parameter (determined empirically, following the procedure outlined in the following section). The first and second terms of Eq. (2.10) represent the vorticity within a slender-body droplet, and the third and fourth terms represent the rate of deformation within the droplet.

Given that a bubble's shape changes from ellipsoidal to slender in a gradual process, the JT model seamlessly connects the two models represented by Eqs. (2.9) and (2.10) as follows:

$$L^{*}_{ij} = f L^{*Eshelby}_{ij} + (1-f) L^{*slender}_{ij}, \tag{2.11}$$

where f $(0 \leq f \leq 1)$ is a blending function, defined as a function of a normalized bubble length a/R_b, such that $L^{*Eshelby}_{ij}$ dominates when a bubble is a compact ellipsoid and $L^{*slender}_{ij}$ dominates when it becomes tube-like. Both the blending function and the orientation parameter can be empirically adjusted for a specific phenomenon observed in polymer science.

2.3 Modification to Jackson and Tucker model

2.3.1 Transition from ellipsoid to slender-body

The JT model was originally developed for the deformation of a droplet with a viscosity close to that of the matrix fluid (i.e., $\lambda \sim 1$), and it was adjusted to fit experimental data for such a droplet. However, the viscosity ratio of a vapor bubble in silicate melt, which is the subject of the present study, is very small, in the range of $10^{-17} < \lambda < 10^{-6}$ (*Rust et al.*, 2003), and thus lies outside the scope of the JT model. Here I readjusted the two empirical functions of the JT model, f and ξ.

The JT model employs the blending function f to explain the experimentally determined critical capillary number for droplet breakup during planar elongation for cases where $\lambda > 10^{-5}$. I calculated the steady bubble shape by the JT model and compared the results with the experimental data of *Rust and Manga* (2002) for an air bubble. I then modified the blending function to obtain a good agreement between the model results and experimental deformation data:

$$f = \begin{cases} 1 & (a/R_b \leq 1.1), \\ 0.5\cos\left[\frac{\pi(a/R_b - 1.1)}{5}\left\{0.9\left(\frac{6.1}{a/R_b}\right) + 0.1\left(\frac{a/R_b}{6.1}\right)\right\}\right] + 0.5 & (1.1 < a/R_b \leq 6.1), \\ 0 & (a/R_b > 6.1). \end{cases} \tag{2.12}$$

This function is plotted in Fig. 2.1. The modified blending function switches from the Eshelby model to the slender-body model earlier than the blending function defined by JT.

The other empirical function, the orientation parameter ξ in the slender-body model, controls the rotation of the major axis of a bubble. For $\xi = 1$, the major axis of a bubble asymptotically approaches the external flow direction in simple shear. When $\xi > 1$, the major axis lies between the flow direction and the maximum tensile direction. JT set the orientation parameter ξ to match the critical capillary number for droplet-breakup in simple shear experiments. I modified the orientation parameter in the same way as the blending function,

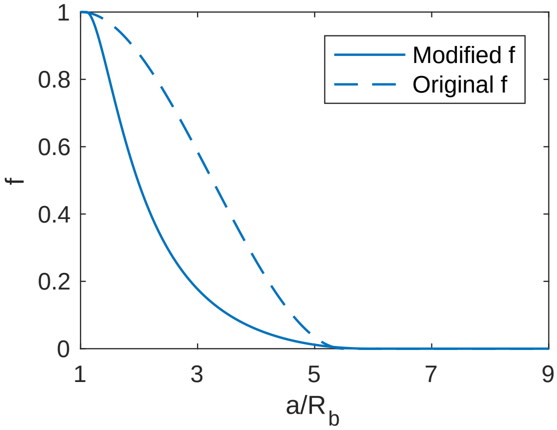

Figure 2.1: Blending function f with respect to the aspect ratio a/R_b. The solid line is the modified f, calculated from Eq. (2.12). The dashed line is the original f defined by *Jackson and Tucker* (2003).

taking account of bubble deformation. The new ξ is

$$\xi = \begin{cases} \xi^{Eshelby} & (a/R_b \leq 1.1), \\ 1 + 10.5237(a/R_b - 0.1)^{-2.83} & (1.1 < a/R_b \leq 6.1), \\ \xi^{slender} & (a/R_b > 6.1), \end{cases} \tag{2.13}$$

where

$$\xi^{Eshelby} = \frac{1 + (R_b/a)^3 + [1 - (R_b/a)^3](3I - 1)(\lambda - 1)}{1 - (R_b/a)^3 + [1 + (R_b/a)^3](3I - 1)(\lambda - 1)}, \tag{2.14}$$

$$I = \frac{\sqrt{1 - (R_b/a)^3} - (R_b/a)^3 \cosh^{-1}(a/R_b)^{3/2}}{2[1 - (R_b/a)^3]^{3/2}}, \tag{2.15}$$

$$\xi^{slender} = \frac{1 + 12.5(R_b/a)^3}{1 - 2.5(R_b/a)^3}, \tag{2.16}$$

and $\xi^{Eshelby}$ is the orientation parameter in the Eshelby model. It is calculated from the B_{ij} and C_{ij} components of the Eshelby model, and is based on the assumption of an axisymmetric droplet. (There is a misprint in JT concerning $\xi^{Eshelby}$.) The orientation parameter in the slender-body model $\xi^{slender}$ is derived from the model of *Khakhar and Ottino* (1986). Although JT introduced the slender-body model, which is based on *Khakhar and Ottino* (1986), they used the empirical function ξ, noting that Eq. (2.16) causes the model to yield unrealistic results. I avoided this issue by modifying the implementation of the Eshelby and slender-body theories when modeling the evolution of bubbles, and thus used Eq. (2.16) for the slender-body theory. Fig. 2.2 compares the ξ values used by *Jackson and Tucker* (2003) and this study.

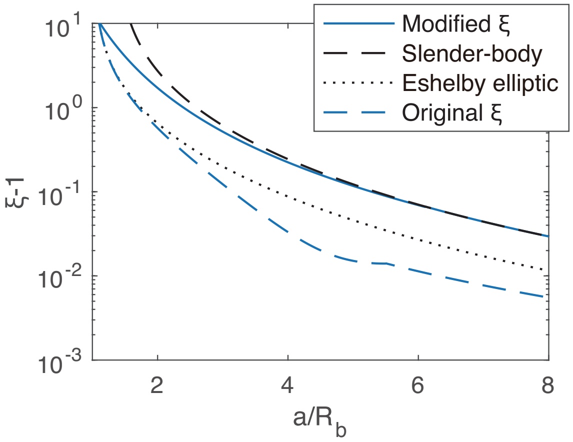

Figure 2.2: Orientation parameter ξ as a function of aspect ratio a/R_b. The solid blue line is the modified ξ curve used in this study, calculated from Eqs.(2.13)–(2.16). The dashed black line is the ξ curve for the slender-body theory calculated from Eq. (2.16). The dotted black line is the ξ curve based on Eshelby theory, calculated from Eqs. (2.14) and (2.15). The dashed blue line is the original ξ curve defined by *Jackson and Tucker* (2003).

2.3.2 Velocity gradient tensor for bubble expansion

The original JT model assumes a constant volume of a bubble during deformation. However, any bubbles in magma will increase in volume as the magma ascends in a conduit due to internal overpressure. When a bubble is non-spherical, an increase in volume driven by internal overpressure tends to moderate its elongation, even without surface tension. In this thesis, I further include the effect of bubble expansion on its shape. To simplify bubble expansion, I assume that bubbles do not coalesce, break up, or nucleate in the melt.

Velocity gradient for a liquid-gas mixture

I consider the velocity gradient tensor for a liquid-gas mixture flowing in a long circular conduit. I use the cylindrical coordinates (z, r, θ), where z is the elevation, r is the radial distance from the conduit center, and θ is the azimuth. Hereafter, the liquid-gas mixture is assumed to be a one-phase and to have an applied uniform velocity field (Fig. 2.3). The applied velocity gradient tensor within the mixture L^C_{ij} can be divided into two components:

$$L^C_{ij} = L^{Non}_{ij} + L^{Vol}_{ij} \tag{2.17}$$

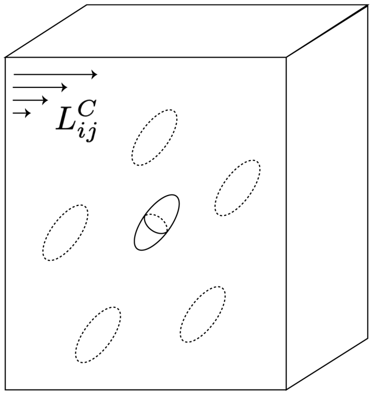

Figure 2.3: Schematic image of the gas-mixtrue.

where L_{ij}^{Non} is the non-volumetric component of the compressible fluid. The isotropic component L_{ij}^{Vol} represents the volumetric change due to bubble growth, given by

$$L_{ij}^{Vol} = \frac{1}{3}\text{trace}\left[L_{ij}^{C}\right]\begin{pmatrix} 1 & 0 & 0 \\ 0 & 1 & 0 \\ 0 & 0 & 1 \end{pmatrix}. \tag{2.18}$$

Because of the linearity of the Stokes equation, *Jackson and Tucker* (2003) assumes that the velocity gradient tensor within the drop L_{ij}^{*} is the sum of two terms, one for a applied flow without surface tension and one for retraction of a deformed bubble due to surface tension. This idea can be extended to the volumetric change, that is, L_{ij}^{C} is the sum of two terms, one for a non-volumetric component L_{ij}^{*Non} and one for a volumetric component L_{ij}^{*Vol}. Because L_{ij}^{*Non} is equal to L_{ij}^{*} defined by Eq. (2.11), the velocity gradient tensor within a bubble with growth can be expressed as

$$\begin{aligned} L_{ij}^{*} &= L_{ij}^{*Non} + L_{ij}^{*Vol} && (2.19) \\ L_{ij}^{*Non} &= fL_{ij}^{*Eshelby} + (1-f)L_{ij}^{*slender}. && (2.20) \end{aligned}$$

Keep in mind that $L_{ij}^{*Eshelby}$ and $L_{ij}^{*slender}$ in Eq. (2.20) must be calculated from L_{ij}^{Non} not L_{ij}^{C} because the JT model does not take account of the dilatational shear. Once I get L_{ij}^{*Vol}, I can calculate bubble deformation by substituting L_{ij}^{*} of Eq. (2.19) into the evolution equation of Eq. (2.6). A flowchart of the modified JT model is shown in Fig. 2.4. In the following paragraphs, I derive L_{ij}^{*Vol} by Eshelby theory (*Eshelby*, 1957) as used in the JT model.

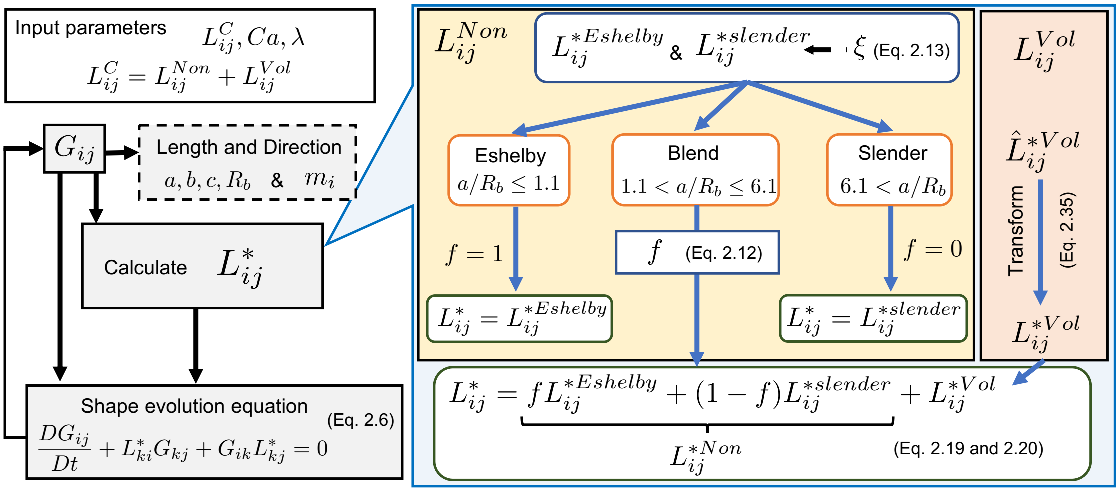

Figure 2.4: Flowchart showing the workflow of the modified JT model developed in the present study. Equation numbers in parentheses refer to equations in the main text.

An inclusion problem in an elastic medium

Before dealing with the problem of bubble expansion in viscous fluid, I consider the expansion of a cavity in an elastic medium. This problem is well studied, and a general theory has been established (e.g., *Aki and Richards*, 2002; *Davis*, 1986; *Amoruso and Crescentini*, 2009; *Mizuno et al.*, 2015). Consider an ellipsoidal cavity filled with fluid embedded in an elastic medium. It undergoes volumetric change because of fluid overpressure ΔP. The deformation of the cavity can be described by the so-called actual strain tensor e_{ij} in Eshelby theory. On the coordinate along the main axes of the ellipsoid, e_{ij} is represented as $\hat{e}_{ij}$:

$$\hat{e}_{ij} = \begin{pmatrix} \Delta a/a & 0 & 0 \\ 0 & \Delta b/b & 0 \\ 0 & 0 & \Delta c/c \end{pmatrix}, \tag{2.21}$$

where Δa, Δb, and Δc indicate the change of the semi-axis lengths, respectively. Here I follow the expression by *Mizuno et al.* (2015). Because $\hat{e}_{ij}$ has only diagonal components, they can be written as

$$\epsilon_i = \hat{e}_{ij}|_{i=j}\,. \tag{2.22}$$

Mizuno et al. (2015) related ϵ_i to ΔP by

$$\epsilon_i = \frac{\Delta P}{3k} S'_{ij} B'_{jk} U_k, \tag{2.23}$$

where k is the bulk modulus of the elastic medium and U_i is a vector with all components being one. S'_{ij} and B'_{ij} are defined as

$$S'_{ij} = S_{ijkl}(\nu)\Big|_{i=j,k=l}, \tag{2.24}$$

$$B'_{ij} = \left(\delta_{ij} - S'_{ij}\right)^{-1}, \tag{2.25}$$

where $S_{ijkl}(\nu)$ is the Eshelby tensor. Here, $S_{ijkl}(\nu)$ is given as a function of $\mathrm{Poisson's\ ratio}$ ν explicitly, although the Eshelby tensor used in the JT model assumes $\nu = 1/2$ for an incompressible material. Because the trace of $\hat{e}_{ij}$ is $\Delta V/V$, where ΔV is the volume change and V is the volume of the cavity before the volumetric change, I obtain

$$\frac{\Delta V}{V} = \frac{\Delta P}{3k} U_i S'_{ij} B'_{jk} U_k. \tag{2.26}$$

From Eqs. (2.23) and (2.26), I have

$$\epsilon_i = \frac{\Delta V}{V} \frac{S'_{ij} B'_{jk} U_k}{U_i S'_{ij} B'_{jk} U_k}. \tag{2.27}$$

An inclusion problem in a viscous fluid

The above derivation comes from the Eshelby theory for an elastic solid. *Eshelby* (1957) and *Bilby et al.* (1975) showed that the inclusion problem in an incompressible fluid with a low Reynolds number can be solved in the same manner as that in an elastic medium, as follows. In the elastic theory, the equation of equilibrium and the constitutive equation are given by

$$\frac{\partial \sigma_{ij}}{\partial x_j} = 0, \tag{2.28}$$

$$\sigma_{ij} = k\epsilon_{kk}\delta_{ij} + 2\mu\left(\epsilon_{ij} - \frac{1}{3}\epsilon_{kk}\delta_{ij}\right), \tag{2.29}$$

where σ_{ij} is the stress, $\epsilon_{ij} = \frac{1}{2}\left(\frac{\partial u_i}{\partial x_j} + \frac{\partial u_j}{\partial x_i}\right)$ is the strain tensor where u_i is the displacement vector, k is the bulk modulus, and μ is the shear modulus. The substitution of Eq. (2.29) into Eq. (2.28) gives

$$\frac{\partial}{\partial x_i}\left(k\epsilon_{kk}\right) + 2\eta\left(\frac{\partial}{\partial x_j}\epsilon_{ij} - \frac{1}{3}\frac{\partial}{\partial x_i}\epsilon_{kk}\right) = 0. \tag{2.30}$$

The poisson's ratio ν is defined as

$$\nu = \frac{3k - 2\mu}{6k + 2\mu}. \tag{2.31}$$

Letting the elastic medium to be incompressible requires $\nu \to \frac{1}{2}$, which can be attained by $k \to \infty$ in Eq. (2.31). The divergence of strain also approaches zero ($\epsilon_{kk} \to 0$) because of the zero compressibility. Under these conditions, the hydrostatic pressure $p = -k\epsilon_{kk}$ can remain a finite value. The equilibrium equation of Eq. (2.30) can be written as

$$-\frac{\partial p}{\partial x_i} + 2\mu \frac{\partial}{\partial x_j}\epsilon_{ij} = 0, \tag{2.32}$$

$$-\frac{\partial p}{\partial x_i} + \mu \left(\frac{\partial^2 u_i}{\partial x_j \partial x_j} \right) = 0. \tag{2.33}$$

When u_i and μ is considered as the velocity vector and the shear viscosity, Eq. (2.33) corresponds to the Stokes equation. The inclusion problem in an elastic medium can be extended to that in a steady and incompressible fluid by letting $\nu \to \frac{1}{2}$.

Eq. (2.27) is the strain vector of the cavity in the elastic medium. The rate of deformation of an expanding bubble in an incompressible viscous fluid is represented by the same equation, but with ΔV replaced by the rate of volume change, $\dot{V}$, and taking the limit of zero compressibility (i.e., $\nu \to \frac{1}{2}$):

$$\dot{\epsilon}_i = \frac{\dot{V}}{V} \lim_{\nu \to 1/2} \frac{S'_{ij} B'_{jk} U_k}{U_i S'_{ij} B'_{jk} U_k}. \tag{2.34}$$

Keep in mind that Eq. (2.34) requires not L_{ij}^{Vol} but V and $\dot{V}$. According to the definition of Eq. (2.22), $\dot{\epsilon}_i$ represents the diagonal components of the rate of deformation tensor on the coordinate along the main axes of the ellipsoid. Corresponding velocity gradient tensor on the same coordinate is

$$\hat{L}_{ij}^{*Vol} = \begin{pmatrix} \dot{\epsilon}_1 & 0 & 0 \\ 0 & \dot{\epsilon}_2 & 0 \\ 0 & 0 & \dot{\epsilon}_3 \end{pmatrix}. \tag{2.35}$$

Given that the base of $\hat{L}_{ij}^{*Vol}$ is on the principal axes of the bubble, this tensor must be rotated into the spacial coordinate to get L_{ij}^{*Vol}.

A numerical calculation of L_{ij}^{*Vol} must take into account that B'_{ij} in Eq. (2.34) diverges infinitely as ν approaches $\frac{1}{2}$, although $\dot{\epsilon}_i$ remains finite. To avoid a numerical error due to the divergence of B'_{ij}, I calculate Eq. (2.34) for ν close to, but not equal to, $\frac{1}{2}$. Fig. 2.5 shows the dependence of $\frac{\dot{\epsilon}_1}{\dot{\epsilon}_3}$ on ν. As ν approaches $\frac{1}{2}$, $\frac{\dot{\epsilon}_1}{\dot{\epsilon}_3}$ becomes close to a constant value. The ratio of the two strain rates appears almost constant for $0.5 - \nu < 10^{-4}$. Thus, I use $\nu = 0.4999$ for S'_{ij} and B'_{jk} when I calculate Eq. (2.34).

As a result, L_{ij}^{*Vol} is given by Eqs. (2.34) and (2.35) as a function of the bubble shape, the bubble volume, and the rate of volume change. The last two parameters are related to the volumetric velocity gradient tensor of the liquid-gas mixture L_{ij}^{Vol} as follows,

$$\frac{\dot{V}}{V} = \frac{1}{\phi} \text{trace} \left[L_{ij}^{Vol} \right]. \tag{2.36}$$

where ϕ is the gas volume fraction per unit volume, which is equivalent to vesicularity in a conduit flow.

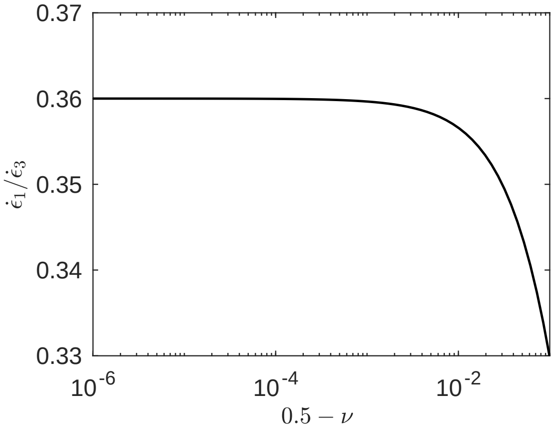

Figure 2.5: Relationship between $\frac{\dot{\epsilon_1}}{\dot{\epsilon_3}}$ and $0.5 - \nu$ for an ellipsoidal bubble ($\frac{b}{a} = 0.8$ and $\frac{c}{a} = 0.6$). As ν approaches $\frac{1}{2}$, $\frac{\dot{\epsilon_1}}{\dot{\epsilon_3}}$ approaches a constant value.

Keep in mind that Eq. (2.35) is the velocity gradient of the ellipsoidal bubble embedded in the fluid which is assumed to be incompressible. Strictly speaking, this assumption is valid only for a small volume of bubble. For a large volume fraction of bubble, such as bubbly magma, the matrix phase behaves as a compressible fluid (*Prud'homme and Bird*, 1978). The difference of bubble growth between incompressible and compressible fluids is discussed in appendix B.

Lastly, I explain the contribution of the surface tension to the volumetric deformation of a bubble. The general boundary condition for the bubble surface is given by

$$\left(\tau_{ij} - \tau_{ij}^{*}\right) n_j = 2\kappa_m \Gamma n_i, \tag{2.37}$$

where τ_{ij} and τ_{ij}^{*} are the stresses outside and inside of the bubble respectively, n_i is the outward unit vector normal to the bubble surface, κ_m is the mean curvature, and Γ is the surface tension. *Jackson and Tucker* (2003) derived a tensor representing the average stress jump across the bubble surface by integrating Eq. (2.37) over the surface of the ellipsoidal bubble. The average stress jump tensor $\Delta\tau_{ij}$ is written as

$$\Delta\tau_{ij} = -\frac{4\Gamma}{\pi R_b} P_{ij}, \tag{2.38}$$

where P_{ij} is given by Eq. (A.4). This stress jump includes both isotropic and deviatoric components. *Jackson and Tucker* (2003) took into account of the deviatoric component of Eq. (2.38) in Eq. (A.1), but did not consider the isotropic component because they considered the deformation of a droplet with a constant volume. I followed the model of *Jackson and Tucker* (2003) to include the deviatoric component in L_{ij}^{*Non} (appendix A).

The isotropic component, which is one-third of the trace of Eq. (2.38), should be included in L_{ij}^{*Vol} through ΔP in Eq. (2.26), and thus it affects the volume rate $\dot{V}$. Once $\dot{V}$ is determined, the individual values of $\dot{\epsilon}_i$, which affect the bubble shape evolution, are determined by Eq. (2.35) regardless of the surface tension effect.

2.4 Results of the modified JT (MJT) model

Hereafter, I call the modified JT model employed in this study the MJT model. Its blending function f and orientation parameter ξ are modified from those in the original JT model. The MATLAB scripts for the MJT model are available online (http://www.eri.u-tokyo.ac.jp/ichihalab/ohashi.html). The model calculates the time evolution of a bubble shape for a constant Ca and an arbitrary shear flow. Some results without volume change are presented in this section.

In the following argument, the word "steady state" is replaced with "equilibrium state" in referring to bubble shapes. Chapter 4 investigates bubble deformation in a conduit flow, where bubbles experience varying Ca as magma rises and thus cannot reach a steady state, even if the conduit flow is "steady". To avoid confusion, I use the term *equilibrium state* for bubble shape. The two stresses influencing bubble shape, viscous stress and surface tension stress, balance each other when the bubble is in its equilibrium state. Therefore, the equilibrium bubble shape depends only on Ca, which is the only characteristic dimensionless number in the system of equations in Fig. 2.4 (see Appendix A for more details).

The MJT model is tested using experimental data and analytical solutions from three typical cases: equilibrium deformation in shear flow, transient deformation in shear flow, and shape relaxation. Two types of shear flow are considered: simple and pure shear. All of the calculations here are performed with $\lambda = 10^{-7}$, which corresponds to vapor bubbles ($\eta^* \sim 10^{-5}\ \mathrm{Pa \cdot s}$) in viscous fluid ($\eta \sim 10^{2}\ \mathrm{Pa \cdot s}$). Smaller λ values do not lead to significantly different results from those presented here.

Fig. 2.6 presents the relationship between the equilibrium bubble shape and capillary number for several models. A bubble remains almost spherical ($D \sim 0$) at small capillary numbers, and becomes elongate ($D \to 1$) as the capillary number increases. Analytical solutions have been obtained for both $Ca << 1$ (*Taylor*, 1934) and $Ca >> 1$ (*Hinch and Acrivos*, 1980). The MJT model for simple shear agrees well with the analytical solutions for both regimes (Fig. 2.6a). The equilibrium bubble shapes calculated by the model are also consistent with the experimental results reported by *Rust and Manga* (2002). Furthermore, the MJT model is appropriate for pure shear, describing well the analytical solutions for both $Ca << 1$ (*Taylor*, 1934) and $Ca >> 1$ (*Acrivos, A. Lo*, 1980) (Fig. 2.6b). However, it fails numerically at large strain in pure shear with $Ca > 2.1$. *Jackson and Tucker* (2003) interpreted the numerical failure of their model as the indication of droplet breakup after large strain above the critical capillary number. I am uncertain whether the numerical failure of the MJT model is related to bubble breakup, but the results presented in chapter 4 were obtained without failure.

Fig. 2.7 shows the evolution of bubble shape under simple and pure shear at a constant rate. The deformation degree D increases gradually with time in both cases. When the time is scaled with the shear rate $\dot{\gamma}$, time can effectively be replaced by strain ($\dot{\gamma}t$). The bubble therefore reaches an equilibrium state when enough strain is applied. The amount of strain needed to reach the equilibrium state is about 4 when $Ca = 1$, which is similar to the numerical simulation results of *Huber et al.* (2013), which dealt with multiple bubbles in a flow. Regardless of whether the bubble reaches the equilibrium state, D in pure shear is larger than that in simple shear at the

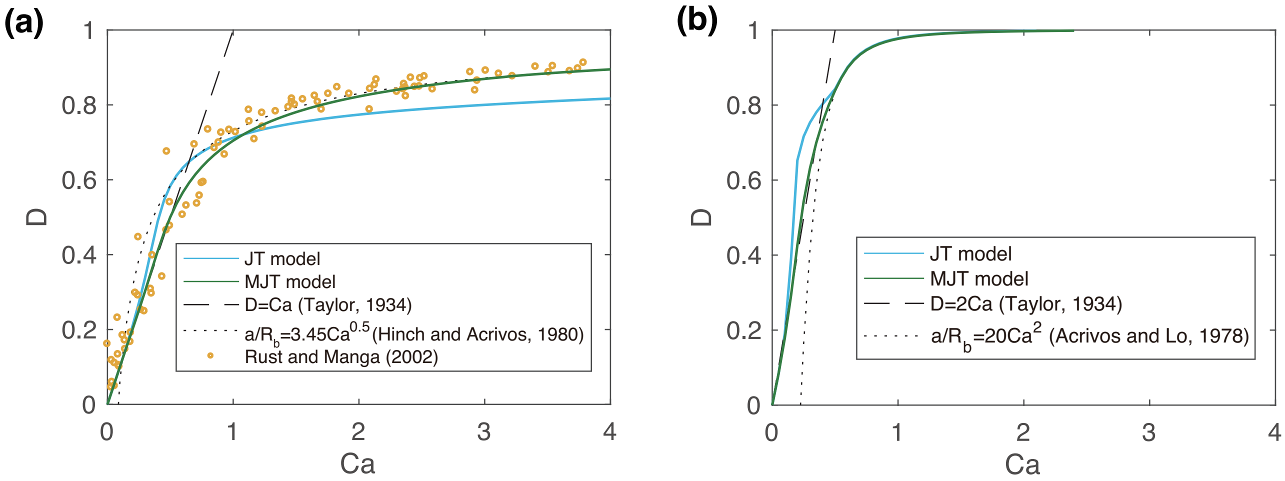

Figure 2.6: Relationship between deformation degree D and capillary number Ca for the equilibrium shapes of bubbles deformed by (a) simple shear and (b) pure shear. The viscosity ratio λ is set to 10^{-7}. The blue and green solid lines are the simulation results of the JT and MJT models, respectively. (a) Equilibrium shapes deformed by simple shear. The dashed line $D = Ca$ is the analytical solution for $Ca \ll 1$ (from *Taylor*, 1934). The dotted line is the analytical solution for a slender bubble ($a/R_b \gg 1$) (from *Hinch and Acrivos*, 1980). The slender-body solution $a/R_b = 3.45Ca^{0.5}$ is converted to $D(Ca)$. The yellow dots are the experimental data of *Rust and Manga* (2002) for the equilibrium shapes of air bubbles in corn syrup ($\lambda = \mathrm{O}(10^{-7})$). (b) Equilibrium shapes deformed by pure shear. The dashed line $D = 2Ca$ is the analytical solution for $Ca \ll 1$ (from *Taylor*, 1934). The dotted line is the analytical solution for a slender bubble ($a/R_b \gg 1$) (from *Acrivos, A. Lo*, 1980), who searched the stable conditions of the slender-body shape under pure shear, and obtained $a/R_b = 20Ca^2$ for $p/\dot{\gamma}\eta = 6$, where p is the pressure in the bubble. I converted a/R_b to D.

same strain.

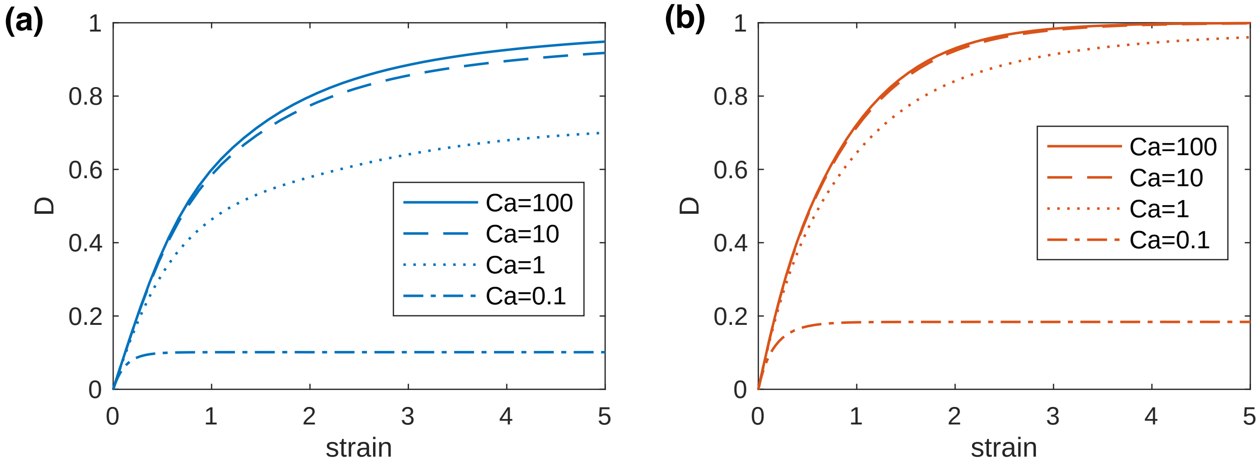

Figure 2.7: Relationship between deformation degree D and strain for the transient shapes of bubbles deformed by (a) simple shear and (b) pure shear.

If the external flow ceases, the shear stress acting on a bubble is removed, and it starts to relax owing to surface tension. Fig. 2.8 demonstrates the relaxation of bubble shape for two different initial aspect ratios. The aspect ratio, a/R_b (*Rust and Manga*, 2002), changes more sensitively with large elongation than does D, such that the values $a_i/R_b = 4.3$ and 7.4 in Fig. 2.8, where a_i denotes the initial value of a, correspond to $D = 0.80$ and 0.91, respectively. Time is scaled by the relaxation timescale (e.g., *Toramaru*, 1988):

$$\tau_{relax} = \frac{R_b \eta}{\Gamma}. \tag{2.39}$$

Despite the different initial aspect ratios, the normalized relaxation curves calculated by the MJT model are very similar. Furthermore, the model results are consistent with the experimental data of *Rust and Manga* (2002).

2.5 Application of the MJT model to bubble shapes in natural samples

We used experimental data for vapor bubbles in viscous fluid (*Rust and Manga*, 2002) to modify the parameters in the JT model (*Jackson and Tucker*, 2003). The MJT model agreed well with both analogue experiments and analytical solutions (Figs. 2.6 and 2.8). In this section, I re-analyze the bubble geometry data presented by *Rust and Cashman* (2007) to determine the ability of the MJT model to reproduce the bubble textures in natural samples. *Rust and Cashman* (2007) examined obsidian samples from pyroclastic deposits from the most recent eruption of Newberry Volcano, Oregon, to analyze the shear rates of the bubbles. This rhyolitic eruption, which occurred 1300 years ago, produced a widespread pyroclastic fall deposit known as Newberry pumice. The juvenile component of the fall deposit is dominated by white pumice, with a small amount of obsidian (1–6 wt%). *Rust and Cashman* (2007) focused on obsidian clasts in the Newberry pumice, and measured bubble

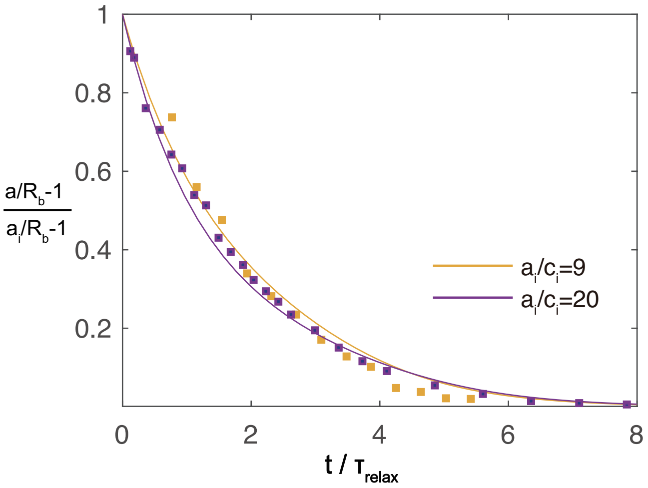

Figure 2.8: Shape relaxation of a bubble after external flow is stopped. One bubble has an initial aspect ratio of $a_i/c_i = 9$ ($a_i/R_b \approx 4.3$), and the other has $a_i/c_i = 20$ ($a_i/R_b \approx 7.4$), where a_i and c_i are the initial semi-major and semi-minor axes of the sheared bubble, respectively. Time is scaled by the relation timescale (Eq. 2.39). Dots represent the experimental data of *Rust and Manga* (2002).

shapes under an optical microscope.

2.5.1 Bubble deformation in the equilibrium state

Fig. 2.9a shows a typical relationship between D and R_b measured by *Rust and Cashman* (2007). Sample E shows a linear increase in D from 0 to 0.5 as R_b increases. This trend can be explained if I consider the equilibrium state of bubble deformation. As long as I focus on bubbles in a small clast, it is reasonable to assume that the strain rate, viscosity, and surface tension are uniform throughout the clast, such that the bubble radius is the only parameter controlling its capillary number. The increase in R_b implies an increase in Ca. Furthermore, Fig. 2.6 shows that the equilibrium bubble shape deformed by simple shear is described by $D = Ca$ for $D < 0.5$ and $\lambda \ll 1$. *Rust and Cashman* (2007) concluded that the linear increase in D with R_b was due to equilibrium bubble deformation. Fig. 2.9b shows the temporal evolution of D calculated by the MJT model for a constant and uniform simple shear, with strain γ used as time on the horizontal axis. Assuming that bubbles were deformed by simple shear, *Rust and Cashman* (2007) obtained Ca for each bubble in the equilibrium state. Bear in mind that a bubble in the equilibrium state records only the Ca during its deformation. I can evaluate the minimum strain to reach the equilibrium state, but cannot obtain the actual strain that the bubble experienced during magma flow.

2.5.2 Bubble deformation in the transient state

A key aspect of the *Rust and Cashman* (2007) data is that D in Samples F and L initially increases with R_b, but then approaches a constant value (0.4 and 0.65, respectively) as R_b increases further (Fig. 2.10a). If all

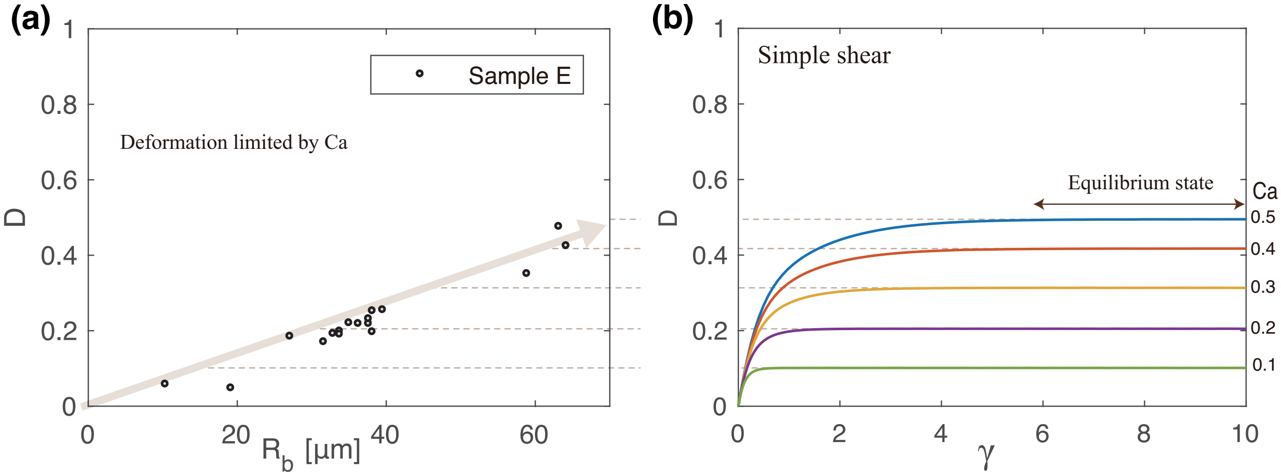

Figure 2.9: (a) Degree of bubble deformation D with respect to bubble radius R_b for a Newberry obsidian clast. Data (Sample E) are from *Rust and Cashman* (2007). (b) Temporal evolution of a bubble shape calculated for simple shear, calculated by the MJT model, where strain (γ) corresponds to the dimensionless time of deformation. I can evaluate the minimum strain to reach the equilibrium state, but cannot obtain the actual strain that the bubble experienced during magma flow.

the bubbles in a clast reach the equilibrium state, then the only possible asymptotic value is $D = 1$ for both simple and pure shear (Fig. 2.6); however, the D values for Samples F and L approach much smaller values. *Rust and Cashman* (2007) considered these bubbles to represent the transient effect of limited strain on bubble deformation. Their deformations stopped owing to insufficient strain before reaching the equilibrium state. *Rust and Cashman* (2007) roughly estimated the strain for these two samples by approximating the strain from the maximum dimensionless elongation of the bubbles (a/R_b). Here I used the results of the MJT model to estimate the shear strain rate and strain more accurately.

Fig. 2.10b shows the temporal evolution of D under a constant simple shear rate as a function of strain, γ. The dependence of the D–γ curves on Ca is large at small Ca ($Ca < 1$). On the other hand, the curves collapse as Ca increases, which defines the maximum D as a function of γ. The maximum D appears as the deformation limit in the D–R_b plot (Fig. 2.10a), with the limit indicating the strain during bubble deformation. The distances between each D–γ curve for different Ca values vary slightly for different maximum D values. For example, the distances between D–γ curves become small for $Ca > 2$ at $D = 0.4$, while they become negligible only for $Ca > 5$ at $D = 0.65$. I therefore assume that all the D–γ curves collapse to a single master curve and that the maximum D value becomes independent of Ca at $Ca > 5$. I compare this master curve with the deformation limits in Samples F and L, assuming that they experienced a constant simple shear (Fig. 2.10b). I then obtain shear strain values for these samples of 0.6 and 1.3, respectively. These modeled strain values are two-to-three times smaller than those estimated by *Rust and Cashman* (2007).

To specify Ca for each bubble, the viscosity, surface tension, and strain rate are needed. The temperature was assumed in the viscosity estimate of *Rust and Cashman* (2007), while the water content of each clast was

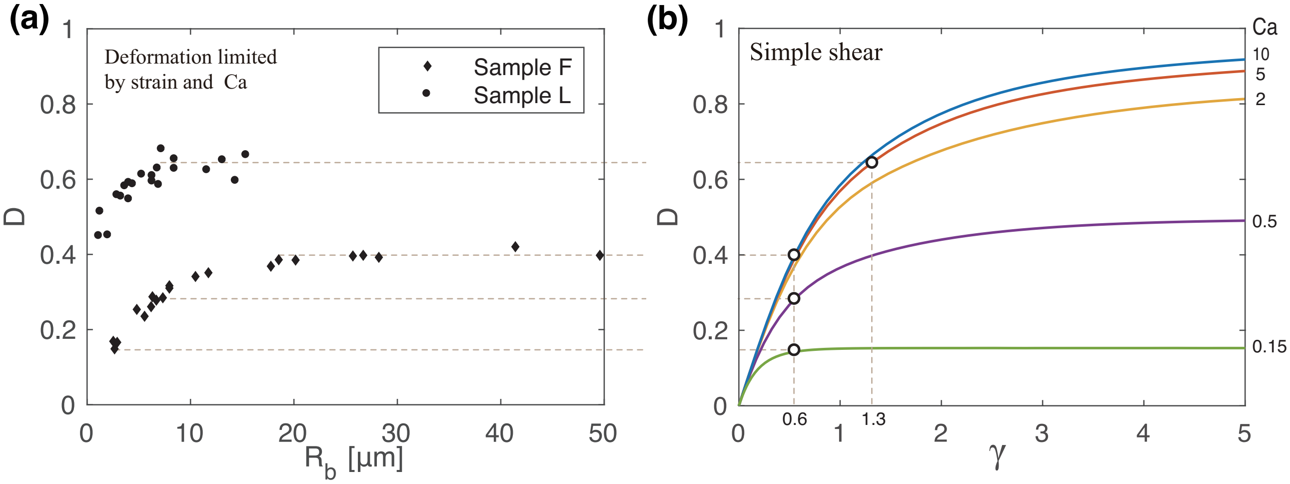

Figure 2.10: (a) Degree of bubble deformation D as a function of bubble radius R_b for two Newberry obsidian clasts. Data (Samples F and L) are from *Rust and Cashman* (2007). As R_b increases, D approaches a maximum value that is much less than 1 (~ 0.4 for Sample F; ~ 0.65 for Sample L). This limitation indicates the transient effect of strain on bubble deformation. (b) Temporal evolution of a modeled bubble's shape due to simple shear, calculated by the MJT model. The dependence of D on Ca becomes negligible for $Ca > 5$. The strains applied to both samples can therefore be estimated from the transient curve at $Ca = 5$ (0.6 and 1.3, respectively).

measured with Fourier transform infrared spectroscopy. I assumed a melt temperature of $850\ ^\circ\mathrm{C}$, following *Rust and Cashman* (2007), and calculated the viscosity using the equation of *Hess and Dingwell* (1996). I also assumed a surface tension of $0.3\,\mathrm{N/m}$, such that the strain rate $\dot{\gamma}$ was the only parameter needed to convert each R_b to Ca.

We therefore estimated the strain rate from the D–R_b data of the obsidian samples. I converted the D–R_b data for Sample F to D–Ca plots by varying the strain rate of simple shear for each clast (Fig. 2.11a). The D–Ca curves were then calculated for $\gamma = 0.6$ by the MJT model. Similar analysis was performed for Sample L with $\gamma = 1.3$ (Fig. 2.11b). I determined the strain rate by least-squares fitting a curve to the data points. Deformation results for both samples are summarized in Table 2.1. The flow times required to deform the observed clast bubbles were determined by dividing the strain by the strain rate, yielding values of 4.0 and 2.7 min for Samples F and L, respectively (Table 2.1). These flow times are an order of magnitude smaller than those obtained by *Rust and Cashman* (2007).

Table 2.1: Results of deformation analysis

Sample	H_20 [wt%][a]	Strain	Log$\dot{\gamma}$ [1/s]	Flow time [min]
F	0.90	0.6	-2.6	4.0
L	0.70	1.3	-2.1	2.7

[a] From *Rust and Cashman* (2007)

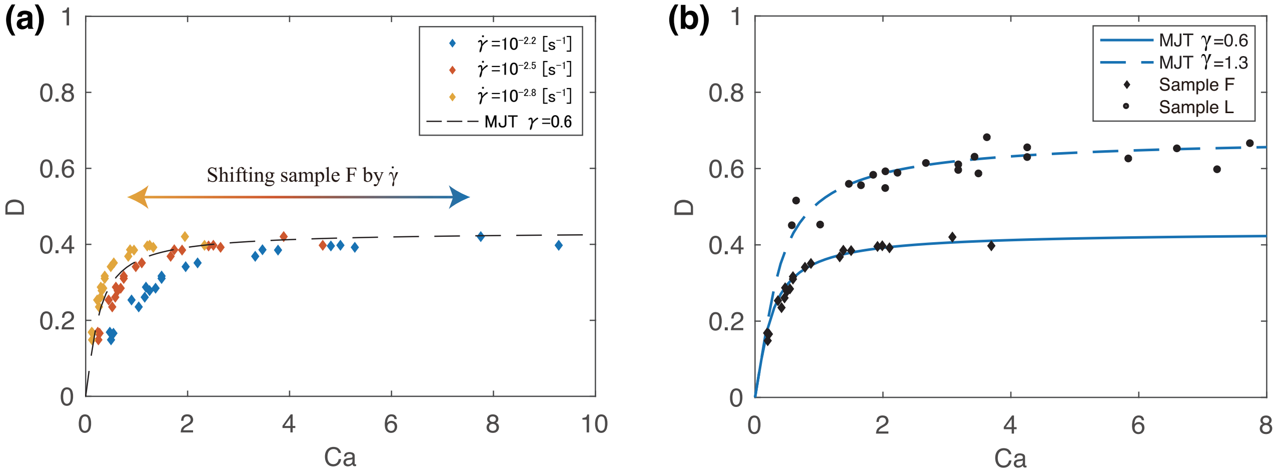

Figure 2.11: (a) Relationship between the degree of bubble deformation D and the capillary number Ca for Sample F (*Rust and Cashman*, 2007), and the simulation curve from the MJT model for simple shear. I shifted the data points of Sample F, varying the strain rate. (b) Relationship between D and Ca for Samples F and L (*Rust and Cashman*, 2007), and the best-fit simulation curves from the MJT model. The strain rate for each sample (Sample F: $10^{-2.6}\mathrm{s}^{-1}$; Sample L: $10^{-2.1}\mathrm{s}^{-1}$) is estimated to yield the best-fit curves to the data.

Our method developed to estimate strain and strain rates has two merits. First, it does not need to approximate strain by the maximum dimensionless elongation of the bubble (a/R_b), as the strain is accurately estimated from the deformation limit in the D–R_b data. I can therefore use the D–γ plot (Fig. 2.10b) directly to link the deformation limit to its corresponding strain. Second, my method can be applied to D–R_b data that do not exhibit a linear increase for $D < 0.5$. *Rust and Cashman* (2007) applied linear fits to the D–R_b data for $D < 0.5$ to convert R_b to Ca. However, the bubbles in obsidian samples do not always have linear trends for $D < 0.5$. For example, it is difficult to apply a linear fit to the D–R_b data of Sample L, because there are only a few data points for which $D < 0.5$. However, my method uses the entire D–R_b dataset from natural samples when fitted by the D–Ca curve.

Chapter 3

Extension experiment with solidifying foam

3.1 Introduction

The experimental validation of the deformation theory for high vesicularity is essential for the analysis of bubble shapes preserved in pumice. In order to assess bubble interaction, I artificially generate tube pumice in a laboratory. While controlling the rheology and shear field, I compare bubbles preserved in end products with the bubble deformation model developed in the previous chapter.

The reproduction of tube pumice requires rheological evolution as well as pre-fragmentation deformation. To our knowledge, products having textures that are similar to tube pumice have been made in fragmentation experiments of gum rosin in acetone (GRA) (*Phillips et al.*, 1995) and rhyolitic melt (*Martel et al.*, 2000). The common characteristic of both experiments is that a flowing material evolves into a solid material after fragmentation. Volatile degassing induced by rapid decompression deforms the sample and increases melt viscosity with rapid bubble expansion. Due to the high strain rate and large viscosity, the flowing sample results in fragmentation. The fragmented material solidifies because of the full degassing of acetone in GRA while quenching in the air for rhyolitic melts. A large number of fragmentation experiments have been conducted over a few decades, but, except for the two experiments mentioned above, these experiments did not include the rheological evolution from fluid to solid, and did not produce a sample having the characteristics of tube pumice.

The fragmentation experiments of GRA and rhyolitic melt reproduced the rheological evolution that is assumed to occur in magma. However, the mechanism of deforming bubbles could not be elucidated in their experiments, because these experiments attempted to investigate the fragmentation mechanism by controlling pressure. The pressure-controlled apparatus makes it more difficult to control and measure the strain and strain rate before fragmentation. Strain and strain rate are the essential parameters for the development of bubble structure (e.g., *Okumura et al.*, 2008; *Caricchi et al.*, 2011; *Shields et al.*, 2014).

We apply controlled strain and strain rate to polyurethane foam by a tensile testing machine, which can apply a uniform pure shear. I chose pure shear because of the following reasons. First, it has been considered as one of the important shear deformations for a conduit flow. It is caused by the acceleration of magma (*Papale*, 1999; *Bouvet de Maisonneuve et al.*, 2009). Decompression along a conduit leads to gas exsolution and bubble growth, which result in flow expansion and acceleration. Second, tube pumice which was observed in climatic eruption products of Mount Pinatubo was assumed to be deformed in pure shear (*Polacci et al.*, 2001). Third, only a few experimental studies have investigated pure shear deformation (e.g., *Moitra et al.*, 2018), while many previous studies in volcanology have focused on bubble deformation in simple shear. Forth, tensile testing has a merit that it can apply a uniform deformation across a sample, and I can directly measure the shear deformation. In torsion experiments that apply simple shear, on the other hand, shear stress and strain are radially variable and are difficult to be quantified without knowing the sample rheology.

In this study, I measure the bubble geometry of fully solidified polyurethane foam by X-ray computed-tomography (CT) after the pure shear experiments. Based on the experimental data, I discuss the deformation parameters recorded by the textures of the solidified products and the method to analyze the deformation of multiple bubbles.

3.2 Experimental methods

3.2.1 Material

Polyurethane foam is produced by mixing polyol, polyisocyanate, catalyst, and foam stabilizer. During the foaming process, chemical reactions start after mixing, and the foam expands in several minutes (Fig. 3.1a). The chemical reactions are complete in several tens of minutes. During the formation of polyurethane foam, two main reactions occur: a degassing reaction and a curing reaction (*Neff et al.*, 1996). The degassing reaction forms carbon dioxide gas and produces a foam structure. The curing reaction generates crosslinked polyurethane and results in the solidification of the foam structure.

In the present study, I used a polyol (Hycel HW-408, TOHO Chemical Industry Co., Ltd.) and a polyisocyanate (Hycel 360P, TOHO Chemical Industry Co., Ltd.). The original product of polyol includes a foam stabilizer to make a homogeneous polyurethane foam with very small spherical bubbles. In order to simulate various bubble textures in pumice, I have the polyol specially blended by the manufacturer excluding the foam stabilizer. Surface tension is an important parameter to control bubble deformation. The surface tensions of polyol and polyisocyanate were measured by the pendant drop method using a tensiometer (*Takeda et al.*, 2019). The surface tensions of polyol and polyisocyanate are 36.1 and $48.6\ \mathrm{mN/m}$, respectively.

3.2.2 Equipment

Extensional experiments were carried out using a tensile testing machine (EZ-SX, Shimadzu), which consists of a stationary lower stage and a moving head attached with a load cell (Fig. 3.1b). A polypropylene cup (diameter: $23.5\ \mathrm{mm}$, height: $49\ \mathrm{mm}$) is mounted on the lower stage, and another is attached upside down to the load cell. The two cups are axially aligned and are initially connected mouth to mouth. When a polyurethane foam sample grows sufficiently in these cups, the upper cup is pulled to extend the sample. The testing machine records the tensile force and extension length at a sampling rate of 50 Hz.

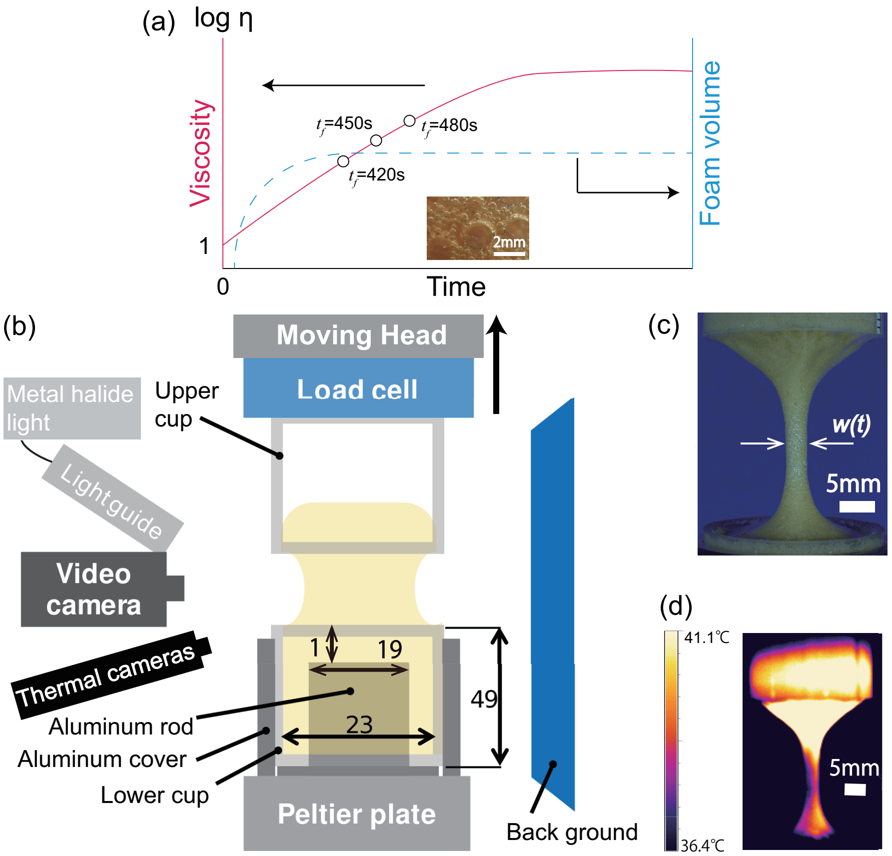

Figure 3.1: (a) Schematic evolution of the physical properties of polyurethane foam used in this experiment. Red and blue lines indicate the temporal change of viscosity and foam volume, respectively. The inset photograph shows polyurethane foam with bubbles growth. All of the main extensions were finished in $t_f \approx 420$, 450, or 480s.(b) Schematic diagram of the experimental equipment. Lengths are shown in millimeters. (c) Photograph of the foam after the main extension (T18121006). (d) Thermal image of the foam (T18121006) after the main extension.

The degassing reaction is exothermic, while the rheological evolution depends significantly on the temperature (*Lipshitz and Macosko*, 1976). To control temperature during the experiments, the lower cup is mantled by an aluminum jacket and is intruded with an aluminum rod (diameter: 19 mm, height: 39 mm). Both the jacket and the rod are mounted on a thermoelectric cooler (Peltier plate), the temperature of which is set to $20°$C during the experiments. The temperature distribution of the foam was monitored by the infrared thermal camera (PI450, Optris) at a rate of 27 frames per second (fps) (Fig. 3.1d).

The experiments were recorded by two video cameras with metal halide lights. A high-resolution video camera (DFK33UX250, The Imaging Source) recorded the stretching of the polyurethane foam. A low-resolution video camera (Pro 9000, Logicool) recorded the entire experiment from bubble nucleation to complete solidification. The framing conditions were a rate of 50 fps and spatial resolutions of $0.015 - 0.026$ mm/pixel for the high-resolution video camera and 30 fps and 0.088 mm/pixel for the low-resolution video camera, respectively.

3.2.3 Procedure

Polyol (5.4 ml) and polyisocyanate (4.8 ml) were poured into a mixing cup and stirred for 20 s with a stirrer. Hereinafter, time t starts from the finish time of mixing polyol and polyisocyanate ($t = 0$). A mixture of 6.8 to 7.4 ml was collected using a syringe and then poured into the lower cup. After pouring the mixture, the moving head was lowered so that the upper cup contacted the lower cup. In the first 120 s, the reactive foam is in the bubble nucleation stage. Bubble rise was observed in this stage because of the small viscosity, but as the polymerization proceeds, it became invisible in $t > 120$ s. As the bubbles grow, the foam inflated into the upper cup.

The extension experiment consisted of (1) preliminary extension stage, (2) first keeping stage, (3) main extension stage, and (4) second keeping stage.

At $t = 360$ s, I applied the preliminary extension of 15 mm by raising the load cell at a constant speed of 1 mm/s. The preliminary extension creates a necking in the middle of the foam. The necking helps to realize a homogeneous uniaxial deformation in the following main extension.

After the preliminary extension, the foam growth continued very slowly. To prevent the foam from bending and keep the necking shape, I pulled the foam slowly at a speed of 0.01 mm/s. The effect of the slow pulling on bubble shape was negligible.

Next, I applied the main extension to the foam by pulling the upper cup at a constant speed (Fig. 3.1c). The pull speed varies from 0.5 to 10 mm/s, and the pull length varies from 5 to 25 mm. Although an exponential pull speed is needed to obtain a constant strain rate (*Moitra et al.*, 2018), I pull the cup at a constant speed due to the instrumental constraint. The constant pull speed had a merit to suppress the increase in viscous stress during the extension with polymerization.

Delaying the start time of pulling t_i increases the instantaneous viscosity at the onset of deformation. The main extension finished at, $t = t_f$, which was varied as t_f = 420, 450, or 480 s (Fig. 3.1a). The experimental conditions are listed in Table 3.1.

Table 3.1: Summary of experimental conditions and results

Sample number	Pull rate $\dot{L}$ [s^{-1}]	Pull length L [mm]	Start time t_i [s][a]	Finish time t_f [s][a]	Extension duration $t_f - t_i$ [s]	Strain rate $\dot{\epsilon}_{\mathrm{ave}}[\mathrm{s}^{-1}]$[b]	Strain ϵ	Shear viscosity η_{ave} [$\mathrm{Pa}\cdot\mathrm{s}$][b]
T18120401	-	-	-	-	-	-	-	-
T18120607	0.5	10	401.6	421.6	20.0	0.043	0.86	881
T19010706	3	10	419.6	422.9	3.3	0.23	0.76	516
T18121006	7	10	421.7	423.1	1.4	0.51	0.71	548
T18121002	10	10	422.0	423.0	1.0	0.52	0.51	687
T19010704	7	5	422.1	422.8	0.7	0.47	0.33	320
T18121704	7	15	421.9	424.0	2.1	0.54	1.15	305
T19010702	7	20	421.3	424.2	2.9	0.35	0.98	894
T19010703	7	25	419.2	422.8	3.6	0.43	1.52	663
T19011411	7	10	450.5	451.9	1.4	0.45	0.62	2493
T19011412	7	10	480.3	481.7	1.4	0.41	0.58	6545

[a] Time starts from the end point of mixing polyol and polyisocyanate

[b] Averaged value by time

Bubble growth continued very slightly after the main extension. In order to keep the foam straight, the foam was pulled at a speed of $0.01\ \mathrm{mm/s}$ until $t = 1080\ \mathrm{s}$. By analyzing the movie image, I roughly estimated the bubble growth rate of $\frac{dR_b}{dt} = 6.6 \times 10^{-6}\ \mathrm{mm/s}$ at $420\ \mathrm{s} < t < 1080\ \mathrm{s}$. Given that the average bubble radius in the fully solidified foam is about $R_b = 0.17\ \mathrm{mm}$, bubble growth did not significantly affect bubble shape during and after the main extension.

After the experiments, three-dimensional images of the foams were obtained by X-ray CT.

3.2.4 Rheology in pure shear

The tensile force during the experiment was measured by the load cell. Stress σ at time t was calculated by dividing the tensile force by the temporal cross-sectional area $A(t)$ perpendicular to the deformation axis at the necking of the foam. If the cross-section is circular, its area can be calculated by the sample width measured from the video images taken from the side. However, some samples have elliptical cross-sections. In order to correct this effect, $A(t)$ was calculated by

$$A(t) = A_{CT} \left(\frac{w(t)}{w_{end}} \right)^2, \tag{3.1}$$

where A_{CT} is the cross-sectional area of the solidified foam measured by X-ray CT, $w(t)$ is the width at the necking of the reactive foam calculated from by the video images, and w_{end} is the width of the fully solidified foam.

The strain rate and strain during the experiments were estimated in the following manner. In the elongational deformation, the strain rate is defined as

$$\dot{\epsilon} = \frac{dv_z}{dz}, \tag{3.2}$$

where v_z is the vertical component of the velocity vector of a sample. In the present study, v_z was measured using a free tool in Matlab, PIVlab (*Thielicke and Stamhuis*, 2014). PIVlab provides velocity vectors on a side surface of the foam from successive video images.

The velocity vectors obtained from PIVlab were averaged in the direction perpendicular to the deformation axis. The grid size of the PIVlab analyses was $0.257\ \mathrm{mm}$. I calculated the strain rate by taking the vertical gradient of the upward velocity using 11 grid points around the necking of the foam. The obtained strain rate and stress time series include high-frequency fluctuations, which I regard as noise due to errors in the image analyses and the tensile machine, respectively. To remove the noise, I smoothed the data by successively applying a median filter and taking a moving average. The lengths of the median filter and moving average were set both to 5 points for stress and to 10 and 5 points for strain rate, respectively. Since one case with the slowest extension (T18120607) has large noise in the strain rate, I took 40 points for the median filter and 20 points for the moving average.

When the deformation is incompressible and uniform across the sample, the axial strain rate $\dot{\epsilon}$ is related to the rate of the width change as

$$\dot{\epsilon} = -\frac{2}{w}\frac{dw}{dt}. \tag{3.3}$$

We confirmed that the strain rate obtained using PIVlab was consistent with the width change of the sample. This result indicates that the strain rate was uniform in the radial direction. The strain ϵ is defined as the time integration of $\dot{\epsilon}$ from t_i to t_f.

Shear viscosity η is usually different from elongational viscosity η_e, which is defined as $\eta_e = \sigma/\dot{\epsilon}$. For an incompressible Newtonian fluid, the shear viscosity has the following relationship as $\eta = \frac{1}{3}\eta_e$ (e.g., *Bird et al.*, 2007). Although polyurethane foam is not a pure Newtonian fluid or incompressible, I approximated the shear viscosity from the above relationship.

3.2.5 X-ray computed tomography and image processing

Three-dimensional images of samples were obtained by a micro X-ray CT scanner (METROTOM800, Carl Zeiss). Images representing the intensities of X-rays transmitted through foam were collected at an energy of 130 kV and a tube current of 60 μA. The samples were rotated $360°$, and 800 projections were taken for each sample. The pixel sizes of the samples were 8.89×8.89 $\mu\mathrm{m}^2$ or 9.37×9.37 $\mu\mathrm{m}^2$, excluding one sample (T18120401, 18.34×18.34 $\mu\mathrm{m}^2$). The parameters of X-ray CT scan are summarized in Table 3.2.

Table 3.2: Summary of measurement conditions for the samples described in Table 3.1.

Sample number	Pixel size [μm]	Original raw image size [pixel]	Analyzed volume [mm^3] [a]	Vesicularity [b]
T18120401	18.34	1459 × 1464 × 1346	170.00	0.65
T18120607	8.89	1001 × 963 × 1664	48.54	0.63
T19010706	8.89	925 × 884 × 1924	50.17	0.59
T18121006	9.37	987 × 910 × 1871	83.157	0.67
T18121002	9.37	796 × 845 × 1859	67.65	0.61
T19010704	8.89	1167 × 1167 × 1346	170.00	0.58
T18121704	9.37	746 × 823 × 1859	54.58	0.62
T19010702	8.89	775 × 577 × 1894	47.00	0.61
T19010703	8.89	604 × 654 × 1862	30.30	0.59
T19011411	8.89	864 × 787 × 1837	67.23	0.57
T19011412	8.89	1011 × 933 × 1852	68.79	0.55

[a] Including bubbles and rigid polymers

[b] Calculated from the three-dimensional rendering images

Image processing of the sample was carried out with commercial 3D image processing software (Simpleware, Synopsys) in the following procedure. First, CT images were converted to binary images by brightness values (Fig. 3.2a). The thresholds of the brightness value were determined manually. Since most of the bubbles are interconnected, I separated them in order to measure the deformations of individual bubbles. Bubble separation was conducted by an opening operation followed by watershed segmentation (Figs. 3.2b and 3.2c). The opening operation involves the erosion and dilation cycle to smooth bubble shape. Watershed segmentation is a method of automatically separating objects that touch or coalesce (*Dingwell et al.*, 2016). The watershed segmentation sometimes results in over-segmentation. Over-segmented bubbles were merged manually.

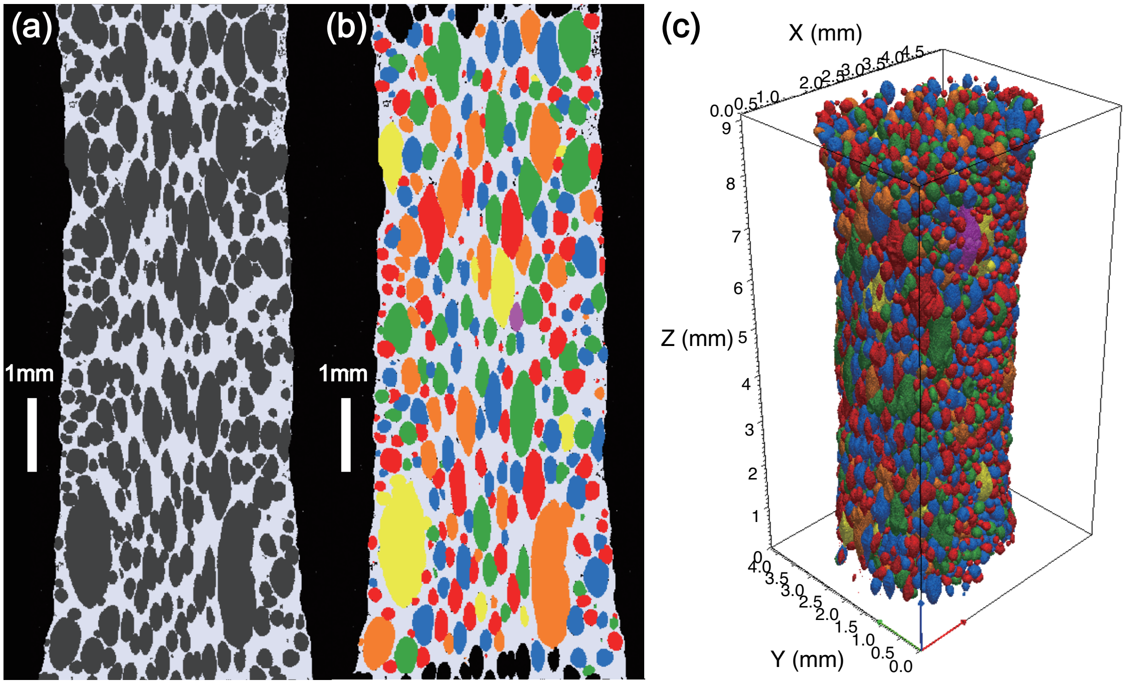

Figure 3.2: (a) Binary image of sample T18121006. (b) Segmented image. Adjacent bubbles with different colors indicate that the bubbles are recognized as different bubbles (i.e., separated bubbles). The bubbles touching the upper and lower boundaries were excluded from the analysis. (c) Three-dimensional rendered image.

The semi-major and semi-minor axes of a bubble were obtained by fitting the bubble by an optimally oriented rectangular that accommodates the bubble. The present study analyzed only bubbles with voxel numbers ≥ 100, because small bubbles were sometimes incorrectly measured. The voxel number of 100 corresponds to a bubble radius of 25.6 μm for 8.89 $\mu\text{m/pixel}$. In the present study, the equivalent bubble radius is used as the bubble radius. The bubble shape is characterized by the deformation degree D (Eq. 1.2). The detail procedure and error of image processing are described in appendix C.

3.2.6 Pure shear deformation

During the main extension, a bubble in the foam was deformed in pure shear. The velocity field of pure shear is expressed in cylindrical coordinates (z, r, θ) as follows:

$$v_z = \dot{\epsilon} z, \tag{3.4}$$

$$v_r = -\frac{1}{2}\dot{\epsilon} r. \tag{3.5}$$

Generally, bubble deformation is controlled by viscous stress and surface stress due to surface tension at gas/liquid interface, and the competition of these two stresses is described by capillary number Ca. Using $\dot{\epsilon}$ in Eq. (3.2), the capillary number in pure shear is defined as

$$Ca = \frac{R_b \dot{\epsilon} \eta_L}{\Gamma}, \tag{3.6}$$

where R_b is the equivalent bubble radius that is defined as the radius of a sphere with a volume equal to the deformed bubble, η_L is the viscosity of the fluid phase, and Γ is the surface tension. Under the condition of a constant Ca, the equilibrium shape of a bubble in pure shear has been investigated experimentally (*Taylor*, 1934; *Delaby et al.*, 1994) and theoretically (*Taylor*, 1934; *Acrivos and Lo*, 1978).

In order to analyze the bubble deformation in our extensional experiment, I compare the experimental results with the MJT model, which is the new bubble deformation model developed in chapter 2, under a constant capillary number. In the present study, I estimated the values of η_L, $\dot{\epsilon}$, and Γ in Eq. (3.6) in the following way.

First, I adopt a mean field approach. In the mean field approach, the foam surrounding a bubble is assumed to be an effective medium. The average shape of multiple bubbles is assumed to be determined by the apparent viscous stress that is the product of bulk strain rate and effective viscosity of the foam rather than liquid viscosity. By using this approach, previous numerical and experimental studies calculated the capillary number from the effective viscosity, revealing that the average shape of deformed bubbles coincided with the shape of a single bubble theoretically estimated from the effective viscosity (*Loewenberg*, 1998; *Caserta et al.*, 2007). This mean field approach is well accepted for a moderately concentrated emulsion. The numerical simulations of *Loewenberg* (1998) showed that this approach was valid for at least $\phi \leq 0.3$. The validity of applying the mean field approach to highly vesiculated foam ($\phi \approx 0.6$) is discussed in the Discussion section.

The capillary number used in the MJT model is assumed to be a function of the shear viscosity of the fluid phase because the model deals with the deformation of a single bubble. In order to calculate the average deformation degree of multiple bubbles, I adopt the mean field approach and use the effective viscosity of the foam η as η_L.

Second, I use the time-averaged values of strain rate and viscosity, which are defined as $\dot{\epsilon}_{\text{ave}} = \frac{1}{t_f - t_i} \int_{t_i}^{t_f} \dot{\epsilon} dt$ and $\eta_{\text{ave}} = \frac{1}{t_f - t_i} \int_{t_i}^{t_f} \eta dt$, respectively. Finally, following the surface tensions of polyol and polyisocyanate (36.1 and $48.6\ \mathrm{mN/m}$, respectively), I assume a constant surface tension of $\Gamma = 40\ \mathrm{mN/m}$ for the reactive polyurethane foam.

3.3 Results

3.3.1 Rheology

The experimental conditions and results are summarized in Table 3.1. The rheology during the extensional experiment is shown in Fig. 3.3. The extensional experiment has three parameters: (1) pull rate $\dot{L}$, (2) pull length L, and (3) finish time t_f. The value of strain rate increases with $\dot{L}$ (Fig. 3.3a). The final strain tends to increase with L (Fig. 3.3e). The viscosity depends on the time of extension, which is represented by the finish time t_f (Fig. 3.3i). With increasing length, the strain rate decreases with time because of the constant pull rate. The stress depends on $\dot{L}$ and t_f and increases with $\dot{L}$ and t_f (Figs. 3.3d through 3.3f). Except for the low $\dot{L}$, the experiments show an initial linear response in which stress increases sharply with applied strain. This sharp increase in stress corresponds to the sharp increase in strain rate. When the strain rate reaches the maximum value, the stress increase slows down. The slow increase in stress was caused by the curing reaction of the two polymers. The effect of the curing reaction is clearly observed in the gradual increase of viscosity (Figs. 3.3g through 3.3i). Delaying t_f leads to the development of a polymer network and an increase in viscosity (Fig. 3.3i).

The viscosity of polyurethane foam is known to increase exponentially with time (*Mondy et al.*, 2013, 2014). The temporal viscosity can be formulated as follows:

$$\eta \quad = \quad \eta_c \exp\left(\alpha t\right), \tag{3.7}$$

where α is an exponential factor, and η_c is a constant effective viscosity. The linear fitting of the viscosities at the end of extension in Fig. 3.3i gives $\alpha = 0.043\ \mathrm{s}^{-1}$ and $\eta_c = 9.91 \times 10^{-6}\ \mathrm{Pa} \cdot \mathrm{s}$.

3.3.2 Qualitative observation

Representative 2-D slice images are shown in Fig. 3.4. The sample to which only the preliminary extension was applied is composed of spherical bubbles (Fig. 3.4a). This result suggests that elongated bubbles in Figs. 3.4b through 3.4k are formed in the main extensional deformation. Comparing the bubble shapes with similar sizes for each sample, the bubble elongation at the central regions is larger than that at the outer regions (e.g., Fig. 3.4d). I performed a quantitative investigation of this feature in the next subsection. As with the rheological data, all CT images are classified by pull rate $\dot{L}$, pull length L, and finish time t_f. Comparing samples under the same L and t_f (i.e., Figs. 3.4b through 3.4e), the bubble elongation increases slightly with $\dot{L}$, which controls the strain rate. Comparing samples under the same $\dot{L}$ and t_f (Figs. 3.4d and 3.4f through 3.4i), the bubble elongation increases with L (strain). The samples with different t_f show that the elongations of large bubbles are similar (Figs. 3.4d, 3.4j, and 3.4k). However, the elongation of small bubbles increases with t_f, namely with the viscosity.

3.3.3 Quantitative measurement

The vesicularities of all samples were measured using three-dimensional rendered images (Table 3.2).

Radial distribution of bubble shape

As mentioned in section 3.2, bubble shapes are different between the central regions and the outer regions. In order to investigate the inhomogeneous distribution of bubble shapes, I plotted the bubble deformation degree D as a function of r, where r is the radial distance from the axis of the foam to the centroid of a bubble. Figure 3.5a shows the relationship between r and D for a typical sample (T18121006; $\dot{L} = 7\ \mathrm{mm/s}$, $L = 10\ \mathrm{mm}$,

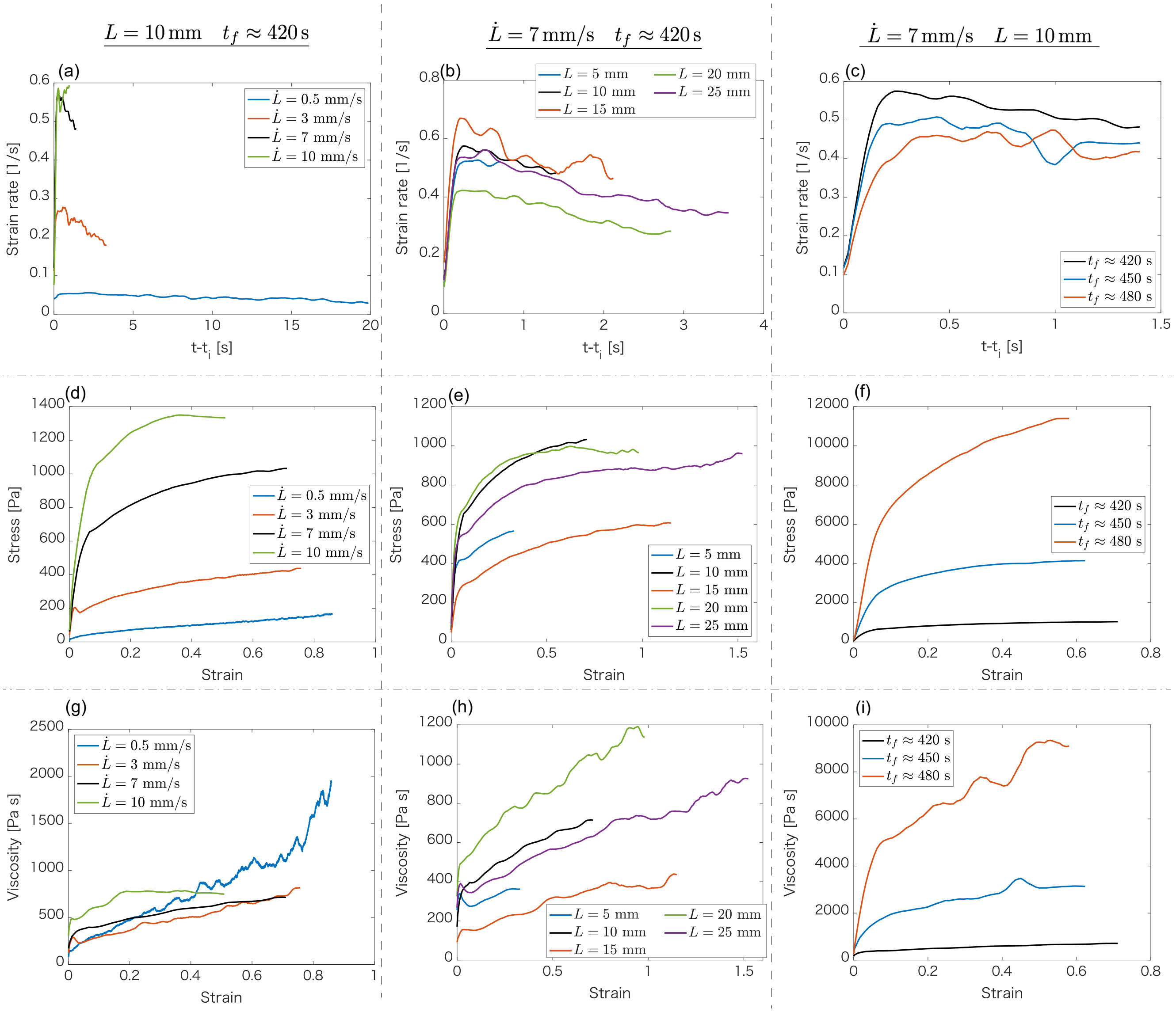

Figure 3.3: Variations of strain rate (a-c), stress (d-f), and shear viscosity (g-i) as a function of time or strain. The data are divided into three groups: (a, d, g) constant pull length and finish time, (b, e, h) constant pull rate and finish time, and (c, f, i) constant pull length and pull rate. Black lines indicate the same experiment with $\dot{L} = 7$ mm/s, $L = 10$ mm, and $t_f = 420$ s. The data indicated by the blue and red lines in (c) are shifted sideways by $+28.8$ s and $+58.7$ s, respectively.

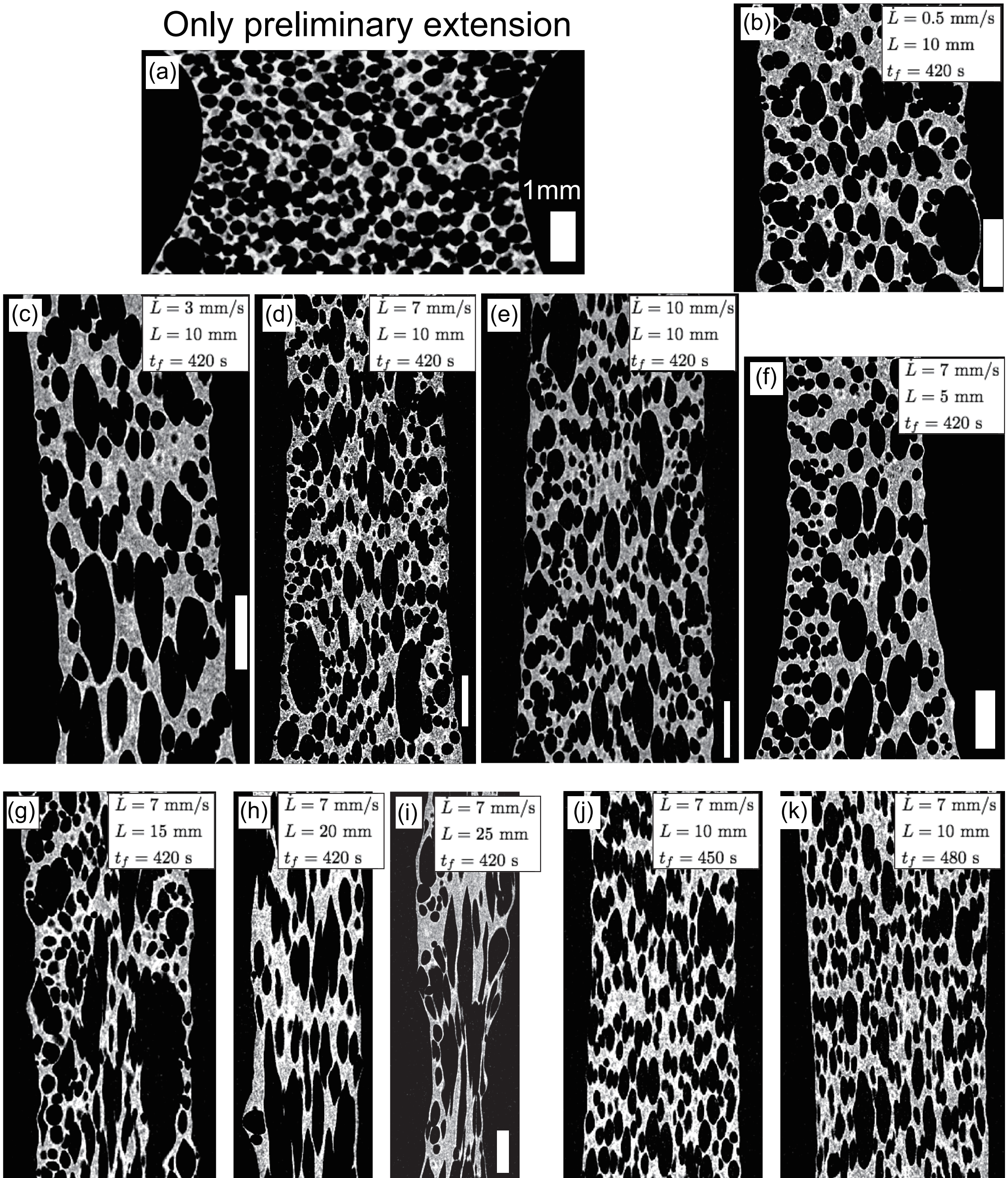

Figure 3.4: Typical 2-D slices of gray CT images. The black and gray parts in the images correspond to pores (air and bubble) and polyurethane. All scale bars are $1\ \mathrm{mm}$. (a) T18120401, (b) T18120607, (c) T19010706, (d) T18121006, (e) T18121002, (f) T19010704, (g) T18121704, (h) T19010702, (i) T19010703, (j) T19011411, and (k) T19011412.

$t_f = 420$ s). The color indicates the equivalent bubble radius. The center region ($r < 0.7$ mm) has a relatively uniform value of D and constitutes elongated bubbles (Fig. 3.5b). On the other hand, the outer region ($r > 1.5$ mm) shows a large variation in D (Fig. 3.5c). Other samples exhibit a similar distribution to this sample as well.

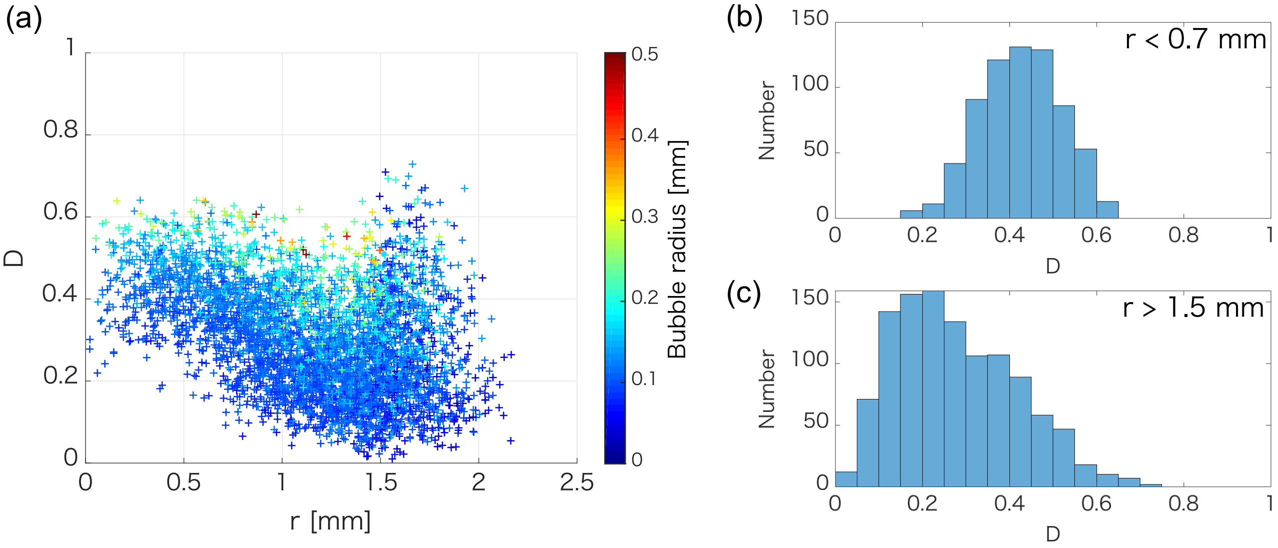

Figure 3.5: (a) Deformation degree of bubbles in sample T18121006 ($\dot{L} = 7$ mm/s, $L = 10$ mm, $t_f = 420$ s) as a function of radial distance from the foam center to the centroid of each bubble. The colorbar indicates the equivalent bubble radius. (b) Histogram of deformation degree for $r < 0.7$ mm. (c) Histogram of deformation degrees for $r > 1.5$ mm. The deformation degree is relatively homogeneous and symmetrical in the center region ($r < 0.7$ mm) but becomes wider in the outer region ($r > 1.5$ mm).

The inhomogeneous distribution of bubbles in the outer regions may be caused by the local rheology on the foam surface. Although the temperature of the lower cup was controlled by the Peltier plate, the polyurethane foam in the outer region showed the inhomogeneous distribution of temperature (Fig. 3.1d). Since the rheology of polyurethane foam is sensitive to temperature (*Lipshitz and Macosko*, 1976), the rheology around the foam surface might be inhomogeneous. The inhomogeneous rheology may change the amount of shape relaxation after the main extension.

In order to avoid the complexity of rheology and shape relaxation, I hereinafter focus on bubbles in the center region, that is defined as $r/r_0 < 1/3$, where r_0 is the radial distance from the center to the furthest foam surface.

Bubble volume distribution

Figure 3.6 shows the volumetric distribution as a function of bubble radius. The horizontal and vertical axes are the bubble radius in the log scale and the volume fraction in linear scale, respectively. The sample with only preliminary extension yields a symmetrical distribution with a peak at $R_b = 0.18$ mm (Fig. 3.6k). In the samples with main extensional deformations, the distribution becomes asymmetrical. The proportion of small bubbles decreases and that of larger bubbles increases with the pull length L (and strain) (Figs. 3.6c and 3.6e through 3.6h). The influence of pull rate and finish time on the bubble size distribution is smaller than that of pull length. For a pull length of $L \geq 20$ mm (Figs. 3.6g and 3.6h), there are large bubbles ($R_b > 0.4$ mm), which are never observed in the experiment without the main extensional deformation. These large bubbles were formed by the coalescence of many small bubbles induced by deformation.

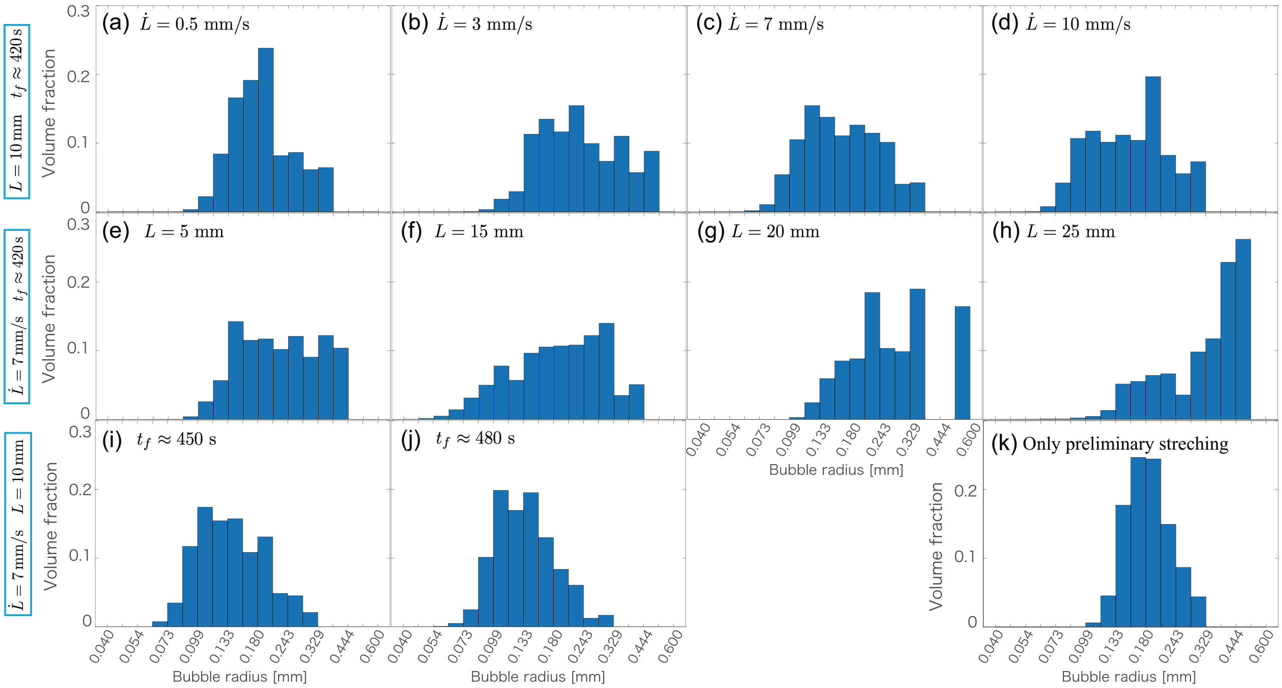

Figure 3.6: Bubble volume distributions for all analyzed samples. The horizontal axis is expressed in log scale. All samples are categorized into constant pull length and finish time (a-d), constant pull rate and finish time (c, e-h), constant pull rate and pull length (c, i and j), and only preliminary extension (k).

Bubble shape distribution for each sample

The relationships between Ca and D for each bubble are shown in Fig. 3.7. The red line indicates the results of the MJT model, which depends on Ca and ϵ, and the dashed line indicates the equilibrium shape of a bubble as a function of Ca. The variation of the capillary number for each sample is caused by the bubble size distribution.

Figures 3.7a through 3.7c show the results for different pull rates. Although there is a scatter of D around the simulation results, the experimental results show a rough agreement with the simulation results. In the experiment with small $\dot{L}$, the bubble deformation degree has a roughly linear relation with Ca (Fig. 3.7a). The linear trend of Ca and D suggests equilibrium shapes (*Rust and Cashman*, 2007). A small bubble (i.e., small Ca) could deform in a manner close to the equilibrium shape because such a bubble requires only a small strain to reach the equilibrium state. In the samples with different $\dot{L}$, D asymptotically approaches a constant value with Ca (Figs. 3.7b and 3.7c). The relation between D and Ca represents the transient effect of the insufficient strain on bubble deformation (*Rust and Cashman*, 2007). The asymptotic value of D ($D < 1$) is an indication of transient deformation and enables us to estimate the accumulated strain during bubble deformation (Fig. 2.10).

Note that bubbles of small Ca are less elongated than the model simulations (Figs. 3.7b through 3.7e). For example, the small bubbles of $Ca < 0.7$ in Fig. 3.7c are consistently less elongated than the model calculation. This deviation can be explained by shape relaxation driven by surface tension.

Figures 3.7c through 3.7f show the results for different pull lengths. These figures indicate that the asymptotic value of D with Ca gradually increases with the pull length, namely strain. With increasing strain, the bubbles gradually approach the equilibrium shapes, which are solely determined by Ca. However, the even largest strain of this data set ($\epsilon = 1.52$) is too small to attain the equilibrium shape. The model calculation shows that a bubble of $Ca = 1$ requires $\epsilon \approx 5$ to reach the equilibrium state (Fig. 2.7).

The experimental results are distributed around the model result. Compared to the other samples, the bubbles which experienced the largest strain (Fig. 3.7f), are more scattered from the model results. The scattering could be caused by bubble coalescences because it is not included in the MJT model. In addition, when half-coalesced bubbles are not separated accurately during image processing, the irregular shape of the bubble fit to a rectangular box produces anomalous D values.

Figures 3.7c, 3.7g, and 3.7h show the results for different pull lengths under the same pull rate and finish time. The delay of t_f contributes to the increase in viscosity, resulting in large Ca. These experiments maintain an approximately constant value of strain ($\epsilon \approx 0.6$), and thus the asymptotic value of D also maintains a constant value ($D = 0.6$). The variation of t_f certainly affects the amount of shape relaxation after the main extensional deformation. The deviation of D from the simulation result becomes small with delaying t_f (i.e., increasing viscosity).

Shape relaxation

Shape relaxation of a bubble has been discussed based on a relaxation timescale (*Toramaru*, 1988), which is given by

$$\tau_{relax} = \frac{R_b \eta_L}{\Gamma}. \tag{3.8}$$

Comparing the relaxation timescale with the cooling timescale, previous studies determined whether bubble shapes were quenched or relaxed (*Okumura et al.*, 2008; *Rust et al.*, 2003). In the present study, the cooling timescale can be regarded as the timescale of increasing viscosity and is explicitly defined by

$$\tau_{visco} = \frac{\eta_L}{\dot{\eta}_L}, \tag{3.9}$$

where $\dot{\eta}_L$ is the increase rate of the liquid viscosity. The liquid viscosity in Eq. (3.9) can be replaced by the effective viscosity η, because I adopt a mean-field approach. According to Eq. (3.7), the timescale of increasing

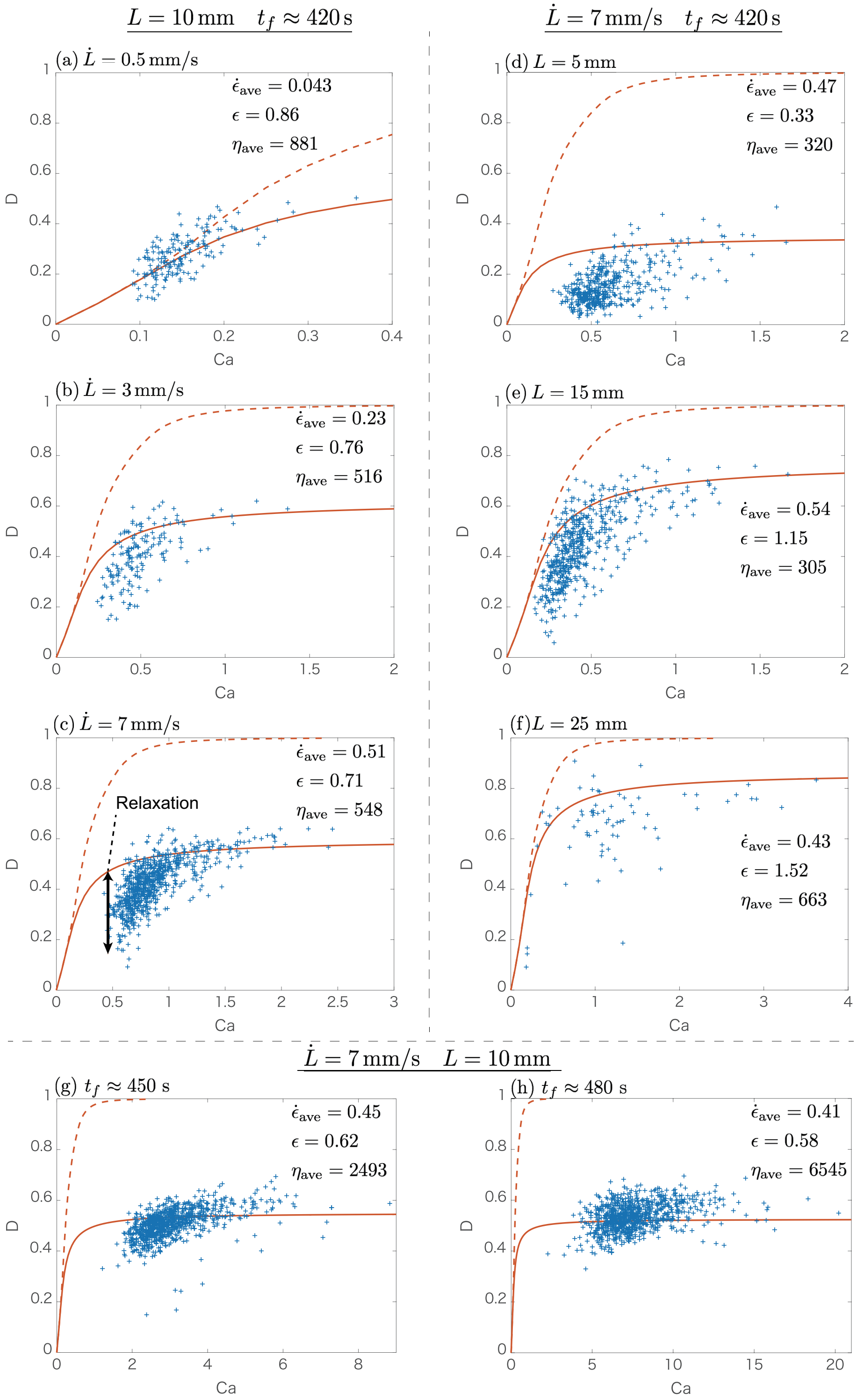

Figure 3.7: Variation of the bubble deformation degree D as function of the capillary number Ca. The plus sign indicates the experimental result. The red solid line indicates the result of MJT model, which depends on strain and Ca. Red dashed lines indicate the equilibrium shape of the bubble, which is calculated from the MJT model. All samples are categorized into constant pull length and finish time (a, b, c), constant pull rate and finish time (d, c, e, f), and constant pull rate and pull length (c, g, h).

viscosity is expressed as

$$\tau_{visco} = \frac{\eta}{\dot{\eta}} = \frac{1}{\alpha}. \tag{3.10}$$

The shape relaxation process can be considered as the competition of the timescale of shape relaxation and increasing viscosity. Here, I propose a new non-dimensional number referred to as the quench number:

$$Qu = \frac{\tau_{relax}}{\tau_{visco}} = \frac{R_b \dot{\eta}}{\Gamma} = \frac{R_b \alpha \eta_0}{\Gamma}, \tag{3.11}$$

where η_0 is the effective viscosity at the onset of shape relaxation. Large Qu means small τ_{visco} compared to τ_{relax}, resulting in the preservation of bubbles shape.

The amount of shape relaxation was analyzed in the following manner. First, I selected the smallest 50 bubbles for each sample because shape relaxation is prominent in smaller bubbles. Next, I calculated the mean bubble deformation degree $\overline{D}$ and the mean bubble radius $\overline{R}_b$ for the 50 bubbles. Using $\overline{R}_b$, I calculated the mean capillary number $\overline{Ca}$ and the mean quench number $\overline{Qu}$. For the mean capillary number $\overline{Ca}$ and strain ϵ applied to the sample, I calculated the MJT model to obtain the numerical deformation degree D_0 at the onset of shape relaxation. The amount of shape relaxation is quantified by $\frac{D_0 - \overline{D}}{D_0}$. The MJT model can also calculate the shape relaxation of an elongated bubble in solidifying foam. For a very small and a very large value of $\overline{Qu}$, the elongated bubble will be completely relaxed and quenched, respectively. I calculated the value of bubble deformation degree D_{solid} when the polyurethane foam completely solidified after the main extension and the shape relaxation. Deformation degree D_{solid} depends on the deformation degree at the onset of shape relaxation D_0 and the quench number $\overline{Qu}$.

Figure 3.8 shows that the shape relaxation $\frac{D_0 - \overline{D}}{D_0}$ from the experiments and $\frac{D_0 - D_{solid}}{D_0}$ from the model as a function of $\overline{Qu}$. The experimental results (circles) show that the shape relaxation becomes small with increasing $\overline{Qu}$. Comparing them with the model results (squares) for the same $\overline{Qu}$ and D_0, bubbles in polyurethane foam are not as relaxed as those in the model results. This difference can be explained by the non-Newtonian behavior of polyurethane foam. The MJT model, which calculates the shape relaxation after the main extension, assumes the Newtonian viscosity which increases exponentially with time. On the other hand, the curing process of polyurethane foam causes not only an increase in viscosity, but also the transition from liquid to solid including the appearance of yield stress (*Lipshitz and Macosko*, 1976). The yield stress makes it difficult for bubbles to relax by surface tension. Therefore, the numerical simulation suggests larger shape relaxation (squares and dashed lines in Fig. 3.8) than the experimental results. I think that quench number is useful for estimating the maximum relaxation effect in samples.

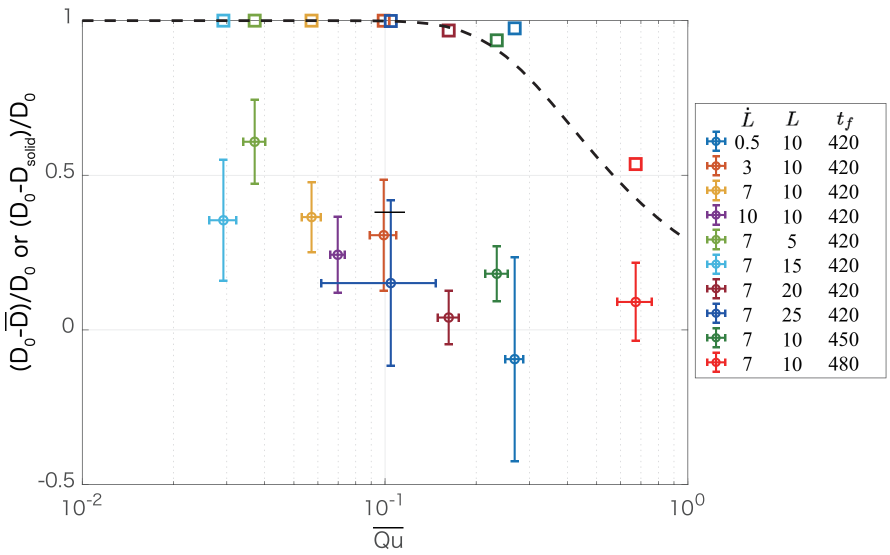

Figure 3.8: The amount of shape relaxation as a function of quench number $\overline{Qu}$. Circles indicate the shape relaxation of the experimental bubble, which is expressed as $\frac{D_0-\overline{D}}{D_0}$, where $\overline{D}$ is the average deformation degree for the smallest 50 bubbles, and D_0 is the numerical bubble deformation degree at the onset of shape relaxation. Squares indicate the numerical simulation of shape relaxation, which is expressed as $\frac{D_0-D_{solid}}{D_0}$, where D_{solid} is the numerical deformation degree when the foam completely solidifies after the main extension and shape relaxation. The dashed line indicates the numerical simulation results under the same initial conditions for $D_0 = 0.5$. The vertical and horizontal error bars are calculated from the standard deviations of D and R_b in a sample, respectively. The amount of shape relaxation becomes small with increasing $\overline{Qu}$. One experimental result ($\dot{L} = 0.5\ \mathrm{mm/s}$, $L = 10\ \mathrm{mm}$, $t_s = 420\ \mathrm{s}$) shows the negative value of shape relaxation because $\overline{D}$ of the foam were just a little more elongated than D_0 calculated from the MJT model.

3.4 Discussion

3.4.1 Bubble interaction

Based on the theoretical and experimental relationship between Ca and the equilibrium shape of a bubble, the shear rates during magma flow have been estimated from bubbles preserved in obsidian or pumice samples (*Polacci et al.*, 1999; *Rust et al.*, 2003; *Rust and Cashman*, 2007; *Dingwell et al.*, 2016). In the above estimations, the effect of bubble interaction has been pointed out as a potential source of the error from applying the deformation theory of a single bubble. This problem is particularly significant in analyzing tube pumice, which is the target of our study. *Wright et al.* (2009) showed that the connected porosity of tube pumice ranges from 0.57 to 0.70, which means actual vesicularities may be larger. They also mentioned that bubbles in tube pumice are stretched to high aspect ratios ($> 5:1$, which corresponds to $D > 0.67$).

Using polyurethane foam as an analogue material of magma, I produced the solid products whose texture is similar to tube pumice. The solidified samples have vesicularities about 0.6 (Table 3.2) and, in the case with large extension, highly elongated bubbles of $D > 0.67$ (Fig. 3.7). Strain and strain rate are known as the essential factors to control bubble shapes. In our experiments, the strain and strain rate that produced the elongated bubbles were well quantified by the data. Therefore, I think that our experimental data are useful for examining the effect of bubble interaction on bubble shapes. In the following discussion, I divide the effects in two processes: (1) through changing the shear field around bubbles and (2) through bubble coalescence.

In bubbly fluid, the shear field around each bubble varies due to the neighboring bubbles, and thus the actual capillary number which each bubble experiences is not equal to the mean capillary number calculated from the average strain rate and bulk viscosity. Because the bubble shape evolution is a non-linear equation, it is not obvious whether the average bubble shape depends on the average capillary number in the same way as a single bubble. The applicability of the average capillary number to the average bubble shape has been shown valid for emulsion under relatively low volume fraction ($\phi < 0.3$) by a direct numerical simulation (*Loewenberg*, 1998). In our experiments, Fig. 3.7 shows that the model for a single bubble represents the average value of the distribution of D for $L < 20\mathrm{mm}$. This result confirms that the deformation theory of a single bubble with the average capillary number can be applied to vesicularities as large as $\phi \sim 0.6$.

Bubble coalescence changes not only bubble shape but also bubble size. Figures 3.6g and 3.6h show that the samples with large pull length contain large bubbles ($R_b > 0.4$ mm). By comparing these samples with a sample without the main extension, it was suggested that the large bubbles were formed by bubble coalescences induced by the main extensional deformation. The point is that the bubble volume distribution (BVD) of the sample with coalesced bubbles exhibits a characteristic distribution, which is often observed in natural pyroclasts. BVD has been used to examine the occurrence of bubble coalescence in natural samples (*Shea et al.*, 2010). Bubble coalescence induced by bubble growth is known to show a distinct mode for large bubble size (*Klug and Cashman*, 1994; *Gurioli et al.*, 2008). Our samples, which experienced bubble coalescence enhanced by pure shear ($L > 20$ mm), also show a distinct mode for large bubble size ($R_b > 0.4$ mm), in addition to regular mode for smaller bubble size (Figs. 3.6g and 3.6h). This result suggests that the BVD is useful also to examine the bubble coalescence induced by shear around the bubbles. BVDs in the samples with

$L < 20\ \mathrm{mm}$ have asymmetrical distribution but lack the distinct mode for large bubble size, suggesting that bubble coalescence in these samples is less dominant than in the samples with the larger strain ($L > 20\ \mathrm{mm}$).

The coalescence of spherical bubbles always increases D, unless the coalesced bubble relaxes. On the other hand, I consider that coalescence of two ellipsoidal bubbles can either increase or decrease D depending on their shapes and relative locations before the coalescence. The coalescence along the long axes of two bubbles increases D, but the coalescence side by side decreases D. In the sample that shows significant bubble coalescence in the BVD (Fig. 3.6h), the bubble deformation degrees are widely distributed around the numerical result (Fig. 3.7f). This result implies that bubble coalescence leads to a wider distribution of D than the sample without bubble coalescence.

In summary, the deformation theory of a single bubble can be extended to the average deformation of non-dilute multiple bubbles, at least in the range of pure shear strain in the experiments ($\epsilon < 1.5$). Bubble deformation degrees are scattered around the model result due to both the inhomogeneous shear field around individual bubbles and bubble coalescence. With increasing strain, bubble coalescence is enhanced, and deformation degrees are more scattered around the model result of a single bubble.

3.4.2 Shape relaxation

In the samples deformed at low viscosities, small bubbles tend to be less elongated than those calculated by the MJT model (Fig. 3.7). This gap can be explained by the effect of shape relaxation, whereby the elongated bubbles were relaxed by the surface tension after pure shear flow ceased (Fig. 3.8). I believe that the quench number is a useful reference for estimating the effect of shape relaxation, although it cannot represent the effect of yield stress. The necessity of rapid cooling for tube pumice has been pointed out for the Minoan eruption (*Taddeucci and Wohletz*, 2001). To preserve elongated bubbles after fragmentation, tube pumice requires a large quench number and/or the appearance of yield stress.

Chapter 4

Simulation of bubble deformation

4.1 Introduction

The new bubble deformation model (MJT model) enabled us to calculate large transient deformations of a single bubble in arbitrary shear flows including volumetric change (Chapter 2). The extension experiment with solidifying foam suggested that the deformation theory of a single bubble can be compared with the average shape of multiple bubbles (Chapter 3). Although the vesicularity of pumice ($0.7 < \phi < 0.9$) is larger than the polyurethane foam used in chapter 3 ($\phi \approx 0.6$), I assume that the above suggestion can be extended to bubbles in pumice. An experimental calibration at higher vesicularities is needed for further work.

In this chapter, I calculate the deformation of a bubble in a volcanic conduit as a forward problem. The parameters needed for the MJT model are obtained by a conduit flow model.

Most conduit flow models which have been developed for the understanding of magma flow are one dimensional, assuming a parabolic velocity profile across a conduit. Strictly speaking, the assumption of a parabolic velocity is only valid for an incompressible laminar flow with a constant viscosity. Previous studies suggested that a plug-like velocity profile is induced by the shear-thinning effect near the conduit wall due to viscous heating or bubble elongation (*Llewellin et al.*, 2002a; *Mastin*, 2005; *Vedeneeva et al.*, 2005). It is expected that the velocity profile significantly affects bubble shape because bubble deformation depends on strain as well as capillary number.

Here, I obtain the velocity field around a bubble from a quasi two-dimensional conduit flow model based on a model of *Barmin et al.* (2004). The quasi two-dimensional model by *Barmin et al.* (2004), which is the same model as *Vedeneeva et al.* (2005), takes account of the effect of viscous dissipation and heat conduction. It is shown that the velocity profile across a conduit becomes a plug-like shape due to intense viscous-heating around conduit walls. The reason why I choose this model is that it is a fundamental model for an explosive eruption with viscous heating. Following the model of *Barmin et al.* (2004), I develop three models of explosive eruption: Newtonian isothermal model, shear-thinning model due to bubble deformation, and viscous-heating model. Depending on the rheology of magma, the velocity profile varies largely.

The rest of this chapter is organized as follows. Section 4.2 introduces the conduit flow models that I used. Section 4.3 describes the numerical method to solve the models. Section 4.4 shows the results of conduit flow simulations. In order to compare the numerical simulations with natural observations of bubble texture, I simulate the conduit flow assuming the 1.8 ka Taupo eruption. Section 4.5 demonstrates the application of the MJT model to the conduit-flow velocity field. Finally, section 4.6 provides the discussion.

4.2 Mathematical formulation

In this section, I describe a conduit flow model that I use. The model is based on a quasi-two-dimensional model proposed by *Barmin et al.* (2004). Our model has corrected their mass conservation equation that neglected density change due to bubble growth. The vertical velocity gradient generated by bubble growth is essential for pure shear deformation.

At first, I describe the model with the effect of viscous heating. Following the basic equations of the viscous heating model, I then introduce models with a Newtonian isothermal viscosity and a shear-thinning viscosity caused by bubble elongation.

4.2.1 Viscous heating model

The conduit flow is assumed to be composed of two regions: a bubbly fluid zone and a gas-particle dispersion region (Fig. 4.1). The two regions are separated by the fragmentation surface. In this thesis, I assume that fragmentation is defined as the depth where the critical void fraction reaches (*Sparks*, 1978).

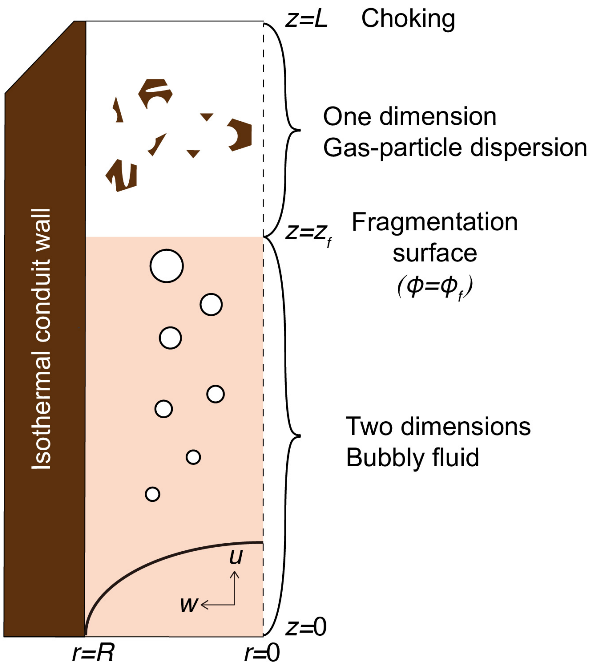

Figure 4.1: Schematic view of a volcanic conduit.

The bubbly fluid zone is assumed to be a quasi two-dimensional flow in which the pressure is homogeneous across the conduit but the other variables (e.g., velocity, temperature, and density) vary axisymmetrically. The magma is composed of melt, gas bubbles, and gas component dissolved in the melt. I ignore crystals. The viscosity of magma is controlled by the concentration of the dissolved gas and the temperature. I assume the gas exsolution to be in chemical equilibrium to simplify the numerical calculation. The magma temperature varies by viscous heating and heat transfer by conduction and advection.

The gas-particle flow part is treated as a one-dimensional flow using the velocity and density averaged over the cross section. The velocities of gas and particles are assumed to be identical. I neglect the temperature variation and viscous friction from the conduit wall, but incorporates the vertical variation of magma density.

Basic equations of the bubbly flow

From section 4.2 to 4.3, I express the basic equations in non-dimensional forms. Dimensional constants are indicated by an overscript $\tilde{}$. The definition of non-dimensional values are described in Eq. (D.34). In the cylindrical coordinate (z, r, θ) with the z-axis taken vertically upward, the non-dimensional conservation equations of the bubbly flow before fragmentation have the following forms.

$$\frac{1}{r}\frac{\partial}{\partial r}(r\rho w) + \frac{\partial}{\partial z}(\rho u) = 0, \tag{4.1}$$

$$p(r,z) = p(z), \quad \frac{dp}{dz} = \frac{2}{EuRe}\frac{1}{r}\frac{\partial}{\partial r}\left(r\eta\frac{\partial u}{\partial r}\right) - \frac{2}{EuFr^2}\rho, \tag{4.2}$$

$$\frac{1}{r}\frac{\partial}{\partial r}(r\rho w e) + \frac{\partial}{\partial z}(\rho u e) = -\frac{EuEc}{2}p\,\mathrm{div}\boldsymbol{v} + \frac{Ec}{Re}\eta\left(\frac{\partial u}{\partial r}\right)^2 + \frac{1}{Pe}\frac{1}{r}\frac{\partial}{\partial r}\left(r\frac{\partial T}{\partial r}\right), \tag{4.3}$$

$$\mathrm{div}\ \boldsymbol{v} = \frac{1}{r}\frac{\partial}{\partial r}(rw) + \frac{\partial u}{\partial z}, \tag{4.4}$$

$$Re = \frac{\tilde{\rho}_m\tilde{u}_0 R}{\tilde{\eta}_0}, \quad Fr = \frac{\tilde{u}_0}{\sqrt{\tilde{g}\tilde{R}}}, \quad Ec = \frac{\tilde{u}_0^2}{\tilde{c}_{Vm}\tilde{T}_0}, \quad Eu^{-1} = \frac{\tilde{\rho}_m\tilde{u}_0^2/2}{\tilde{p}_0}, \quad Pe = \frac{\tilde{\rho}_m\tilde{u}_0\tilde{R}\tilde{c}_{Vm}}{\tilde{\kappa}}. \tag{4.5}$$

Here, Eq. (4.1), Eq. (4.2), and Eq. (4.3) represent the conservations of the mass, the momentum, and the internal energy, respectively. The equations have been simplified with assumptions that the non-dimensional conduit length scale L is much larger than its radius and that the flow inertia effects are negligible. The detail of their derivation is given in appendix D. The vertical and radial velocity components are given by u and w, respectively. The velocity vector $\boldsymbol{v}$ is defined as $\boldsymbol{v} = (u, w, 0)$. ρ, p, η, e, and T are the density, the pressure, the melt viscosity, the internal energy density, and the temperature increment from the initial temperature at the conduit inlet. When obtaining the non-dimensinoal equations, I used the following characteristic dimensional values: $\tilde{R}$ is the conduit radius, $\tilde{u}_0$ is a characteristic velocity, $\tilde{\rho}_m$ is the melt density, $\tilde{T}_0$ is the initial temperature at the conduit inlet, $\tilde{p}_0$ is the hydrostatic pressure at the conduit inlet ($\tilde{p}_0 = \tilde{\rho}_m\tilde{g}\tilde{L} + \tilde{p}_{atm}$ where $\tilde{p}_{atm}$ is the atmospheric pressure and $\tilde{g}$ is the gravity acceleration), $\tilde{c}_{Vm}$ is the specific heat of the melt, and $\tilde{\eta}_0$ is the characteristic magma viscosity. Following *Barmin et al.* (2004), I set $\tilde{u}_0$ to a constant value of $1\ \mathrm{m/s}$ in order to represent the non-dimensional mass discharge rate Q_m as an explicit parameter. The non-dimensionalization gives the dimensionless number defined in Eq. (4.5): Re is the Reynolds number, Fr is the Froude number, Ec

is the Eckert number, Eu is the Euler number, and Pe is the Peclet number. In the Peclet number, $\tilde{\kappa}$ indicates the thermal conductivity. The assumption that the inertia effect is negligible is equivalent with that all of Re, Fr, Ec, and Eu^{-1} are small.

The melt viscosity model, which was developed by *Hess and Dingwell* (1996), depends on the temperature increment T and the mass fraction of the dissolved gas c which follows the equilibrium solubility law:

$$\eta(c,\,T) = \frac{1}{\tilde{\eta}_0} 10^{A(c,\,T)}, \quad A(c,\,T) = 0.291 + 0.833\ln(c) - \frac{1304 + 2368\ln(c)}{\tilde{T}_0(1+T) - (344.2 + 32.25\ln(c))}, \tag{4.6}$$

$$c = c(p) = \min(c_0\sqrt{p}, c_{max}), \quad c_0 = \tilde{C}_f\sqrt{\tilde{p}_0}, \tag{4.7}$$

where $\tilde{\eta}_0$ is the dimensional magma viscosity corresponding to the pressure $\tilde{p}_0$ and the temperature $\tilde{T}_0$, c_{max} is the concentration of gas in the melt in the absence of bubbles in magma, and $\tilde{C}_f$ is the solubility parameter.

The bulk density and the equation of state for the gas phase follow the following forms

$$\frac{1}{\rho} = \frac{1-c_{max}}{1-c} + \frac{c_{max}-c}{1-c}\frac{1}{\rho_g}, \quad \rho_g = \rho_{g0}\frac{p}{T+1}, \quad \rho_{g0} = \frac{\tilde{p}_0}{\tilde{\rho}_m \tilde{R}_g \tilde{T}_0}, \tag{4.8}$$

where ρ_g is the non-dimensional gas density and $\tilde{R}_g$ is the gas constant. The melt density is assumed to be a constant and is scaled as unity. The gas volume ratio ϕ is given by

$$\frac{1}{\phi} = 1 + \frac{1-c_{max}}{c_{max}-c}\rho_g. \tag{4.9}$$

The internal energy density e is defined as

$$e = \psi(p)(T+1), \quad \psi(p) = \frac{1-c_{max}}{1-c} + \frac{c_{max}-c}{1-c}c_{Vg}, \tag{4.10}$$

where c_{Vg} is the non-dimensional specific heat of the gas phase at constant volume. The specific heat of the melt phase is scaled as unity.

At the conduit inlet, the velocity profile is assumed to be parabolic and the temperature is homogeneous across the conduit:

$$z = 0: \quad w(r,0) = 0, \quad u(r,0) = 2u_{a0}\left(1 - r^2\right), \quad T(r,0) = 0, \tag{4.11}$$

where u_{a0} is the average velocity which is given by

$$u_{a0} = \frac{Q_m}{4\pi\int_0^1 \rho(r,0)\,(1-r^2)\,rdr}, \tag{4.12}$$

where Q_m is the non-dimensional mass discharge rate.

At the conduit axis, the axisymmetric boundary condition should be satisfied:

$$r = 0: \quad w(0,z) = 0, \quad \frac{\partial u}{\partial r}(0,z) = 0, \quad \frac{\partial p}{\partial r}(0,z) = 0, \quad \frac{\partial T}{\partial r}(0,z) = 0. \tag{4.13}$$

At the conduit wall, I impose the no-slip condition for the velocity. For the temperature, *Barmin et al.* (2004) considered two conditions: the adiabatic or isothermal condition. In our study, I use the isothermal condition that the wall temperature is the same as the initial temperature at the conduit inlet.

$$r = 1: \quad w(1,z) = 0 \quad u(1,z) = 0 \quad T(1,z) = 0. \tag{4.14}$$

The viscous-heating model is composed of the basic equations Eqs. (4.1)-(4.3), the temperature-dependent viscosity model Eq. (4.6), and the volatile solubility model Eq. (4.7), together with the boundary conditions Eqs. (4.11)-(4.14).

Basic equations of the gas-particle flow

The basic equations after fragmentation are cross-sectionally averaged. The velocities of gas and particles are equal and the flow is isothermal. The non-dimensional equations are expressed as follows

$$u(p) = \frac{Q_m/\pi}{\rho_g(p)\phi(p) + (1-\phi(p))}, \tag{4.15}$$

$$\frac{dp}{dz} = \frac{1}{f(p)}, \quad f(p) = -Fr^2\left(\frac{\pi}{Q_m}\frac{Eu}{2} + \frac{du}{dp}\right)u(p), \tag{4.16}$$

$$\rho_g = \rho_{g0}p, \tag{4.17}$$

where u is the cross-sectional averaged flow velocity in gas-particle region. Eq. (4.15) represents the mass conservation. Eq. (4.16) is obtained from the momentum conservation, and Eq. (4.17) is the equation of state for the gas phase with the assumption of $T = 0$. Since the temperature increase in the bubbly flow region due to the viscous-heating effect is concentrated in a very narrow zone near the wall, the average temperature of the mixture is assumed to be equal to the initial temperature. In the gas-particle flow, the viscous-heating effect is negligible. The effect of gas expansion on the temperature is also neglected due to the large heat capacity of the particles. Therefore, I do not solve the energy equation. Then, the gas density is controlled only by the pressure. The derivation of Eqs. (4.15)-(4.17) are described in appendix D.

From Eq. (4.15), I have

$$\frac{du}{dp} = \frac{Q_m}{\pi}\frac{d}{dp}\left(\frac{1}{\rho}\right) = -\frac{\pi}{Q_m}\frac{Eu}{2}Ma^2, \quad Ma = \frac{u}{a}, \quad a = \sqrt{\frac{Eu}{2}\frac{dp}{d\rho}}, \tag{4.18}$$

where Ma is the Mach number and a is the dimensionless speed of sound. When $Ma = 1$ is satisfied, Eq. (4.18) gives $f(p) = 0$. This condition corresponds to the choking condition.

From Eq. (4.16), the fragmentation level z_f can be determined:

$$z_f = L - \int_{p_f}^{p_{out}} f(p)dp, \tag{4.19}$$

where p_f is the pressure when the gas volume fraction reached the critical concentration $\phi = \phi_f$. Eq.(4.9) gives the fragmentation pressure p_f

$$p_f = \left(\frac{-c_0(1-\phi_f) + \sqrt{c_0^2(1-\phi_f)^2 + 4\rho_{g0}c_{max}(1-c_{max})\phi_f(1-\phi_f)}}{2\rho_{g0}(1-c_{max})\phi_f} \right)^2 . \tag{4.20}$$

The fragmentation pressure depends on c_0, ϕ_f, ρ_{g0}, and c_{max}.

At the conduit outlet, the pressure p_{out} should satisfy the following condition:

$$p_{out} = \max(p_a, p^*), \tag{4.21}$$

where p_a is the dimensionless atmospheric pressure and p^* is the solution of $f(p) = 0$. The pressure of p^* corresponds to the pressure when choking occurs.

4.2.2 Newtonian isothermal model and shear-thinning model due to bubble deformation

Newtonian isothermal model assumes that the viscosity is Newtonian and the temperature is isothermal throughout the conduit. The non-dimensional conservation equations of mass and momentum are the same as the viscous-heating model.

We also consider the conduit flow with the shear-thinning effect induced by bubble elongation. The non-dimensional basic equations are the same as the viscous-heating model except viscosity. Instead of solving the energy equation to calculate the temperature-dependent viscosity, I use the bulk viscosity of bubbly fluid η_b.

The shear-thinning effect caused by bubble elongation has been investigated over the past decades. Although there are still some debates in modeling the rheology of bubbly fluid, I employ the model by *Llewellin et al.* (2002b). The simple form of the viscosity model by *Llewellin et al.* (2002b) is summarized in *Mader et al.* (2013). The relative viscosity $\eta_r = \frac{\eta_b}{\eta}$ under simple shear flow is given by the form of a Cross model (*Cross*, 1965),

$$\eta_r = \eta_{r,\infty} + \frac{\eta_{r,0} - \eta_{r,\infty}}{1 + (\frac{6}{5}Ca)^2}. \tag{4.22}$$

The above viscosity model assumes a bubbly flow under simple shear. In addition, the momentum equation of (4.2) takes into account the shear stress of simple shear. I calculate Ca with the simple shear rate $\dot{\gamma}$:

$$\dot{\gamma} = \frac{\partial u}{\partial r}. \tag{4.23}$$

The asymptotic relative viscosities at low and high Ca are represented by $\eta_{r,0}$ and $\eta_{r,\infty}$, respectively. For large gas fractions, they are given by *Pal* (2003) as follows:

$$\eta_{r,0} = (1-\phi)^{-1}, \tag{4.24}$$

$$\eta_{r,\infty} = (1-\phi)^{\frac{5}{3}}. \tag{4.25}$$

Fig. 4.2 shows the relative viscosity η_r as a function of the capillary number Ca and gas volume fraction ϕ. The relative viscosity varies sharply around $Ca = 1$.

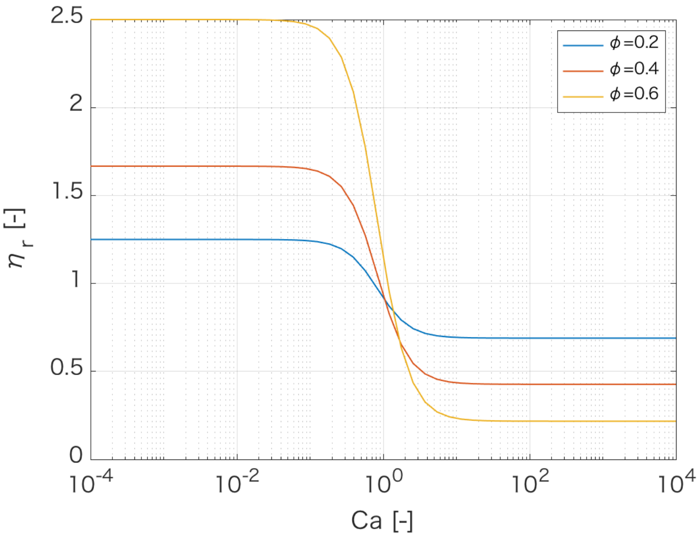

Figure 4.2: Relative viscosity η_r as a function of the capillary number Ca for different gas volume fractions. The relative viscosity was calculated by the rheology model of *Llewellin et al.* (2002b).

The capillary number depends on the spherical bubble radius $\tilde{R}_b$. The conduit flow model which I used here does not resolve the evolution of bubble radius, but it does calculate the gas volume fraction ϕ as a function of z. Neglecting bubble coalescence, I calculate $\tilde{R}_b$ by,

$$\frac{4\pi}{3}\tilde{R}_b^3 = \frac{\phi}{(1-\phi)\tilde{N}_b}, \tag{4.26}$$

where $\tilde{N}_b$ is the number of bubbles per unit volume of melt. Eq. (4.26) is also used in combining the conduit flow model to the bubble deformation model.

4.3 Numerical method

The undetermined parameters are the dimensional conduit radius $\tilde{R}$ and the dimensional initial pressure $\tilde{p}_{in}$. They are determined by solving the following boundary problem.

4.3.1 Fragmentation surface

The fragmentation level z_f is calculated from Eqs. (4.19) and (4.20). Fig. 4.3 shows the fragmentation level as a function of the conduit radius $\tilde{R}$ and the magma discharge rate $\tilde{Q}_m$. The relative location of the fragmentation surface z_f decreases with the conduit radius. This trend is caused by the dynamics in the gas-particle region.

As mentioned in Eq. (4.21), the boundary condition at the exit is determined by the choking condition. For the isothermal condition, the sound velocity of the gas-particle mixture is approximated as follows (*Kieffer*, 1977)

$$\tilde{a} = \sqrt{\frac{d\tilde{p}}{d\tilde{\rho}}} \sim \sqrt{\frac{\tilde{p}}{\tilde{\phi}\tilde{\rho}}} = \frac{\tilde{p}}{\tilde{\rho}\sqrt{\alpha \tilde{R}_g \tilde{T}}}, \tag{4.27}$$

where α is the gas mass fraction. Following the mass conservation law $\tilde{Q}_m = \pi \tilde{R}^2 \tilde{\rho}_{out} \tilde{a}$, I obtain

$$\tilde{p}^* \sim \frac{\tilde{Q}_m}{\pi \tilde{R}^2} \sqrt{\alpha_{out} \tilde{R}_g \tilde{T}}. \tag{4.28}$$

where $\tilde{p}^*$, $\tilde{\rho}_{out}$, and α_{out} are the pressure, the density, and the gas mass fraction at the conduit exit, respectively. Eq. (4.28) indicates that the pressure at the exit decreases with the conduit radius for a given mass flux (Fig. 4.3). The decrease in $\tilde{p}_{out}$ leads to the increase in the pressure gradient from the exit to the fragmentation surface ($\tilde{p}_f - \tilde{p}_{out}$), resulting in increasing the gas-particle region ($\tilde{L} - \tilde{z}_f$). In this way, the dynamics of the gas-particle flow region requires that the fragmentation surface goes down with the conduit radius.

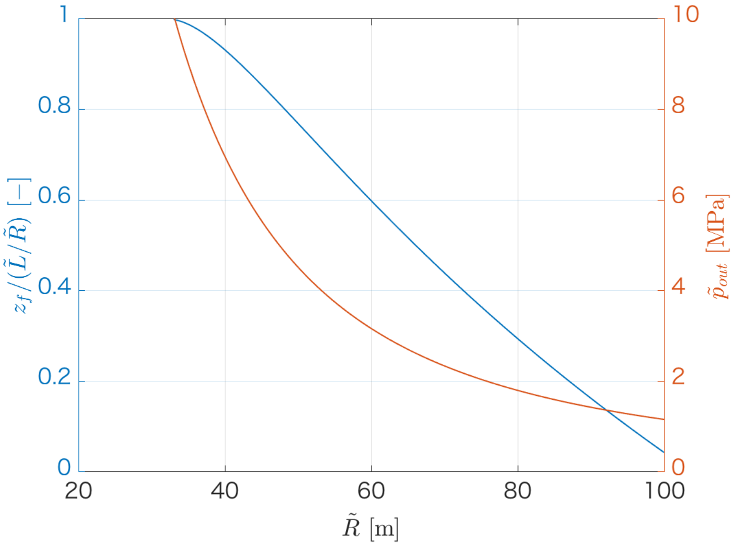

Figure 4.3: Blue line shows the relative location of the fragmentation surface $z_f/(\tilde{L}/\tilde{R})$ as a function of the conduit radius $\tilde{R}$. Red line indicates the exit pressure $\tilde{p}_{out}$ as a function of $\tilde{R}$. The dimensional parameters are the same as the simulation of the Taupo plinian eruption except for the conduit radius.

4.3.2 Initial pressure

Barmin et al. (2004) solved the boundary problem about the non-dimensional magma discharge rate Q_m as a function of the given pressure p_{in} at the conduit entrance under the fixed conduit radius. In our study, the dimensional discharge rate $\tilde{Q}_m$ is fixed, while the dimensional conduit radius $\tilde{R}$ and the initial pressure $\tilde{p}_{in}$ are varied. For the given R, I calculate Q_m and solve Eqs. (4.19) and (4.21) for the gas-particle flow part to obtain z_f and p_{out}. Then, I solve the basic equations before fragmentation (Eqs. 4.1-4.3), and find the adequate p_{in} which satisfies the boundary condition $p = p_f$ at the fragmentation surface $z = z_f$. I assume a value of R and find an adequate p_{in} by the shooting method in the following way.

4.3.3 Solving the viscous heating model

In the viscous-heating model, the differential equations (4.1)-(4.3) and the equation of state (4.8) have four variables: the pressure, two velocity components, and temperature. These variables were solved by the finite difference method. In the vertical direction, the unknown pressure was found by the combination of the explicit scheme and the iteration method. Under a fixed pressure, the radial profile of temperature is determined by the implicit scheme. The radial profile of two velocities are also found by the explicit scheme. The detail numerical method is summarized in appendix D.

4.4 Results of the simulations

Since I am interested in dimensional values, I show numerical results in dimensional forms. Hereafter, all the quantities are given in dimensional forms unless specified, so that I omit the overscript $\tilde{}$.

4.4.1 Parameter values

The parameters used in the simulations are summarized in Table. 4.1. For Taupo plinian eruption, I considered a cylindrical conduit $4\,\mathrm{km}$ in depth, an initial $\mathrm{H_2 0} = 4.3\,\mathrm{wt\%}$ (*Dunbar et al.*, 1989a; *Legros et al.*, 2000), and an initial temperature $T_0 = 850\,^{\circ}\mathrm{C}$ (*Dunbar et al.*, 1989b). The parameters required for the viscous heating model are derived from *Barmin et al.* (2004). Mass discharge rate is from *Wilson and Walker* (1985).

4.4.2 Boundary problems

Fig. 4.4 is the graph of the initial pressure p_{in} as a function of the conduit radius R. All models show that p_{in} decreases with increasing R because of the lower fragmentation level (Fig. 4.3). In the case of the Newtonian isothermal model (Fig. 4.4, blue line), p_{in} becomes equal to the lithostatic pressure when $R = 53\,\mathrm{m}$. In the case of shear-thinning model (red line), p_{in} becomes lower than in the case of Newtonian isothermal model. This result is explained by the decrease of flow resistance. In the case of viscous-heating model (yellow line), the effect of decreasing flow resistance becomes more significant than that in the other two models. The initial pressure cannot be equal to the lithostatic pressure even in the case of the smallest assumed R.

Table 4.1: Parameters for the simulation of Taupo plinian eruption (TP) and Taupo Ignimbrite (TI)

Parameter	Notation	Value
Conduit length [a]	L	$4000\ \mathrm{m}$
Representative velocity	u_0	$1.0\ \mathrm{m/s}$
Melt density [c]	ρ_m	$2500\ \mathrm{kg/m^3}$
Initial temperature [b]	T_0	$1123\ \mathrm{K}$
Representative pressure	p_0	$98\ \mathrm{MPa}$
Heat capacity of the melt phase [c]	$c_{Vm}(c_{V0})$	$1200\ \mathrm{J/(kg \cdot K)}$
Heat capacity of the gas phase [c]	c_{Vg}	$1560\ \mathrm{J/(kg \cdot K)}$
Gas constant [c]	R_g	$462\ \mathrm{J/(kgK)}$
Water content [a]	c_{max}	0.043
Solubility coefficient [c]	C_f	$4.1 \times 10^{-6}\mathrm{Pa}^{-1/2}$
Gravity acceleration [c]	g	$9.8\ \mathrm{m/s^2}$
Thermal conductivity [c]	κ	$0.8\ \mathrm{J/(m \cdot s \cdot K)}$
Critical volume fraction [d]	ϕ_f	0.79 for TP
Mass discharge rate [e]	Q_m	$2.5 \times 10^8\ \mathrm{kg/s}$

[a] Conduit length and initial water content from *Dunbar et al.* (1989a)

[b] Initial temperature from *Dunbar et al.* (1989b)

[c] Parameters from *Barmin et al.* (2004)

[d] Critical volume fraction is equal to the average vesicularity of pumice

[d] Mass discharge rate from *Wilson and Walker* (1985)

The conduit radius of the viscous heating model is set to the smallest value of $R = 33\ \mathrm{m}$ in order to set p_{in} to a high value (Fig. 4.4). Further reduction of R cannot cause fragmentation in the conduit (Fig. 4.3).

The initial pressure p_{in} should be close to the lithostatic pressure, because of the mechanical strength of the rocks of conduit walls. *Barmin et al.* (2004) noted that p_{in} can not exceed the lithostatic pressure by more than $20 - 30\,\mathrm{MPa}$. In our study, I find p_{in}, which is the closest to the lithostatic pressure, by changing the conduit radius R. Table 4.2 summarizes the conduit radius for each model. It should be noted that the viscous heating model does not satisfy the lithostatic condition of $p_{in} = p_0$. This problem will be discussed in section 4.6.2.

Table 4.2: Parameters for the simulation of Taupo plinian eruption

Case	Model	Conduit radius [m]
Case 1	Newtonian isothermal model	53
Case 2	Shear-thinning model due to bubble deformation	48
Case 3	Viscous heating model	33

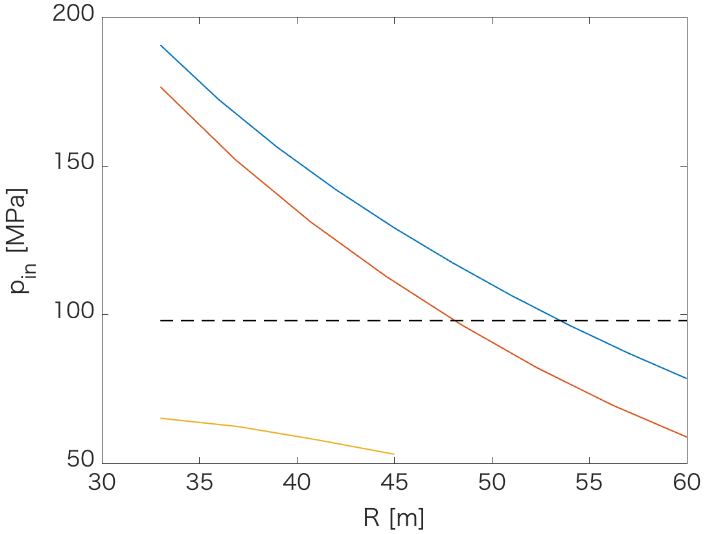

Figure 4.4: Initial pressure p_{in} as a function of the conduit radius R. Blue, red, and yellow line corresponds to the Newtonian isothermal, the shear-thinning due to bubble deformation, and the viscous-heating model, respectively. Black dashed line indicates the lithostatic pressure (98 MPa).

4.4.3 Results of the conduit flow

Case 1: Newtonian isothermal model

Fig. 4.5 shows the radial profile of the vertical velocity component, u, and the vertical variation of pressure. As expected from Eq. (D.89) in appendix D, the velocity profile keeps a parabolic shape. The steep pressure gradient just below the fragmentation surface reflects the increase in viscous friction, which is caused by increasing the viscosity as well as increasing the strain rate.

Case 2: Shear-thinning model due to bubble deformation

Fig. 4.6 shows the radial distribution of two velocity components (u, w), and the vertical distribution of pressure. The radial profile of u slightly flattened around the conduit center (Fig. 4.6a), but it is a similar to the parabolic shape which was already shown in the Newtonian isothermal model (Fig. 4.5a). On the other hand, the upward pressure decrease of this model is more gradual than the Newtonian isothermal model (Fig. 4.6c). These behaviors reflect the radial distribution of the capillary number (Fig. 4.6d). As the magma rises in the conduit, the capillary number increases and the small Ca region gradually narrows. The conduit flow around the fragmentation surface is dominated by the high Ca region, which leads to a decrease in the bulk viscosity (Fig. 4.6e). Therefore, the viscous friction in this model is smaller than the Newtonian isothermal model. The development of plug-like velocity profile needs $Ca \ll 1$ around the conduit center and $Ca \gg 1$ near the conduit wall (*Llewellin et al.*, 2002a; *Colucci et al.*, 2017). Because most of the conduit cross-section show the $Ca \gg 1$ region (Fig. 4.6d), the velocity profile keeps a parabolic profile.

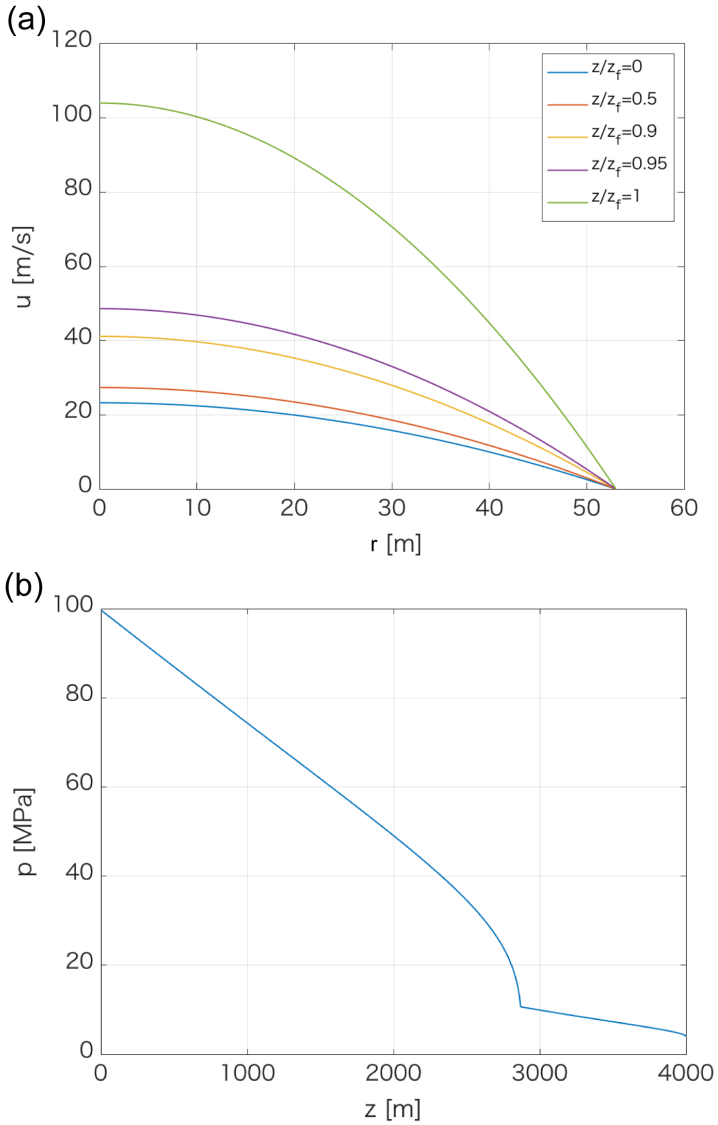

Figure 4.5: The calculation result of the Newtonian isothermal model. (a) Velocity distribution across the conduit at $z/z_f = 0, 0.5, 0.9, 0.95, 1$. The fragmentation surface z_f is 2869 m. (b) Pressure profile along with the conduit axis.

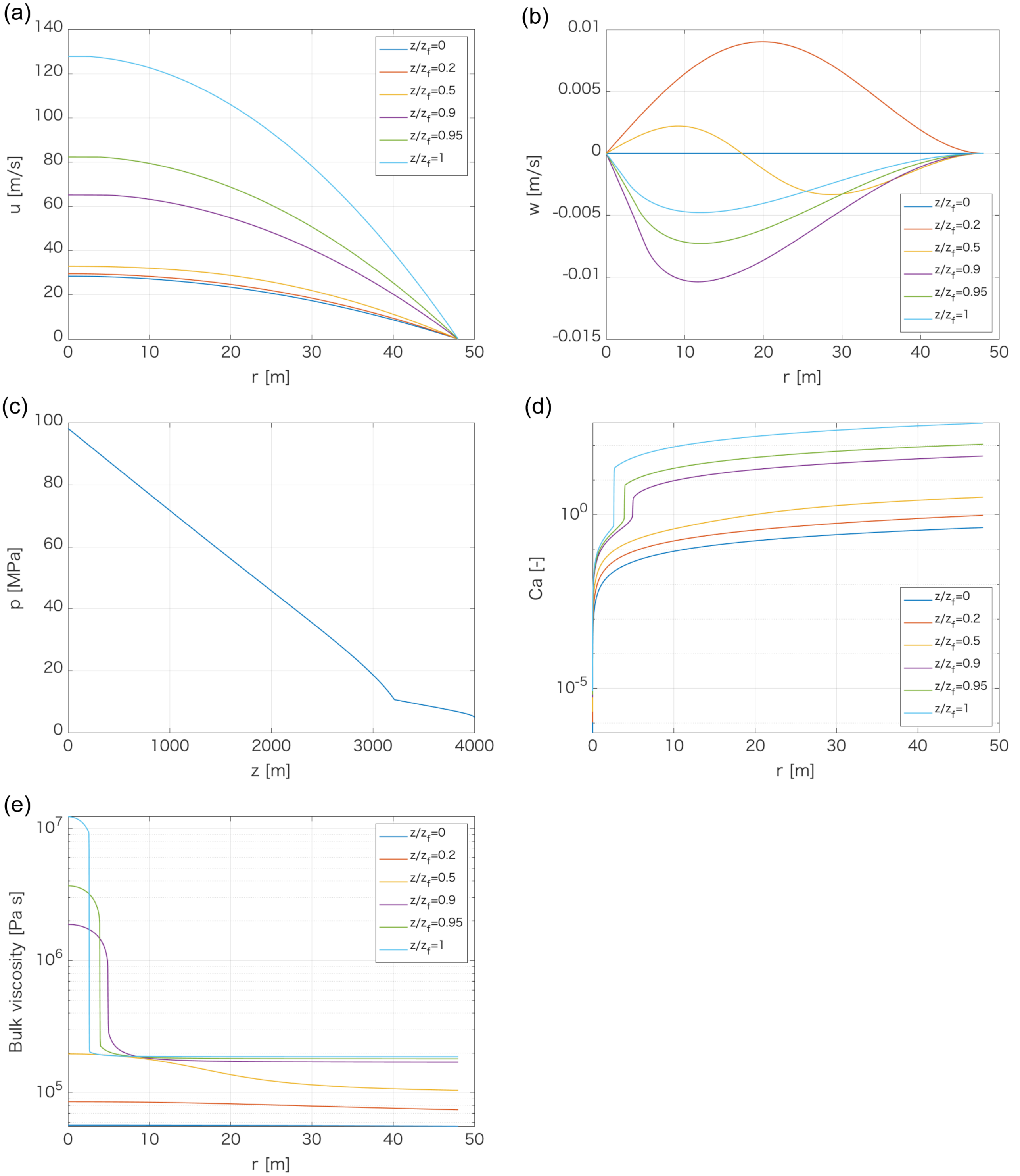

Figure 4.6: The calculation result of the shear-thinning model. (a) Vertical velocity distribution across the conduit at $z/z_f = 0, 0.2, 0.5, 0.9, 0.95, 1$. The fragmentation surface z_f is 3214 m. (b) Horizontal velocity distribution. (c) Pressure profile along with the conduit axis. (d) Capillary number. (e) Bulk viscosity.

We use the viscosity model in the steady state to simulate the conduit flow, although one of our research goals is to calculate transient bubble deformation. In order to check the validity of using the steady viscosity, I calculate a dynamic capillary number Cd proposed by *Llewellin et al.* (2002b,a). It is given by

$$Cd = \tau_{relax} \frac{\ddot{\gamma}}{\dot{\gamma}} = \frac{R_b \eta}{\Gamma} \frac{\ddot{\gamma}}{\dot{\gamma}}, \tag{4.29}$$

where $\ddot{\gamma}$ is the rate of change in the strain rate and τ_{relax} is the relaxation time scale ($\tau_{relax} = R_b\eta/\Gamma$). In this case, the stain rate $\dot{\gamma}$ is defined as the simple shear rate (Eq. 4.23). The dynamic capillary number represents the competition between the timescale for a bubble to reach the steady state (τ_{relax}) and that for a change in the shear field ($\dot{\gamma}/\ddot{\gamma}$). A bubble under $Cd \ll 1$ is expected to keep its steady state. On the other hand, if $Cd \gg 1$, a bubble does not have time to respond to any changes in the external shear field.

Fig. 4.7 shows the distribution of the dynamic capillary number and the capillary number. Most of the conduit flow satisfies $Cd \ll 1$ except for the region just below the fragmentation surface. In the small Cd region, I think the steady-viscosity model of *Llewellin et al.* (2002b) is applicable. However, this viscosity model cannot be directly applied for the unsteady region that shows large Cd.

The rheology model has been investigated in recent decades, but the viscosity in the unsteady-state is not well understood. *Llewellin et al.* (2002b) investigated the rheology of bubble suspensions in the oscillatory flow at small total strains and strain-rates ($Ca \ll 1$), They confirmed that the Oldroyd-type rheology model of *Frankel and Acrivos* (1970) provided a good fit to their experimental data. Contrary to the study of *Llewellin et al.* (2002b), I deal with the large deformation of bubbles under the large Ca condition. I am not sure of the applicability of the rheology model to our simulation. If the rheology model is valid at even large deformation and large Ca, the model indicates the limiting viscosity at $Cd \gg 1$ equals to the viscosity at $Ca \gg 1$ (*Llewellin et al.*, 2002a). Fig. 4.7 shows that the large Cd region overlaps with the Ca region.

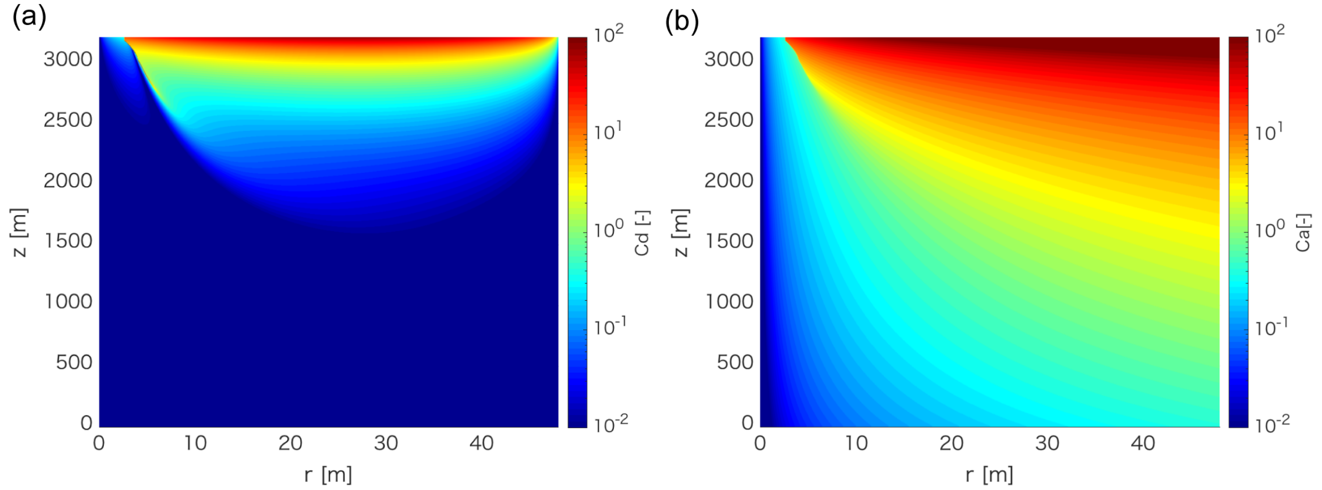

Figure 4.7: The distribution of (a) the dynamic capillary number and (b) the capillary number. The large Cd region overlaps with the large Ca region.

Case 3: Viscous heating model

The distributions of two velocity components (u, w) and the profile of pressure p in the viscous-heating model are shown in Fig. 4.8. The radial distributions of u, temperature, viscosity, and void fraction close to the conduit wall are shown in Fig. 4.9.

The viscous heating forms a thin thermal boundary layer around the conduit wall, which is characterized by high temperature and low viscosity (Fig. 4.9b and c). Strong viscous heating changes the velocity profile from a parabolic shape to a plug-like shape just above the inlet. As the velocity profile flattens towards the center of the conduit, w has positive values (Fig. 4.8b). The value of w can be as large as u near the inlet where the plug-like profile is formed, but w stays much smaller than u afterward.

The pressure profile along the conduit axis is completely different from the Case 1 and 2. In the viscous-heating model, the pressure gradient before fragmentation is not sharp but gradual (Fig. 4.8c). Intense viscous heating around the conduit wall leads to a decrease in viscous friction. Then, the vertical pressure gradient is determined by the hydrostatic value when the inertia effect is neglected (see section 4.6.3). In *Barmin et al.* (2004), the pressure gradient before fragmentation is nearly linear because they assume that the density of bubbly magma before fragmentation is constant. Contrary to their study, I take account of the decrease in the density induced by bubble growth, and therefore the pressure gradient becomes smaller upward.

The hot region propagates inward because of thermal diffusion and the constant wall temperature, but most of the interior region keeps the initial temperature (Fig. 4.9b). This calculation result verifies the assumption that the temperature in gas-particle region after the fragmentation is equal to the initial temperature.

The void fraction of the magma near the conduit wall is a little higher than at the inner conduit. This difference is caused by the temperature distribution across the conduit. Because the gas phase follows the ideal gas flow, void fraction depends on temperature as well as pressure.

It should be noted that the temperature in the thermal boundary layer reaches very high values (up to $3400\,^{\circ}\mathrm{C}$ at the fragmentation surface). This value exceeds the reasonable range of temperature for which the model of *Hess and Dingwell* (1996) is applicable. The wall rocks around the conduit wall perhaps experience the intense melting. This problem will be discussed in section 4.6.2.

4.4.4 Viscous friction

Viscous friction in the bubbly fluid region is shown in Fig. 4.10. In the case 1 and 2, the viscous friction increases with z because of the magma acceleration and the increased melt viscosity. Due to the shear-thinning effect, the viscous friction in the case 2 is a little lower than the case 1. Contrary to the two cases, the viscous friction in the case 3 rapidly decreases due to the decrease in melt viscosity caused by shear heating. Viscous friction near the conduit inlet ($z = 0$) is larger in the case 3 than in the cases 1 and 2, because the vertical velocity is set larger due to the small conduit radius.

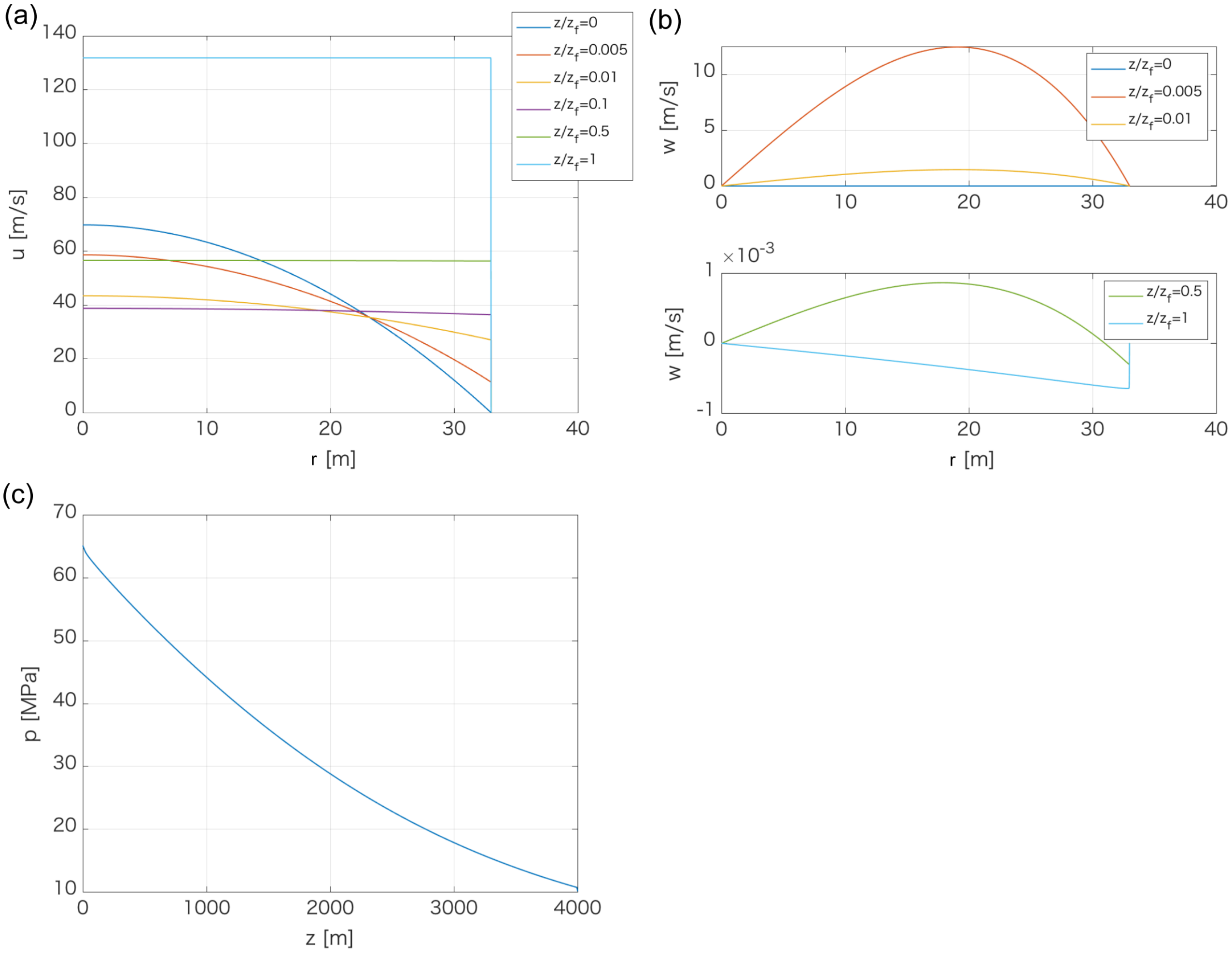

Figure 4.8: The calculation result of the viscous-heating model. (a) Vertical velocity distribution across the conduit at $z/z_f = 0, 0.005, 0.001, 0.1, 0.5, 1$. The fragmentation surface z_f is $3994\,\mathrm{m}$. (b) Horizontal velocity distribution. (c) Pressure profile along with the conduit axis.

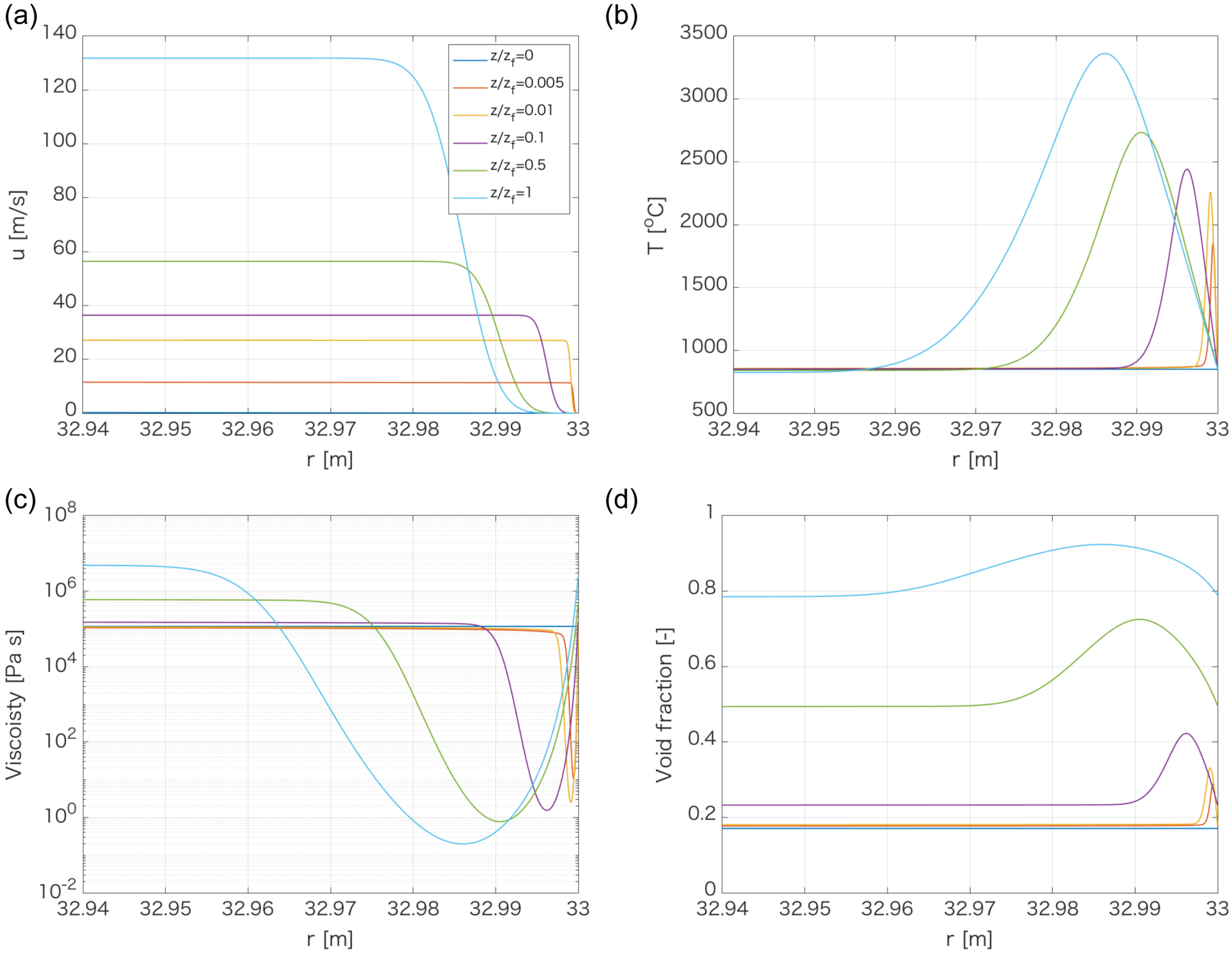

Figure 4.9: The calculation result of the viscous-heating model at the narrow region around the conduit wall. (a) Vertical velocity. (b) Temperature. (c) Viscosity. (d) Void fraction.

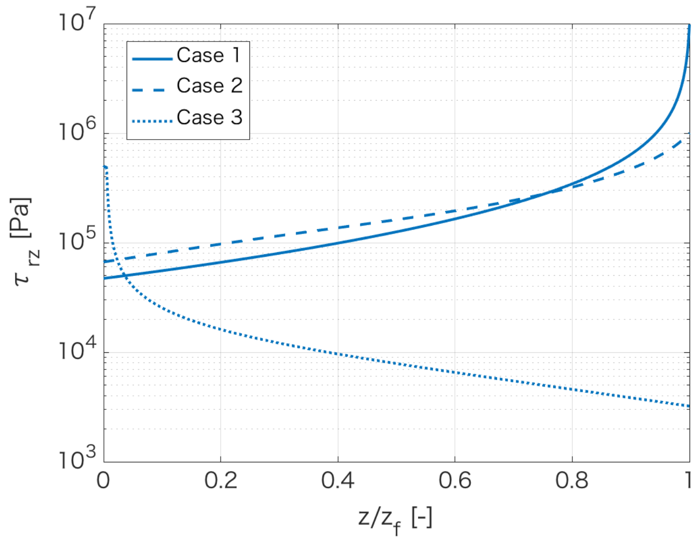

Figure 4.10: Viscous friction at the conduit wall $\tau_{rz}(R, z) = \eta \frac{\partial u}{\partial r}$ in the bubbly fluid region. Solid, dashed, and dotted lines represent the Newtonian isothermal model (Case 1), the shear-thinning model due to bubble deformation (Case 2), and the viscous heating model (Case 3).

4.5 Bubble deformation

Using the results of the flow simulation in the previous section, I calculate the deformation of a bubble in the conduit.

4.5.1 Implementation of the MJT model in the conduit flow

Deriving the velocity gradient

The velocity profile obtained from the conduit flow simulation is regarded to make the velocity gradient tensor L_{ij}^C for the MJT model. In the axisymmetry flow, the velocity gradient tensor L_{ij}^C is given by

$$L_{ij}^C = \begin{pmatrix} \frac{\partial u}{\partial z} & \frac{\partial w}{\partial z} & 0 \\ \frac{\partial u}{\partial r} & \frac{\partial w}{\partial r} & 0 \\ 0 & 0 & \frac{w}{r} \end{pmatrix}. \tag{4.30}$$

The velocity gradient tensor constitutes the two velocities and their derivatives. I set the spatial coordinate used in the MJT model (e_z, e_x, e_y) to the cylindrical coordinate fixed to the conduit (e_z, e_r, e_θ).

The particle trajectory in the steady flow corresponds to the streamline. The temporal variation of the velocity gradient tensor L_{ij}^C is calculated along with the streamline. Fig. 4.11 shows the streamlines for the three models. In the Newtonian isothermal model, the streamline is straight because of the absence of horizontal velocity. In the shear-thinning model due to bubble deformation, the streamline is curved slightly but almost straight. Contrary to the two cases, the viscous heating model shows that the streamlines move toward the conduit wall just above the inlet. This behavior is explained by the large horizontal velocity which is associated with the development of a plug-like velocity profile.

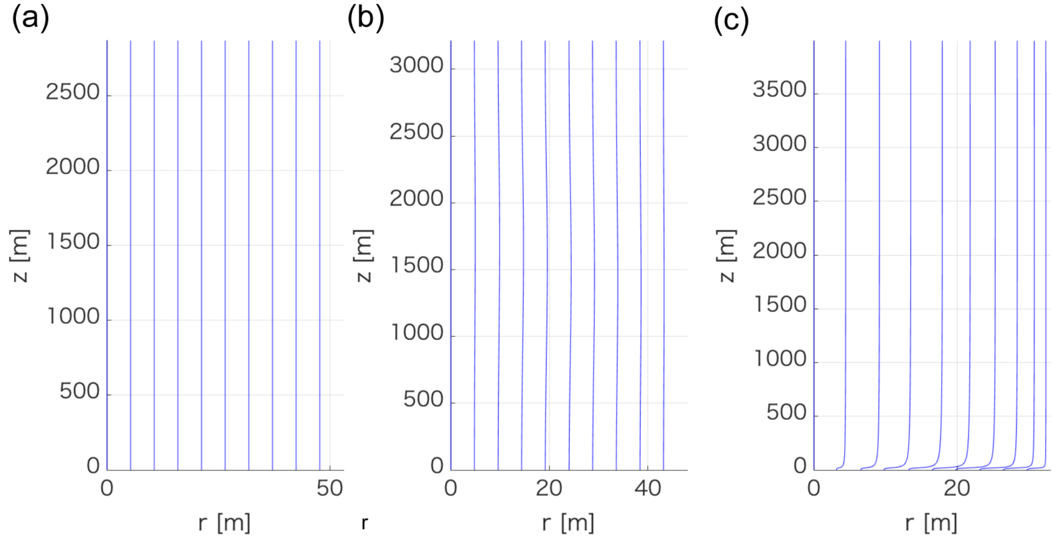

Figure 4.11: Streamlines of (a) the Newtonian isothermal model, (b) the shear-thinning model due to bubble deformation, and (c) the viscous-heating model. Every stream line starts from the conduit inlet ($z = 0$).

Parameters needed for the MJT model

The MJT model requires the spherical bubble radius R_b, the surface tension Γ, and viscosity η.

First, the spherical bubble radius and bubble volume are calculated by Eq. (4.26). The bubble volume is used to calculate $\dot{V}/V$ in L_{ij}^{*Vol} (Eq. 2.34).

Second, I fixed the surface tension to $\Gamma = 0.3$ N/m, based on the results of *Bagdassarov et al.* (2000) for Armenian rhyolite. Even though the melt viscosity is highly sensitive to water content (*Hess and Dingwell*, 1996), surface tension is insensitive to small differences in magma composition (*Bagdassarov et al.*, 2000).

Finally, I use the melt viscosity as the viscosity in the MJT model for all cases. If I calculate the deformation of multiple bubbles by using the mean-field approach, I should input the effective bubbly viscosity into the MJT model. However, it is difficult to calculate the effective viscosity in an arbitral shear field. Although some rheology models about bubbly fluid have been developed until now, they are based on a simple (or pure) shear field and can not describe the effective viscosity in the combination of simple and pure shear flows. In order to avoid complications accompanying the calculation of effective viscosity, I here input the melt viscosity into the MJT model.

Converting elevation into time

The MJT model needs the temporal flow parameters associated with an individual bubble. The conduit flow model gives the parameters in terms of z and r, which is fixed to the conduit. Here I assume that a spherical bubble with radius R_{bo} starts to rise in the conduit flow from the bottom of the conduit at time $t = 0$. The elevation of the bubble at time t is represented by $z_b(t)$:

$$z_b(t) = \int_0^t u_s(r, t')dt', \tag{4.31}$$

where $u_s(r, t)$ is the vertical velocity of a bubble on the stream line. Eq. (2.6) is numerically integrated by evaluating L_{ij}^C for the velocity gradient in the conduit flow at elevation $z_b(t)$ for each time step. I calculate t from

$$Dt = \frac{dz}{u_s}, \tag{4.32}$$

where Dt is the time interval, which is fixed to the bubble (in the MJT model), and dz is the elevation interval, which is fixed to the conduit (in the conduit flow model). The conduit flow model gives u as a function of z_b. I then obtain the flow parameters as a function of the elapsed time by iteratively calculating Eq. (4.32) through the conduit.

4.5.2 Numerical results for bubble deformation

Case1: Newtonian isothermal model

Fig. 4.12 shows the radial distribution of bubble deformation for the Newtonian isothermal model. The line style indicates the depth of the radial distribution. For all depth, the bubble near the conduit wall becomes more elongated than around the conduit center. As the magma ascends in the conduit, all bubbles elongate.

The dynamics of bubble deformation is easily understood from the view points of simple and pure shear components. In the Newtonian isothermal mode, the velocity gradient in the conduit L_{ij}^C can be written as a simple form because of the absence of the horizontal velocity:

$$L_{ij}^C = \begin{pmatrix} \frac{\partial u}{\partial z} & \frac{\partial u}{\partial r} & 0 \\ 0 & 0 & 0 \\ 0 & 0 & 0 \end{pmatrix}. \tag{4.33}$$

It is decomposed into three components:

$$L_{ij}^C = L_{ij}^{Vol} + L_{ij}^{pure} + L_{ij}^{simple}, \tag{4.34}$$

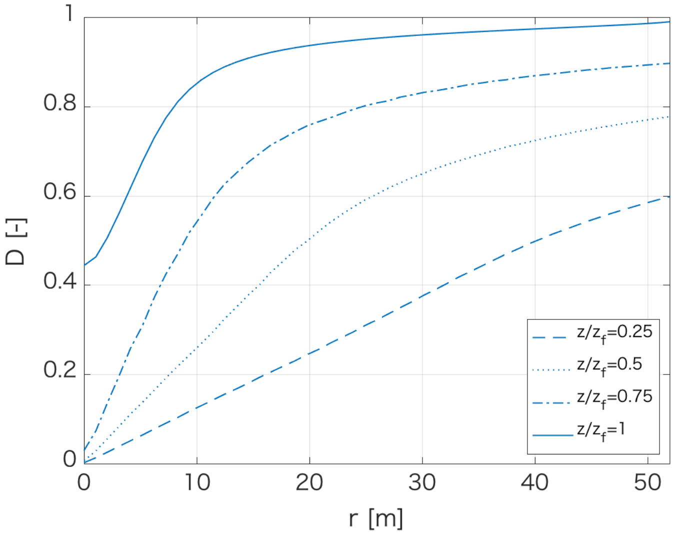

Figure 4.12: The radial distribution of bubble shape for the Newtonian isothermal case. The line style indicates the depth normalized by the fragmentation surface.

where

$$L_{ij}^{Vol} = \begin{pmatrix} \frac{1}{3}\frac{\partial u}{\partial z} & 0 & 0 \\ 0 & \frac{1}{3}\frac{\partial u}{\partial z} & 0 \\ 0 & 0 & \frac{1}{3}\frac{\partial u}{\partial z} \end{pmatrix}, \tag{4.35}$$

$$L_{ij}^{pure} = \dot{\epsilon} \begin{pmatrix} 1 & 0 & 0 \\ 0 & -\frac{1}{2} & 0 \\ 0 & 0 & -\frac{1}{2} \end{pmatrix}, \quad \dot{\epsilon} = \frac{2}{3}\frac{\partial u}{\partial z}, \tag{4.36}$$

$$L_{ij}^{simple} = \dot{\gamma} \begin{pmatrix} 0 & 1 & 0 \\ 0 & 0 & 0 \\ 0 & 0 & 0 \end{pmatrix}, \quad \dot{\gamma} = \frac{\partial u}{\partial r}. \tag{4.37}$$

where $\dot{\epsilon}$ and $\dot{\gamma}$ are the strain rates of pure and simple shear, respectively. The isotropic component L_{ij}^{Vol} represents the volumetric changes due to bubble inflation. The second and third non-volumetric components represent the velocity gradient tensors for pure shear L_{ij}^{pure} and simple shear L_{ij}^{simple}, respectively.

Given that the MJT model (and the JT model) assumes a linear relationship between L_{ij}^{C} and L_{ij}^{*}, I can obtain the corresponding velocity gradient tensors within a bubble individually for L_{ij}^{pure} and L_{ij}^{simple}, and sum them to obtain L_{ij}^{*}. Note that values of G_{ij} calculated individually for L_{ij}^{pure} and L_{ij}^{simple} cannot be superimposed, because Eq. (2.6) is not linear.

Fig. 4.13 shows the evolution of bubble deformation and some parameters for the Newtonian isothermal case. Color of lines indicates the initial position of the bubble at the conduit inlet r_i. Black lines indicate values independent of the radial position in the conduit. As discussed in Fig. 4.12, the bubble deformation degree increases with z (Fig. 4.13b-d).

Bubble deformation is fundamentally controlled by capillary number and strain. Because of the parabolic velocity profile in the Newtonian isothermal model, it is expected that simple shear deformation is more dominant than pure shear deformation. The simple shear is absent only at the conduit center due to the axisymmetry boundary condition. Therefore, I take $\dot{\epsilon}$ as the strain rate at $r_i = 0\ \mathrm{m}$ and $\dot{\gamma}$ at $r_i = 16$ and $48\ \mathrm{m}$. Fig. 4.13f shows the strain rates for the three initial locations. The strain rate of simple shear at $r_i = 16$ or $48\ \mathrm{m}$ is much bigger than the strain rate of pure shear at $r = 0\ \mathrm{m}$. The total strain that a bubble experiences from the inlet to the fragmentation is calculated by

$$\gamma = \int_0^t \dot{\gamma} Dt = \int_{z_0}^{z} \frac{\dot{\gamma}}{u} dz', \tag{4.38}$$

$$\epsilon = \int_0^t \dot{\epsilon} Dt = \int_{z_0}^{z} \frac{\dot{\epsilon}}{u} dz'. \tag{4.39}$$

The total strain of simple shear is also much larger that of pure shear (Fig. 4.13g).

The equilibrium bubble shape depends only on the capillary number. Using the capillary number (Fig. 4.13h), I calculate the equilibrium bubble shape of pure shear deformation at $r_i = 0\ \mathrm{m}$ and that of simple shear deformation at $r_i = 16$ and $48\ \mathrm{m}$ (dashed line in Fig. 4.13b-d). At $r_i = 16$ and $48\ \mathrm{m}$, the deviation between the bubble shapes by the MJT model and by the equilibrium theory is small, because there is enough strain at each stage for the bubble shape to follow the change of Ca in a quasi-equilibrium manner (Fig. 4.13g and h). In addition, Ca is large and thus the bubble can elongate substantially. The bubble in simple shear deviates from the equilibrium shape just below the fragmentation surface. On the other hand, at $r_i = 0\ \mathrm{m}$, the bubble calculated by the MJT model cannot keep up with the equilibrium bubble shape. The pure shear strain rate undergoes an abrupt increase beneath the fragmentation surface, where the vesicularity (i.e., the bubble radius) rapidly increases. The rapid increase of $\dot{\epsilon}$ means that the strain under the condition of $Ca \gg 1$ is too small to elongate substantially.

Case2: Shear-thinning model due to bubble deformation

Fig. 4.14 shows the evolution of bubble shape for the shear-thinning model due to bubble deformation. The distribution of bubble shape is almost the same as that of the isothermal Newtonian model. Since the flat region expands around the conduit center, less elongated bubbles increase slightly (Fig. 4.14a).

Case3: Viscous-heating model

Fig. 4.15 shows the radial distribution of bubble deformation for the viscous heating model. Contrary to the case 1 and 2, the bubble shape at the fragmentation surface is homogeneous except for the near-wall region. In most of the conduit, the bubble shapes are less elongated than case 1 and 2. This difference can be explained by the evolution of the velocity profile across the conduit.

Fig. 4.16 shows the evolution of the bubble shape and the vertical velocity profile. For all bubbles, the

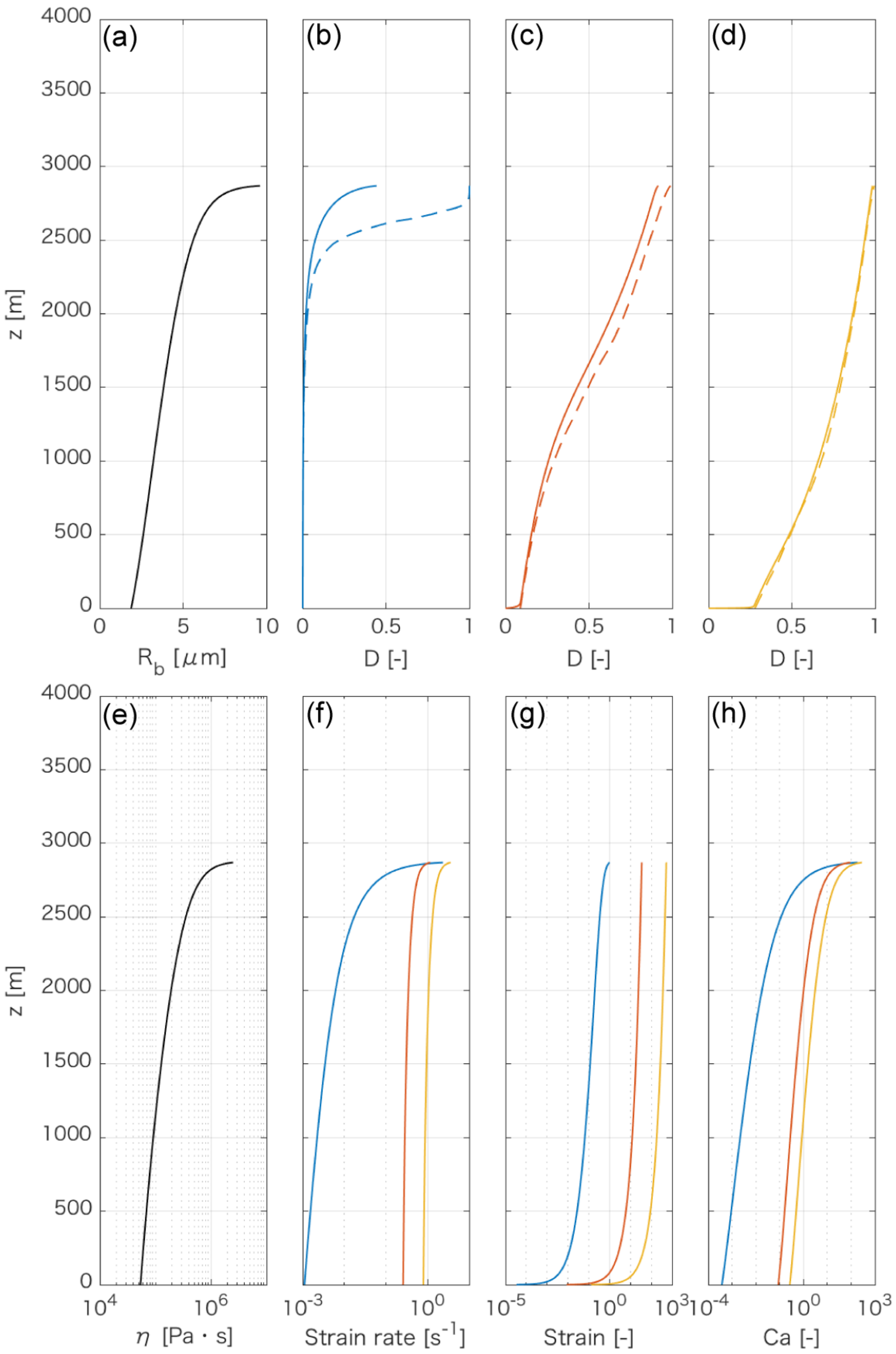

Figure 4.13: Bubble deformation in a conduit flow up to the fragmentation surface. The color indicates the initial position of the bubble at the conduit inlet: $r_i = 0$ m for blue line, $r_i = 16$ m for red line, and $r_i = 48$ m for yellow line. Black lines indicate values independent of the shear components. (a) Bubble radius. (b-d) Bubble deformation degree. Broken lines indicate the deformation degree of an equilibrium bubble shape depending only on Ca. (e) Viscosity. (f) Strain rate. At $r_i = 0$ m (blue), I take $\dot{\epsilon} = \frac{2}{3}\frac{\partial u}{\partial z}$ as strain rate. At $r_i = 16$ m (red) and 48 m (yellow), I use $\dot{\gamma} = \frac{\partial u}{\partial r}$ as strain rate. (g) Strain. (h) Capillary number.

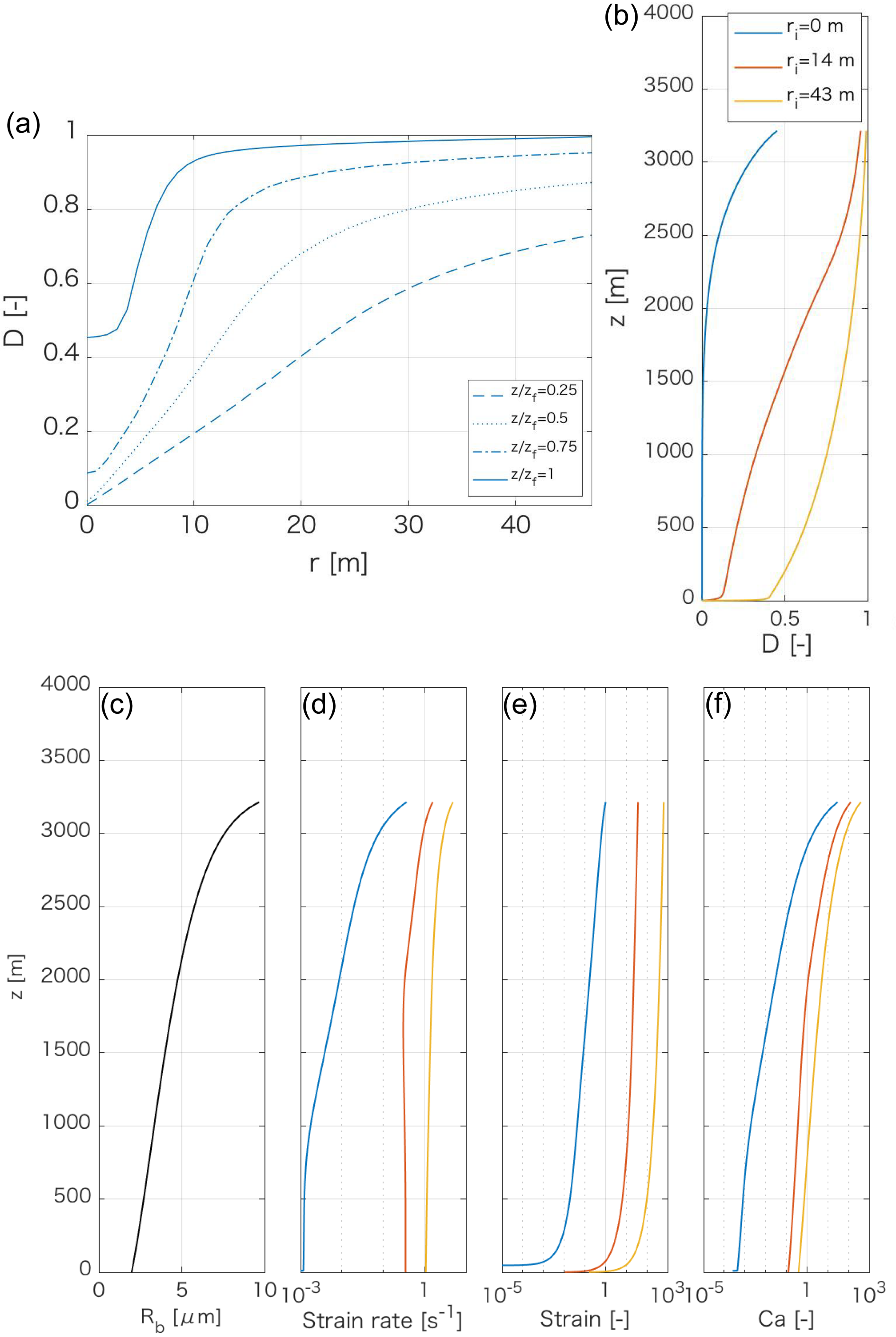

Figure 4.14: (a) The radial distribution of bubble shape for the shear-thinning model due to bubble deformation. The line style indicates the depth normalized by the fragmentation surface. (b) The vertical evolution of bubble shape. The color indicates the initial position of a bubble at the conduit inlet. (c) Bubble radius which is independent of the bubble location. (d) Strain rate. At $r_i = 0\mathrm{m}$ (blue), I take $\dot{\epsilon} = \frac{2}{3}\frac{\partial u}{\partial z}$ as strain rate. At $r_i = 14\ \mathrm{m}$ (red) and $43\ \mathrm{m}$ (yellow), I use $\dot{\gamma} = \frac{\partial u}{\partial r}$ as strain rate. (e) Strain. (f) Capillary number.

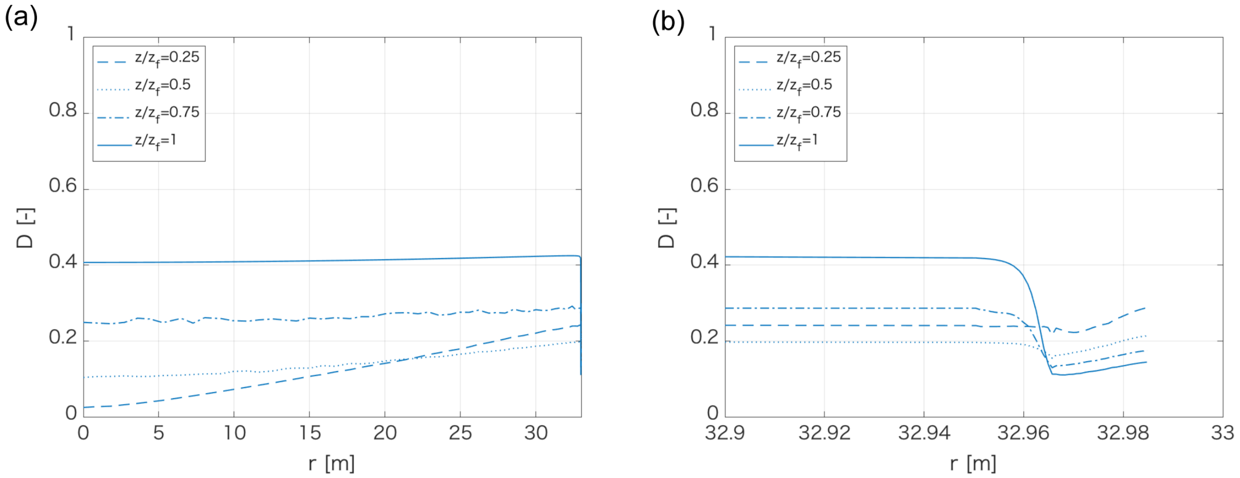

Figure 4.15: (a) The radial distribution of bubble shape for the viscous heating model. The line style indicates the depth normalized by the fragmentation surface. (b) The radial distribution of bubble shape in the near-wall zone.

bubble deformation degree reaches the highest value at $z = 20 \sim 40$ m where the velocity profile changes from a parabolic shape to a plug-like shape (Fig. 4.8, $z/z_f \sim 0.01$). When the velocity profile becomes a complete plug-like shape, the bubble shapes start to return a spherical bubble. As the magma accelerates by the inflation of bubbles, the bubble shapes gradually elongate.

In the viscous-heating model, I cannot decompose simply the shear field into the simple and pure shear components because of the non-zero horizontal velocity. In order to get an overview of the shear field, I plot the evolution of the components of the velocity gradient tensor L^C_{ij} at two initial locations $r_i = 0$ and 10 m (Fig .4.17). The collapse of the velocity profile into the plug-like shape leads to a decrease in $\frac{\partial u}{\partial z}$ and increase $\frac{\partial w}{\partial r}$. These two components deform a bubble into an oblate shape and increase the bubble deformation degree. When the velocity profile becomes a plug-like shape, these two components return to zero. As the magma ascends in the conduit and, the pure shear component of $\frac{\partial u}{\partial z}$ increases in the positive direction because of the decrease in the bulk density. This magma acceleration deforms the bubble into a prolate shape.

The radial gradient of the vertical velocity $\frac{\partial u}{\partial r}$ contributes to the bubble deformation degree only at the beginning of the flow where the velocity profile is parabolic, contrasting that it is the main shear component controlling the bubble deformation in the other two cases.

Fig. 4.18 shows the evolutions of R_b, η, and Ca. For the simplicity, I approximate the pure shear rate by $\epsilon = \frac{2}{3}\frac{\partial u}{\partial z}$ and use it for Ca. This approximation is reasonable except around the parabolic-to-plug flow transition where the contribution of w is significant. It is found that the capillary number reached about 1 at the fragmentation surface.

It is expected that bubbles in the shear localized region will be highly deformed. However, Fig. 4.15b shows that the bubbles in the near-wall region are less elongated than in the inner region. To investigate bubble deformation in the shear localized region, I plot the vertical evolution of bubbles in Fig. 4.19. The bubble starting from $r_i = 32.340$ m shows the similar evolution as the bubbles in Fig. 4.16. The bubble starting from

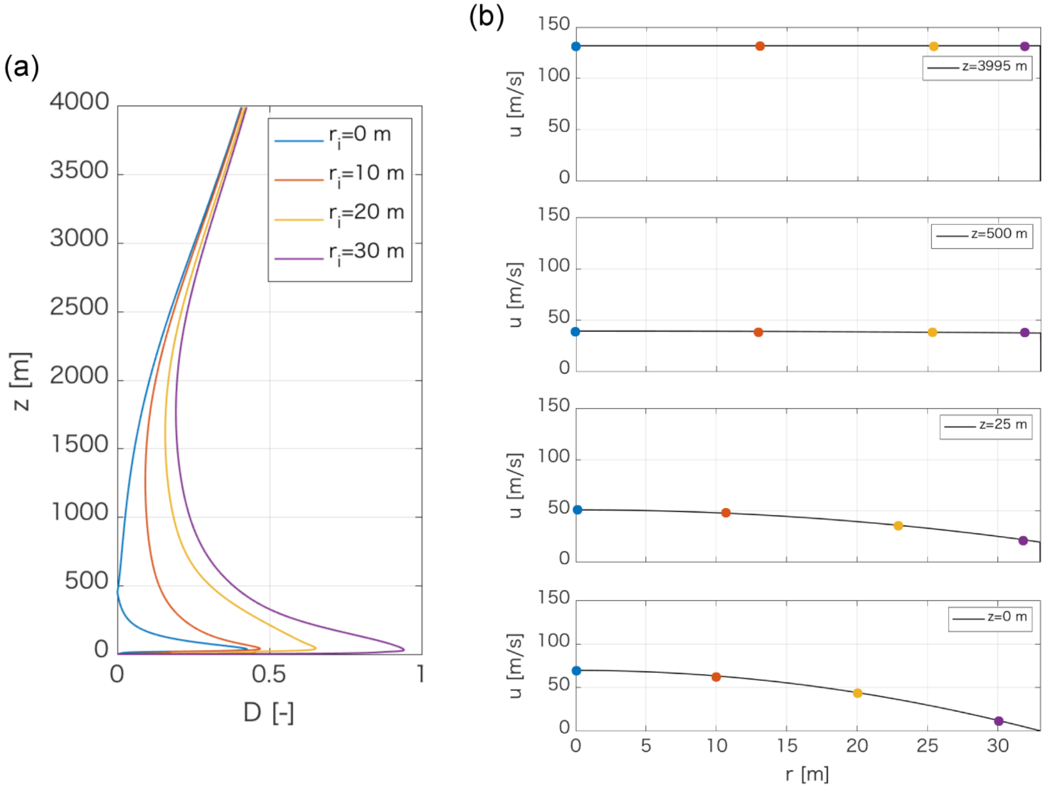

Figure 4.16: (a) The vertical evolution of the bubble shape. Color indicates the initial position of the bubble at the conduit inlet. (b) The velocity profile across the conduit. The color indicates the position of the corresponding bubble which is plotted in (a).

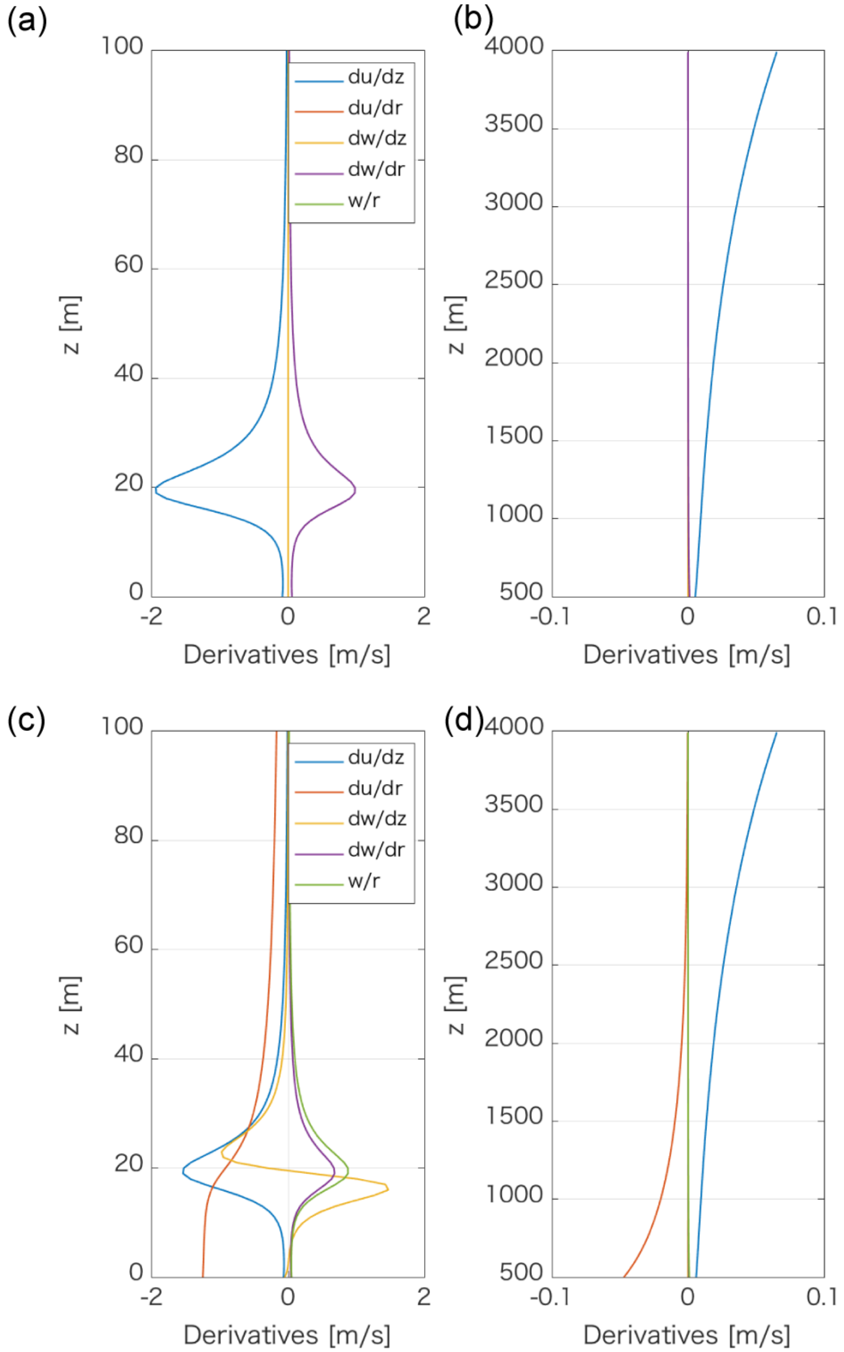

Figure 4.17: The vertical evolution of the components of the velocity gradient tensor L_{ij}^{C} for the bubbles at $r_i = 0$ (a and b) and at $r_i = 10$ m (c and d). The evolution of the lower region is plotted in (a and c), and that of the upper region is plotted in (b and d).

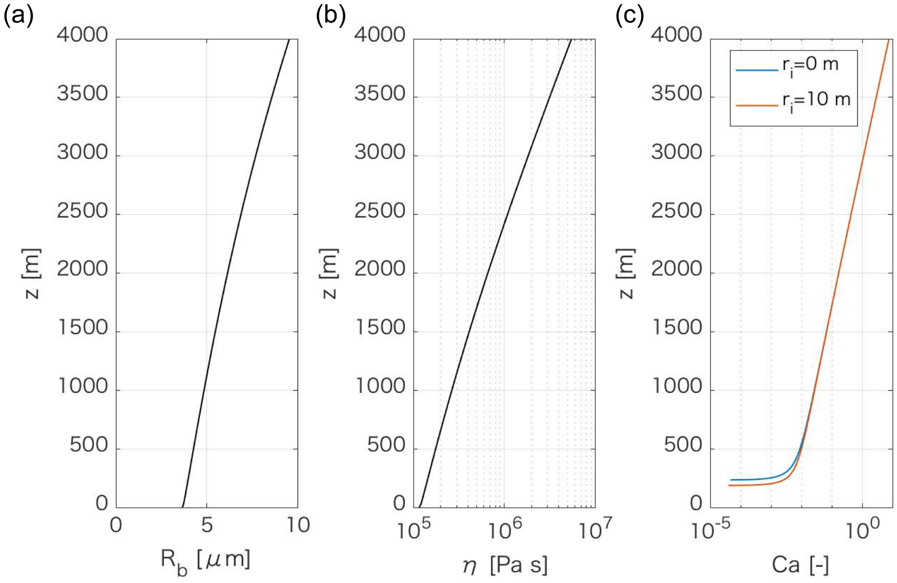

Figure 4.18: The vertical evolutions of (a) R_b, (b) η, and (c) Ca. For the simplicity, I define the pure shear rate as $\epsilon = \frac{2}{3}\frac{\partial u}{\partial z}$ and use it for Ca. Color indicates the initial position of the bubble at the conduit inlet.

$r_i = 32.776$ m does not elongate at $z > 2000$ m although this bubble ascends through the edge of the shear localized region.

The deformation around the shear-localized region is controlled by both the rise in the simple shear rate and the reduction of the viscosity. Fig. 4.20 describes the evolution of the shear field and the rheology of the bubble starting from $r_i = 32.776$ m. The strain rate of simple shear component $\frac{\partial u}{\partial r}$ increases in the negative direction. However, as $\left|\frac{\partial u}{\partial r}\right|$ increases, the melt viscosity also steeply decreases due to the increase in temperature. The apparent viscous stress acting on a bubble shape, which is defined by $\eta\frac{\partial u}{\partial r}$, consequently decreases.

In summary, the bubbles around the shear-localized region cannot elongate substantially due to the reduction of the viscosity. The shapes of most bubbles are controlled by the pure shear component caused by the magma acceleration.

Flux of pumice

We calculate the flux of bubble deformation degree at the fragmentation surface in order to compare the simulation results with the natural observation. The normalized volume flux of pumice F from $r = r_i$ to r_j is defined by

$$F = \frac{\int_{r_i}^{r_j} u(r')2\pi r' dr'}{\int_0^R u(r')2\pi r' dr'}. \tag{4.40}$$

The normalized flux F can be written as a function of D.

Fig. 4.21 shows the volume flux of pumice as a function of the bubble deformation degree. As expected

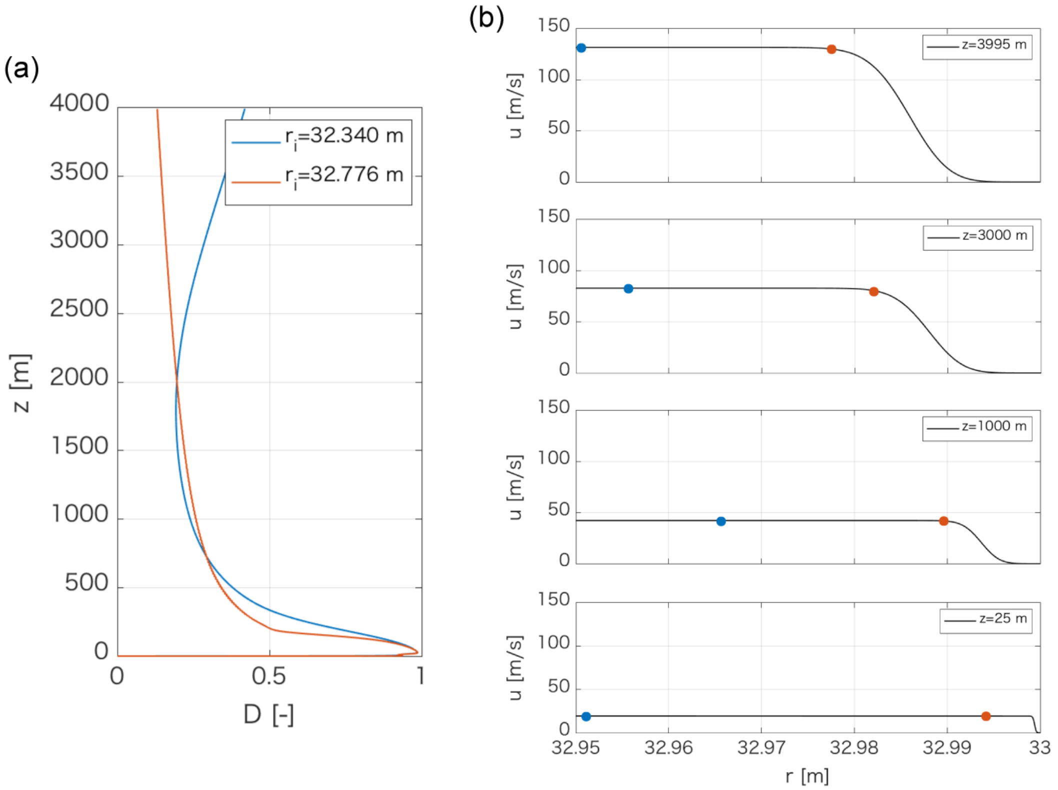

Figure 4.19: (a) The vertical evolution of bubble shape in the near-wall region. Color indicates the initial position of the bubble at the conduit inlet. (b) The velocity profile across the conduit. The colored circles mark the trajectories of bubbles, of which deformation degrees are shown with the corresponding colors in (a).

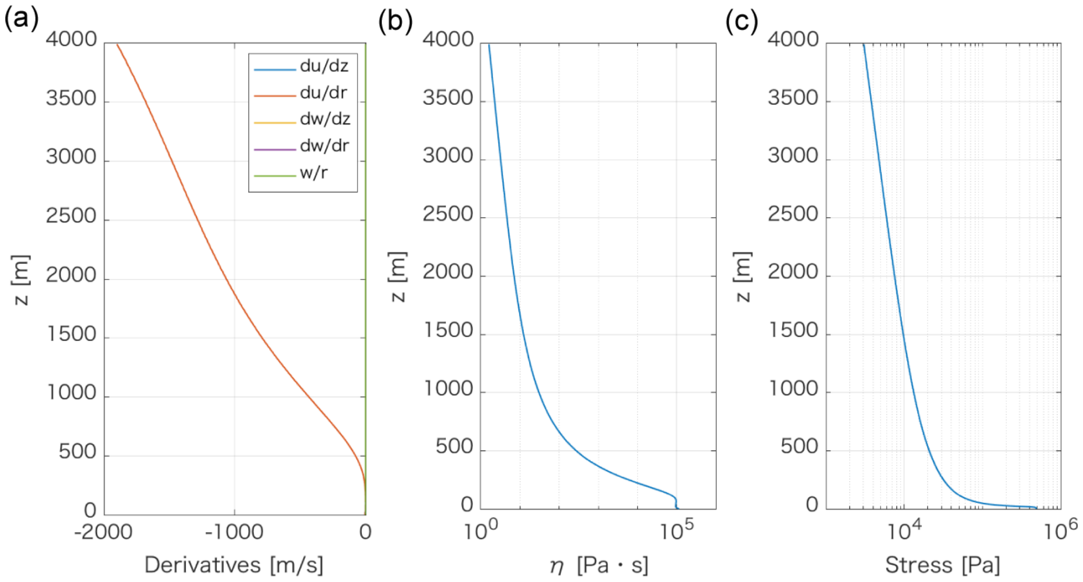

Figure 4.20: (a) The horizontal evolution of the bubbles at $r_i = 32.776$ m. (a) Components of the velocity gradient tensor L^C_{ij}. (b) Viscosity. (c) Apparent viscous stress ($\eta \frac{\partial u}{\partial r}$).

from the radial distribution of D (Fig. 4.6, 4.14, 4.15), the histograms of the case 1 and 2 have a peak around the upper limit of $D = 1$. Since the velocity profile shifts just slightly to a plug-like shape, the histogram of case 2 shows more elongated bubbles than that of case 1. On the other hand, the viscous-heating model has a uniform distribution which has a peak around $D = 0.4$. Although the bubbles moving along with the conduit wall are less elongated (Fig. 4.15b), the volume fraction of pumice containing these bubbles are very small (note a small fraction around $D = 0.1$ in Fig. 4.21 c). This result suggests that the pumice experiencing viscous heating around the conduit wall is difficult to find in the natural deposits.

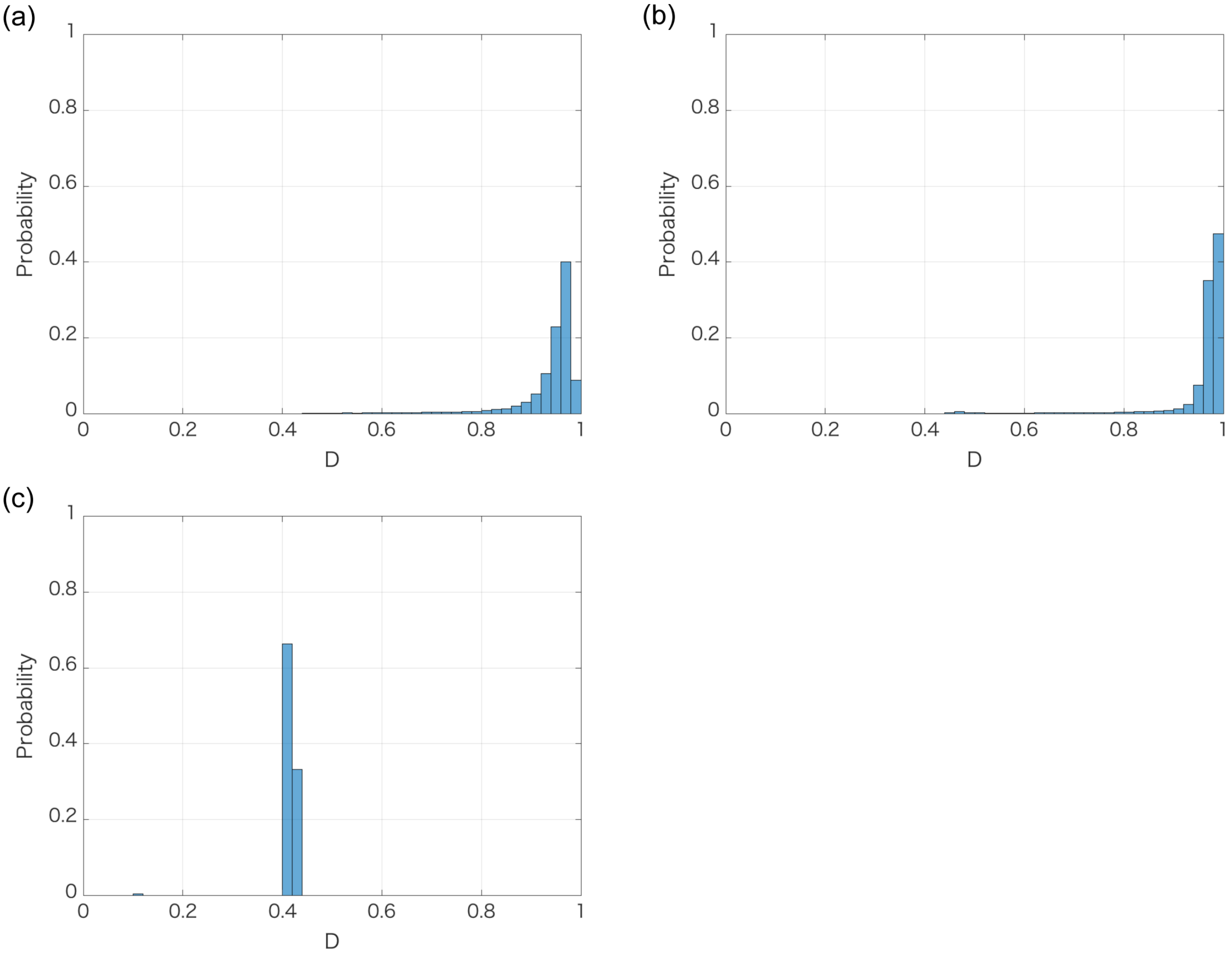

Figure 4.21: The histogram of bubble shapes at the fragmentation surface. (a) Case 1: Newtonian isothermal model. (b) Case 2: Shear-thinning model due to bubble deformation. (c) Case 3: Viscous heating model. The vertical axis is normalized by the total volume flux. The gap of D is 0.02.

4.6 Discussion

The viscous-heating model has several assumptions and limitations, which might make the wall temperature extremely high and the initial pressure below the lithostatic value. Here, I outline and comment on the major assumptions of the model.

4.6.1 Validity of a steady model

In this thesis, the conduit flow for the Taupo plinian is simulated by a steady flow model. The assumption of steady state is used for most conduit flow models (e.g., *Wilson et al.*, 1980; *Papale*, 1999; *Mastin*, 2002). This assumption is considered to be appropriate for eruptions that are sustained for several minutes to hours (i.e., lava fountains and plinian eruptions) because their durations are longer than magma ascent times from magma chamber to vent (*Mastin and Ghiorso*, 2000; *Campagnola et al.*, 2016). In this section, the steady-state approximation is checked from the viewpoints of viscous flow and thermal conduction.

At first, I consider a case in which the flow with a constant viscosity reach the steady state. The fluid contained in a long tube is initially at rest, and then is moved by a sudden pressure gradient. The variation of the velocity profile is a function of a dimensionless timescale, $\frac{\eta t}{\rho R^2}$ where t is the time, η is the viscosity of the fluid, ρ is the density, and R is the conduit radius (*Batchelor*, 1967). The flow after a long time $\frac{\eta t}{\rho R^2} \gg 1$ attains a steady parabolic velocity profile. Parameters for a typical silicic eruption ($\eta = 10^6$ Pas, $\rho = 2000$ kg/m^3, $R = 30$ m) yields the timescale to reach the steady state of $t \gg 1.8$ s. Therefore, I think that the viscous flow easily attains the steady state.

In this chapter, I used a viscous-heating model in which the viscosity is affected by temperature rise due to shear-heating. It is required to check the timescale to reach the thermal equilibrium. Here, I consider a similar case in which a stagnant fluid with uniform temperature suddenly moves along a circular tube. When viscous-heating dominates radial conduction, the timescale to reach a spatially maximal temperature is given by *Pearson* (1977) as follows

$$\tau_{heat} \sim Na^{-1}, \tag{4.41}$$

where $\tau_{heat} = \frac{\kappa t}{\rho c_V R^2}$ is the dimensionless time, $Na = \frac{\eta_0 U_0^2 b}{\kappa}$ is the dimensionless parameter called Nahme number, η_0 is the initial viscosity, b is the coefficient of the viscosity dependency with temperature at a reference temperature of T ($b = \frac{1}{\eta_0}\left(\frac{d\eta_0}{dT}\right)_T$), U_0 is the initial mean vertical velocity which is defined as $U_0 = Q_m/(\rho_0 \pi R^2)$. The Nahme number is the competition of the temperature rise caused by viscous-heating and that required to change the viscosity by the factor e. Substituting the parameters for the Taupo plinian eruption into Eq. (4.41), I obtain the dimensional timescale of $t = 24$ s. Although the accurate eruption duration is unknown, this timescale might be much shorter than the eruption duration. Therefore, I think that the conduit flow attains maximum temperature in a very short time and reaches the steady flow.

The steady-state approximation is also verified from the geological point that the bubble textures of the Taupo plinian eruption are homogeneous throughout the stratigraphy (Fig. 5.19).

Keep in mind that the above discussion validates the steady-state assumption for the viscous-heating model of the Taupo plinian eruption. When taking account other mechanisms, such as conduit-widening and fracture-healing, the conduit flow is expected to be an unsteady flow.

4.6.2 Strong viscous heating around the conduit walls

The numerical result (Fig. 4.9) shows that the temperature in the thermal boundary layer reaches very high values (up to $3400\,^{\circ}\mathrm{C}$), which is above the applicable temperature range of the viscosity model (*Hess and Dingwell*, 1996, $< 1723\ ^{\circ}\mathrm{C}$). This high temperature leads to the strong reduction of the melt viscosity and the viscous friction (Fig. 4.9 and 4.10), resulting in the low initial pressure at the conduit entrance.

The problem of viscous heating models that show the unrealistically high temperature at the wall has been discussed in previous researches (*Vedeneeva et al.*, 2005; *Costa et al.*, 2007). The viscous heating models including the present one do not consider several possible mechanisms to reduce the temperature. One is the thermal erosion of conduit wallrocks. Once the temperature in the near-conduit region exceeds the melting temperature of the wallrock which is usually much higher than that of the flowing magma due to the anhydrous conditions, the intense melting of wallrocks will happen within a narrow layer around the conduit wall. The second mechanism is the effective heat exchange caused by the thermal instabilities (*Costa and Macedonio*, 2005). Rapid variations of the cross-sectional area in the vertical direction and/or the instabilities of the flow profile with vortex formation could mix the layers strongly, resulting in effective heat transportation. The third mechanism is the formation of brittle failure in nearby magma or conduit wallrock. *Okumura et al.* (2013) has shown experimentally that brittle failure starts to form when the shear stress is larger than $3 - 4 \times 10^5$ Pas. This value is comparable with the shear stress of the viscous-heating model at the conduit wall (Fig. 4.10). The fourth mechanism is the shear-thinning effect due to bubble deformation (*Llewellin et al.*, 2002b). The reduction in bulk viscosity can suppress the viscous-heating around the conduit walls and decrease the magma temperature. The simulation result of the model combining the viscous-heating model and the shear-thinning model due to bubble deformation is shown in appendix E.

As a possible mechanism to reduce the high temperature, *Vedeneeva et al.* (2005) discussed the validity of the boundary condition at the conduit wall. If the magma ascends through the crust while making a new crack at its tip, the wallrock temperature could be significantly lower than the initial magma temperature. The thermal conduction from the conduit wall perhaps suppresses the temperature rise. However, I expect that this effect can be negligible in our simulations because a conduit flow in common explosive eruptions, including the Taupo plinian eruption, is dominated by viscous heating rather than heat conduction from the conduit wall (*Costa et al.*, 2007). The loss of thermal energy caused by conduction from the conduit wall is much less than by viscous heating. Therefore, the choice of the temperature at the conduit wall is not an important issue in our simulations.

We think the high temperature can be suppressed by taking account of the thermal erosion, the flow instability, the brittle failure, and the shear-thinning effect due to bubble deformation. A viscous-heating model taking account of these mechanisms is required for further study.

Although the temperature in the thermal boundary layer reaches $3400\ ^{\circ}\mathrm{C}$ at the fragmentation surface, I think that the obtained velocity field can be used for calculating the shape of a bubble because the parabolic-to-plug flow transition occurs at relatively low temperature (1750 °C at $z/z_f = 0.005$, Fig. 4.9). Although there is no geological evidence constraining the temperature at the thermal boundary layer in the Taupo volcano, I regard that the model result is valid in the temperature range of the viscosity model (up to 1723 °C). The velocity profile will keep the plug-like shape after the parabolic-to-plug flow transition. Therefore, the velocity field, which is mainly controlled by the transition of the velocity field, can be used for the bubble deformation model.

It should be noted that a new model taking account of the potential mechanisms is essential for the pressure variation along the conduit. The reduction of the temperature rise around the conduit walls will increase viscous resistance and make the pressure gradient steeper than the current model. The initial pressure at the conduit inlet consequently increases and may become close to the lithostatic pressure.

4.6.3 Inertia term in the momentum equation

The conservation equation of momentum (Eq. 4.2) neglects the inertia term under the assumption of $Re \ll 1$ (Appendix D). However, Fig. 4.10 shows the viscous friction in the viscous-heating model decreases as the magma ascends in the conduit. Around the fragmentation surface, the inertia force is perhaps comparable with the viscous friction.

To check the validity of the simulation result of the viscous-heating model, I calculate the acoustic velocity ($a = \sqrt{\frac{dp}{d\rho}}$) from the vertical profile of p. The vertical velocity in the bubbly flow region must not exceed the acoustic velocity under the subsonic condition. Fig. 4.22a shows the vertical profiles of u and a. The vertical velocity increases close to the acoustic velocity a around the fragmentation surface ($z_f = 3994$ m), but it is smaller than a throughout the conduit. Therefore, I think the obtained velocity profile is reasonable.

The inertia term affects the pressure profile along the conduit. Here, I approximately calculate the pressure gradient $\frac{dp}{dz}$ including the inertia effect from the following equation:

$$\frac{dp}{dz} = \frac{dP}{dz} - \rho u \frac{du}{dz}, \tag{4.42}$$

where $\frac{dP}{dz}$, ρ, and u are the pressure gradient, the density, and the vertical velocity obtained by the viscous-heating model. For simplicity, ρ and u are the values at the conduit center. Fig. 4.22b shows the pressure calculated from Eq. (4.42). As the magma approaches the fragmentation surface, the pressure gradient becomes steeper than the original model without the inertia force. If I could make a new model coupling the pressure decrease with the inertia force, I may obtain a larger value of the initial pressure. The development of the model with the inertia term is our future study.

4.6.4 Chemical equilibrium

The model assumes that gas exsolution follows the equilibrium solubility law (Eq. 4.7). This assumption has been used by many models (e.g., *Wilson et al.*, 1980; *Papale*, 1999; *Mastin*, 2002), although experimental studies suggested a disequilibrium degassing in explosive eruptions (*Mangan and Sisson*, 2000). Only a few models

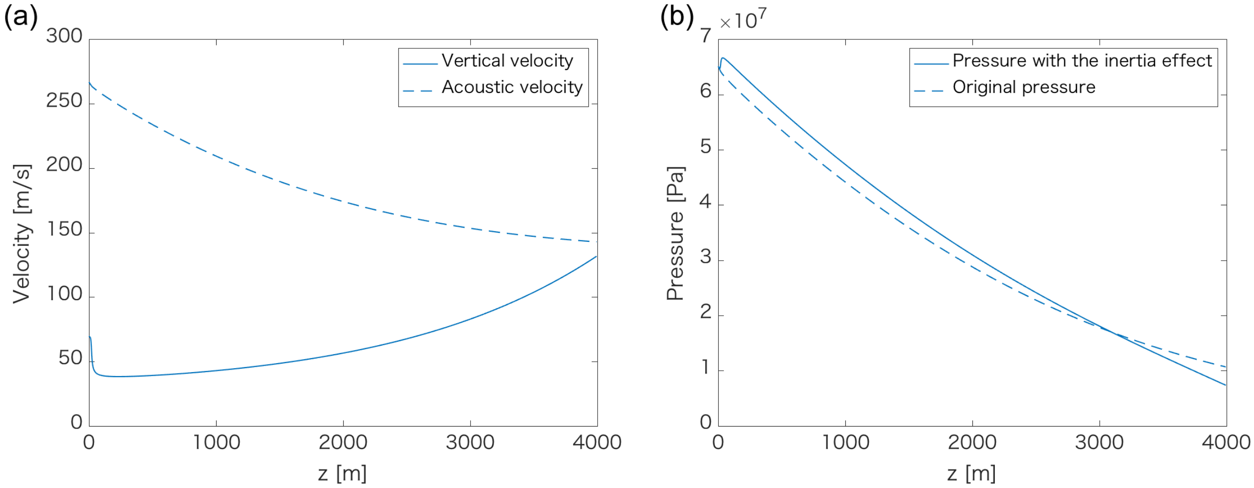

Figure 4.22: (a) The vertical velocity at the conduit center and the acoustic velocity of the viscous heating model. The vertical velocity does not exceed the acoustic velocity. (b) The pressure with the inertia effect calculated from Eq. (4.42) and the original pressure of the viscous-heating model. The inertia force makes the pressure gradient slightly steeper.

took into account of a disequilibrium bubble growth in a conduit flow (*Mangan et al.*, 2004; *Proussevitch and Sahagian*, 2005; *Campagnola et al.*, 2016).

The kinetic of bubble growth in an ascending magma is fundamentally controlled by three processes: decompression of a bubbly magma, deformation of viscous melt surrounding a growing bubble, and diffusion of volatile into a bubble (*Toramaru*, 1995; *Lensky et al.*, 2004). These processes are coupled intricately and are solved by a numerical approach. The general features of bubble growth are conveniently explained by the timescale of each process. Hereafter, I follow the expression by *Lensky et al.* (2004).

The ambient pressure of a bubble varies as the magma ascends in a conduit. The timescale of decompression in a conduit is give by

$$\tau_{dec} = \frac{p_i}{\left|dp_{amb}/dt\right|_i}, \tag{4.43}$$

where p_i is the initial pressure and $\left|dp_{amb}/dt\right|_i$ is the absolute value of the initial decompression rate. The timescale of viscosity-limited growth is expressed as

$$\tau_{vis} = \frac{4\eta_i}{p_i}, \tag{4.44}$$

where η_i is the initial viscosity. In Eq. (4.44), p_i plays a role as an overpressure. The timescale of diffusion-limited growth is

$$\tau_{dif} = \frac{(R_{bi})^2}{D_i}, \tag{4.45}$$

where R_{bi} is the initial bubble radius and D_i is the initial diffusivity. Eq. (4.45) characterizes the diffusion of volatiles in the melt around a bubble at the initial stage.

Dimensionless number which is the ratio of Eqs. (4.43)-(4.45) is useful to characterize the kinetics of bubble growth. For a sudden decompression, Peclet number, $Pe = \tau_{dif}/\tau_{visc}$, was often used to estimate the competition between viscous resistance and mass diffusion during bubble growth. For a successive decompression, such as magma ascent, it is essential to compare the timescales of bubble growths with decompression. Following the study of *Toramaru* (1995), *Lensky et al.* (2004) proposed two dimensionless numbers,

$$\begin{aligned} \Theta_V &= \frac{\tau_{visc}}{\tau_{dec}} = \frac{4\eta_i \left|dp_{amb}/dt\right|_i}{(p_i)^2}, & (4.46) \\ \Theta_D &= \frac{\tau_{diff}}{\tau_{dec}} = \frac{(R_{bi})^2 \left|dp_{amb}/dt\right|_i}{D_i p_i}. & (4.47) \end{aligned}$$

The disequilibrium bubble growth can be explained by these dimensionless numbers together with the dimensionless time $\hat{t} = t/\tau_{dec}$.

Using Θ_V and Θ_D, *Lensky et al.* (2004) expressed the bubble growth regime of decompression magma (Fig. 4.23). As Θ_V increases, bubble growth is limited by viscous resistance from the surrounding melt. On the other hand, bubble growth is limited by the diffusion of volatiles as Θ_D increases. Red cross in Fig. 4.23 is the growth condition of the viscous-heating model of the Taupo plinian eruption.

Θ_V and Θ_D are 3×10^{-4} and 7×10^{-2} at the conduit inlet, respectively. As can be seen in Fig. 4.23, the bubble growth condition falls in the transition regime from equilibrium to quasi-static diffusion. This result indicates that the bubble growth in the Taupo plinian eruption is outside the chemical equilibrium regime and is controlled by the kinetics of volatile diffusion.

When bubble growth in an ascending magma is limited by diffusion, the magma barely degasses in a conduit and erupts with high oversaturation (*Proussevitch and Sahagian*, 1996). Dissolved volatiles cannot be exsolved even if the ambient pressure decreases rapidly. Therefore, it is expected that the rapid acceleration based on chemical equilibrium (Fig. 4.8) does not occur in the model based on the disequilibrium model. Suppressing the magma acceleration may also lead to a decrease in shear stress along the conduit walls, resulting in the reduction of temperature rise.

The implementation of the disequilibrium bubble growth into a conduit flow model is a challenging problem even for one-dimensional conduit models. I leave this problem to a subsequent study.

4.6.5 Fragmentation criterion

In this thesis, I used the vesicularity criterion ϕ_f for fragmentation in the conduit flow model. The fragmentation criterion is known to strongly influence the pressure profile along the conduit (*Campagnola et al.*, 2016), and other criteria has been developed in recent decades (*Alidibirov*, 1994; *Papale*, 1999; *Zhang*, 1999). The fragmentation criterion affects magma acceleration just beneath the fragmentation surface and controls the vesicularity at fragmentation. As shown later in section 7.2.1, the amount of pure shear is a function of the vesicularity. The fragmentation criterion consequently influences the rapid elongation just beneath the

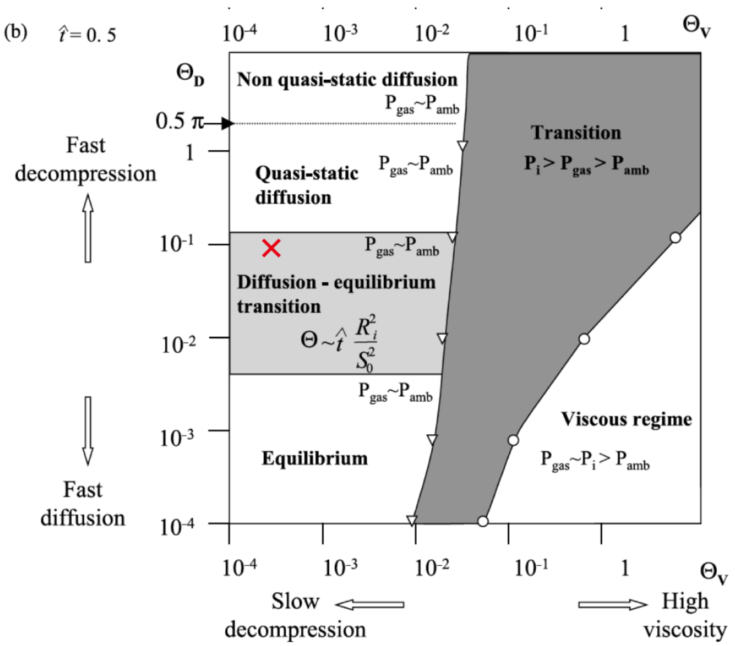

Figure 4.23: The bubble growth regime of decompressing magma as function of Θ_V and Θ_D at $\hat{t} = 0.5$ (*Lensky et al.*, 2004, Fig. 3b). Red cross indicates the growth condition of the viscous-heating model of the Taupo plinian eruption. The parameters used in Θ_V and Θ_D are the initial values obtained by the viscous-heating model: $\eta_i = 1.2 \times 10^5$ Pas, $|dp_{amb}/dt|_i = 3.5 \times 10^6$ Pa/s, $p_i = 65$ MPa, and $R_{bi} = 3.6\ \mu$m. The diffusivity D_i is 10^{-11} m^2/s (*Zhang and Behrens*, 2000).

fragmentation. The dependence of bubble deformation on the fragmentation criterion is required for further study.

Chapter 5

Textural analysis of pumice from the Taupo 1.8 ka eruption

5.1 Introduction

The quasi two-dimensional conduit flow model was developed in the previous chapter. To compare the numerical simulation with bubble texture of natural pyroclasts, I address pumice from the 1.8 ka eruption of Taupo volcano, New Zealand. The pumice from this huge eruption demonstrates various bubble texture, such as elongate bubbles and equant bubbles (*Houghton et al.*, 2003, 2010). The Taupo eruption is also remarkable for the lack of compositional variation with respect to H_20 and trace elements (*Dunbar and Kyle*, 1993), which indicates that the great diversity of bubble textures in pumices may reflect purely physical processes in the eruption. In addition, the theoretical and geological consideration suggests that the ignimbrite was formed by a single vent, not a ring-fissure (*Legros et al.*, 2000). Therefore, the Taupo eruption allows us to compare the natural bubble texture with the steady and cylindrical conduit flow model.

In the rest of the chapter, section 5.2 provides a brief introduction about the 1.8 ka Taupo eruption. Sampling and analysis methods are described in section 5.3 and 5.4, respectively. Section 5.5 shows the analysis results. The discussions about the shape relaxation of a bubble are given in section 5.6.

5.2 Brief introduction about the Taupo 1.8 ka eruption

5.2.1 Taupo volcano

Taupo volcano is an active caldera volcano in the Taupo Volcanic Zone, New Zealand. This huge volcano is famous for having experienced two recent caldera-forming eruptions: Oruanui eruption at 26.5 ka and Taupo eruption at 1.8 ka. Oruanui eruption is known as the largest 'wet' eruption, producing $430\ \mathrm{km}^3$ of the fall deposits, $320\ \mathrm{km}^3$ of the ignimbrite, and $\sim 420\ \mathrm{km}^3$ of the primary intracaldera material, equivalent to $\sim 530\ \mathrm{km}^3$ of magma (*Wilson*, 2001). The shape of Lake Taupo was mainly established during this eruption, and modified by the later smaller eruptions (*Wilson*, 1993). Between the two big eruptions, 26 other explosive and dome-building eruptions have been recognized (*Wilson*, 1993).

5.2.2 The 1.8 ka Taupo eruption

The Taupo eruption at 1.8 ka was one of the most violent rhyolitic eruptions in the world in the last 5000 years (*Wilson and Walker*, 1985). This eruption is notable for several reasons:

1. It generated a great diversity of eruptive products: two dry Plinian fall deposits, three phreatomagmatic fall deposits, several intraplinian flow units, and a climatic widespread ignimbrite which was known as a low-aspect ration ignimbrite (*Walker et al.*, 1980; *Wilson and Walker*, 1985; *Wilson*, 1985).

2. It includes the extreme powerful Plinian event and violent ignimbrite-forming event. The former Plinian event has been considered as a typical case of 'ultraplinian event', of which column height exceeded $50\ \mathrm{km}$ (*Walker*, 1980). However, the recent study by *Houghton et al.* (2014) re-estimated the column hight range of $35-40\ \mathrm{km}$ by including the wind effect and questioned if the term ultraplinian is adequate for this eruption.

3. Multiple vents were located within the Taupo Lake. From the detailed geological studies, *Smith and Houghton* (1995) suggested that the Taupo eruption involved at least three vents lying along a NE-SW fissure (Fig. 5.1).

4. Pumice and melt inclusions show the chemical homogeneity during the Taupo eruption. *Dunbar and Kyle* (1993) measured $\mathrm{H_2O}$ content of the melt inclusions in the deposits from different stratigraphic layers and concluded that there is no pre-eruptive volatile difference between the plinian and ignimbrite eruption styles. The Cl and F contents during the eruption also show only a small variation.

On the basis of the above characteristics, *Houghton et al.* (2010) considered that the Taupo eruption is a suitable case to interpret the great diversity of eruption products, eruptive styles, and pyroclast characteristics in terms of physical influences.

In addition, I think that the Taupo eruption is a good target of my study in the following points.

5. The magma of the Taupo eruption is characterized as crystal-poor. The phenocrystal abundance ranges from 3 to $5\ \mathrm{vol\%}$ (*Dunbar and Kyle*, 1993). Microlites are also poor in the groundmass (Fig. 5.2).

6. Although some caldera-forming eruptions occurred in a ring-fissure conduit, the Taupo ignimbrite was emplaced from a single vent. *Legros et al.* (2000) performed numerical simulations of magma ascent in a cylindrical conduit connected to a single vent and in a ring fissure conduit, and compared the modeling results with geological observations. Since the lithic content of Taupo ignimbrite unit was too small to be produced by the ring-fissure conduit, they concluded that the ignimbrite was formed with a cylindrical conduit.

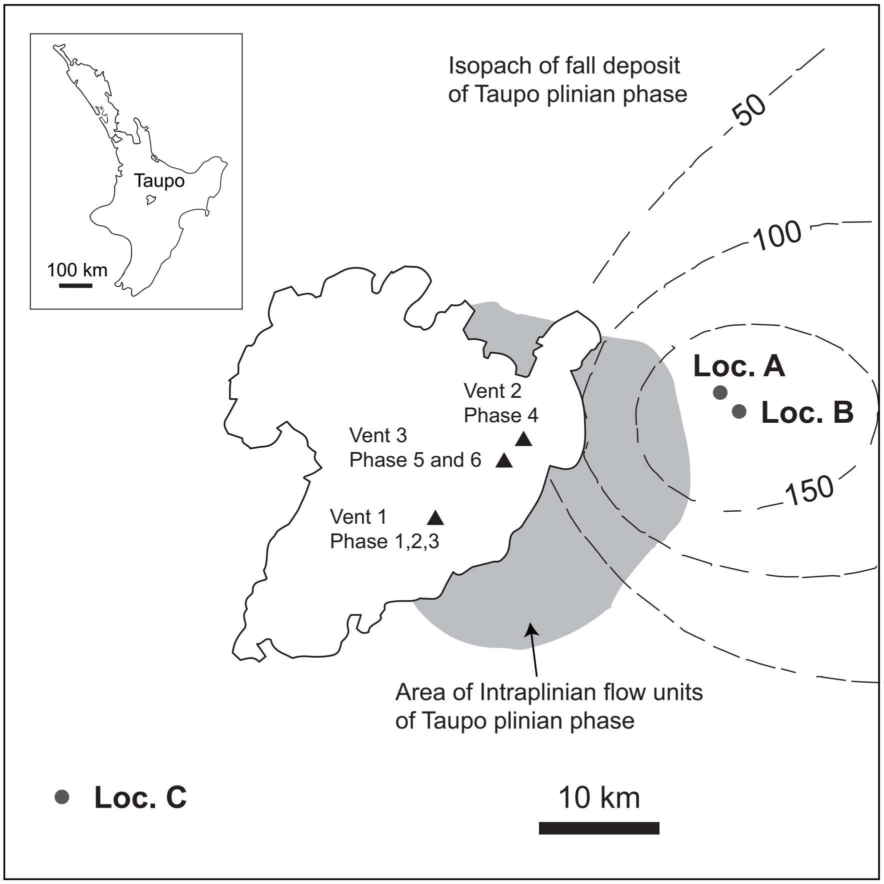

Figure 5.1: Location map showing the vent positions of 1.8 ka eruption after *Smith and Houghton* (1995) and the outcrops where I collected samples. Location A, B, and C are the outcrops where I collected the samples of the Hatepe plinian (phase 2), the Taupo plinian (phase 5), and the Taupo ignimbrite (phase 6), respectively. Isopach of fall deposit of Taupo plinian phase (unit 5) is from *Walker* (1980). Values are in centimeters. Area of intraplinian flow units of Taupo plinian phase is from *Wilson and Walker* (1985). Inset map shows the location of Taupo within North Island, New Zealand.

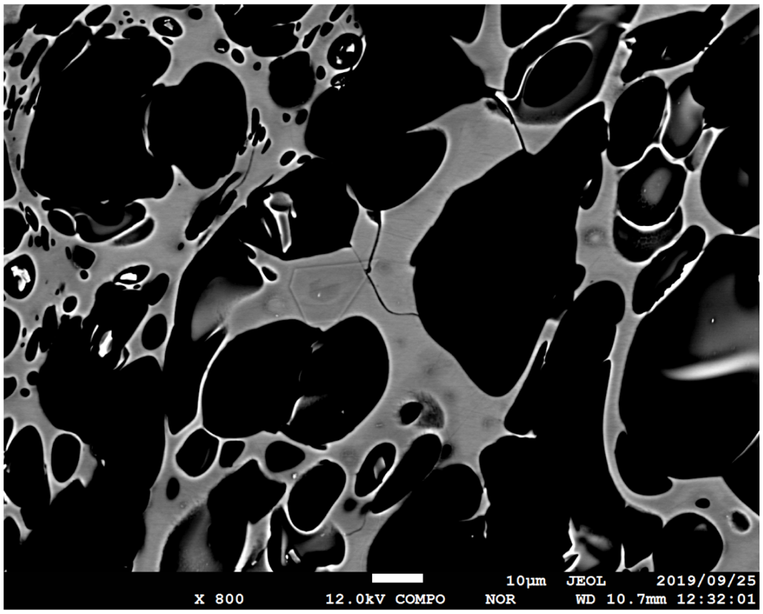

Figure 5.2: SEM image of a pumice from the Taupo plinian eruption. There is a microlite in the center of the image.

The Taupo eruption thus allows us to examine the behavior of bubble deformation in a cylindrical conduit flow without the consideration of the crystal and conduit geometry effects.

In this study, I follow the unit names given by *Houghton et al.* (2010). The volume of each unit is from *Wilson and Walker* (1985). The seven units are individually associated with the seven distinct eruption phases (Fig. 5.7). The initial phase was phreatomagmatic, forming a fine-grained fall deposit. The volume of unit 1 is minor ($0.005\ \mathrm{km}^3$ in DRE) compared with the following units. Phase 2 was a sustained plinian eruption ($1.6\ \mathrm{km}^3$ DRE), that was called as Hatepe plinian. Unit 3 and 4 were phreatoplinian eruptions called as Hatepe phreatoplinian and Rotongaio phreatoplinian. The two eruptions produced fine grained fall deposits of $1.1\ \mathrm{km}^3$ (DRE) for unit 3 and $0.8\ \mathrm{km}^3$ for unit 4. Phase 5 is a powerful plnian eruption that is called as Tuapo plinian eruption. This eruption generated a widely dispersed fall deposit of $5.8\ \mathrm{km}^3$ DRE (unit 5a in Fig. 5.7) and relatively weak intraplinian flow deposit of $0.6\ \mathrm{km}^3$ DRE (unit 5b in Fig. 5.7). The explosive eruption ended with the generation of unit 6 ($12.1\ \mathrm{km}^3$ DRE), called as Taupo ignimbrite. This unit shows many different facies, which reflected the depositional style from the head and body of the pyroclastic flow (*Wilson*, 1985). During phase 7, rhyolitic lava domes were extruded onto the floor of the Lake Taupo.

The detailed stratigraphic analysis of units 3 and 4 by *Smith and Houghton* (1995) revealed that the Taupo eruption involved at least three vents on a NE-SW fissure (Fig. 5.1). Phases 1-3 of the eruption were from a southwestern vent, phase 4 from a northeastern source, and phases 5 and 6 from a source between the two sources.

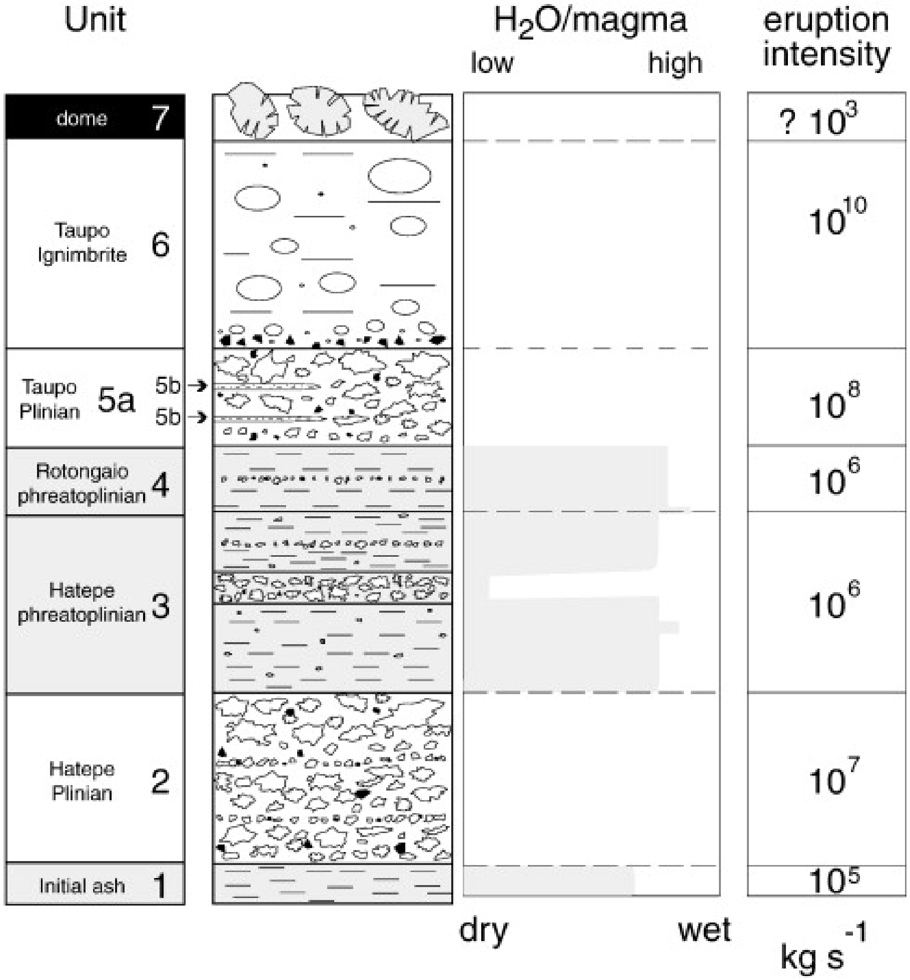

Figure 5.3: Stratigraphy of the 1.8 ka Taupo eruption (*Houghton et al.*, 2010, Fig. 2). In the first column, phreatomagmatic units are shown as gray. The third and fourth columns are degree of water interation and mass discharge rates inferred by *Wilson and Walker* (1985).

5.2.3 Bubble texture of pumice from the Taupo eruption

Houghton and Wilson (1989) measured the apparent density of the pumices using Archimedes' principle and obtained their vesicularities. In the magmatic dry eruptions (units 2 and 5), the vesicularity lies uniformly in the range $70-80\%$. On the other hand, in the phreatomagmatic wet eruptions (units 3 and 4), the vesicularity varies widely, reflecting the complex vesiculation and water-induced fragmentation.

Houghton et al. (2003, 2010) documented the bubble texture of the pumice clasts by using a scanning electron microscope. *Houghton et al.* (2010) classified pyroclastic clasts from each eruption unit into the five textural components (Fig. 5.4): (A) white and microvesicular pumice dominated by equant bubbles, (B) white vesicular pumice containing equant milimetersized bubbles, (C) white and long-tube microvesicular pumice with elongated bubbles, (D) white and long-tube coarsely vesicular pumice with elongated bubbles, and (E) grey and dense material with sparse and deformed bubbles of varying sizes. There are slight differences in bulk vesicularity among the clast types.

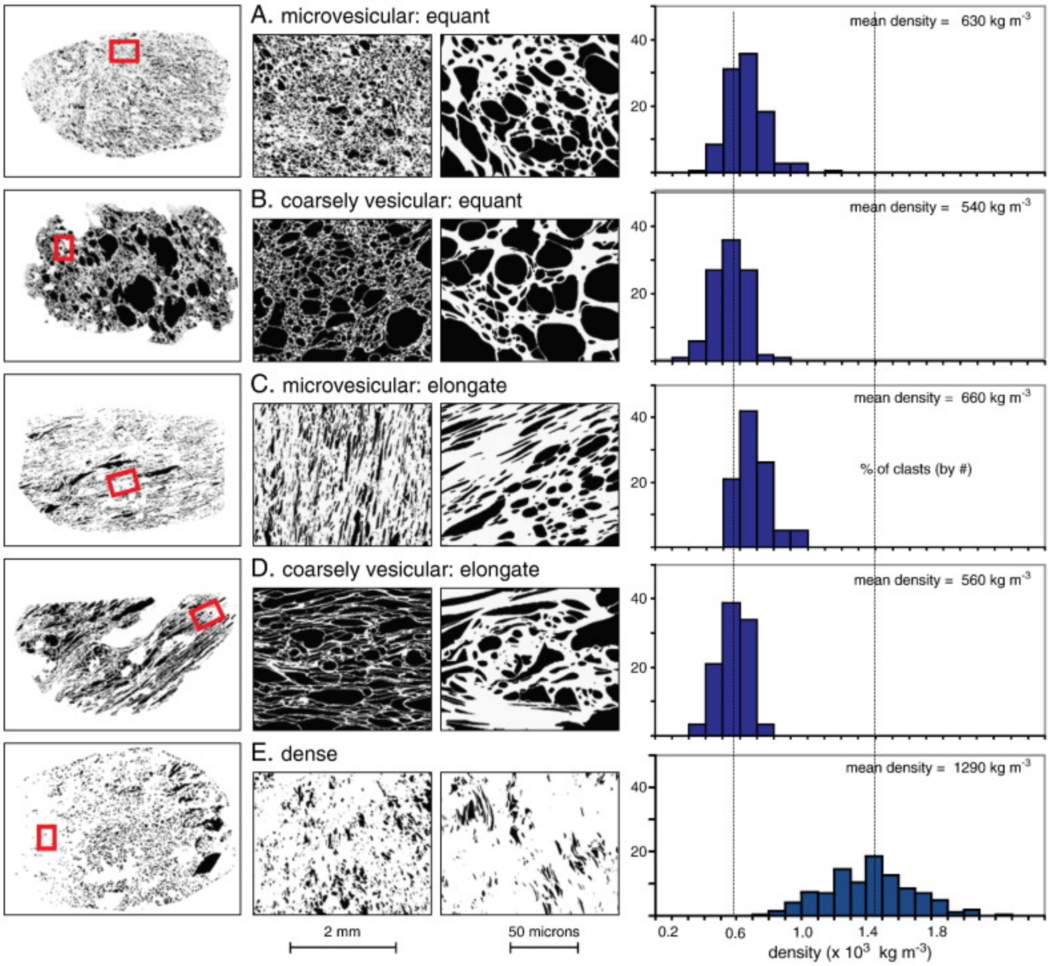

Figure 5.4: Microtextures of the principal types of pumice observed in the Taupo deposits (*Houghton et al.*, 2010, Fig. 3).

Fig. 5.5 shows the mean bulk density and the abundance of pumice with elongated bubbles (C+D), coarsely vesicular pumice (B+D), and dense clasts (E) (*Houghton et al.*, 2010). Separation of each textural component was conducted by visual observation. White microvesicular pumice (A+C) is dominant in units 1, 2, and 3. Then, there is a drastic increase in dense vesicular clast in unit 4. The explosive plinian phases (units 5 and 6) are characterized by an increase in the proportion of tube pumice. *Houghton et al.* (2010) interpreted that the high abundance of tube pumice reflected magma experienced more opportunity for bubble deformation along conduit margins.

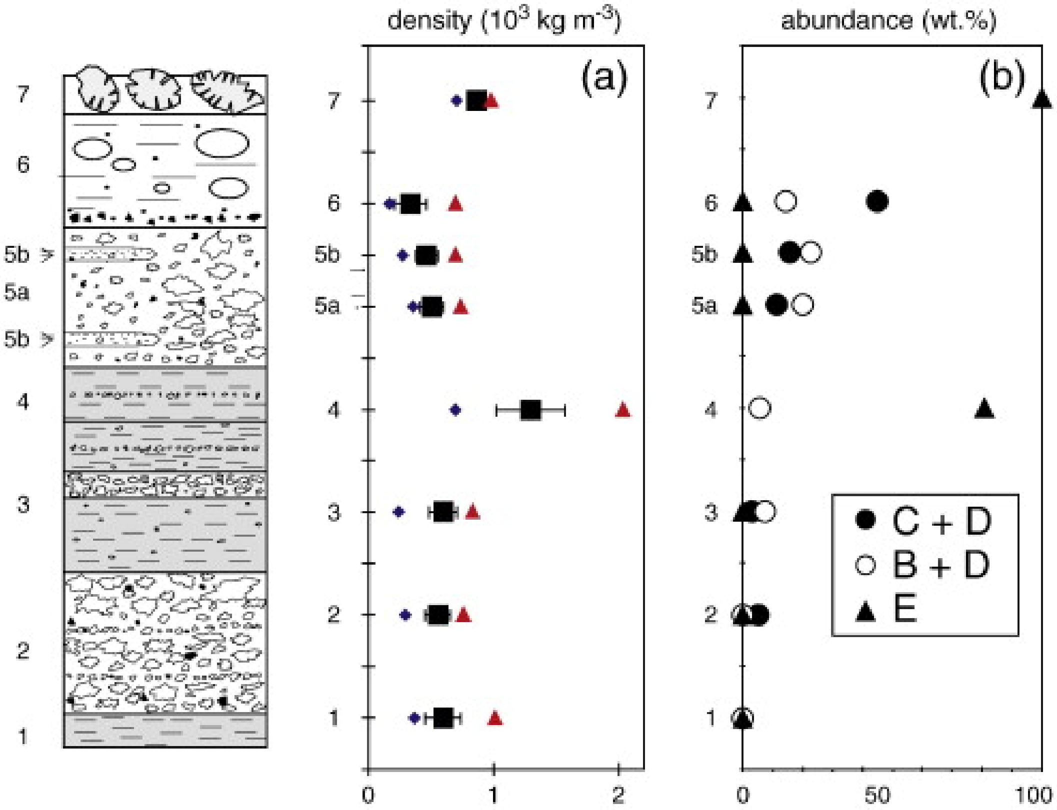

Figure 5.5: Mean density (squares) and one standard deviation (shown as error bars) for 100 clasts, together with average values calculated for the three densest (triangles) and three lightest (diamonds) clasts in each sample (*Houghton et al.*, 2010, Fig. 4). The right-hand column plots the abundance in weight % of all elongated pumice (closed circles), all coarsely vesicular pumice (open circles), and dense clasts (closed triangles).

5.3 Sampling

In this study, I focus on 'dry' plinian eruptions. I collected samples from the units of the two plinian eruptions (units 2 and 5) and the ignimbrite (unit 6). Fig. 5.6 shows the outcrops where I collected the samples. The schematic stratigraphy is shown in Fig. 5.7. The locations of outcrops are shown in Fig. 5.1. The fall deposits of Hatepe plinian (unit 2) were sampled at location A about 25 km away from the vent 1 (Fig. 5.6a). This outcrop shows the whole sequence of the 1.8 ka Taupo eruption and has been investigated for previous studies (*Walker*, 1980, 1981). The thickness of unit 2 is about 150 cm.

In many caldera-forming eruptions, pumice fall deposits underlie the main ignimbrite (*Bacon*, 1983; *Rosi et al.*, 1999). The precursory fall deposit is thought to record the mechanisms for withdrawal of a volume of magma sufficient to initiate caldera collapse (*Geshi and Miyabuchi*, 2016). In order to investigate the transition from plinian fall to ignimbrite, I conducted a detailed sampling of unit 5 at location B, which is about 20 km away from the vent 3 and reaches its maximum thickness of 210 cm (Fig. 5.6b and c). This outcrop is located on the main dispersal axis of unit 3 and is outside the area covered by intraplinian flow (Fig. 5.1). In the location B, the Taupo plinian fall deposit can be divided into two sub-units according to a sharp change in color, lithic clasts, and grain size of the pyroclasts: (1) a fine lower unit (30 cm), which is characterized by brown pumice clasts and rich in lithic fragments, (2) a coarse upper unit (180 cm), which is characterized by vesiculated white pumice clasts and poor lithic content (Fig. 5.6c). I collected pyroclasts from the bottom to the top of unit 5 at 20 cm intervals. In the lowermost sub-layer, the interval was 10 cm.

The flow deposits of Taupo ignimbrite (unit 6) were collected at location C 48 km away from the vent 3 (Fig. 5.6d and e).

5.4 Methods

5.4.1 Grain size and component analysis

For the samples of unit 5, I measured the median grain size and conducted the component analysis. The median grain size is defined as the midpoint of the grain size distribution by weight, that is, a half weight of the grains are coarser and another half weight of the grains are finer than the median grain size. The clasts larger than 1 mm were classified into pumice, lithic, and crystal based on the visual inspection.

5.4.2 Apparent density and bulk vesicularity

Apparent density and bulk vesicularity were measured using the method *Houghton and Wilson* (1989), which recommends 100 pumice clasts with the diameter range from 16 to 32 mm (-5Φ to -4Φ). I collected 100 clasts with a diameter of $16-32$ mm in unit 2, but due to the restriction of the baggage weight, I could not bring a sufficient number of clasts in units 5 and 6. When the number of pumice with $16-32$ mm is less than 100, I used pumice clasts of different sizes. In all sublayers of unit 5, I used total 25 pumice clasts with a diameter of $8-16$ mm as well as 1075 clasts with $16-32$ mm. In unit 6, I used 79 clasts with $16-32$ mm and 21 clasts with $32-64$ mm.

All pumice clasts were dried at $T = 60$ °C for 24 hours. The apparent density of pumice was measured by Archimedes method (*Houghton and Wilson*, 1989). First of all, I measured the weight of a clast in air ω_{air}. The pumice clasts then were covered with an impermeable film (Parafilm), whose weight in water is ω_{water}^{film}. The covered pumice weighed within water ω_{water}. The density of water is $\rho_{water} = 1000\ \mathrm{kg/m^3}$. Apparent density

Figure 5.6: Photos of the outcrops I collected samples. (a) Location A where I collected fall deposits of unit 2. (b) Location B where I collected fall deposits of unit 5. (c) Close view of location B. (d) Location C where I collected flow deposits of unit 6. (e) Close view of location C.

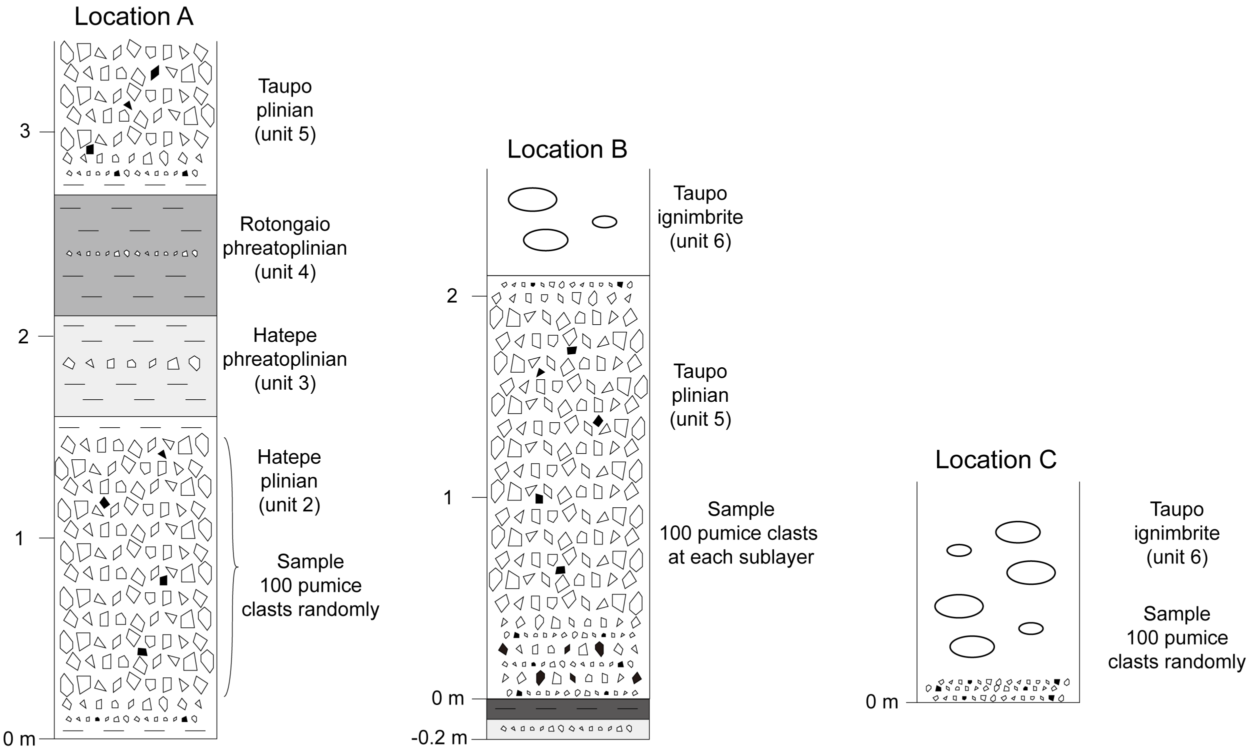

Figure 5.7: Simplified stratigraphy of the outcrops.

can be calculated by the following equation

$$\rho = \frac{\omega_{air}}{\omega_{air} - \omega_{water} + \omega_{water}^{film}} \rho_{water}. \tag{5.1}$$

The apparent density value was converted into the vesicularity by using a $\mathrm{DRE} = 2400\ \mathrm{kg/m^3}$ measured by *Houghton and Wilson* (1989).

5.4.3 Bubble texture

Volcanologists use the bubble textures of pyroclasts to identify the processes occurring before, during and immediately after eruption. The most common approach to characterize bubble texture has long been the 2D approach by thin sections (e.g., *Klug and Cashman*, 1994; *Klug et al.*, 2002; *Houghton et al.*, 2010). Thin section images taken by a scanning electron microscope provide 2D textural data such as bubble number density and vesicularity. The obtained data then are stereoscopically converted into 3D data. This approach has an advantage of accurately resolving the size and shape of small bubbles. The bubble texture of tube pumice has been investigated in detail through the 2D approach by thin sections (*Polacci et al.*, 2001, 2003; *Bouvet de Maisonneuve et al.*, 2009), but transforming the complex bubble shapes to 3D textures are challenging.

Recently, the 3D approach by X-ray CT (computed tomography) has been increasingly used to bubble textures in pyroclasts (e.g., *Gurioli et al.*, 2008; *Polacci et al.*, 2009; *Giachetti et al.*, 2011). This approach can accurately get the bubble texture in three dimensions and can be further used to calculate permeability (*Wright et al.*, 2009; *Degruyter et al.*, 2010b). However, the spatial resolution of standard X-ray CT scanners is not enough to resolve very thin glass walls within pumice and to measure small bubbles. The recent development of high-resolution tomography technique allows us to resolve very thin glass walls in three dimensions (*Degruyter et al.*, 2010b; *Dingwell et al.*, 2016).

Although the microscopic texture has been revealed in the previous works, the bubble texture was not well studied quantitatively or staistically. Since making thin sections is time-consuming work, the 2D approach by thin sections cannot be applied to a large number of pumices. The measurement by the 3D approach requires a relatively shorter time than by the 2D approach, but the machine time is limited. *Shea et al.* (2010) recommended to use at least 100 clasts to get statistically meaningful information of a deposit.

The macroscopic classification of pumices into several types, such as spherical and tube pumice, is helpful to get a general view of the bubble texture in an eruption. The abundance of each component gives us insights into the mechanical dynamics (*Taddeucci and Wohletz*, 2001; *Polacci et al.*, 2003; *Houghton et al.*, 2010). However, this approach depends on the judgment of the observer. In addition, the boundaries between pumice types are frequently not sharp, and one type may grade into another. In order to get a quantitative distribution of the bubble texture of whole deposit, a new approach, which allows us to characterize bubble textures in a short time, is required.

In this study, I develop a new method based on a digital stereo microscope. This method measures bubble shapes from the cutting surface in a short time, allowing to analyze the bubble texture of a statistically sufficient number of pumices (an order of thousand). Because this method cannot characterize bubble texture in three dimensions, I also measured the bubble texture of the representative samples by using an X-ray CT scanner. The combination of the new method and the X-ray tomography enables us to get a general view of bubble deformation in a conduit-scale.

2D texture: digital stereo microscope

We measured the 2D bubble texture for the pumices whose vesicularities were measured by the Archimedes method, namely 100 clasts for each subunit of unit 5 and 100 clasts for units 2 and 6. First of all, pumice clasts were cut along the plane parallel to the direction of elongation. I cannot always identify the elongation direction, and I sometimes cut a sample in a plane slightly off the elongation direction. The artificial error caused by wrong cutting sections will be discussed later with Fig. 5.20.

Grayscale images of the cutting surface were taken with a digital stereo microscope (VHX-1000, Keyence) at a magnification of ×20. The most distinctive point of the new 2D approach is to illuminate the cutting surface from the sides. I cannot recognize the boundaries between a bubble and matrix glass with a conventional microscope, because it illuminates the surface vertically (Fig. 5.8a). Using an adjustable illumination adapter (VH-K20, Keyence), I can illuminate the surface at shallow angles. The illumination from the sides makes a shadow inside the bubbles, which makes the boundaries distinct (Fig. 5.8b).

The image processing was conducted by Matlab codes. First, the grayscale images were transformed into binary images. Due to the ring lights aligned along the circumference of the lens, the center of a gray image is bright, but its corner is dark. To recognize bubbles correctly, I used an adaptive threshold algorithm, which computes a locally adaptive threshold of the brightness value (*Bradley and Roth*, 2007). Second, I erased bubbles with pixel numbers smaller than 20 for removing the effect of noise in the brightness values. Bubbles contacted with the borders were also removed automatically because these bubbles do not reflect the original shapes. Third, I manually removed the trace holes of crystals, which were made in the cutting process. The obtained binary image is shown in Fig. 5.8c. Large bubbles are segmented correctly. On the other hand, small bubbles are not recognized. If I raise the sensitivity of the adaptive threshold of brightness, those small bubbles will be recognized, but all bubbles will be connected because the glass walls separating the bubbles are too thin for the camera resolution. In order to segment large bubbles correctly, I remove the surrounding small bubbles by setting low sensitivity of threshold. The bubble shape was obtained by fitting an ellipse to the area. Each bubble was approximated as an ellipse, wherein two principle axes pass through the center of gravity of the bubble (Fig. 5.8d). The relationship between the semi-major and semi-minor axes of the ellipsoid was used to evaluate the deformation of the bubbles.

3D texture: Low resolution X-ray CT

Nine pumice clasts were selected from each unit (units 2, 5, 6) on the basis of the digital stereo microscope observation of their morphological features. Although the number of the samples was limited by the machine time, I think the pumice clasts selected for the X-ray tomography cover various bubble shapes from a nearly spherical shape to a highly elongated shape.

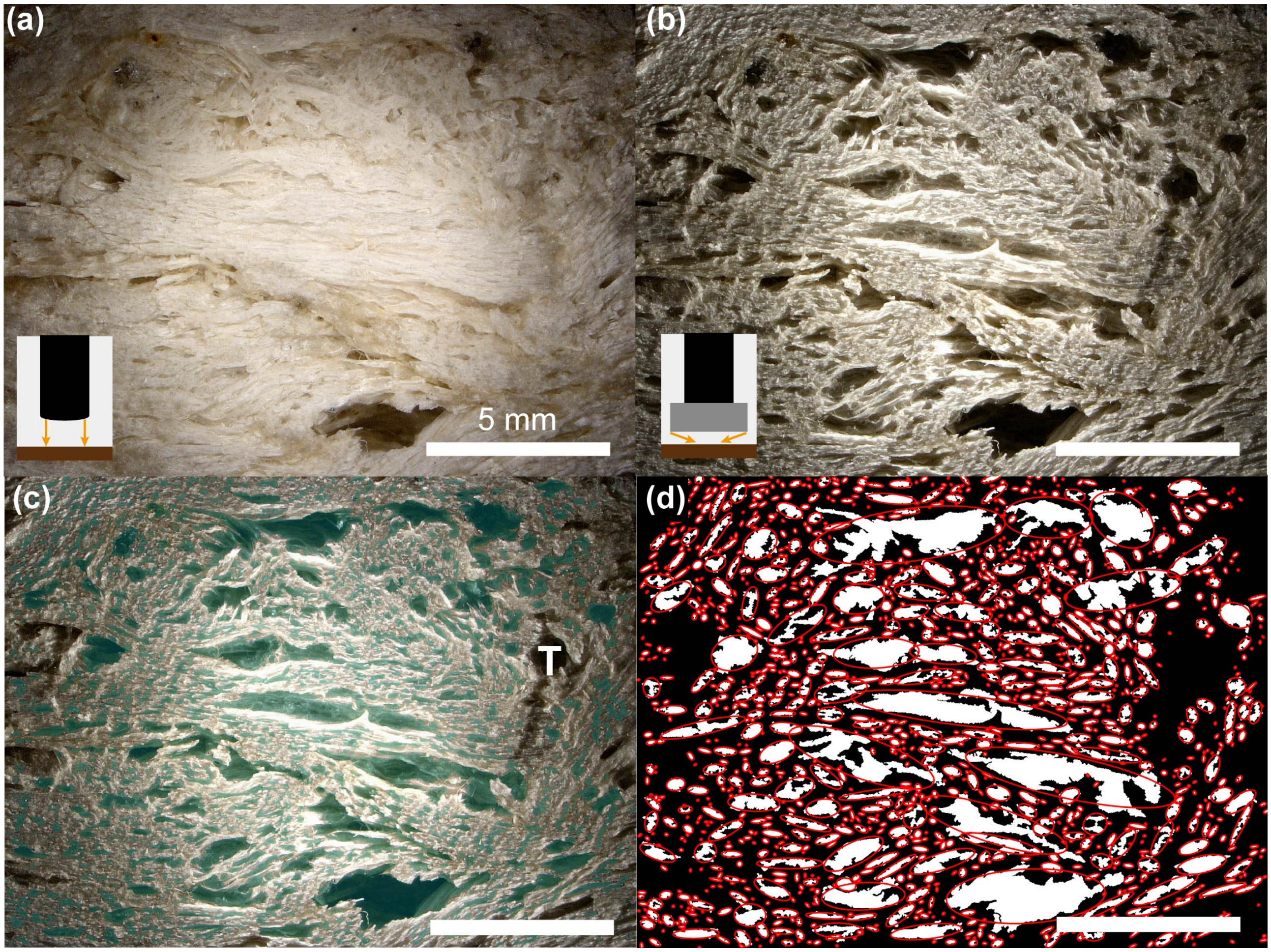

Figure 5.8: Digital stereo microscope image with (a) the conventional light and (b) the adjustable illumination adapter. Inset images show the schematic images of the conventional light and the adjustable illumination. (c) Binary image overlying the grayscale image. The track of crystal is shown by T. Green color indicates the recognized bubbles. (d) Fitted ellipsoids are shown in red color. All white bars indicate $5\ \mathrm{mm}$.

Representative pumice clasts from units 2, 5, and 6 were imaged by METROTOM 800 (Carl Zeiss) at Saitama Industrial Technology Center (Saitama, Japan). The samples having a cuboid shape were mounted on the rotational stage in the X-ray CT system and rotated 360° in steps of 0.45° (800 projections). The configuration used for each tomographic scan was a tube voltage of $130\ \mathrm{kV}$, a tube current of $60\ \mu\mathrm{A}$, and a voxel size with edge lengths in each direction of $8\ \mu\mathrm{m}$. The resulting tomographic data was visualized as volume renderings via the commercial software (Simpleware, Synopsys). Fig. 5.9 shows the representative sample of the rendered image of tube pumice.

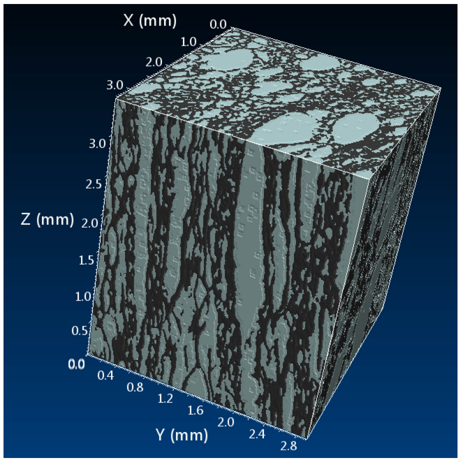

Figure 5.9: Representative sample of the rendered image of tube pumice from the Taupo Ignimbrite. The image is binarized to make it easy to observe tube-like bubbles.

Bubbles in most Taupo pumice are entirely connected, as shown in Fig. 5.9. Therefore, I need to separate those bubbles into an individual bubble before measuring bubble shapes. In chapter 3, I used the watershed segmentation technique to separate bubbles in three dimensions (appendix C). The basic idea of this technique is flooding water on a topographic surface, which is the grayscale intensity calculated from the X-ray CT images. Water is flooded from each regional minimum of the surface, and walls are built where the different waters meet (Fig. 5.10). In the watershed segmentation used in chapter 3, the grayscale intensity was defined as the distance from each inner air pixel to the nearest solid medium pixel, as the further is the lower intensity (topography). The gray-scale mapping and watershed segmentation methods used in chapter 3 for the experimental foams failed to separate bubbles in Taupo pumice. One reason is that the spatial scale of the texture is finer in the pumice than in the foam, and the other is that the bubbles are more significantly distorted and connected.

The spatial resolution of the X-ray scanner (METROTOM 800) is not enough to resolve thin glass walls, and a voxel containing both air and glass wall shows an intermediate density between air and matrix glass. In this chapter, I used the gradient of density itself as a grayscale topography (the small gradient is the lower topography). This definition is suitable for porous materials whose intended boundaries have a gradation of density and is applicable for connected bubbles in pumice. To overcome the segmentation problem for the bubbles with complicated texture, I use the marker-controlled watershed algorithm (*Meyer and Beucher*, 1990).

To perform the grayscale mapping based on the density values and the marker-controlled watershed seg-

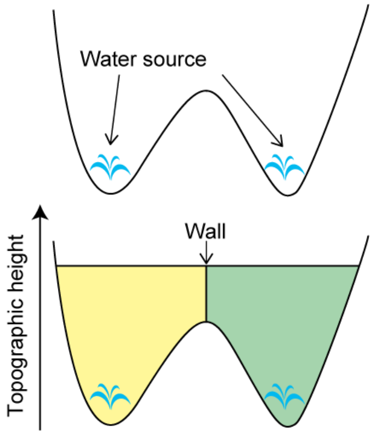

Figure 5.10: Schematic image of watershed segmentation in 1D.

mentation, I used an image processing software, Fiji (*Schindelin et al.*, 2012). The detailed procedure of the image processing for pumice is described in appendix F.

3D texture: High resolution X-ray CT

To resolve the fine textures, I performed high-resolution X-ray CT for some representative samples by SkyScan 1272 (Bruker) at Saitama Industrial Technology Center. Unfortunately, I could not measure all pumice clasts, which were analyzed in low-resolution X-ray CT, because X-ray from this CT scanner is too weak to penetrate a dense pumice clast. I analyzed only a few pumices that are highly vesiculated and composed of very thin bubble walls. The samples were cut into small cuboids with a square base of about $1\ \mathrm{mm} \times 1\ \mathrm{mm}$ and a height of about $2\ \mathrm{mm}$. They were imaged by a $50\ \mathrm{kV}$ - $200\ \mu$A conventional energy source and rotated 360^{o} in steps of 0.1^{o} (3600 projections). The spatial resolution is $0.45\ \mu\mathrm{m/pixel}$, and the image size is 4904×3280 pixel. Three-dimensional images were reconstructed by the NRecon software. The method of image analysis of bubbles is the same as that for the low-resolution X-ray CT. In the following sections, I explicitly indicate the results with the high-resolution X-ray CT, while data and results are from the standard X-ray CT otherwise.

5.5 Results

5.5.1 Component analysis and bulk vesicularity

Variation of geological parameters in the Taupo plinian fall (unit 5) is shown in Fig. 5.11 as a function of stratigraphic height. Throughout the whole outcrop, reverse grading was found from bottom to top of the unit 5. Lower fall unit (< 30 cm) is finer-grained with the median diameter ranges from $4 - 6$ mm, and is rich in lithics (19 wt.%). The dominant lithic lithology in unit 5 is rhyolite, followed by altered rhyolite and obsidian. These lithics were observed in the Taupo ignimbrite by *Cole et al.* (1998). Upper fall unit is coarser-grained with the median diameter ranges from $5 - 11$ mm, and is poor in lithics ($9 - 15$ wt.%). Lithic types do not change from lower to upper fall unit. Relative abundance of free crystals does not change in unit 5, and is dominant in plagioclase. The bulk vesicularity data is consistent with the previous studies of *Houghton and Wilson* (1989) and *Houghton et al.* (2010), which showed the homogeneous vesicularity throughout unit 5. The average vesicularity of pumice in unit 5 is about 78.8 %.

Only the bulk vesiculariy of pumice was measured for the Hatepe plinian fall (unti 2) and the Taupo ignimbrite (unit 6). The average pumice vesicualrity of unit 2 is 78.6 % which is very close to the value of unit 5, and that of unit 6 is 88.2 % which is higher than the two plinian fall deposits.

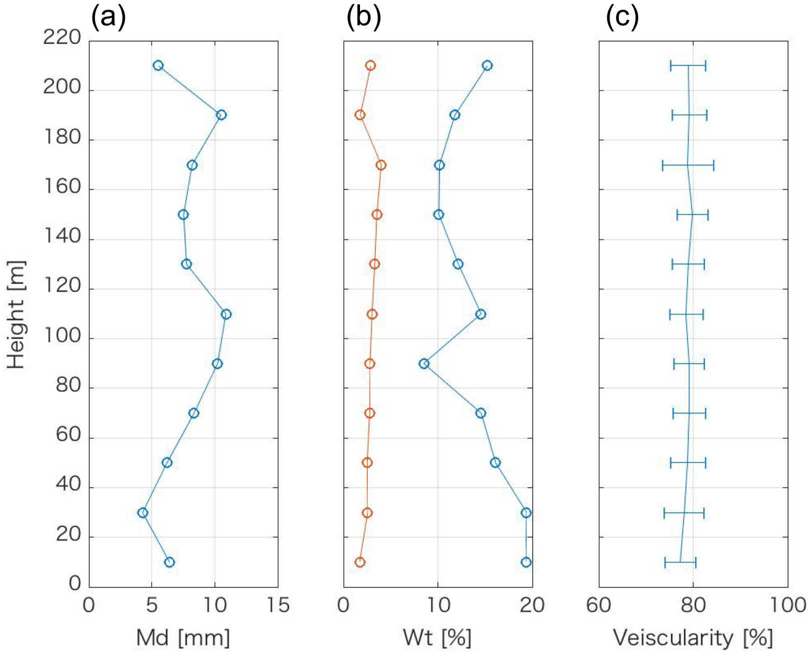

Figure 5.11: Vertical variation of (a) the median diameter of grain size, (b) the components, and (c) the bulk vesicularity of pumice clats in the Taupo Plinian fall (unit 5). In the component analysis, blue and red lines indicate the relative portion (wt. %) of lithics and crystals, respectively.

5.5.2 Representative samples of units 2, 5, 6

Fig. 5.12 shows the images of the representative pumice clasts taken by the digital microscope and the low-resolution X-ray CT. Tube and spherical pumices were chosen from each unit by visual observation. As *Houghton et al.* (2010) pointed out, there is a wide range of bubble texture in these clasts. Bubble size and elongation vary among these clasts, and it seems that there is no correlation between elongation and size. Some pumices show the internal heterogeneous texture. For example, bubbles around crystals are nearly spherical while most of the bubbles are deformed largely (Fig. 5.12b).

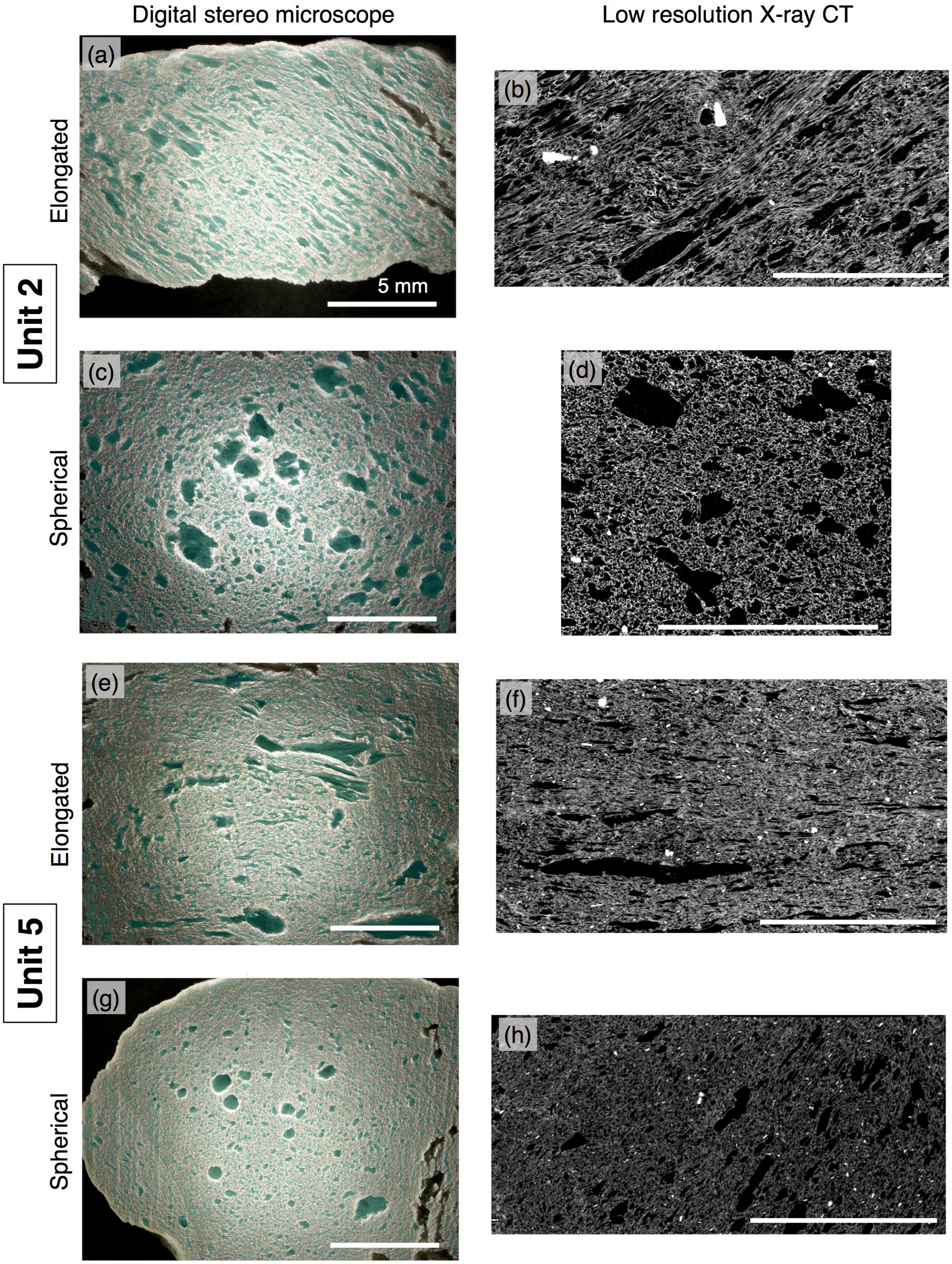
Digital stereo microscope
Low resolution X-ray CT
Unit 2
Elongated
Spherical
Unit 5
Elongated
Spherical
(a)
(b)
(c)
(d)
(e)
(f)
(g)
(h)
5 mm

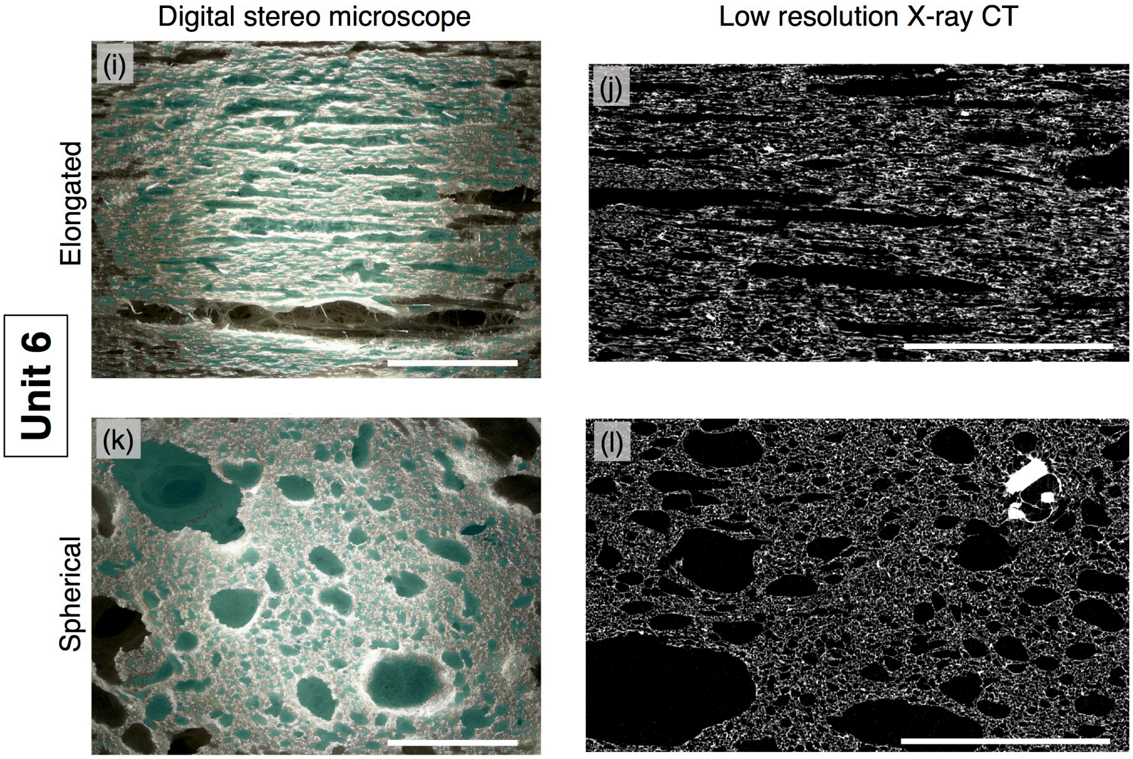

Figure 5.12: Representative images of pumices from units 2, 5, and 6. Images on the left sides are the photos taken by the digital stereo microscope, and those on the right side are the cross-section of the X-ray CT images. Green sheds in the digital stereo microscope images indicate the analyzed bubbles. All scalebars are $5\ \mathrm{mm}$. (a, b) Sample 45 from unit 2. (c, d) Sample 27 from unit 2. (e, f) Sample 09_04 from unit 5. (g, h) Sample 10_25 from unit 5. (i, j) Sample 2_38 from unit 6. (k, l) Sample 1_11 from unit 6.

5.5.3 Quantitative analyses of bubble textures

We analyzed the 2D and 3D image data for the relationship between bubble deformation degree D and spherical bubble radius R_b as I found the relationship indicative for the dynamics of bubble deformation (section 2.5). Fig. 5.13 shows the results for the representative clasts (same clasts as Fig. 5.12). All results show the positive correlations between D and R_b. There is only small differences between the results of the digital stereo microscope (2D) and the X-ray CT (3D). Only the plots of sample 10_25 (Fig. 5.13g and h) are significantly different.

We think that this discrepancy between the 2D and 3D approaches was caused by the direction of the cutting surface. When making the flat surface of pumice, I tried to cut clasts in the direction parallel to bubble elongation. However, visual observation of pumice appearance sometimes results in cutting in the wrong direction. If I cut elongated bubbles perpendicular to elongation direction, the cutting surface shows the nearly spherical bubbles. The cutting surface of this sample shows nearly spherical bubbles (Fig. 5.12g), while the tomography image exhibits elongated bubbles (Fig. 5.12h). I think that this discrepancy was caused by the deviation of the cutting surface from the direction of bubble elongation.

The striking feature of the bubble shapes is that most of the distributions of D suggest the effect of transient deformation. As assumed in section 2.5, it is reasonable to assume that strain rate, viscosity, and surface tension are homogeneous throughout a volcanic pyroclast. Therefore, the capillary number depends on only the bubble radius. Specifically, Ca is proportional to R_b. If bubble deformation were in the equilibrium state, as R_b increases, D must approach to unity with large R_b regardless of simple or pure shear. Except for the highly elongated bubbles in unit 6 (Fig. 5.13i and j), D approaches a much smaller value ($D < 1$). This trend suggests a transient deformation, whereby the bubble deformation stopped on the way to reach the equilibrium state due to the insufficient strain. The distributions of D affected by the transient deformation allow us to estimate the strain applied to the bubbles.

The high-resolution X-ray CT images contribute to the check of the validity of the results from the standard X-ray CT. Fig. 5.14 shows the result of the high-resolution analysis for the tube pumice from unit 6 (sample 2_38), which is the same sample as i and j of Figs. 5.12 and 5.13. I can recognize thin bubble walls in the cross-sectional image (Fig. 5.14a). The distribution of D shows an almost constant value of $D \sim 0.65$ for bubbles with $0.25 < R_b < 1.5 \times 10^{-4}$ m (Fig. 5.14b). On the other hand, the low resolution X-ray CT provides the smaller D ($0.4 < D < 0.65$) in the corresponding range of R_b. This result suggests that all data imaged by the low-resolution X-ray CT may not be measured accurately in the range of $R_b < 1.5 \times 10^{-4}$ m.

The three-dimensional bubble shape is characterized by two ratios, a/b and b/c. The ellipsoidal shape is often expressed by Flinn diagram (*Flinn*, 1962). Fig. 5.15 shows the Flinn diagram for pumices containing elongated bubbles. All pumice clasts contain prolate and oblate ellipsoids. The elongated bubbles are closer to prolate ellipsoids than oblate ellipsoids. It should be noted that the prolate bubbles are not the evidence of pure shear deformation because of the surface tension. Contrary to strain ellipsoids in earth materials, bubbles contain the surface tension. The cross-section perpendicular to the main axis is relaxed to a circular shape (*Jackson and Tucker*, 2003). A highly deformed bubble by simple shear becomes a prolate shape.

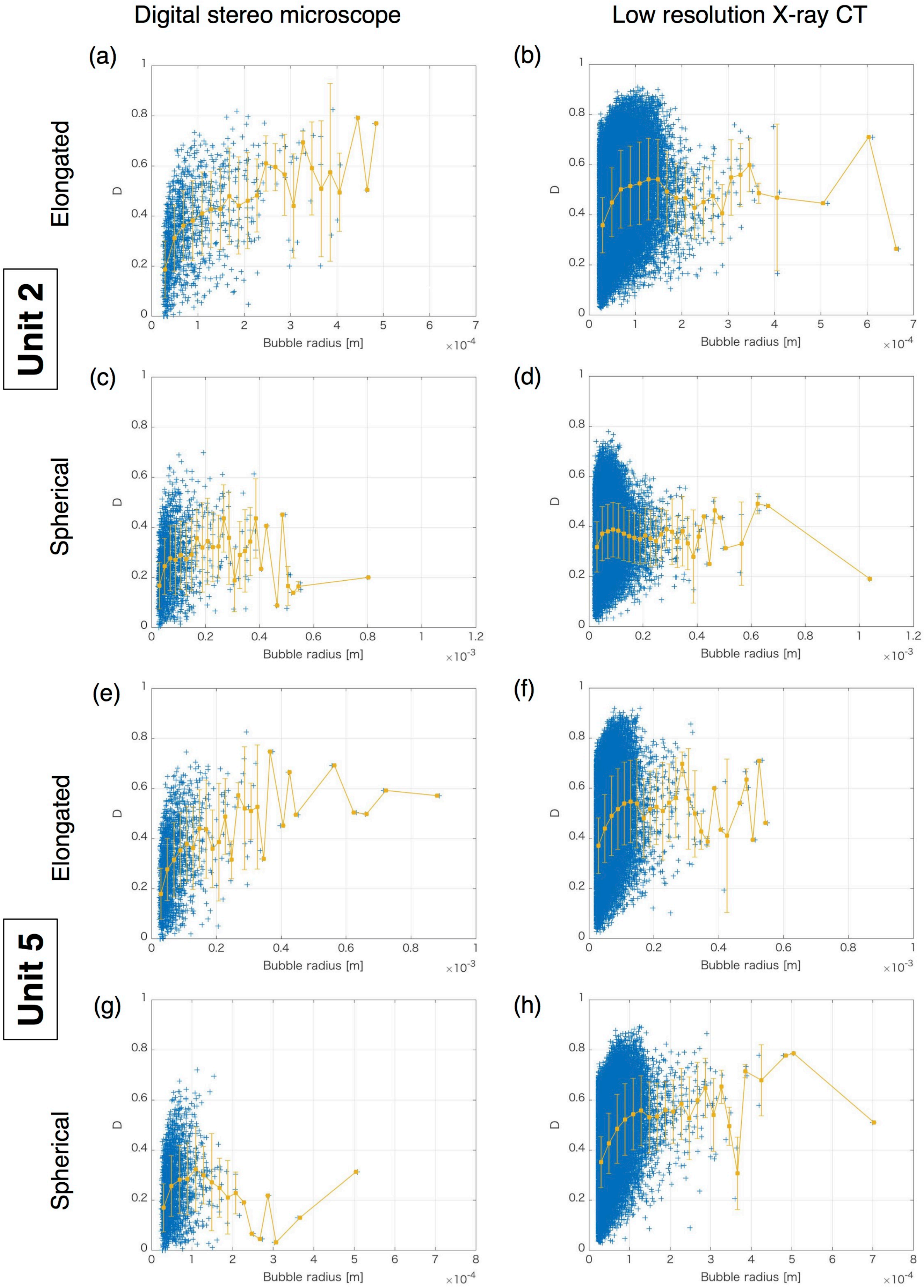
Digital stereo microscope
Low resolution X-ray CT
Unit 2
Elongated
Spherical
Unit 5
Elongated
Spherical
(a)
(b)
(c)
(d)
(e)
(f)
(g)
(h)
D
0
0.2
0.4
0.6
0.8
1
Bubble radius [m]
×10^-4
0 1 2 3 4 5 6 7
×10^-3
0 0.2 0.4 0.6 0.8 1 1.2
0 0.2 0.4 0.6 0.8 1
0 1 2 3 4 5 6 7 8

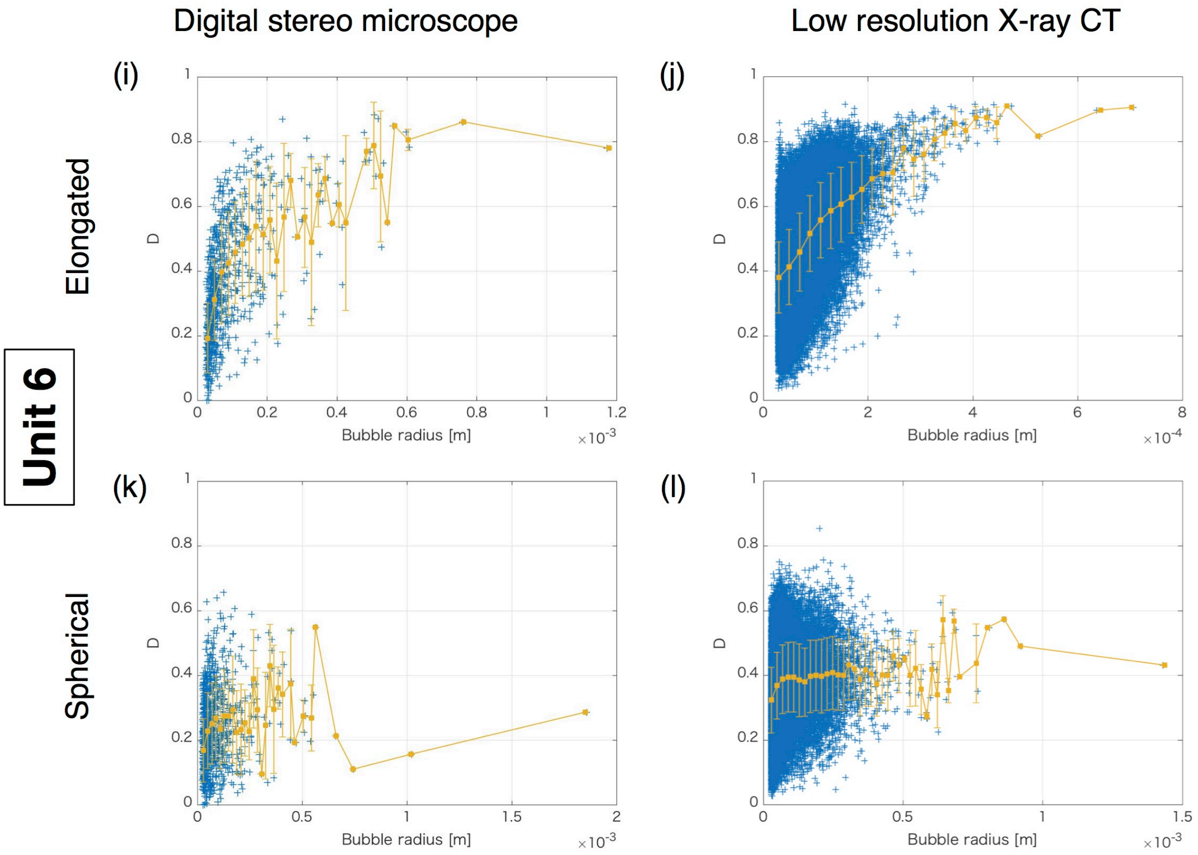

Figure 5.13: Relationships between the bubble deformation degree D and the spherical bubble radius R_b for the same samples as Fig. 5.12. Yellow dot indicates the average values of D in each subgrid with 2×10^{-5} m. Errorbar expresses the standard deviation of D.

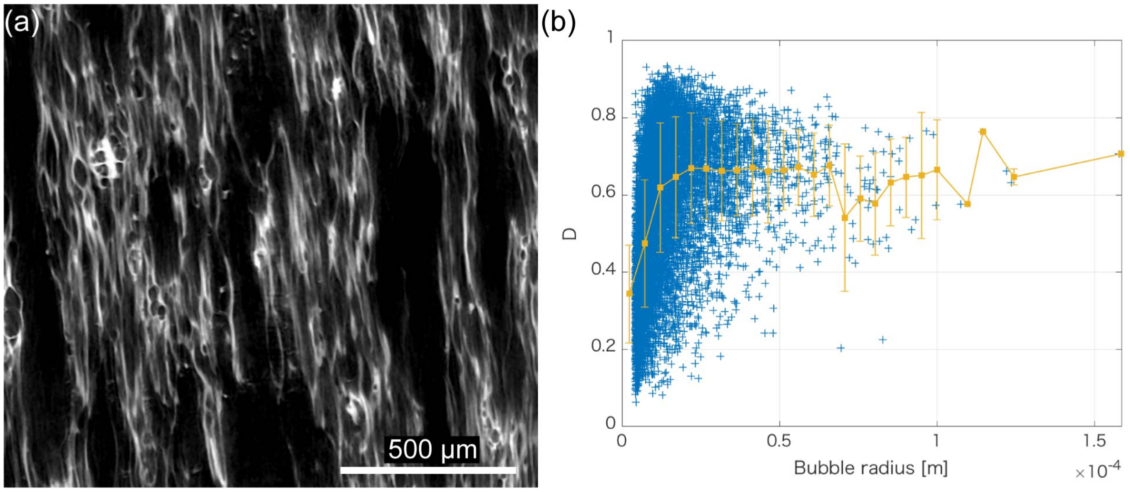

Figure 5.14: High resolution X-ray CT for the tube pumice from unit 6 (sample 2_38), which is the same sample as Fig. 5.12i and j. (a) Cross section image. (b) Relationship between D and R_b. Yellow dot indicates the average values of D in each subgrid with 5×10^{-6}m.

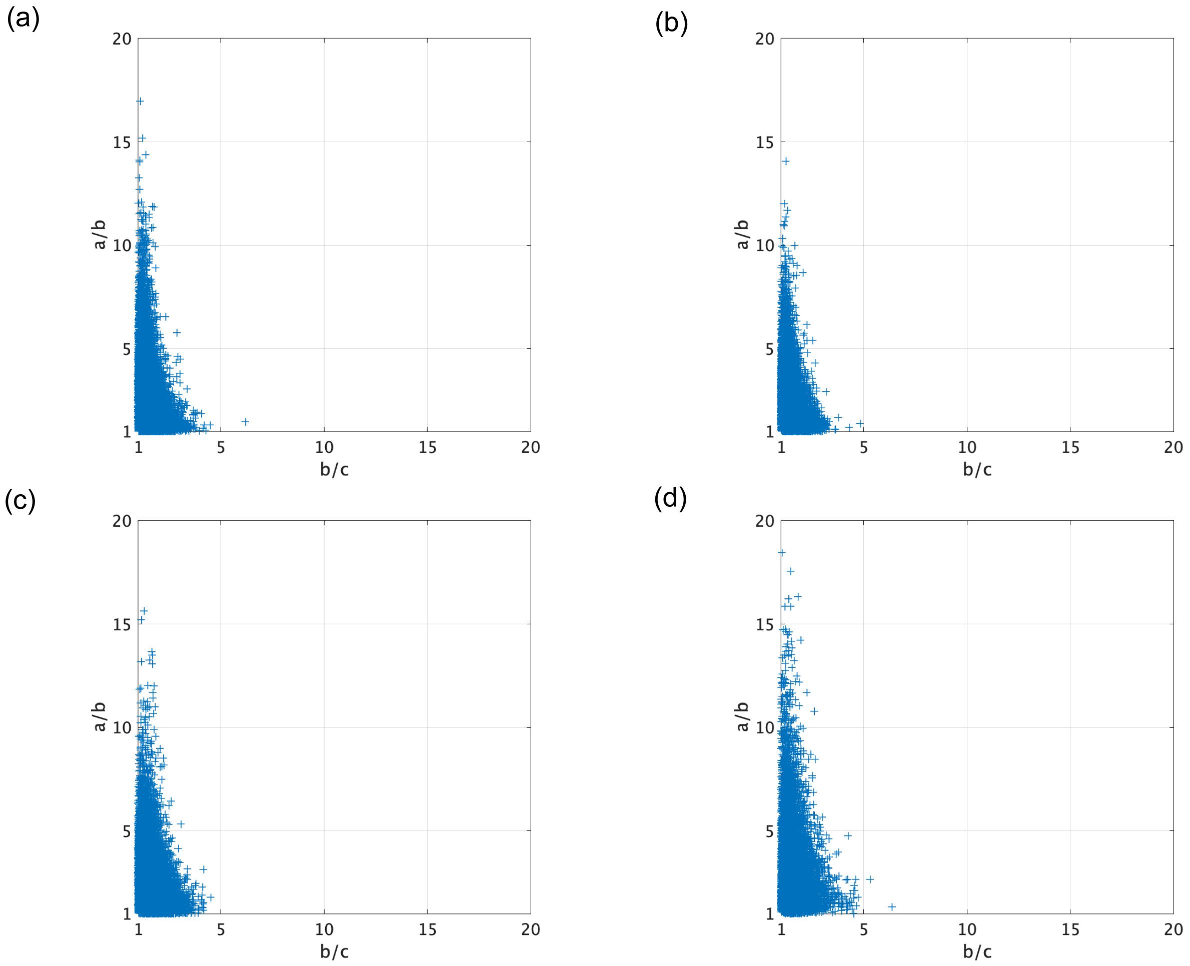

Figure 5.15: The Flinn diagram for elongated bubbles. (a) Sample 45 from unit 2. (b) Sample 10_25 from unit 5. (c) Sample 2_38 from unit 6. (d) Sample 2_38 from unit 6. The low resolution X-ray CT data are used except for (d). The high resolution X-ray CT data are used for (d).

5.5.4 Statistical approach

Hereafter, I report the analytical results for bubbles with the spherical bubble radius greater than 1.5×10^{-4} m in order to measure bubble shape accurately. This constraint is applied for the data of both low-resolution X-ray CT and digital stereo microscope.

The stratigraphic change of the relative abundance of tube pumice is one of the important references to interpret the dynamics of a conduit flow. In order to investigate the bubble textures quantitatively, I define a representative bubble deformation degree for each pumice clast. It is the normalized bubble deformation degree by the bubble size. The representative bubble deformation degree for the data of the digital microscope D_{R2} is given by

$$D_{R2} \equiv \frac{\Sigma D_{i2} A_i}{\Sigma A_i}, \tag{5.2}$$

where D_{i2} and A_i are the bubble deformation degree and the bubble area measured by the digital microscope. The corresponding representative bubble deformation degree for the low-resolution X-ray CT D_{R3} is given by

$$D_{R3} \equiv \frac{\Sigma D_{i3} R_i^2}{\Sigma R_i^2}, \tag{5.3}$$

where D_{i3} and R_i are the bubble deformation degree and the equivalent bubble radius measured by the X-ray CT.

Fig. 5.16 compares D_{R3} with D_{R2}. In most cases, the representative bubble deformation degree based on the low-resolution X-ray CT is a little larger than the digital stereo microscope because the cutting surface is not always parallel to the elongation direction of the bubbles within the pumice. Although there is a slight difference between D_{R2} and D_{R3}, D_{R2} well represents the features of bubble texture within pumice clasts. Table. 5.1 summarizes D_{R2} and D_{R3} for the representative samples.

We think that this discrepancy between the 2D and 3D approaches was caused by the direction of the cutting surface. When making the flat surface of pumice, I tried to cut clasts in the direction parallel to bubble elongation. However, visual observation of pumice appearance sometimes results in cutting in the wrong direction. If I cut elongated bubbles perpendicular to elongation direction, the cutting surface shows the nearly spherical bubbles.

To check the error caused by cutting a pumice clast in the wrong direction, I obtain the cross-section from 3D data in an arbitral angle. Fig. 5.17 shows the cross-sections cut out from the 3D data of Sample 10_25. This sample showed the discrepancy between the 2D and 3D approaches (Fig. 5.13g and h). As the inclined angle from the bubble elongation direction increases, the bubble becomes close to a spherical shape.

Next, I calculate the representative bubble deformation degree D_{R2} (Eq. 5.2) for all cross-sections with a certain inclined angle. Fig. 5.18 shows the mean D_{R2} as a function of the inclined angle. The mean D_{R2} decreases with the angle from the elongation direction. The representative bubble deformation degrees estimated by the digital microscope and the X-ray tomography are $D_{R2} = 0.23$ and $D_{R3} = 0.56$, respectively. If I cut the sample in a plane with an angle of more than 50 degrees, this discrepancy between 2D and 3D

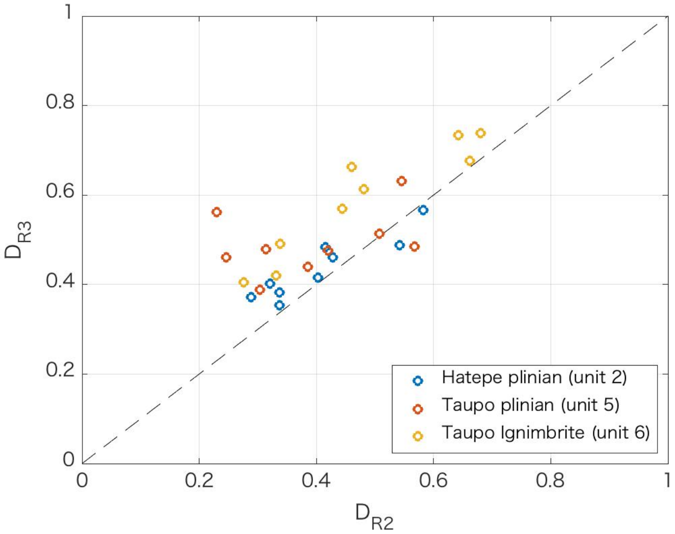

Figure 5.16: Relationships between D_{R2} and D_{R3} for the representative samples. In most samples, D_{R3} is a little larger than D_{R2}.

approaches can be explained.

The stratigraphic change of D_{R2} in unit 5 is shown in Fig. 5.19, and no stratigraphic variation is observed. It is reminded that the pumice vesicularity is also homogeneous in Unit 5 (Fig. 5.11c). Fig. 5.20 shows the relationship between the vesicularity and D_{R2} for the pumice clasts from unit 5 and unit 6. Any systematic trend can not be observed in both units.

The abundance of bubble texture is shown in Fig. 5.21 as the histogram of D_{R2}. The number of analyzed sample is 100 for unit 2 and 6, and 1100 for unit 5. The plinian fall eruptions (units 2 and 5) show similar histograms which are characterized by a single peak around $D_{R2} = 0.35$ with a half width of about 0.1. The peak of D in unit 5 is slightly larger than that of unit 2.

The histogram of the Taupo Ignimbrite (unit 6) is markedly different from the plinian units. The highest peak of unit 6 lies at $0.55 < D_{R2} < 0.60$, and the distribution is broad from 0.28 to 0.70. My new method enables us to quantitatively analyze the bubble textures of a large number of samples. I expect that the statistical distribution of bubble deformation degrees of pumice clasts in one layer provides information on the shear deformation field across the conduit. In the next chapter, I calculate the radial variation of bubble shape and magma flux across a conduit to interpret the result of Fig. 5.21.

5.6 Discussion

In this thesis, I analyzed bubble shapes under the assumption that they were frozen at the fragmentation surface. However, bubble shapes at the fragmentation surface might not always be the same as those preserved in pumice clasts. After fragmentation, deformed bubbles within a pumice may return to spherical shapes due to surface

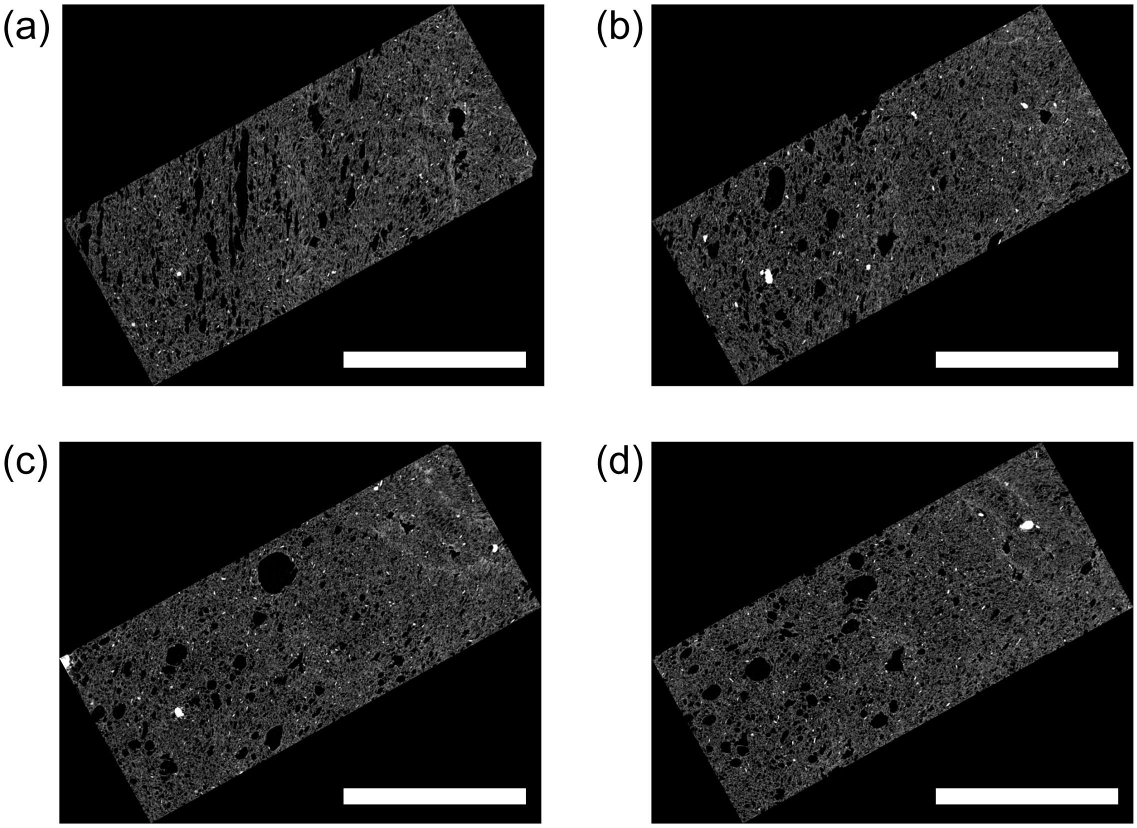

Figure 5.17: Cross sections cut out from the 3D data of Sample 10_25. (a) Cross section parallel to the bubble elongation direction. (b) Cross sections inclined 30° from the bubble elongation direction. (c) Cross section inclined 60°. (d) Cross section inclined 90°. All scalebars are $5\ \mathrm{mm}$.

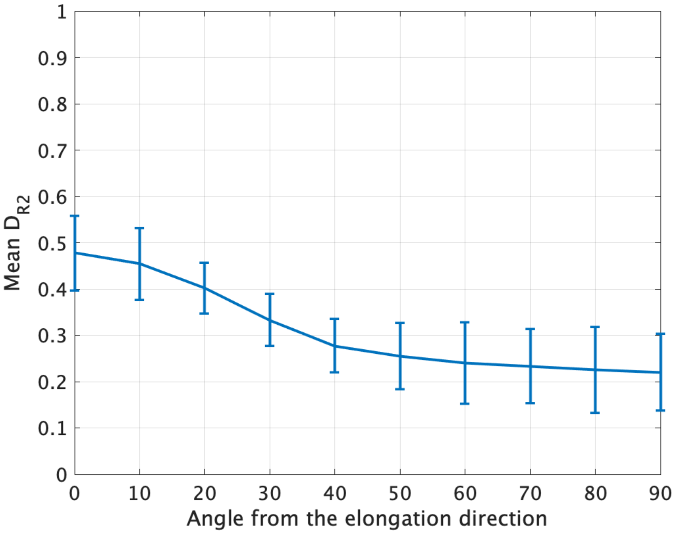

Figure 5.18: The mean D_{R2} as a function of the inclined angle. The errorbar indicates the standard deviation of D_{R2}.

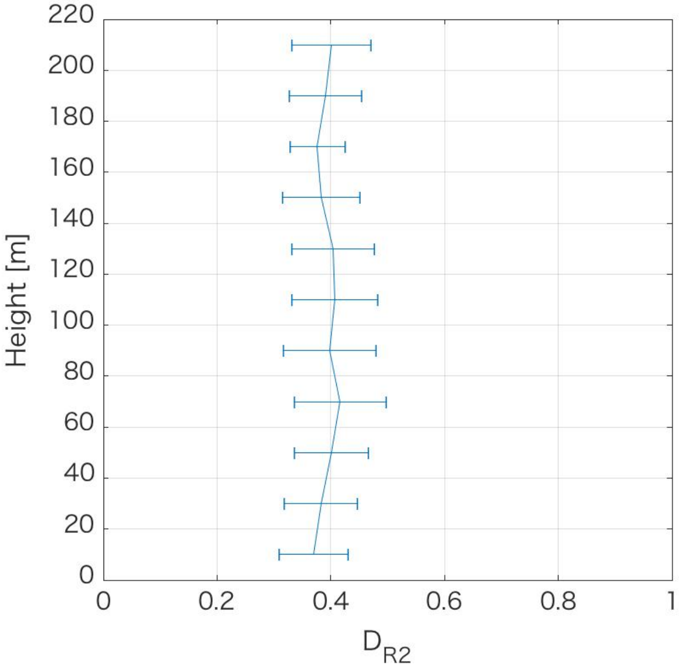

Figure 5.19: Stratigraphic change of D_{R2} for the Taupo plinian (unit 5). Errorbar indicates the standard deviation of D_{R2}.

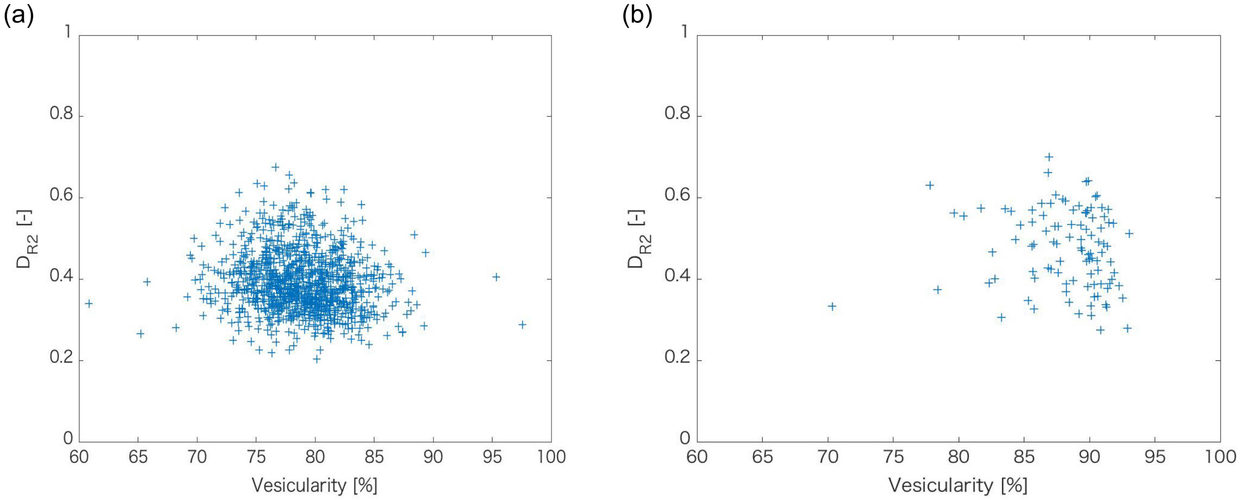

Figure 5.20: Relationship between the vesicularity and D_{R2} for the pumice clasts from (a) the Taupo plinian (unit 5) and (b) the Taupo ignimbrite unit 6.

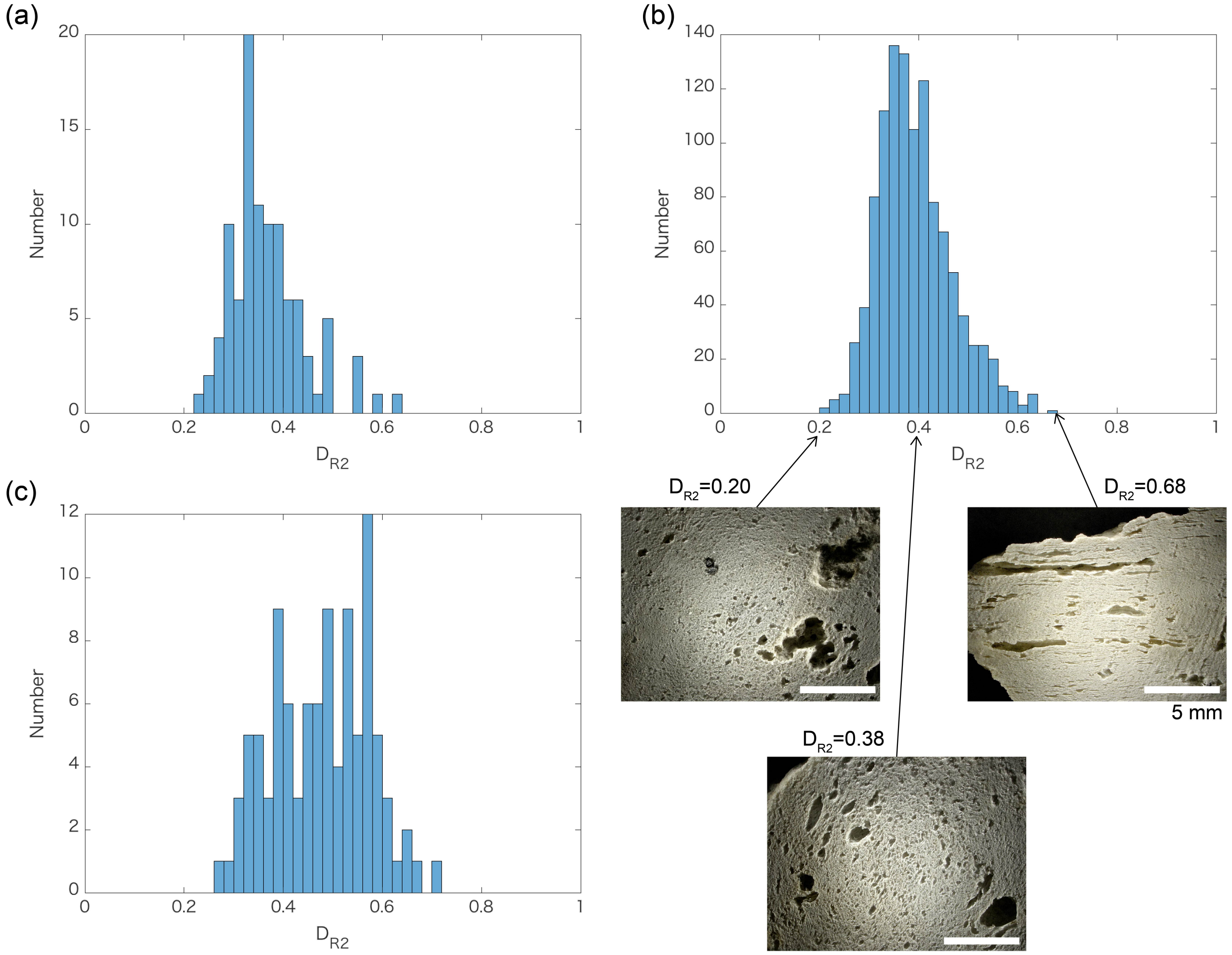

Figure 5.21: Histogram of D_{R2} for (a) the Hatepe plinian (unit 2), (b) the Taupo plinian (unit 5), and (c) the Taupo ignimbrite (unit 6). The number of analyzed sample is 100 for units 2 and 6, and 1100 for unit 5.

Table 5.1: Textural characteristics of the representative pumice clasts.

Sample	Unit	Vesicularity % [a]	D_{R2}	D_{R3}
03	unit 2	77.7	0.40	0.41
17	unit 2	76.6	0.32	0.40
18	unit 2	75.0	0.43	0.46
23	unit 2	72.6	0.42	0.48
27	unit 2	83.6	0.34	0.35
32	unit 2	80.0	0.29	0.37
45	unit 2	78.1	0.54	0.49
47	unit 2	82.8	0.58	0.46
48	unit 2	86.9	0.34	0.44
09_04	unit 5	76.9	0.51	0.51
09_12	unit 5	74.1	0.57	0.49
09_25	unit 5	76.4	0.54	0.63
09_28	unit 5	76.7	0.25	0.46
09_34	unit 5	78.1	0.30	0.39
10_01	unit 5	76.5	0.31	0.48
10_08	unit 5	82.8	0.38	0.44
10_25	unit 5	80.5	0.23	0.56
10_31	unit 5	81.9	0.42	0.48
1_11	unit 6	90.9	0.28	0.41
1_27	unit 6	89.9	0.46	0.66
1_39	unit 6	91.4	0.48	0.61
1_40	unit 6	91.3	0.33	0.42
1_42	unit 6	89.9	0.64	0.73
2_3	unit 6	89.7	0.68	0.74
2_4	unit 6	91.3	0.34	0.49
2_38	unit 6	86.8	0.66	0.68
2_50	unit 6	89.8	0.44	0.57

[a] Measured by the Archimedes method (*Houghton and Wilson*, 1989)

tension and/or bubble growth, if the pumice has enough time in the stress-free condition before it quenches. In this section, I discuss this problem.

5.6.1 Shape relaxation caused by surface tension

The amount of shape relaxation can be considered as the competition of the relaxation timescale τ_{relax} and the solidifying time scale. In section 3.4.2, I evaluate the effect of shape relaxation by using the pumice number Pu.

Cooling of a tephra clast after fragmentation has been investigated from several viewpoints. *Thomas and Sparks* (1992) made a model for the cooling of a clast during fallout from an explosive eruption column, showing that the cooling condition controls welding in deposits. *Hort and Gardner* (2000) investigated the cooling and degassing of pumice during an eruption column, indicating that large pumice is easily to loss volatiles syneruptively. From the petrological viewpoints, *Tait et al.* (1998) studied changes in pumice color and Curie temperature, using clasts of Minoan plinian eruption of Santorini volcano. Recently, *Matsumoto and Nakamura* (2017) investigated the oxidation kinetics of pyrrhotite, suggesting that the pumice surfaces remained a higher temperature than the assumed temperature of 293 K.

In order to study the shape relaxation of bubbles after fragmentation, here, I solve heat conduction in a pumice clast during an eruption column. I try to constrain the possibility of shape relaxation in the Taupo plinian eruption by combining a cooling model with the bubble deformation model (MJT model) proposed in section 2. First, I obtain the ambient temperature of a pumice clast in the eruption column, using a steady-state eruption column model, Plumeria (*Mastin*, 2007). The parameters for the Plumeria are determined to simulate the eruption column of the Taupo plinian eruption (unit 5). Next, I solve thermal conduction in a pumice clast and get the temporal profiles of temperature and viscosity. Finally, I calculate the shape relaxation of a bubble with the MJT model. The detail procedure and parameters are described in appendix G.

The simulation results of the eruption column are shown in Fig. 5.22. The average velocity above the conduit inlet decreases due to the large gravitational force (Fig. 5.22a). As the eruption column ascends, the density decreases because of the thermal expansion caused by the high initial magma temperature (Fig. 5.22b). Then, the velocity turns to increase (Fig. 5.22c). The maximum height is about 27 km. The average temperature decreases monotonically. Assuming that a pumice clast moves up confluently, I can calculate its risetime to be 197 s.

The history of thermal conduction within a pumice clast is shown in Fig. 5.23. The interior of the pumice clast cools much slower than the pumice surface because of the small thermal diffusivity (Fig. 5.23a). The temperature at the pumice surface is slightly higher than the column temperature as a result of inefficient heat transfer. Fig. 5.23b indicates that the temperature history is largely controlled by the pumice size.

Fig. 5.24 shows the shape relaxation of a bubble in a pumice center. When the pumice radius is less than 2 cm, the shape of a deformed bubble is almost frozen even in a pumice center (Fig. 5.24a). The amount of shape relaxation is largely controlled by clast size as well as bubble location. As a pumice clast becomes the large size, a bubble at the pumice center is relaxed before the pumice quenches (Fig. 5.24b).

In this chapter, I analyzed natural pumice clasts whose diameter ranges from 1.6 to 3.2 cm. The numerical simulation of Fig. 5.24 suggests that bubble shapes within the clasts might have been almost frozen. In addition, if bubbles had been relaxed before the clast frozen, there would have been the radial variation of bubble shape, that is, elongated bubbles had located on the clast surface and spherical bubbles had been in the clast center. However, as far as I analyze, I could not find such a pumice clast. Even if a pumice clast showed a heterogeneous bubble texture, it was anisotropic. For the above reasons, I think that shape relaxation after fragmentation may not be an important factor for explosive eruptions.

5.6.2 Shape relaxation caused by bubble growth

Another possibility of shape relaxation of a bubble is growth after fragmentation. *Thomas et al.* (1994) and *Kaminski and Jaupart* (1997) theoretically showed that a pumice clast can expand in the volcanic conduit and

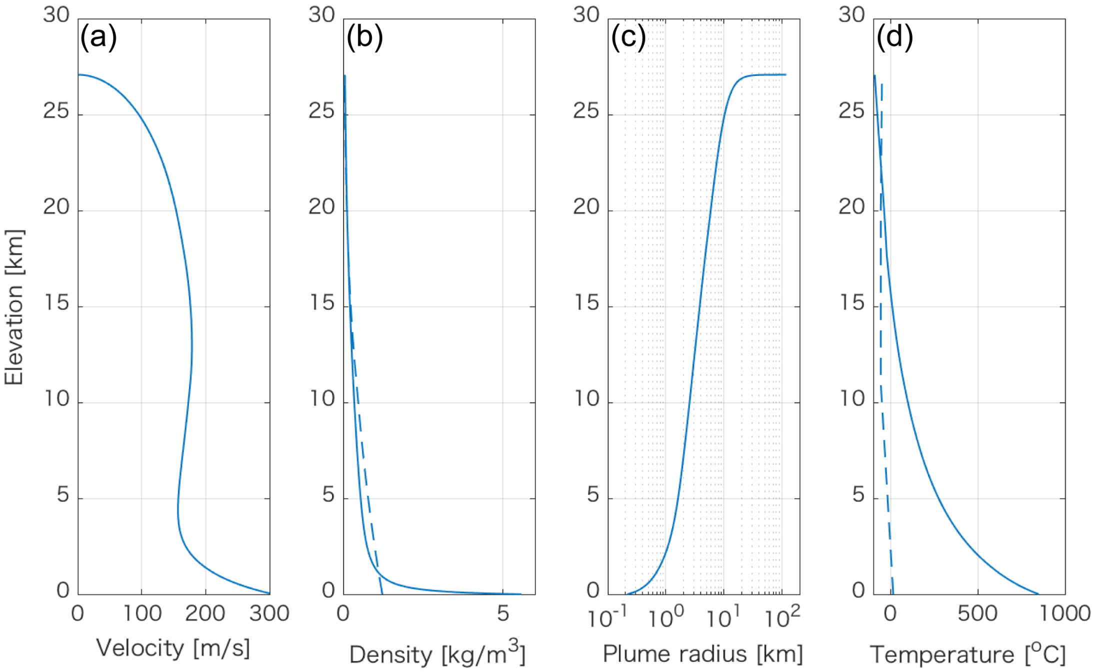

Figure 5.22: Vertical variation of (a) averaged velocity, (b) plume density, (c) plume radius, and (d) averaged temperature. Dashed lines in (b) and (d) indicate the atmospheric density and temperature, respectively.

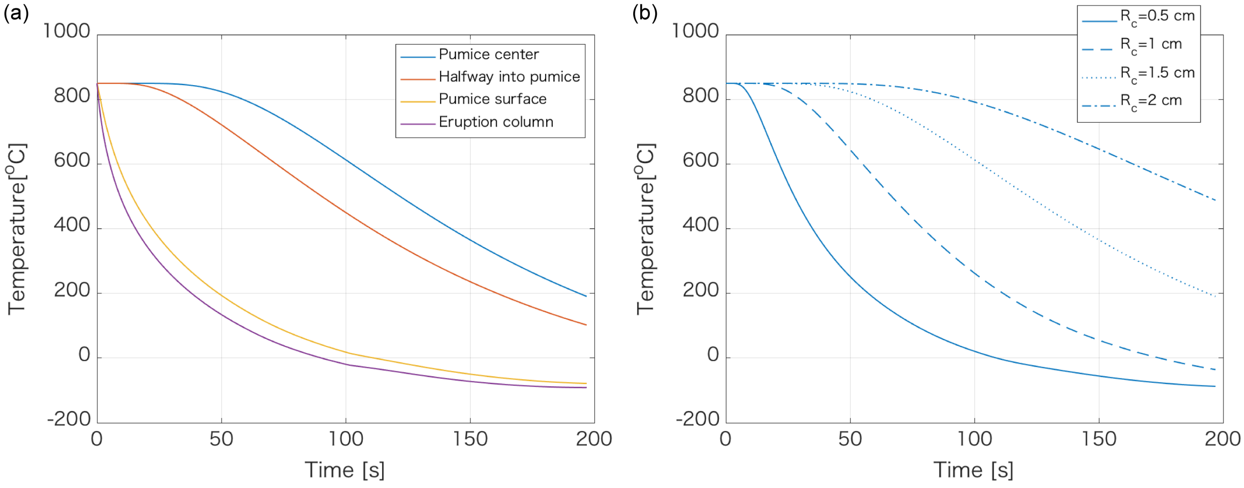

Figure 5.23: (a) Temporal profile of temperature within a pumice with the clast radius of $R_C = 1.5$ cm. Line color indicates the positions within the clast as well as the column temperature. (b) Temporal evolution of temperature at the pumice center. Line type indicates the clast radius.

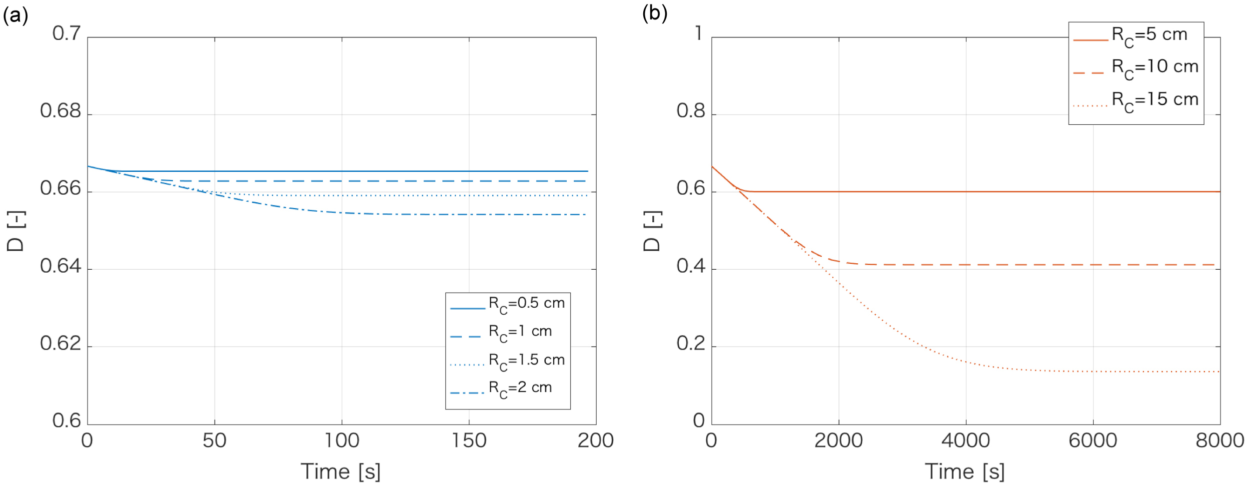

Figure 5.24: The history of shape relaxation of a bubble at the pumice center. (a) small clasts and (b) large clasts. The initial D is 0.667 and the initial bubble radius is 0.15 mm. Keep in mind that the ranges of vertical axes (D) are different between (a) and (b). In the calculation of (b), I assumed that the ambient temperature kept the temperature at the column top after the pumice clast reached there.

the atmosphere, depending on the pressure and temperature history. According to this research, the range of vesicularity within samples from the same stratigraphic layer reflects the different paths in the eruption column. If post-fragmentation growth occurs in pumice, the bubbles inside will return to spherical shapes.

We think such a post-fragmentation bubble growth is significant only inside large pumice, and it can be negligible for small pumice. Recently, *Mitchell et al.* (2018) performed a detail investigation of variations in bulk density of pumice over a size range of $4 - 128$ mm from the Hatepe eruption (unit 2) of the 1.8 ka Taupo eruption. According to this research, a clear shift of bulk density appeared between $\geq -5\Phi$ and $\leq -4.5\Phi$ which corresponds to 32.0 mm and 22.6 mm. Densities for diameters -5Φ and -4.5Φ clasts are 600 and $700\ \mathrm{kgm^{-3}}$, respectively (i.e., vesicularities of 0.74 and 0.71). The authors also qualitatively classified pumice clast into two types: microvesicular and macrovesicular. Microvesicular pumice was characterized with small bubbles, assumed to be frozen at the fragmentation surface. On the other hand, macrovesicular pumice had large bubbles inside together with more quenched rind. This type was assumed to be affected by post-fragmentation vesiculation. The author showed that the number of macrovesicular pumice increased with clast size, especially from -5Ψ. For the above reasons, the authors concluded that there was clear evidence of post-fragmentation vesiculation at > 32 mm.

In this thesis, I used pumice clasts with a diameter of < 32 mm in the units 2 and 5. Therefore I basically think that the effect of post-fragmentation growth on bubble shape can be negligible for those clasts.

In order to estimate the error of D caused by post-fragmentation vesiculation, here I provide the simplified problem. I assume that a pumice clast is composed of prolate bubbles with uniform bubble size and deformation degree. The post-fragmentation vesiculation is assumed to elongate two minor-axes while keeping the main axis constant. In this situation, the bubble deformation degree is independent of the bubble number density and the bubble size and is controlled only by vesicularity. Fig. 5.25 shows the temporal change of D caused by post-fragmentation vesiculation. The amount of shape relaxation depends on the initial D and vesicularity. For example, when the vesicularity increases from 0.7 to 0.75, D changes from 0.5 to 0.45 (yellow). Given that the average vesicularities of microvesicular and macrovesicular pumice are 0.71 and 0.74, respectively, I estimate the effect of post-fragmentation growth on bubble shape to $\Delta D < 0.05$ where ΔD is the amount of shape relaxation.

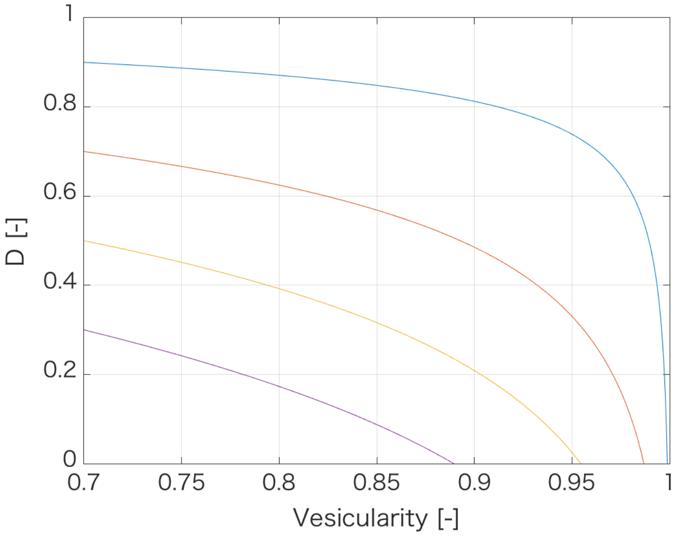

Figure 5.25: The temporal change of D caused by post-fragmentation bubble growth. The pumice clast is assumed to have the vesicularity of 0.7 at the fragmentation. Initial D is set to 0.9 (blue), 0.7 (red), 0.5 (yellow), and 0.3 (purple).

In the unit 6 (Taupo ignimbrite), I used larger clasts (> 32 mm) as well as smaller clasts ($16 - 32$ mm). The post-fragmentation vesiculation might have be more significant in unit 6 than units 2 and 5, because pumice clasts were transported in a hot pyroclastic flow. However, I think that the effect of post-fragmentation vesiculation on bubble shape was small in tube pumice, because its permeability is higher than a pumice composed of spherical bubbles (*Wright et al.*, 2006, 2009). If the post-fragmentation vesiculation occurs in tube pumice, exsolved gas may escape through the interconnected tube bubbles. In addition to that, I could not find tube pumice with radial heterogeneous bubble texture. If the post-fragmentation vesiculation had affected on bubble shapes, spherical bubbles would have been found inside the pumice.

For the above reasons, I conclude that the effect of post-fragmentation on bubble shape can be negligible.

Chapter 6

Comparison of bubble shape

6.1 Introduction

In the previous chapter, I quantitatively analyzed 2D bubble textures within a total of 1300 pumice clasts from the 1.8 ka Taupo eruption. Assuming that a large number of analyzed clasts reflect the radial distribution of bubble shapes at the fragmentation surface, I here compare the natural bubble shapes with those calculated by the quasi-two dimensional conduit flow model. This comparison is of great interest because it can be used to identify whether the velocity profile across the conduit has a parabolic or plug-like shape.

First, the bubble shapes in the Taupo plinian fall are compared with the numerical simulations based on the three conduit flow models. The comparison suggests that the velocity profile is close to a plug-like shape. I then simulate the conduit flow of the Taupo ignimbrite, using the viscous-heating model. The calculated bubble shapes at the fragmentation surface well reproduce the natural feature of the bubble texture in the Taupo ignimbrite.

6.2 Comparison for the Taupo plinian fall (unit 5)

6.2.1 Histogram of the Taupo plinian fall

In Fig. 5.21, I showed the histogram of D_{R2} preserved in pumice clasts from the Taupo plinian fall deposit. In order to compare it with the numerical simulation of Fig. 4.21, I normalize the vertical axis of Fig. 5.21.

Fig. 6.1 shows the comparison of the bubble shapes in the plinian fall (unit 5) with the numerical simulations. In the numerical simulations which showed the parabolic velocity profiles, the calculated bubble shapes are much more elongated than those observed in unit 5 (Fig. 6.1a and b). On the other hand, the bubble shapes calculated by the viscous-heating model, which showed the plug-like velocity profile, are in the range of the bubble shapes observed in unit 5 (Fig. 6.1c). This result suggests that bubbles in the Taupo plinian event were deformed in the conduit flow with the plug-like velocity profile, which was likely to be caused by intense viscous heating around the conduit walls.

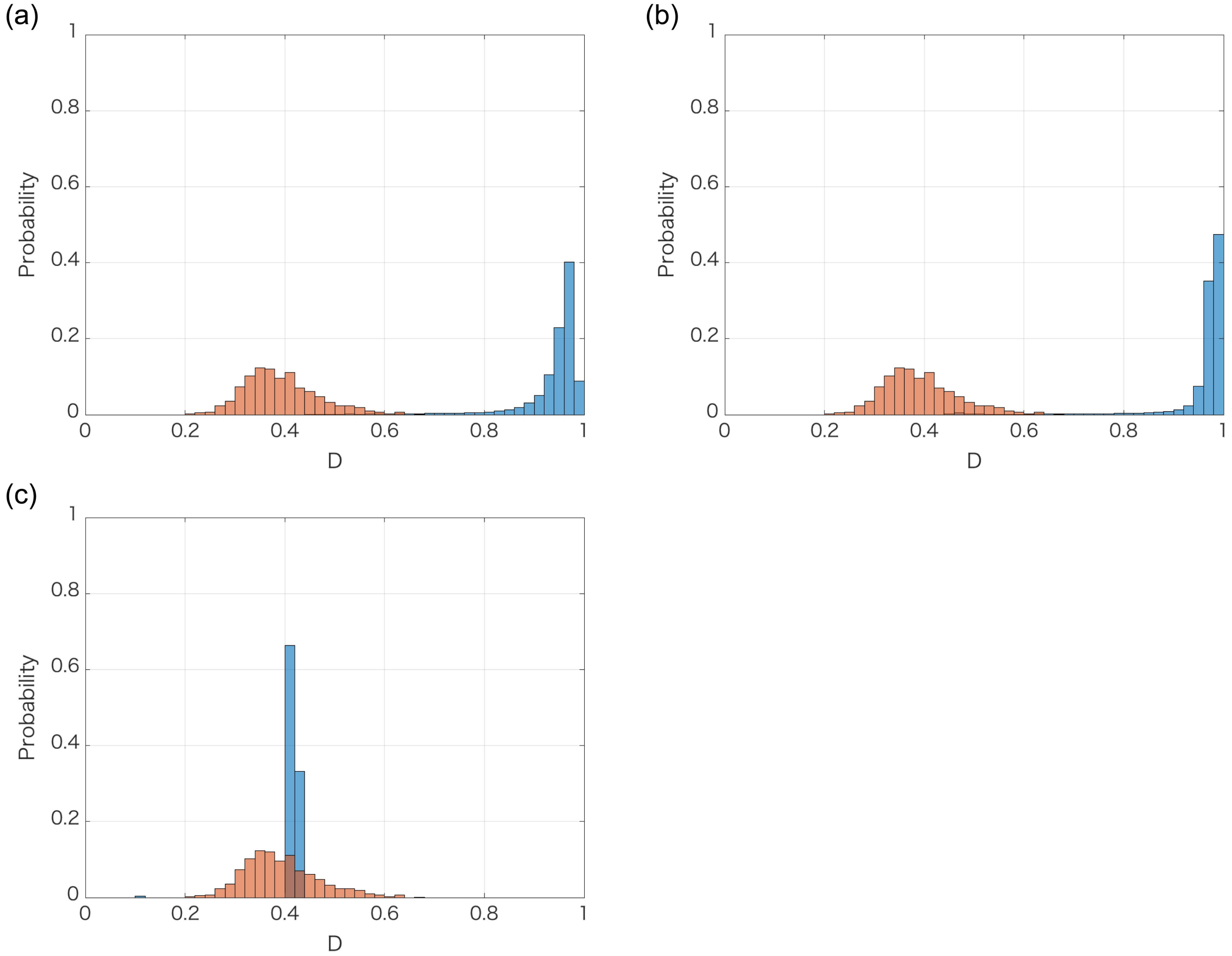

Figure 6.1: The comparison of bubble shapes in the Taupo plinian fall with the numerical simulations. Histogram of D_{R2} in Taupo plinian fall is shown in red color. Blue histograms represent D calculated by (a) the Newtonian isothermal model, (b) the shear-thinning model due to bubble deformation, and (c) the viscous heating model. All the vertical axes are normalized.

6.2.2 Discrepancy between observation and numerical simulation

The distribution of bubble shape calculated by the numerical model is not exactly the same as the observed bubble shapes. I consider the following reasons.

First, the numerical shear filed in the conduit may be slightly different from the real shear field because of the simplicity of the conduit flow model I used. When deriving the basic equations of the quasi two-dimensional conduit flow model (appendix C), I have not considered several terms that potentially change the flow field, such as inertia terms and vertical viscous stresses. Neglecting these terms may be more serious as magma gets close to the fragmentation surface where the Reynolds number and expansion rate are large. Strictly speaking, the assumption of a constant pressure across a conduit is not valid around the fragmentation surface (appendix C). The horizontal gradient of pressure may cause the additional radial flow, leading to the radial variation of the bubble deformation degree.

Second, the volcanic conduits may be far from the idealized cylindrical shape. Rapid variations of the cross-sectional area with depth may lead to a much stronger mixing of the thermal boundary layer around the conduits (*Costa and Macedonio*, 2005). The vertical variation of the cross-sectional area also contributes to the vertical velocity gradient (pure shear).

Third, the parameters for the Taupo eruption (Table 4.1) have uncertainties, which may affect the histogram of D. For example, the mass discharge rate for the Taupo plinian eruption ranges from 10^8 to 10^9 $\mathrm{kg/s}$ and that for the Taupo ignimbrite eruption ranges from 10^9 to 10^{11} $\mathrm{kg/s}$, depending on the estimation method (*Wilson et al.*, 1980; *Wilson and Walker*, 1985; *Carey and Sigurdsson*, 1989; *Houghton et al.*, 2014; *Michaud-Dubuy et al.*, 2018). The mass discharge rate, which I used here for the Taupo plinian eruption (2.5×10^8 $\mathrm{kg/s}$), is a little lower value. If I use a higher mass discharge rate, the widening of the conduit will occur, leading to a reduction in viscous-heating effect. The amount of tube pumice will increase in the same way as the Taupo ignimbrite eruption shown in the next section. The increase in elongated bubbles is consistent with the discrepancy that the natural observation contains more elongated bubbles than the simulation result (Fig. 6.1).

Fourth, the shapes of bubbles in a conduit flow are controlled not only by deformation but also by coalescence. The analogue experiment in chapter 3 showed that the average shape of multiple bubbles was explained by the deformation model of a single bubble. Based on this result, I define the representative deformation degree of bubbles in pumice D_{R2} (Eq. 5.2) and compare it with the numerical simulation. However, the analogue experiments also showed that a deformation degree for each bubble was more scattered around the model result with increasing bubble coalescence (Fig. 3.7c-f). The scatter caused by bubble coalescence is expected to be intense in highly vesiculated foam. Since the Taupo pumice ($\approx 75\%$) is more vesiculated than the analogue foam ($\approx 60\%$), coalescence might have largely affected the bubble shape. The scattering may occur not only within a sample but also in the conduit scale. In this study, I conveniently neglect the effect of bubble coalescence by taking the average bubble deformation degree (i.e., D_{R2}), but I am required to investigate the effect of bubble coalescence for further study.

Finally, the bubble deformation degree measured by the digital stereo microscope is a little different from a true three-dimensional bubble shape. The measured bubble shape changes depending on the direction of the cutting plane, and I could not measure small bubbles separated by thin glass walls because of the space resolution of the microscope. Even if all bubbles were measured precisely in the correct plane, I do not have an effective methodology whereby the 2D data for highly elongated bubbles can be converted to the 3D data.

Although the comparison of the numerical results with the observed bubble shapes has several problems as described above, I believe that the comparison is still effective in determining the velocity profile which drastically changes depending on the rheology model. The plug-like velocity profile caused by viscous heating is the most reasonable case among the considered models.

6.3 Comparison for the Taupo ignimbrite

Next, I simulate the conduit flow for the Taupo ignimbrite (unit 6) by using the viscous heating model and then obtain the flux of bubble shape at the fragmentation surface.

6.3.1 Conduit flow based on the viscous-heating model

The parameters used in the simulation for the Taupo ignimbrite are the same as the Taupo plinian eruption (Table. 4.1) except the mass discharge rate Q_m and critical volume fraction at fragmentation ϕ_f. Based on the geological study by *Wilson and Walker* (1985), Q_m is set to 5×10^{10} kg/s. I also set ϕ_f to be equal to the average vesicualrity of pumice from unit 6 ($\phi_f = 0.88$). The initial pressure p_{in} and conduit radius R are determined from the boundary problem as discussed in the Taupo plinian simulation (section 4.4.2). In the simulation for the Taupo ignimbrite, p_{in} and R are set to 39 MPa and 700 m, respectively. As with the case of the Taupo plinian eruption, the initial pressure is less than the lithostatic pressure (98 MPa), while the conduit radius is comparable with the previously estimated value of 500-600 m by *Legros et al.* (2000).

The distribution of velocities and the profile of pressure are shown in Fig. 6.2. The horizontal distributions of vertical velocity, temperature, viscosity, and void fraction in the near-wall zone are plotted in Fig. 6.3. As in the case for the Taupo plinian, the velocity profile evolves into a plug shape as the magma ascends in the conduit. A striking feature of the simulation for the Taupo ignimbrite is the timing at which the velocity profile changes from a parabolic to plug-like shape. In the case for the Taupo plinian, the velocity profile changes just above the conduit inlet (Fig. 4.8a), but in the case for the Taupo ignimbrite, it changes at around $z/z_f = 0.3$. This difference significantly affects bubble deformation inside the conduit.

6.3.2 Bubble deformation in a viscous-heating flow

Using the results of the conduit flow simulation for the Taupo ignimbrite, I calculate the deformation of a bubble inside the conduit. The calculation method is the same as the simulation for the Taupo plinian.

Streamlines for the Taupo ignimbrite are shown in Fig. 6.4a. When the velocity profile changes from a parabolic to a plug shape at $z \sim 1000$ m, the streamlines bend to the conduit wall. The radial distributions of bubble shapes are shown in Fig. 6.4b. The bubbles around the conduit walls are always more elongated than in the conduit center. An important point is that the evolution of bubble shape is not monotonous. Fig. 6.5 shows

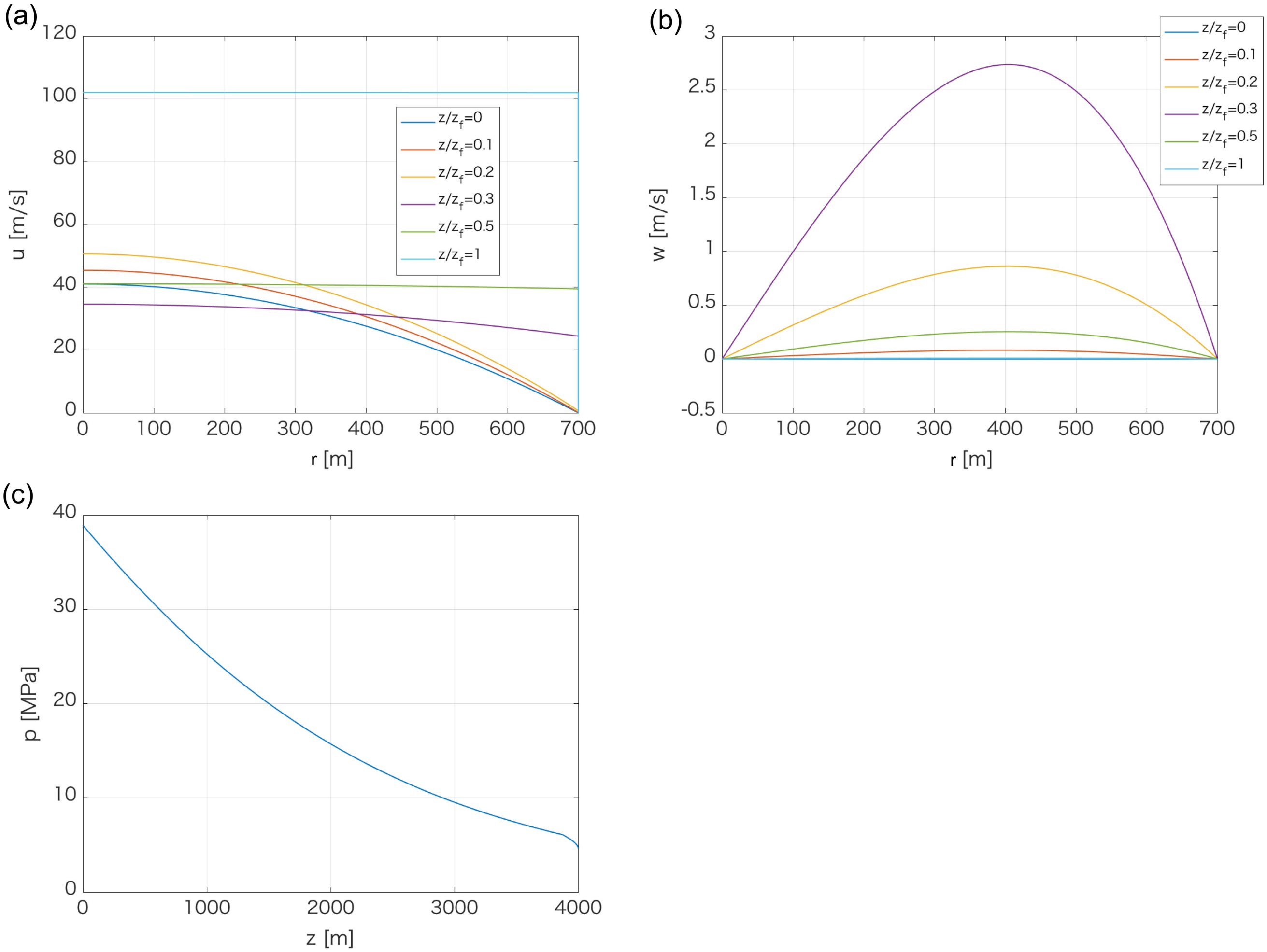

Figure 6.2: The calculation results of the Taupo ignimbrite based on the viscous-heating model. (a) Vertical velocity distribution across the conduit at $z/z_f = 0$, 0.005, 0.001, 0.1, 0.5, 1. The fragmentation surface is 3874 m. (c) Horizontal velocity distribution. (c) Pressure profile along with the conduit axis.

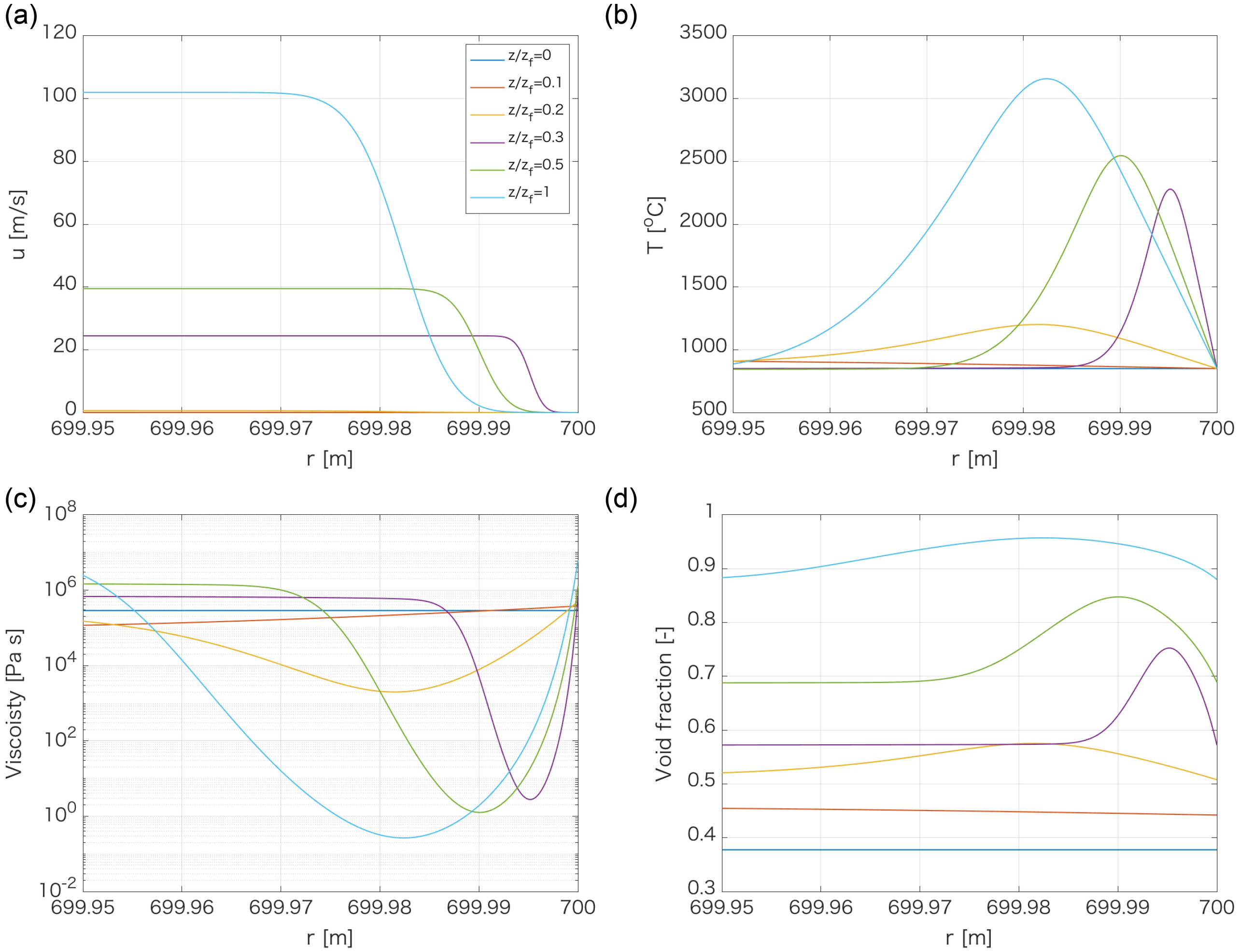

Figure 6.3: The horizontal distribution of the Taupo ignimbrite in the near-wall region. (a) Vertical velocity. (b) Temperature. (c) Viscosity. (d) Void fraction.

the vertical evolution of bubble shape as a function of the initial bubble position. All bubbles repeat elongation and relaxation, depending on the initial position.

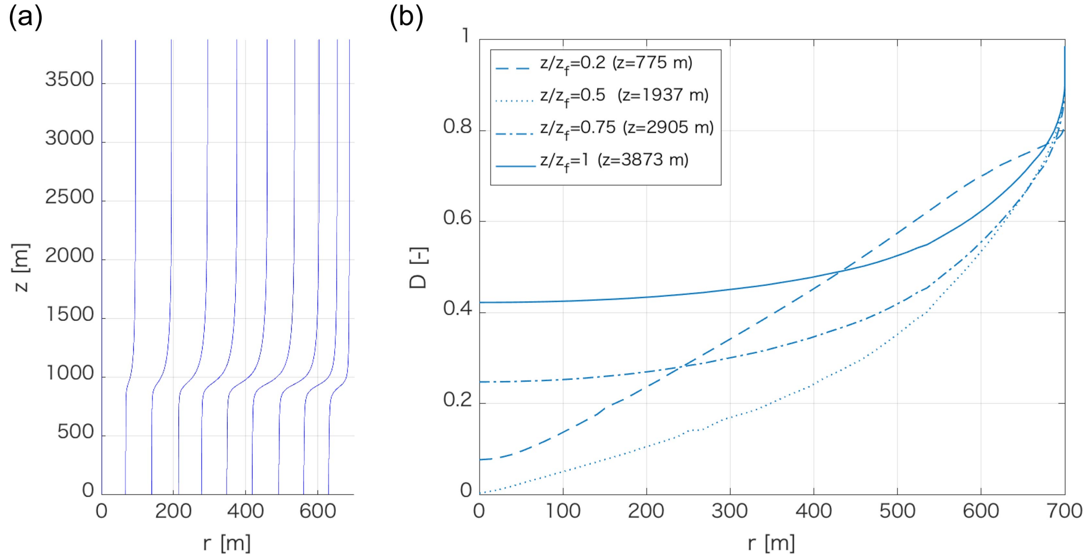

Figure 6.4: (a) Streamlines for the Taupo Ignimbrite. (b) The radial distribution of the bubble shapes at each depth.

In order to understand the complex evolution of bubble shape, I investigate the components of the velocity gradient tensor L_{ij}^{∞}. The evolution of L_{ij}^{∞} starting from the conduit center is shown in Fig. 6.6a. This bubble does not have a simple shear component by the symmetry boundary condition. The velocity gradient tensor comprises the diagonal components of $\frac{\partial u}{\partial z}$ and $\frac{\partial w}{\partial r}$. Decompression along the conduit accelerates the bubbly magma, resulting in a positive value of $\frac{\partial u}{\partial z}$. When the velocity profile collapses into a plug shape, the magma near the conduit center shrinks vertically and bubbles in it elongate in oblate. This bubble elongation has a peak around $z = 1000$ m where the velocity profile transforms into a plug shape. Above the transition of the velocity profile, the bubble starts to elongate vertically in prolate because of pure shear due to the magma acceleration. When the laterally flattened bubble starts to elongate vertically, the bubble deformation degree once decreases apparently. Then it increases again, reflecting a prolate shape along the pure shear direction.

The evolution of L_{ij}^{∞} along another bubble trajectory starting around the conduit wall ($r_i = 600$ m) is shown in Fig. 6.6b. Contrary to the previous case, the bubble deforms by simple shear ($\frac{\partial u}{\partial r}$) as well as pure shear. Therefore it shows large D. In addition to simple shear, the formation of the plug flow results in not decreasing but increasing $\frac{\partial u}{\partial z}$ in the positive direction. In summary, at the transition to the plug-like flow, bubbles around the conduit center elongate laterally, while those around the conduit walls elongate vertically.

A key point of bubble deformation of the Taupo ignimbrite event is that the transition of the velocity profile occurred after ascending in the conduit for a while. Initial bubble deformation in the parabolic velocity profile was not completely overwritten by the plug-like velocity profile, but continued to affect the final shape at the fragmentation surface. Bubbles around the conduit walls elongated longer than inside because of simple shear

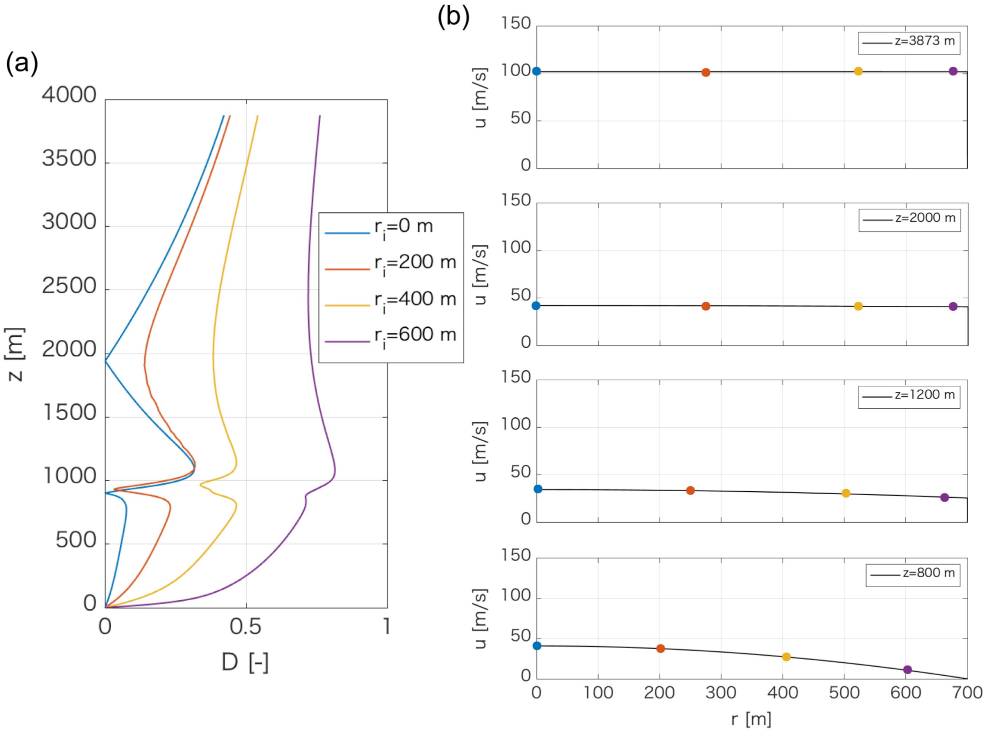

Figure 6.5: (a) The vertical evolutions of bubble shape for the Taupo ignimbrite event. The color indicates the initial position of the bubble at the conduit inlet. (b) The velocity profile across the conduit. The color indicates the position of the corresponding bubble which is plotted in (a).

component and vertical elongation during the transition of the velocity profile.

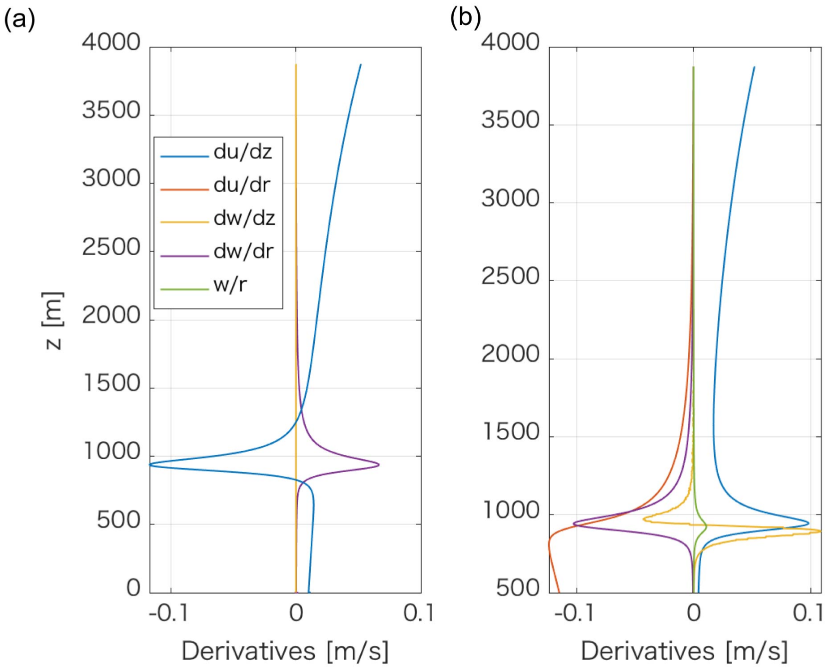

Figure 6.6: The vertical evolution of the components of the velocity gradient tensor L_{ij}^{∞} for the bubble starting from (a) $r_i = 0$ and (b) $r_i = 600\ \mathrm{m}$.

6.3.3 Comparison the simulation result with the natural bubble texture

Finally, I calculate the flux of the bubble deformation degree at the fragmentation surface by using Eq. (4.40). Blue histogram in Fig. 6.7 shows the normalized flux of bubble shape at the fragmentation surface. Contrary to the Taupo plinian event, the simulation based on the viscous-heating model provides a wide distribution of bubble shape. Less elongated bubbles with $D \approx 0.4$ were erupted from the conduit center, while those with $D \sim 0.8$ were from the region close to the conduit wall. Because the radial change of bubble shape is steep around the conduit wall (Fig. 6.4b), the histogram of bubble shape has a peak at $D = 0.43$ which came from the inner conduit.

Red histogram in Fig. 6.7 shows the histogram of D_{R2} for the Taupo ignimbrite. Although the histogram of the numerical bubble shapes does not exactly overlap with that of the natural bubble shapes, it captures the qualitative features of the wide distribution including highly elongated bubbles. This result suggests that the increase of tube pumice in the Taupo ignimbrite was caused by the shallower transition of the velocity profile from parabolic to plug-like.

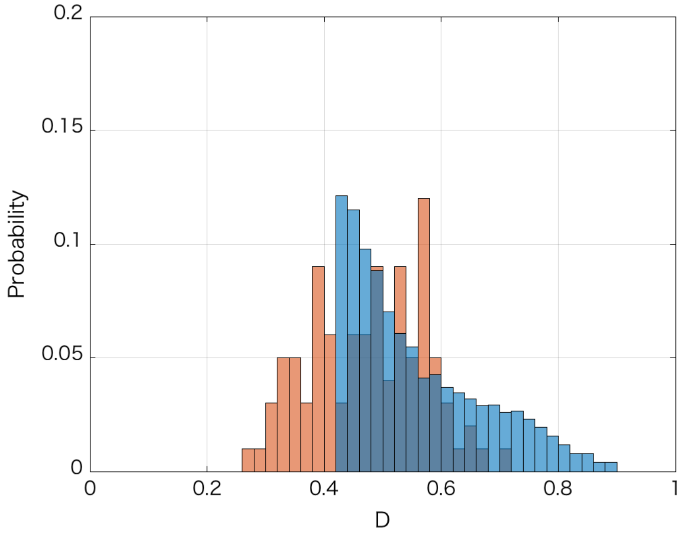

Figure 6.7: The histogram of bubble shapes for the Taupo ignimbrite. Blue histogram represents the numerical bubble shape. Red histogram represents D_{R2}. The vertical axis is normalized. The gap of D is 0.02.

6.4 Discussion

6.4.1 Transition from a parabolic to plug-like shape

The simulation of the Taupo ignimbrite suggests that the transition of the velocity profile significantly changes the shear field and affects bubble deformation within a conduit. The velocity profile of viscous-heating flow has been investigated in detail.

Costa et al. (2007) proposed a regime number to identify the behaviour of the cylindrical conduit flow with radius R and length L. It is defined as

$$\Sigma = \frac{Na}{\sqrt{Gz}} = \frac{b\eta_0}{R}\sqrt{\frac{U_0^3 L}{\rho_0 \kappa c_V}} \tag{6.1}$$

where Na is the non-dimensional Nahme number, Gz is the non-dimensinoal Graetz number, η_0 is the initial viscosity, b is the coefficient of the viscosity dependency with temperature at a reference temperature of T ($b = \frac{1}{\eta_0}\left(\frac{d\eta_0}{dT}\right)_T$), Q_m is the mass discharge rate, U_0 is the initial mean vertical velocity which is defined as $U_0 = Q_m/(\rho_0 \pi R^2)$, ρ_0 is the initial density, κ is the thermal conductivity, c_V is the heat capacity. Large Σ means that a conduit flow is dominated by viscous-heating and has a plug-like velocity profile. On the other hand, small Σ means that a conduit flow is characterized by conductivity heat loss and has a parabolic velocity profile.

Since *Costa et al.* (2007) assumed an incompressible magma with constant density, the density and the mean velocity are constant throughout the conduit. In addition, the water concentration dissolved in the melt was assumed to be constant for the computational reason. Here, I extend the regime number to evaluate the behaviour of the compressible viscous flow at each depth in the conduit. The extended regime number Σ_E is defined as

$$\Sigma_E = \frac{b(c,T)\eta(c,T)}{R}\sqrt{\frac{U^3 L}{\rho(c,T,p)\kappa c_V}}, \tag{6.2}$$

$$= \frac{b(c,T)\eta(c,T)}{R}\sqrt{\frac{Q_m^3 L}{\pi^3 \rho(c,T,p)^4 R^6 \kappa c_V}}. \tag{6.3}$$

The viscosity sensitivity b, melt viscosity η, and bulk density ρ are the values at the conduit center. These parameters are given at each depth in the conduit, depending on the water concentration, temperature, and pressure.

Fig. 6.8 shows the variations of Σ_E for the Taupo plinian event and the Taupo ignimrbite event. The extended regime number for the Taupo plinian is always larger than that for the Taupo ignimbrite by an order of magnitude. Fig. 6.8 indicates that the conduit flow of the Taupo plinian is significantly affected by viscous heating and easily evolves into the plug-like velocity profile. The difference of Σ_E can be explained by the size of conduit radius. Most of the parameters used in Eq. (6.3) are in the same order of magnitude except for the conduit radius which differs by an order of magnitude ($R = 33$ m for the Taupo plinian and $R = 700$ m for the Taupo ignimbrite). In the 1.8 ka Taupo eruption, the change of conduit radius may have controlled not only the significant variation of mass discharge rate but also the velocity profile.

The effect of the conduit radius on viscous-heating is intuitively explained by the shear strain rate at the conduit wall. The shear strain rates at the wall just above the inlet were $\frac{\partial u}{\partial r} = 4.2\ \mathrm{s}^{-1}$ for the Taupo plinian eruption and $\frac{\partial u}{\partial r} = 0.12\ \mathrm{s}^{-1}$ for the Taupo ignimbrite eruption. The shear strain rate in the Taupo ignimbrite eruption was smaller than the Taupo plinian eruption by an order of magnitude. Therefore, the conduit flow experienced a weak viscous-heating which suppressed the transition of the velocity profile

6.4.2 Simulation results with the different bubble number densities

In chapter 4, I showed the simulation results of bubble deformation in the conduit flow of the Taupo plinian eruption. Because I focus on bubble shape (i.e., bubble deformation degree), I did not explain much about bubble radius at the fragmentation surface. Regardless of the model, bubble radius at the fragmentation is about $10\ \mu\mathrm{m}(= 0.1\ \mathrm{mm})$ (Figs. 4.13, 4.14, 4.18). This value is one order of magnitude smaller than the bubble radius which I analyzed in chapter 5 ($R_b > 0.15$ mm). The bubble radius is calculated from the bubble volume (Eq. 4.26) as a function of vesicularity ϕ and bubble number density N_b. Although $N_b = 10^{15}\ \mathrm{m}^{-3}$ is from the textural analysis of *Houghton et al.* (2010), I can conveniently obtain the simulation results with large bubble radius by inputting smaller N_b values.

Here, I show the simulation results with the different bubble radius.

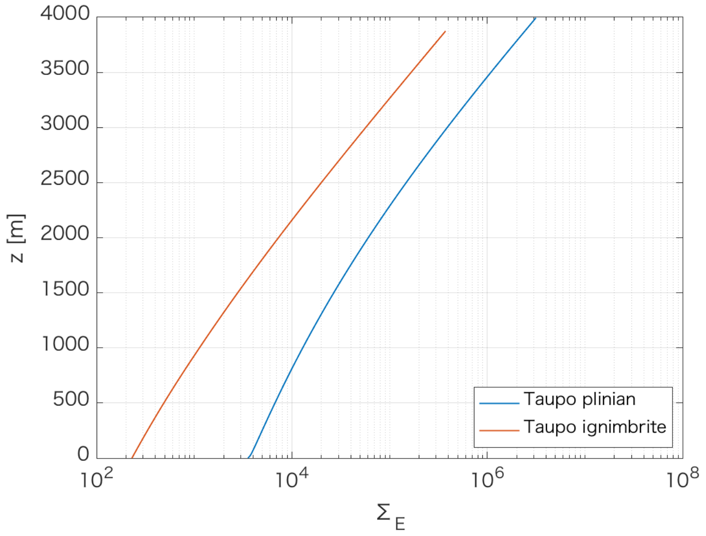

Figure 6.8: Vertical variation of the extended regime number for the Taupo plinian (blue) and the Taupo ignimbrite (red).

Case1: Newtonian isothermal model

Fig. 6.9 shows the simulation results based on the Newtonian isothermal model. Line types indicate the different N_b values. The bubble radius and the capillary number increase with decreasing N_b (Fig. 6.9a and b). For $N_b = 10^{11}\ \mathrm{m}^{-3}$, the bubble radius at the fragmentation surface is as large as the radius that I analyzed in chapter 5. The bubble deformation degrees for $N_b = 10^{13}\ \mathrm{m}^{-3}$ and $10^{11}\ \mathrm{m}^{-3}$ are slightly more elongated than for $N_b = 10^{15}\ \mathrm{m}^{-3}$, but the distribution of D does not change largely. Highly elongated bubbles occupy most of the area at the fragmentation surface.

Case2: Shear-thinning model due to bubble deformation

Fig. 6.10 shows the simulation results based on the shear-thinning model due to bubble deformation. As with Fig. 6.9, highly elongated bubbles occupy most of the area.

Case3: Viscous-heating model

Fig. 6.11 shows the simulation results based on the viscous-heating model. Contrary to the previous models, the radial distributions of D at the fragmentation surface are different, depending on the bubble number density N_b (Fig. 6.11c). The D value around the conduit wall increases with the increase in R_b (i.e., the decrease in N_b). This difference was caused by decreasing the shape relaxation after the transition of the velocity profile. Bubbles were largely deformed just above the conduit inlet because the velocity profile collapsed to a plug-like shape (Fig. 6.11b). After the velocity profile became a plug-like shape, the shear field around a bubble ceased. The bubbles started to return to a spherical shape until the magma accelerated sufficiently.

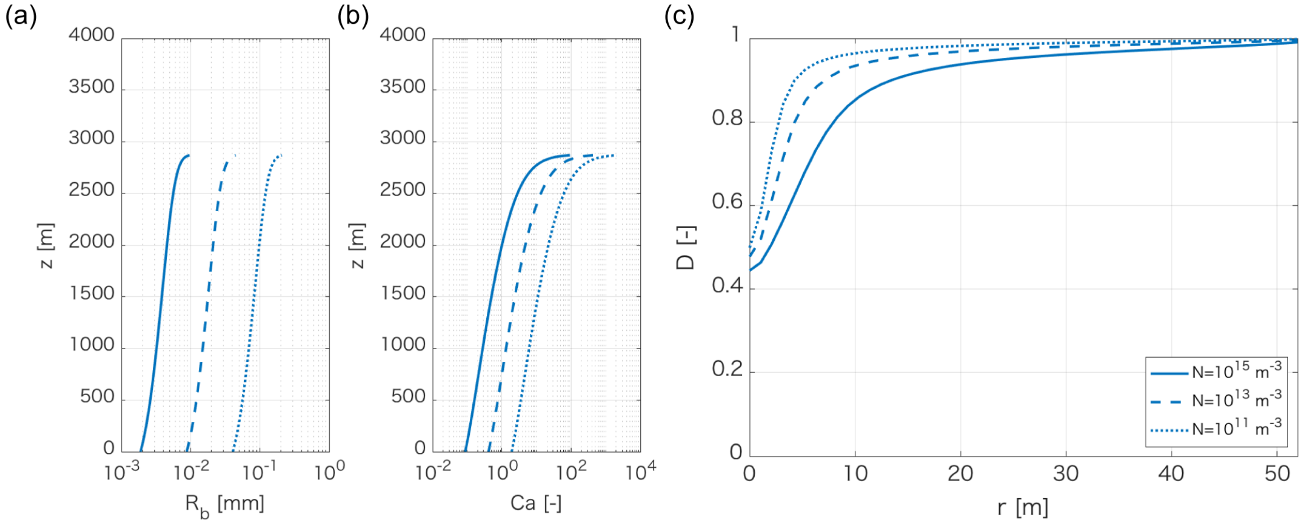

Figure 6.9: The calculation results of the Newtonian isothermal model. (a) Bubble radius. (b) Capillary number of a bubble starting from $r_i = 16$ m (c) Horizontal distribution of D at the fragmentation surface. Solid, dashed, and dotted lines are $N_b = 10^{15}$ m^{-3}, 10^{13} m^{-3}, and 10^{11} m^{-3}, respectively.

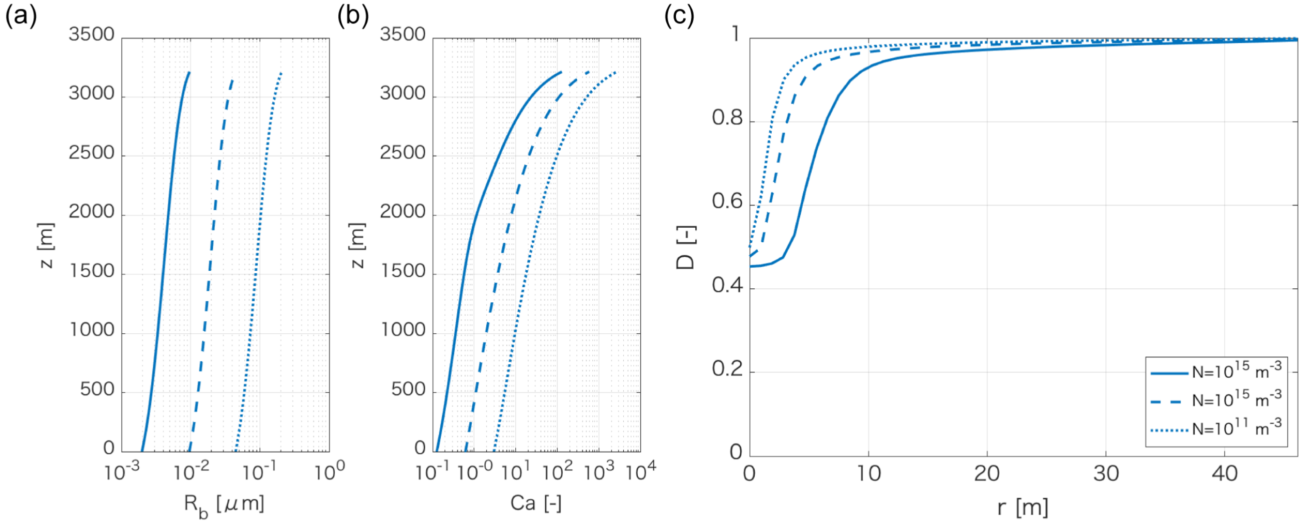

Figure 6.10: The calculation results of the shear-thinning model due to bubble deformation. (a) Bubble radius. (b) Capillary number of a bubble starting from $r_i = 16$ m (c) Horizontal distribution of D at the fragmentation surface. Solid, dashed, and dotted lines are $N_b = 10^{15}$ m^{-3}, 10^{13} m^{-3}, and 10^{11} m^{-3}, respectively.

The relaxation process is largely controlled by the timescale of shape relaxation $\tau_{visco} = \frac{R_b \eta}{\Gamma}$. Fig. 6.12 shows the vertical evolution of Ca and τ_{visco}. The timescale of shape relaxation increased as the magma ascend in the conduit because the viscosity increased due to water exsolution. For the result with $N_b = 10^{15}\ \mathrm{m}^{-3}$, τ_{visco} is quite small above the conduit inlet ≈ 1 s. This range of τ_{visco} is small enough to relax a bubble shape, given that the magma reached the fragmentation surface in about 70 seconds. On the other hand, τ_{visco} is comparable with the ascending time if $N_b = 10^{11}\ \mathrm{m}^{-3}$. Therefore, those large bubbles do not relax and keep highly elongated shapes until the fragmentation surface.

The simulation results in this section showed that the large bubble kept the highly elongated shape because of the long timescale of shape relaxation. In this thesis, I was not able to find a numerical solution that explains both the bubble deformation degree and the bubble size of the natural observation. In order to overcome this problem, I first need to improve the calculation method of the bubble radius. In the simulations, the bubble radius is given by Eq. (4.26) that assumes a constant bubble number density during bubble growth. However, strictly speaking, this assumption is not realistic because of bubble coalescence. If it occurs, the bubble number density at nucleation is larger than that of pumice, leading to a small bubble radius in the lower part of the conduit flow. I also require an accurate initial pressure. Due to the strong viscous heating around the conduit walls, the initial pressure used in this appendix ($65\ \mathrm{MPa}$) is smaller than the lithostatic pressure ($98\ \mathrm{MPa}$). If it is equal to the lithostatic pressure, the bubbles at the conduit inlet become smaller than the current estimated value. Those small bubbles will relax instantaneously after the velocity profile evolved into a plug-like shape and will deform only by pure shear caused by magma acceleration.

In summary, in order to calculate the bubble size correctly, it is required to incorporate bubble coalescence and to resolve the problems of strong viscous heating discussed in section 4.6.2. Although the bubble in the viscous-heating model is smaller than the natural observation, I think that the present calculation results give the important implication to bubble deformation from the viewpoint of the velocity profile.

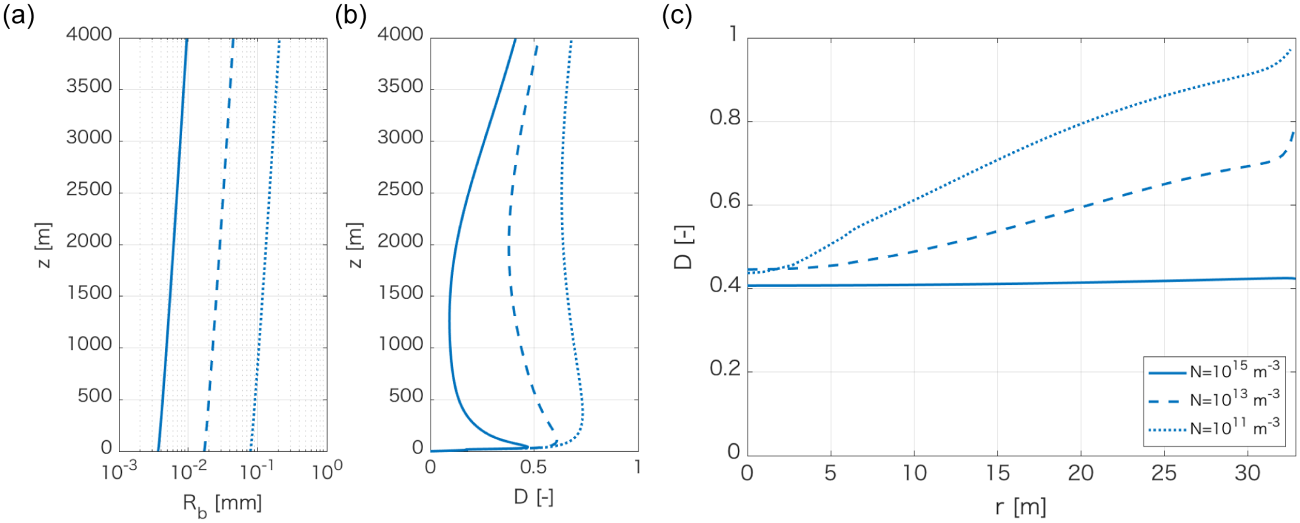

Figure 6.11: The calculation results of the viscous-heating model. (a) Bubble radius. (b) Deformation degree of a bubble staring from $r_i = 10$ m. (c) The radial distribution of D at the fragmentation surface.

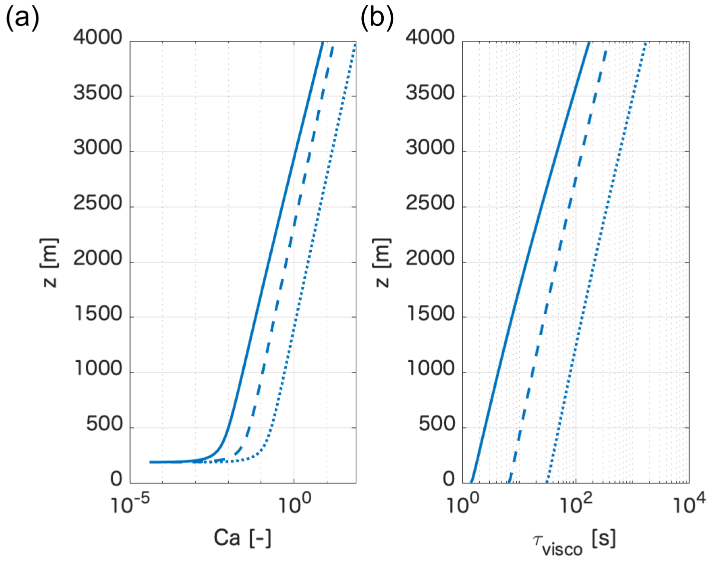

Figure 6.12: The vertical evolution of the capillary number Ca and the timescale of shape relaxation τ_{visco}. (a) The capillary number of a bubble starting from $r_i = 10$ m. I use $\frac{2}{3}\frac{\partial u}{\partial z}$ as the strain rate of pure shear. (b) The timescale of shape relaxation of the same bubble as (a). Solid, dashed, and dotted lines are $N_b = 10^{15}\ \mathrm{m}^{-3}$, $10^{13}\ \mathrm{m}^{-3}$, and $10^{11}\ \mathrm{m}^{-3}$, respectively.

Chapter 7

Discussion

7.1 Introduction

The main aim of this thesis, which was noted in the introduction chapter, was to identify the mechanism of forming tube pumice and estimate strain and strain rate during bubble deformation. By the combination of the bubble deformation model, the tensile tests, and the conduit flow models, I identify that bubble deformation during the 1.8 ka Taupo eruption was mainly controlled by the velocity profile across the conduit. Less elongated bubbles in the Taupo plinian were deformed in the plug-like velocity profile in which pure shear dominates. Highly elongated bubbles, which will become tube pumice after the fragmentation, reflected the simple shear deformation during the parabolic velocity profile.

This chapter provides the estimation method of strain and discusses the implications for volcanic phenomena. Section 7.2 describes the acquired strain during pure shear. In section 7.3, I discuss the importance of viscous heating in explosive eruptions. Finally, in section 7.4, some implications for the volcanic phenomena are discussed.

7.2 Strain during pure shear deformation

In this section, I discuss bubble deformation in pure shear flow. Bubble deformation in the Taupo plinian is tractable as the inverse problem because bubbles inside the conduit flow were deformed in mostly pure shear.

In the following subsections, I first derive the analytical expression of pure shear strain caused by bubble growth, and then estimate the strain from the distribution of the observed bubble deformation degree D in a pumice clast. Finally, I explain the meaning of the strain estimated from the bubble shape.

7.2.1 Analytical study of bubble deformation in pure shear

Here, I derive a strain of pure shear analytically. I assume the conduit flow with a plug-like velocity profile and no lateral velocity. The velocity gradient in the conduit center L_{ij} can be written as,

$$L_{ij} = \begin{pmatrix} \frac{\partial u}{\partial z} & 0 & 0 \\ 0 & 0 & 0 \\ 0 & 0 & 0 \end{pmatrix}. \tag{7.1}$$

Keep in mind the absence of the horizontal velocity gradient $\frac{\partial u}{\partial r} = 0$. It is decomposed into two components:

$$L_{ij} \quad = \quad L_{ij}^{Vol} + L_{ij}^{pure}, \tag{7.2}$$

where

$$L_{ij}^{Vol} = \dot{\gamma}_{volume} \begin{pmatrix} \frac{1}{3} & 0 & 0 \\ 0 & \frac{1}{3} & 0 \\ 0 & 0 & \frac{1}{3} \end{pmatrix}, \quad \dot{\gamma}_{volume} = \frac{\partial u}{\partial z}, \tag{7.3}$$

$$L_{ij}^{pure} = \dot{\epsilon} \begin{pmatrix} 1 & 0 & 0 \\ 0 & -\frac{1}{2} & 0 \\ 0 & 0 & -\frac{1}{2} \end{pmatrix}, \quad \dot{\epsilon} = \frac{2}{3}\frac{\partial u}{\partial z}, \tag{7.4}$$

where L_{ij}^{Vol} and L_{ij}^{pure} represent the volumetric and extensional deformation rates, respectively, and $\dot{\gamma}_{volume}$ and $\dot{\epsilon}$ are the volumetric strain rate and pure shear rate, respectively.

The volumetric strain rate is defined by

$$\dot{\gamma}_{volume} = \frac{1}{\delta V}\frac{d\delta V}{dt}, \tag{7.5}$$

where δV is the volume of the liquid-gas mixture. The cumulative volume strain γ_{volume} that a bubble experiences from time t_1 to t_2 is

$$\gamma_{volume} = \int_{t_1}^{t_2} \dot{\gamma}_{volume} dt, \tag{7.6}$$

where t is time. Denoting the values of δV and the gas volume fraction at time t_i by δV_i and ϕ_i, respectively, the conservation of liquid volume requires that

$$\delta V_1(1-\phi_1) = \delta V_2(1-\phi_2). \tag{7.7}$$

Substituting Eq. (7.5) to Eq. (7.6) and using Eq. (7.7), I can calculate γ_{volume} as

$$\gamma_{volume} = \int_{\delta V_1}^{\delta V_2} \frac{d\delta V}{\delta V} = \ln\left(\frac{\delta V_2}{\delta V_1}\right) = \ln\left(\frac{1-\phi_1}{1-\phi_2}\right). \tag{7.8}$$

According to Eq. (7.3) and Eq. (7.4), the pure shear strain ϵ is related to γ_{volume} by

$$\epsilon = \frac{2}{3}\gamma_{volume} = \frac{2}{3}\ln\left(\frac{1-\phi_1}{1-\phi_2}\right). \tag{7.9}$$

Fig. 7.1 shows ϵ for $\phi_1 = 0$ and ϕ_2 as a variable ϕ.

For the Taupo eruption, I want to estimate the pure strain from the conduit inlet to the fragmentation surface. Assuming that the pressure at the inlet is equal to the lithostatic pressure (98 MPa), I set $\phi_1 = 0.032$ according to Eq. (4.9). For ϕ_2, I use the average vesicularity in the Taupo plinian deposits, that is $\phi_2 = 0.788$. Then, the strain is estimated to be $\epsilon \sim 1.0$.

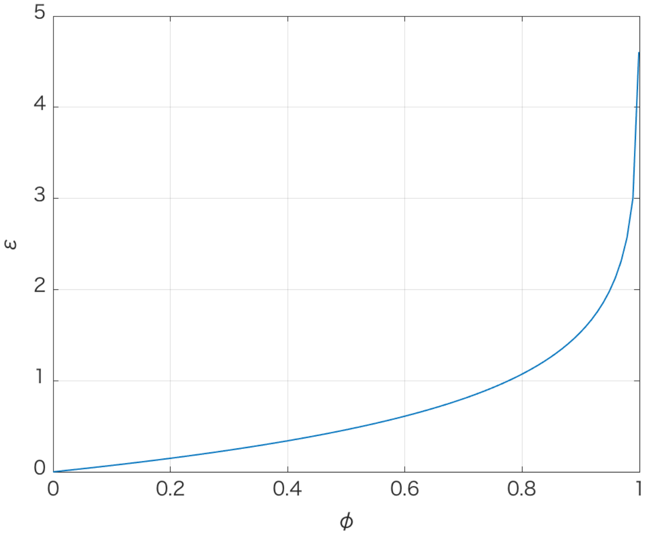

Figure 7.1: The strain of pure shear as a function of gas volume ratio. For the simplicity, ϕ_1 is set to 0.

7.2.2 Estimation of strain from the distribution of D in a pumice clast

In section 2.5, I estimated strain and strain rate from the published data of bubble shapes within an obsidian clast. Using the similar method, I try to estimate strain from bubble shapes preserved in a pumice clast erupted from the 1.8 ka Taupo eruption.

Fig. 7.2a shows the typical relationship between bubble deformation degree and bubble radius in pumice from the Taupo plinian deposit. Using the simulation result of the MJT model, I estimate strain during bubble deformation. The numerical simulation of bubble deformation in the conduit implied that the bubble in the Taupo plinian event was mainly deformed by pure shear in the plug-like velocity profile. Fig. 7.2b shows the temporal evolution for D under a constant pure shear rate. As Ca increases, D depends only on strain ϵ. As with the case of simple shear, I assume that $D - \epsilon$ curves collapses into a single master curve at $Ca > 5$. By comparing the deformation limit ($D = 0.44$) with the master curve, I obtain the pure strain of 0.46. I emphasize that the estimation of strain does not require the rheology of melt, but uses only the type of shear filed (simple or pure shear).

As discussed in Fig. 5.14, small bubbles measured by the low resolution X-ray CT might have been over-segmented because of the CT noises. Fitting the calculation result of the MJT model to the distribution of D needs the increase of D in the range of small bubble radius (i.e., small Ca), and thus, I cannot estimate the strain rate from the bubble shapes in pumice. High resolution computed tomography in a synchrotron radiation may allow us to measure accurate shapes of small bubbles and estimate strain rate.

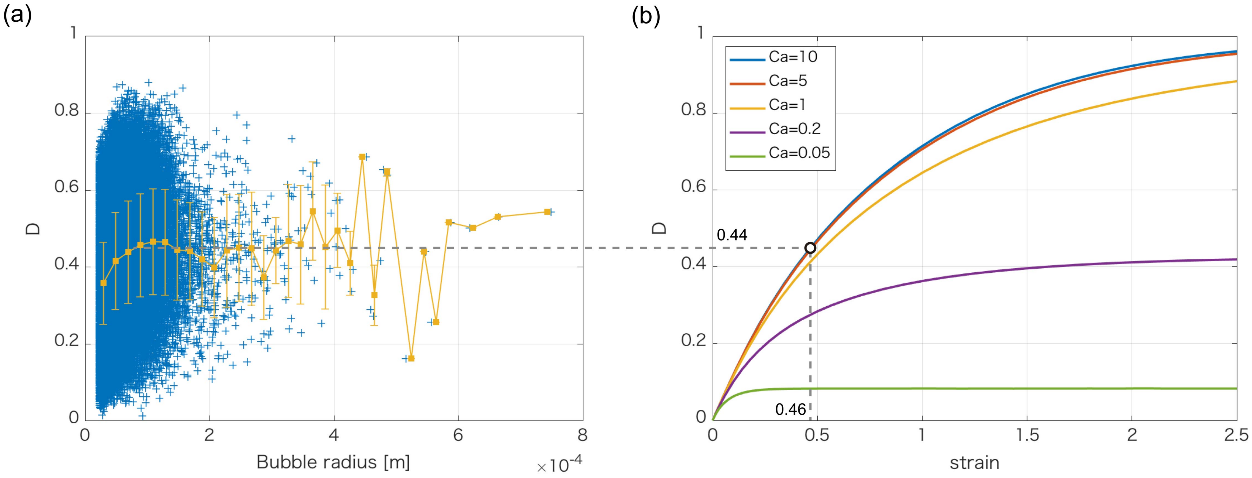

Figure 7.2: (a) Degree of bubble deformation D as a function of bubble radius R_b for the pumice clast from the Taupo plinian event (sample 09_04: Fig. 5.13f). The bubble shapes were measured by the low resolution X-ray CT. As bubble radius increases, D approaches a maximum value that is much less than 1 ($D \approx 0.44$) (b) Temporal evolution of bubble shape in pure shear flow, calculated by the MJT model. The dependence of D on Ca becomes negligible for $Ca > 5$. The strains applied to the sample can therefore be estimated from the transient curve at $Ca = 5$.

7.2.3 Meaning of strain estimated from vesicularity or bubble shapes

In the previous sections, I estimated pure shear strain during the Taupo plinian event by two ways. The analytical estimation based on the vesicularity yielded $\epsilon = 1.0$, and on the other hand, the estimation using the distribution of D provided the smaller pure strain of $\epsilon = 0.46$. Here, I discuss the different meanings of the estimated strains based on the numerical simulation of the conduit flow model.

Fig. 7.3 summarizes the numerical simulation of bubble shape in the Taupo plinian event. A bubble starting from the conduit center $r_i = 0$ reaches $D = 0.41$ at the fragmentation surface (Fig. 7.3b). This bubble deformation degree is very close to that within the natural pumice analyzed in Fig. 7.2a. Although the shear filed in the conduit cannot be expressed by only pure shear due to the presence of horizontal velocity, I here conveniently apply $\dot{\epsilon}$ defined for the 1-D flow by Eq. (7.4) and integrate it from the conduit inlet to fragmentation surface to obtain ϵ. It has a negative value at $0 < z < 2500$ m, because $\frac{\partial u}{\partial z}$ is negative when the parabolic velocity profile collapses into a plug shape.

The pure strain as a function of vesicularity (Eq. 7.9) can be considered as 'the maximum strain' which

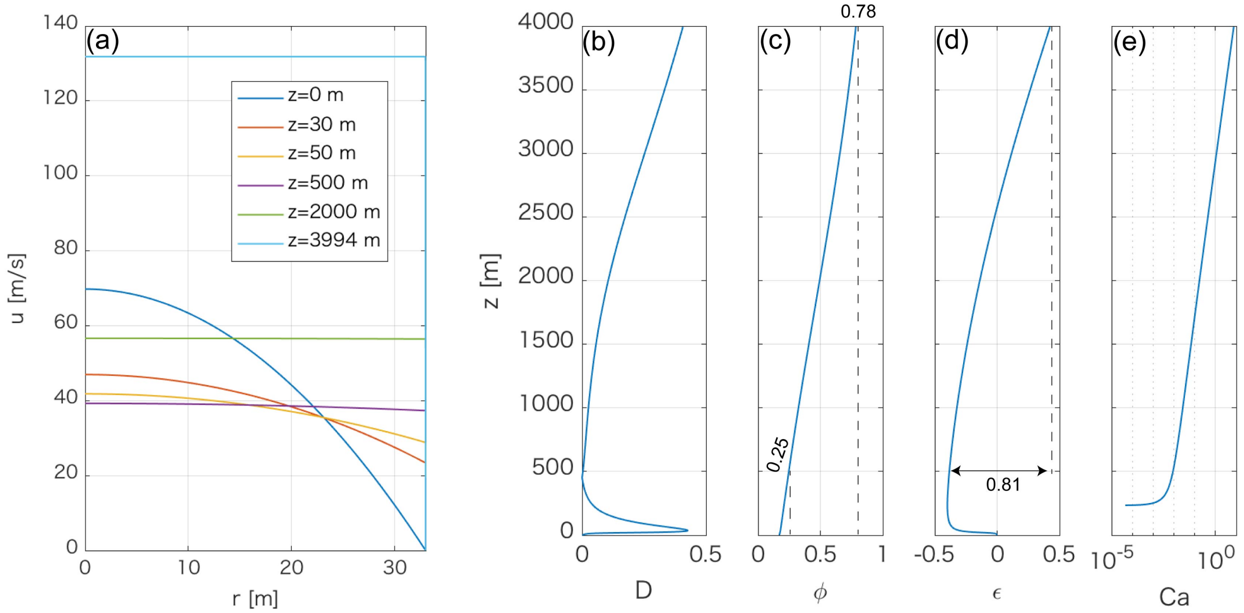

Figure 7.3: (a) Vertical velocity profile of the Taupo plinian event based on the viscous-heating model. (b-e) Vertical variations for a bubble starting from $r_i = 0$. (b) Deformation degree. (c) Vesicularity. (d) Pure strain. (e) Capillary number. I use $\frac{\partial u}{\partial z}$ as the pure strain rate.

takes account only of magma acceleration. In the lower part ($z < 500$ m), the shear filed is largely affected by the transition of the velocity profile, and Eq. (7.9) cannot be used. However, the shear filed in the upper part ($z > 500$ m) is composed only of pure shear, and therefore Eq. (7.9) can be used. In the upper part, the vesicularity increases from $\phi = 0.25$ to 0.78. Using Eq. (7.9), I estimate the pure strain acquired in the upper part:

$$\epsilon = \frac{2}{3}\ln\left(\frac{1-0.25}{1-0.78}\right) = 0.82. \tag{7.10}$$

The integration of $\dot{\epsilon}$ from $z = 500$ m to z_f gives a similar value of $\epsilon = 0.81$. This result indicates that the estimation based on vesicularity well reflects the pure shear filed around a bubble.

On the other hand, the pure strain estimated from the distribution of D within a pumice can be considered as 'the minimum strain'. In Fig. 7.2b, I used the $D - \epsilon$ curve under a constant capillary number of $Ca = 5$, but the capillary number of a bubble in the conduit varies as the magma ascends in a conduit (Fig. 7.3e). The bubble, which was deformed in low capillary number ($Ca < 5$), would be less elongated than that in high capillary number ($Ca \geq 5$). Therefore, the pure strain estimated the distribution of D is smaller than the true strain. In addition, this estimation method neglects the effects which return an elongated bubble to a spherical one, such as bubble growth.

We should keep in mind that pure strains estimated by either the vesicularity or the distribution of D have the different meanings. However, the point is that the pure strains are much smaller than the simple shear strains in the parabolic velocity profile ($\gamma \sim 10 - 1000$ in Fig. 4.13g). This information gives us many insights into the eruption dynamics, such as fragmentation and outgassing. This problem will be discussed in section 7.4.

7.3 Viscous heating in explosive eruption

One of the main conclusions of this thesis is that the bubble shapes in pumice support the occurrence of viscous heating in the 1.8 ka Taupo eruption. Viscous heating so far has been investigated from numerical, experimental, and geological approaches.

Most of conduit flow models, which have been developed especially for explosive eruptions, are one dimensional, assuming a parabolic velocity profile across a conduit. This velocity profile is derived from the Hagen - Poiseuille solution for a steady flow in a pipe and is only valid for an incompressible fluid with constant Newtonian viscosity. Because the viscosity of magma strongly depends on its temperature as well as volatile content and composition, the validity of a parabolic velocity profile needed to be confirmed. Numerical simulations including temperature-dependent viscosity and viscous heating have shown that the velocity profile can evolve from parabolic to plug-like with a thermal diffusion layer around conduit walls (*Costa and Macedonio*, 2002; *Barmin et al.*, 2004; *Mastin*, 2005; *Vedeneeva et al.*, 2005; *Costa et al.*, 2007; *Hale and Mühlhaus*, 2007). The thin low viscosity layer drastically decreases the viscous friction, leading to prevent a steep pressure gradient just beneath the fragmentation surface. As a result, the given mass discharge rate is achieved with a narrower conduit with the viscous heating model than with the one-dimensional isothermal model.

Viscous heating has also been investigated by experiments. Using a uniaxial compression apparatus with natural melt, *Hess et al.* (2008) and *Cordonnier et al.* (2012) confirmed that internal viscous dissipation increases temperature and causes the reduction of viscosity.

Although numerical and experimental studies about viscous dissipation have been performed, there have been few geological evidences, especially in the case of explosive eruptions. The 1991 eruption of Mount Pinatubo produced two different pumice types: (1) white pumice (~ 85 vol%) having higher vesicularity, more elongated bubbles, and abundant phenocrysts ($40 - 50$ vol%), (2) gray pumice (~ 15 vol%) having lower vesicularity, less elongated bubbles, and broken phenocrysts (15 vol%). *Polacci et al.* (2001) interpreted that these pumices were formed in the different regions within the conduit; the white pumice formed in the conduit center where the temperature and strain rates were lower, whereas the grey pumice formed near the conduit walls where the temperature and strain rates were higher. Variations of temperature and strain rate were assumed to be the results of viscous heating. The similar pumices were also found at Quilotoa volcano in Ecuador (*Rosi et al.*, 2004). An important common feature of the eruptions at Pinatubo and Quilotoa is that original magma was rich in crystal.

Our study suggests that bubbles preserved in pumices from the Taupo 1.8 ka eruption were deformed in the viscous heating conduit flow with a plug-like velocity profile. As far as I know, this thesis is the first study to show bubble deformation as an evidence of viscous heating in an explosive eruption. I have not identified the pumice that was formed in the thermal layer around the conduit walls. I think finding such pumice in a deposit is difficult if the thermal layer is very thin (5 cm in the Taupo plinian eruption, Fig. 4.9).

7.4 Implications for volcanic phenomena

7.4.1 Degassing

Degassing of vesiculated magma, which is defined as the formation of a permeable network through shear deformation, is a key factor in controlling explosive-effusive transition. Recent experimental studies showed that the generation of permeable bubble and fracture networks drastically increases magma permeability (*Okumura et al.*, 2008, 2013; *Caricchi et al.*, 2011; *Pistone et al.*, 2013; *Shields et al.*, 2014). These experiments gave us the condition of the permeable network as a function of simple shear strain and bubble or crystal fraction. For example, the torsional experiments by *Okumura et al.* (2009) demonstrated that bubble-bearing magma with $\phi > 0.3$ increases permeability sharply when simple shear strain exceeds 8. *Laumonier et al.* (2011) experimentally showed that degassing occurs in crystal-bearing magma (crystal fraction > 0.5) at lower bubble contents with $\phi = 0.11$ with small simple shear strain ($\gamma = 1.3$). In order to compare the experimental conditions of degassing with the natural settings, simple shear strain in a conduit was calculated based on the assumption of the Poiseuille flow with a parabolic velocity profile (*Okumura et al.*, 2009).

This thesis showed that a parabolic velocity easily shifts into a plug-like velocity profile by viscous heating, depending on the conduit radius. If magma ascends in a narrow conduit like the Taupo plinian eruption, the velocity profile evolves into a plug-like velocity profile. Since most of bubbly magma in the conduit will not be affected by simple shear, degassing will be localized only in the thermal boundary layer. I speculate that the localized degassing will not change the eruption style from explosive to effusive.

We emphasize that the estimation of the velocity profile across a conduit plays an important role in the condition of degassing. The effect of viscous heating around the conduit wall should be investigated in more detail in the future.

7.4.2 Transition from fall to flow activity

Our simulations showed that bubbles in the Taupo ignimbrite event were more deformed than those in the Plinian fall due to the significant simple shear effect before the transition to a plug-like flow (Fig. 6.5). The essential cause of the difference was that I assumed a larger conduit radius for the ignimbrite eruption, which was necessary to explain the huge mass discharge rate. Fig. 7.4 schematically shows the conduit flows for the two eruptions.

The transition from fall to flow activity has been focused on in a few decades and has been investigated for its relationship between bubble texture and lithic content. In the plinian fall deposit of the Minoan eruption, the stratigraphic increase in the relative abundance of tube pumice was observed toward the interlayered ash flow (*Taddeucci and Wohletz*, 2001). This increase of tube pumice was considered as reflecting an increase in shear stress which was caused by the collapsing of conduit walls. The similar stratigraphic change of bubble texture was also observed in the pre-ignimbrite fallout eruption associated with the Campanian Ignimbrite eruption (*Polacci et al.*, 2003). The increased amount of tube pumice is thought to reflect a gradual transition from fallout to ignimbrite, and it was interpreted as a result of increased erosive activity near the conduit wall, or

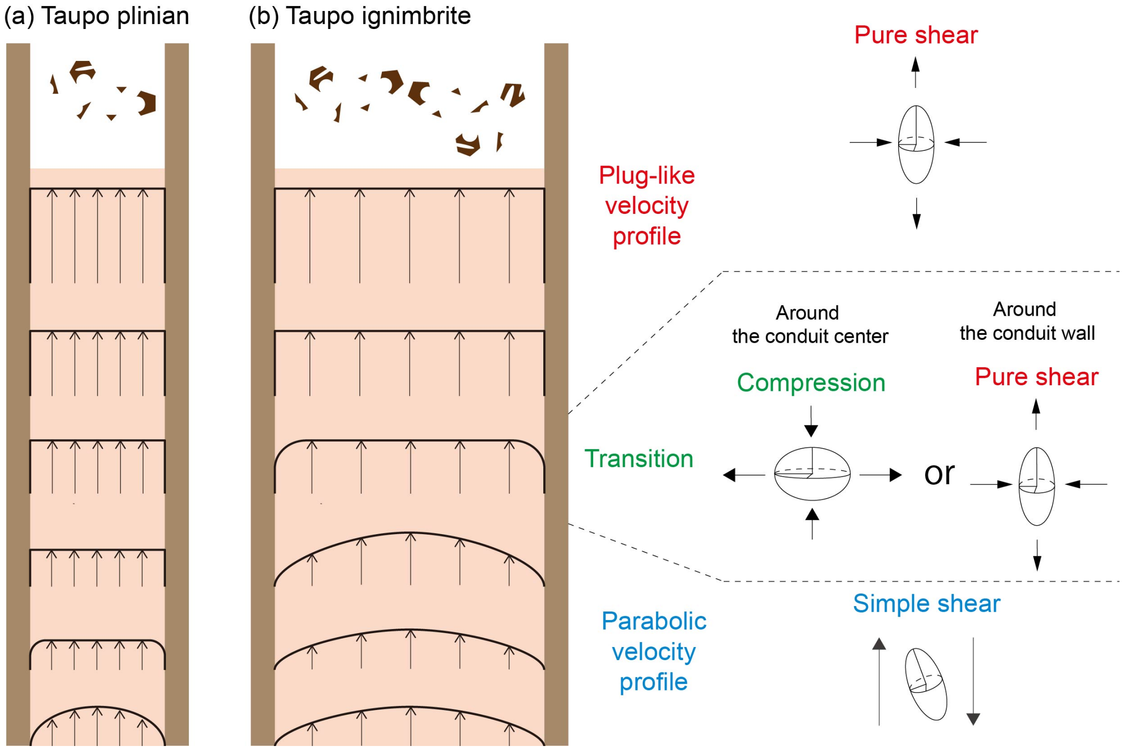

Figure 7.4: Schematic image of a conduit flow for (a) the Taupo plinian event and (b) the Taupo ignimbrite event. Images of bubble deformations in the parabolic velocity profile, the transition, and the plug-like velocity profile are shown on the right side.

a greater conduit area available for shearing. In this fallout deposit, the increase in lithic content toward the ignimbrite was also found together with the increase of tube pumice (Fig. 7.5), suggesting a change in eruptive style resulting from enhanced conduit and vent erosion (*Rosi et al.*, 1999).

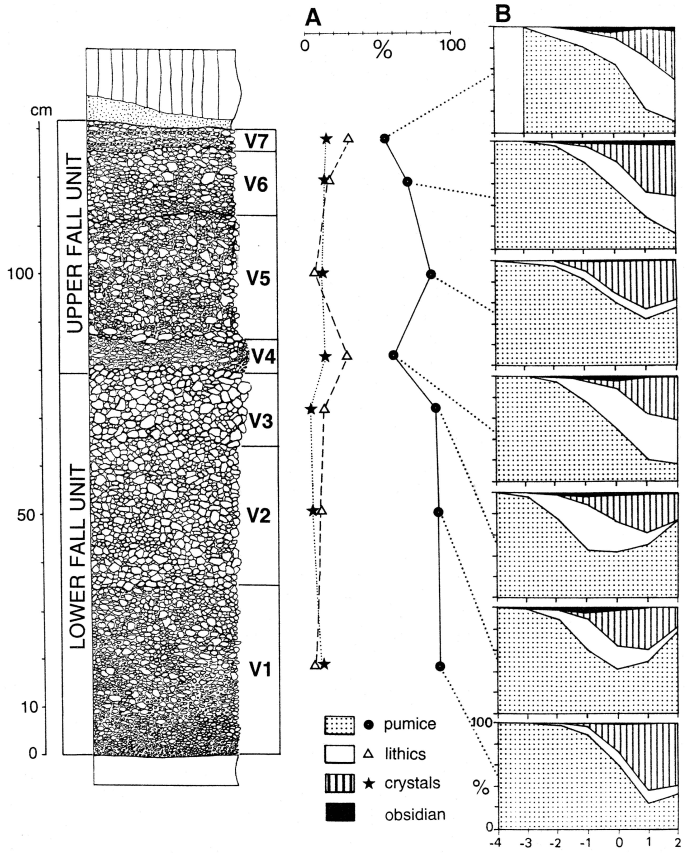

Figure 7.5: Vertical variation of the components of the Campanian Ignimbrite fall deposit (*Rosi et al.*, 1999, Fig. 10). (A) Weight percentage of pumice, accidental lithics and crystals. (B) Their relative portion.

In contrast, the Tapopo plinian deposit (unit 5) shows the relatively gradual variation of lithic contents (Fig. 5.11). Although the lithic content in the upper part (> 160 cm) gradually increases to the ignimbrite, I am not certain whether this lithic increase was related to the onset of ignimbrite formation, because of the small increment of 5 wt.% compared to the other eruption (20 wt.% in the Campanian Ignimbrite eruption).

The transition from fall to flow event in the Taupo eruption was correlated with the drastic increase in the discharge rates from $8 \times 10^4 - 2.4 \times 10^5$ $\mathrm{m^3s^{-1}}$ for the Taupo plinian fall to 3×10^7 $\mathrm{m^3s^{-1}}$ for the Taupo Ignimbrite (*Wilson and Walker*, 1985). *Wilson and Walker* (1985) considered that the abrupt transition from fall to flow was not simply due to gradual vent widening which initiated the collapse of the Taupo plinian column. They suggested that the high eruption rate during the plinian event caused the fragmentation level of the bubbly magma to drop, resulting in a major collapse of the vent walls which greatly widened the vent. However, this idea does not explain the homogeneous vesicularity and bubble texture throughout the plinian fall deposit (Fig. 5.11 and 5.19).

The reason why the eruption activity drastically changes form fall to flow is not yet elucidated. Perhaps, the topmost part of the Taupo plinian deposit in the outcrop had been eroded by and/or mixed with the pyroclastic flow that deposited the subsequent ignimbrite. However, the transition of eruptive behaviour seems to be related to the drastic change in the conduit flow. In this thesis, I theoretically associated the abundance of tube pumice in the Taupo ignimbrite with the conduit enlargement.

7.4.3 Future works

The bubble deformation model in chapter 2 can calculate the large transient deformation in an arbitrary velocity field. The application of the developed model is not restricted to bubbles in pumice but will be extended to other volcanic products.

As shown in section 2.5, I applied the model to the bubbles in obsidians and estimated strain and flow time. The formation mechanism of obsidian is not well understood (*Rust et al.*, 2003; *Rust and Cashman*, 2007). The information concerning strain and flow time during bubble deformation will contribute to the elucidation of the formation mechanism of obsidian. The bubble deformation model can also be applicable to bubbles in lava. Contrary to previous studies (*Coward*, 1980; *Polacci et al.*, 1999), the developed method in chapter 2 has the merit to estimate both strain and strain rate. The information of the shear field of lava will be helpful to clarify the emplacement process and the pāhoehoe-ʻaʻā transition.

Several features are not incorporated into my study that could strongly influence the discussion about tube pumice. First, the conduit model I used is fundamental, leading to the discrepancy between the measured and calculated bubble shapes. The update in the viscous-heating model is required to simulate bubble deformation precisely. In addition, the parameter study for the conduit flow is needed to investigate the discrepancy between the natural observation and the numerical simulation (Fig. 6.1).

Second, the initial velocity pressure should be investigated extensively. In this thesis, the parabolic velocity profile is assumed at the conduit inlet. I think that the assumption of the parabolic shape is basically reasonable because viscous-heating is weak in the shallower part. An incompressible flow with a constant viscosity is known to have a parabolic velocity profile. Regardless of the velocity profile at the conduit inlet, it transitions to a parabolic shape after a short rise. The velocity profile at the inlet can be determined by the geometry of the conduit and the magma chamber, which are not well understood now. The parametric study of the initial velocity profile is required for further study.

Third, I explain bubble shape mainly by deformation of a single bubble, assuming that the effect of bubble interaction can be conveniently neglected by focusing on the average bubble shape. Although the extension test showed the validity of the assumption, it is expected that bubble interactions, including bubble coalescence, vary depending on the type of shear fields (simple vs. pure shear). Simple shear experiments in the wide range of the bubble fraction and the capillary number are needed for further investigation about bubble interaction.

Finally, due to the low spatial resolution of X-ray CT, I could not measure the shape of small bubbles, which are necessary to estimate the strain rate by fitting the theoretical deformation curve. High-resolution X-ray CT in a synchrotron (e.g., Spring8) is required to resolute thin glass walls and measure small bubbles.

Chapter 8

Conclusion

Bubble shape in pumice has been thought to be related to the movement of magma under the fragmentation. The velocity profile of the bubbly flow controls several essential eruption processes, such as degassing and brittle fragmentation. Therefore it is important to explore the possible link between bubble shape preserved in pumice and the velocity profile.

Toward the goal, four different approaches were combined in this study. First, we developed a bubble deformation model by modifying the empirical functions of a deformation model for a liquid droplet proposed by Jackson and Tucker (2003). The new model enables us to calculate the large transient deformation of a single bubble in an arbitrary velocity field.

Second, extension tests with polyurethane foam were performed to comprehend the effect of bubble interaction on its shape. The experimental results indicate that the deformation model of a single bubble can be extended to the average deformation of multiple bubbles ($\phi \approx 0.6$) at least in the range of pure shear strain in the experiments ($\epsilon < 1.5$). This information gives the validity of comparing the average shape of bubbles in pumice with the numerical simulation in a conduit flow.

Third, we calculate the deformation of a bubble in a conduit flow of the 1.8 ka Taupo eruption by applying the bubble deformation model to the quasi-two-dimensional conduit flow model based on Barmin et al. (2004). The simulation results showed that the bubble shape at the fragmentation surface greatly depends on the velocity profile across the conduit. In the Newtonian isothermal model, the parabolic velocity profile kept up to the fragmentation surface. Bubble deformation was dominated mainly by simple shear, and highly elongated bubbles ($D > 0.8$) were produced. In the viscous-heating model, the velocity profile changed from a parabolic to a plug-like shape just above the conduit inlet, because the intense viscous-heating caused a drastic reduction in viscosity around the conduit walls. Bubbles in the plug-like velocity profile were deformed by pure shear, resulting in less elongated shape at the fragmentation surface ($D \approx 0.4$).

Finally, I compared the model results with the natural bubble textures in pumice of the 1.8 ka Taupo eruption in order to discuss the velocity profile of the conduit flow. Bubble shapes in pumices from two plinian eruptions and an ignimbrite were measured by a digital stereo microscope and an X-ray CT scanner. The comparison suggests that the velocity profile at the Taupo plinian eruption was close to a plug-like shape rather than a parabolic shape. Assuming that the conduit flow was affected by viscous-heating, I simulated the bubble deformation in the Taupo ignimbrite eruption. The geological feature that tube pumice increased from the plinian to the ignimbrite eruption was explained by the transition depth at which the velocity profile changed from parabolic to plug-like. Large conduit radius in the ignimbrite eruption weakened viscous-heating, resulting in shallowing the transition depth.

We recognize that there are still some problems which should be solved in the feature. However, I emphasize that this thesis will be helpful in connecting natural bubble textures with the dynamics of explosive eruption.

Appendix A

Full expression of D_{ij}^{*surf}, $D_{ij}^{*slender}$, and D_{ij}^{*axi}

This section describes the abbreviated terms in $L_{ij}^{*Eshelby}$ and $L_{ij}^{*Slender}$ (Eqs. 2.9 and 2.10). First, we explain the rate of the deformation tensor for an ellipsoidal bubble retraction D_{ij}^{*surf}, which *Jackson and Tucker* (2003) define as

$$D_{ij}^{*surf} = -\frac{2q\dot{\gamma}}{\pi Ca}(B_{ijmn}S_{mnkl})P'_{kl}, \tag{A.1}$$

where q is a scalar factor that was introduced to explain the recirculating motion within a droplet, and the value of q is set to $\frac{5}{2}$ with the assumption that the stress due to the recirculating motion is negligible; S_{ijkl} is the Eshelby tensor for an incompressible material, which is a function of the ellipsoid axis ratios (*Wetzel and Tucker*, 2001); and P'_{ij} is the deviatoric part of the tensor P_{ij}:

$$P'_{ij} \quad = \quad P_{ij} - \frac{1}{3}\mathrm{tr}(P_{ij}). \tag{A.2}$$

Representing P_{ij} on the coordinate along the main axes of the ellipsoid is calculated as $\hat{P}_{ij}$

$$\hat{P}_{ij} \quad = \quad \begin{pmatrix} \frac{R_b}{c}\mathrm{E}\left(1-\frac{c^2}{b^2}\right) & 0 & 0 \\ 0 & \frac{R_b}{a}\mathrm{E}\left(1-\frac{a^2}{c^2}\right) & 0 \\ 0 & 0 & \frac{R_b}{b}\mathrm{E}\left(1-\frac{b^2}{a^2}\right) \end{pmatrix}, \tag{A.3}$$

where $E()$ is the complete elliptic integral of the second kind. Each of the diagonal components of $\hat{P}_{ij}$ is a quarter of the length of the perimeter of a cross-section of the ellipsoid in a plane consisting of two of the main axes. Therefore, P'_{ij} represents the deviation of the ellipsoid from a sphere, and D_{ij}^{*surf} represents the rate of deformation of an elongate bubble returning to a spherical shape under the influence of surface tension.

Second, we illustrate the rate of the deformation tensor causing the elongation of a slender bubble $\hat{D}_{ij}^{*slender}$.

This tensor is adapted from the work of *Khakhar and Ottino* (1986), who derived the evolution equation for the long axis of a droplet. *Jackson and Tucker* (2003) transformed their equation into the rate of the deformation tensor, assuming a constant volume of the droplet during deformation. Therefore, $\hat{D}_{ij}^{*slender}$ is

$$\hat{D}_{ij}^{*slender} = \left[D_{ij}^{\infty} m_i m_j - \frac{\dot{\gamma}}{2\sqrt{5}Ca} \frac{\sqrt{a/R_b}}{1 + 0.8\lambda (a/R_b)^3} \right] \begin{bmatrix} 1 & 0 & 0 \\ 0 & -\frac{1}{2} & 0 \\ 0 & 0 & -\frac{1}{2} \end{bmatrix} . \tag{A.4}$$

Third, we explain the rate of the deformation tensor representing cross-sectional relaxation due to surface tension $\hat{D}_{ij}^{*axi}$. This tensor is defined as follows (*Sarkar and Schowalter*, 2001):

$$\hat{D}_{ij}^{*axi} = \frac{4R_b}{3r_{axi}} \frac{\dot{\gamma}}{Ca(1+\lambda)} \left(1 - \frac{r_{axi}}{b} \right) \begin{bmatrix} 0 & 0 & 0 \\ 0 & -1 & 0 \\ 0 & 0 & 1 \end{bmatrix} , \tag{A.5}$$

where $r_{axi} = \sqrt{bc}$ is the radius of the droplet's cross-section. This tensor forces the slender-body shape to be axisymmetric. The above tensors on the ellipsoid axes, $\hat{P}_{ij}$, $\hat{D}_{ij}^{*slender}$, and $\hat{D}_{ij}^{*axi}$, must be transformed into the spatial coordinate axes before they are used in Eqs. (A.2) or (2.10). Note that D_{ij}^{*surf}, $D_{ij}^{*slender}$, and D_{ij}^{*axi} are all proportional to $\dot{\gamma}/Ca$ and that these tensors include the dimensionless parameters λ and the shape parameters.

Appendix B

Mean field approach

The velocity gradient tensor of Eq. (2.35) expresses bubbles growth in the fluid which is assumed to be incompressible. Strictly speaking, this assumption is valid only for a small volume of bubble. It is known that the fluid containing bubbles behaves as a compressible fluid (*Prud'homme and Bird*, 1978). The difference of bubble growth between incompressible and compressible fluids should be investigated.

The constitutive equation for the compressible fluid is given by

$$\sigma_{ij} = -p\delta_{ij} + \chi\dot{\epsilon}_{kk} + 2\eta\left(\dot{\epsilon}_{ij} - \frac{1}{3}\dot{\epsilon}_{kk}\delta_{ij}\right), \tag{B.1}$$

where p is the pressure, χ is the second viscosity (the dilatational viscosity), $\dot{\epsilon}_{ij} = \frac{1}{2}\left(\frac{\partial u_i}{\partial x_j} + \frac{\partial u_j}{\partial x_i}\right)$ is the strain rate tensor where u_i is the velocity vector, and η is the shear viscosity. The pressure can be defined as

$$p = p_0 - k\epsilon_{kk}, \tag{B.2}$$

where k is the bulk modulus of the fluid, determined by the equation of state ($k = \rho\frac{\partial p}{\partial \rho}$) and p_0 is the reference pressure at which the zero volumetric strain is defined. I omit p_0 below because we can eliminate it by subtracting it from both pressures in the liquid and in the inclusion.

The constitutive equation for the compressible fluid is clearly different from that for the elastic medium (Eq. 2.29). The Eshelby theory with the strain replaced by the strain rate can not be directly applied to the dilatation of an inclusion in compressible fluid. Previous studies have applied the Eshelby theory to inclusion problems in viscous fluid for two cases.The first is with an incompressible fluid, which has an infinite bulk modulus ($k \to \infty$) and thus zero volumetric strain ($\epsilon_{kk} = 0$) (*Eshelby*, 1957; *Bilby et al.*, 1975). As shown in section 2.3.2, the Eshelby theory can be extended to an inclusion in the incompressible fluid. The second is for a mixture consisting of an incompressible fluid and empty voids (*Taya and Seidel*, 1981; *Budiansky et al.*, 1982). This mixture can be considered as an effective compressible fluid. Since the voids have zero pressure, the volume change of the mixture, that is the volume change of the voids, does not recover. In other word, the bulk modulus of the effective fluid is zero. From Eq. (B.2), the pressure change of the effective medium is zero.

Then, constitutive equation for the compressible fluid becomes

$$\sigma_{ij} = \chi^e \dot{\epsilon}_{kk} + 2\eta^e \left(\dot{\epsilon}_{ij} - \frac{1}{3}\dot{\epsilon}_{kk}\delta_{ij} \right), \tag{B.3}$$

where χ^e and η^e are the effective second viscosity and shear viscosity, respectively. Eq. (B.3) is comparable with the constitutive equation for the compressible elastic medium by replacing $\dot{\epsilon}_{ij}$ by ϵ_{ij}, and thus the Eshelby theory can be applied.

As the gas-liquid mixture has a finite bulk modulus, the Eshelby theory can not be applied to bubble growth in it. However, the solution with a finite compressibility is expected to lie between those of the inclusion embedded in an incompressible fluid ($k \to \infty$) and in a perfectly compressible fluid ($k \to 0$). I have presented the former problem in the main text. Here I show the solution for the latter.

The parameter corresponding to the Poisson's ratio of an elastic medium is denoted by ν^e, which is calculated by replacing the bulk modulus and the rigidity by χ^e and η^e. The effective shear viscosity η^e can be calculated by two methods. First, assuming that the fluid surrounding an inclusion is an isotropic homogeneous mixture with spherical inclusions, *Taya and Seidel* (1981) gives χ^e and η^e as follows:

$$\chi^e = \frac{4\eta(1-\phi)}{3\phi}, \tag{B.4}$$

$$\eta^e = 1 + \eta\left(\frac{5\phi}{3(1-\phi)}\right), \tag{B.5}$$

where ϕ is the volume fraction of voids and η is the viscosity of matrix phase. In this method, the effective shear viscosity increases with ϕ because the effective mixture is deformed by simple shear. The distorted stream lines around spherical inclusions increase the effective viscosity. The parameter corresponding to the Poisson's ratio is written as

$$\nu^e = \frac{3\chi^e - 2\eta^e}{6\chi^e + 2\eta^e} = \frac{2\alpha - 1}{4\alpha + 1}, \tag{B.6}$$

$$\alpha = \frac{1-\phi}{\phi\left(1 + \frac{5}{3}\frac{\phi}{1-\phi}\right)}. \tag{B.7}$$

The equivalent of Poisson's ratio, ν^e, becomes $1/2$ when $\phi = 0$.

Second, by using a cell model, *Prud'homme and Bird* (1978) and *Prousevitch et al.* (1993) calculate the growth rate of a bubble in a cell and derive χ^e and η^e as follows:

$$\chi^e = \frac{4\eta(1-\phi)}{3\phi} \tag{B.8}$$

$$\eta^e = \eta(1-\phi), \tag{B.9}$$

In this method, the effective shear viscosity decreases with ϕ because the dissipation layer around a bubble becomes thin. The parameter corresponding to the Poisson's ratio is written as

$$\nu^e = \frac{2-\phi}{4+\phi}. \tag{B.10}$$

Although the different η^e is derived in Eqs. (B.5) and (B.9), it is a difficult problem which definition should be used for the the calculation for ν^e. Here, I calculate the Eshelby tensor from both η^e and obtain the strain rate from Eq. (2.34). Fig. B.1 compares the expansion rate of an ellipsoid in an incompressible fluid ($\phi = 0$, which is equivalent with $k = \infty$) and that in a perfectly compressible fluid ($k = 0$) with various ν^e. As ϕ increases, the strain rate perpendicular to the major axis increases but only slightly. The difference between the definition of η^e is slight in Fig. B.1a and b. Thus, I conclude that the effect of compressibility is minor.

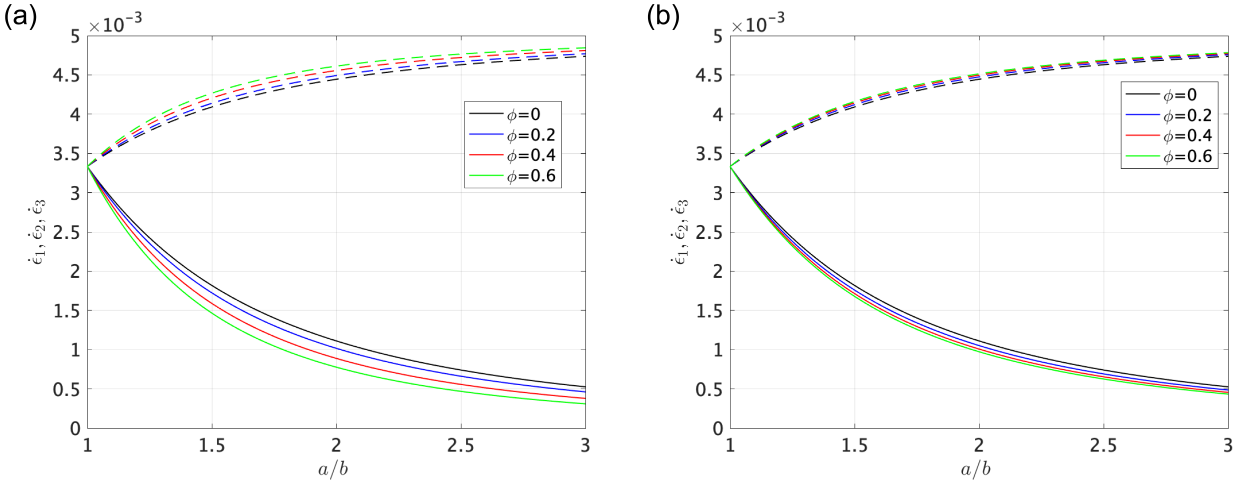

Figure B.1: Relationships between the strain rates and the cavity shapes as a function of the void fraction of cavity. (a) The effective shear viscosity is from Eq. (B.5). (b) The effective shear viscosity is from Eq. (B.9). The solid and dashed line indicate $\dot{\epsilon}_1 = \frac{\dot{a}}{a}$ and $\dot{\epsilon}_2 = \frac{\dot{b}}{b}$, respectively. The cavity is assumed to be a prolate shape ($b = c$). The non-dimensional volume rate is $\frac{\dot{V}}{V} = 0.01$. When $\phi = 0$, the obtained strain rates are equal to those of a growing bubble in an incompressible fluid.

Appendix C

Image processing of solidified foam

C.1 Image analysis

Image analysis was performed with a commercial 3D image processing software (Simpleware, Synopsys). The analysis procedure is summarized as follows. All procedures were performed in three dimensions.

First of all, raw image data obtained by a micro X-ray CT scanner was imported into Simpleware. We selected the part of the sample that has been uniformly stretched (the red rectangle in Fig. C.1a), and cropped the part manually (Fig. C.1b). The grayscale images were converted into binary images by thresholding (Fig. C.1c). The threshold value was slightly changed for each sample, depending on the noise level. This binarization procedure distinguishes the air part (blue) and the solid matrix (green) in Fig. C.1c.

Next, we want to extract bubbles (the air part within the foam). We made a mask covering only inside the foam (the green mask in Fig. C.1d). For this, we first eliminated the bubbles on the foam surface by applying a closing procedure to the green part in Fig. C.1c. The closing procedure consists of a volume dilatation followed by a volume erosion. We repeated it several times until small pores on the surface disappeared. Then, we filled the internal pores using one of the software functions. By selecting the common parts between the blue mask in Fig. C.1c and the green one in Fig. C.1d, I obtained the bubbles in the foam (Fig. C.1e).

Almost all the voxels belonging to the obtained blue mask in Fig. C.1e are connected in three dimensions. Before measuring bubble shapes, I needed to separate the connected bubbles. The segmentation of connected bubbles was achieved by the opening procedure followed by watershed segmentation. The opening procedure is the opposite of the closing, that is a volume erosion followed by a volume dilation. This procedure is supposed to separate impinging bubbles (Fig. C.1f). Automatic separation of connected bubbles is the most challenging part of three-dimensional image analysis, and several methods have been proposed *Dingwell et al.* (2016); *Giachetti et al.* (2011). Here, I used a watershed segmentation. Fig. F.1 shows the example of the watershed segmentation. For the simplicity, I here explain in two dimensions. Connected bubbles are shown in Fig. F.1a. The watershed procedure first calculates the distance map from the binary image (Fig. F.1b). Each pixel in the bubbles (black mask) is replaced with a grayscale pixel which expresses the distance to the nearest solid medium pixel (white mask). The watershed procedure also finds the local maxima of the distance map that are the farthest points from the surrounding solid medium. The local maxima are then dilated individually as distinguished by different colors in Fig. F.1c until their edges reach the bubble wall (white pixels) or a region of a neighbor bubble (an area with any different color). Watershed segmentation works well for spherical bubbles which do not overlap too much.

The result of three-dimensional watershed is shown in Fig. C.1g. The connected bubbles were separated into individual bubbles effectively. Because of the ellipsoidal shape of a bubble, watershed segmentation sometimes resulted in over-segmentation (Fig. C.1e). Over-segmented bubbles were merged manually.

The semi-major and semi-minor axes of a bubble were obtained by fitting the bubble by an optimally oriented rectangular that accommodates the bubble. The present study analyzed only bubbles with voxel numbers ≥ 100, because small bubbles were sometimes incorrectly measured.

C.2 Error related to the image processing

Error related to the image processing depends on bubble shape. It is easy to separate less elongated bubbles whose individual bubble is an ideal ellipsoidal shape. However, it is challenging to separate highly elongated bubbles. In order to evaluate the validity of watershed segmentation to those bubbles, I carried out a test, using the data of T19010703 that had the most elongated bubbles.

We compare the bubble shape obtained by watershed with the one traced manually by eye. Fig. C.3a is the original grayscale image and Fig. C.3b is the cross-section of separated bubbles after watershed segmentation. The watershed segmentation was performed in three dimensions. In order to accurately measure the shape of a bubble, I omitted bubbles contacting the upper and lower boundaries. The watershed segmentation could not wholly avoid making some artificial walls (see the white allow on Fig. C.3b). In Fig. C.3c, I traced bubble walls manually by eye. This manual reconstruction was performed in two dimensions. Based on the image of Fig. C.3c, each bubble was colored in Fig. C.3d.

Here, bubble shapes were obtained by fitting a two-dimensional ellipse to each bubble. The histograms of D for the images segmented by the automatic watershed and the manual drawing are shown in Fig. C.4. The two histograms show similar distributions, though the number of elongated bubbles (i.e., large D) in the image by manual drawing is slightly larger than that by the watershed segmentation. The average deformation degree is 0.45 for the automatic watershed segmentation and 0.50 for the manual drawing. The cumulative frequency curve of the watershed segmentation is shifted from that of the manual drawing to the low value of D with the maximum difference of 0.1 when the cumulative frequency reaches 0.6 (Fig. C.5).

This error estimation indicates that the watershed segmentation produces less elongated bubbles than the drawing walls manually. The difference of D between the two approaches is at most 0.1 in this sample (T19010703), which contains the most elongated and distorted bubbles of all our experimental samples. Most of our samples contain nearly ideal ellipsoidal bubbles (Fig. 4 in the main text), which are separated by the watershed segmentation more successfully like Fig. S1g in the supplement and Fig. 2b in the main text. Therefore, I regard that the errors in the estimation of D for those samples are smaller than 0.1.

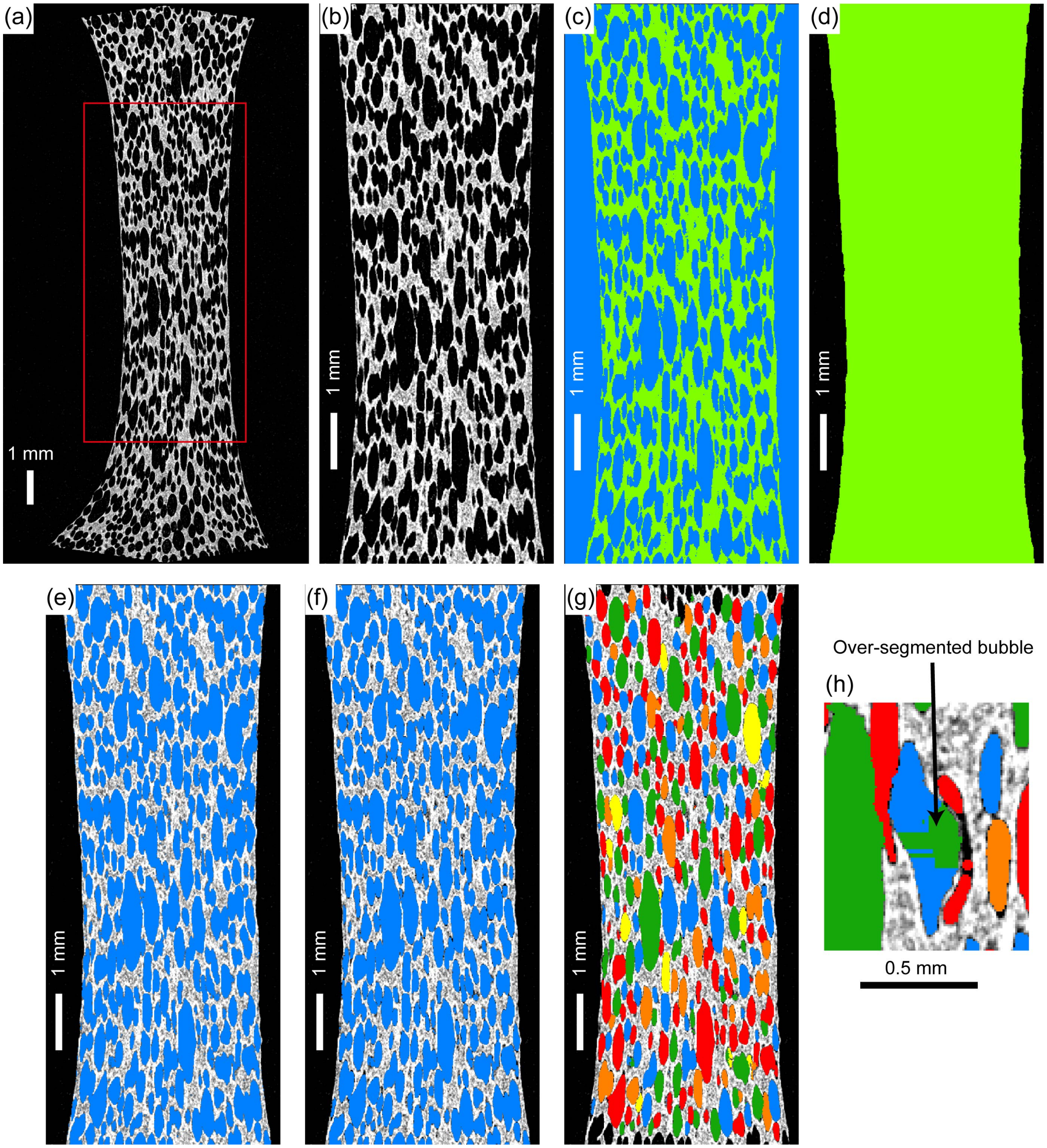

Figure C.1: Image analysis of T19011412. (a) Original raw image. Red square indicates the cropped area. (b) Cropped grayscale image. (c) Binarized image. Blue and green masks indicate air and solid medium, respectively. (d) The green area is the mask covering the inside foam. (e) The blue area is the mask covering the inside connected bubbles. (f) Bubbles after opening procedure. (g) Separated bubbles after watershed segmentation. Adjacent bubbles with different colors indicate that the bubbles are recognized as different bubbles (i.e., separated bubbles). (h) Over-segmented bubble.

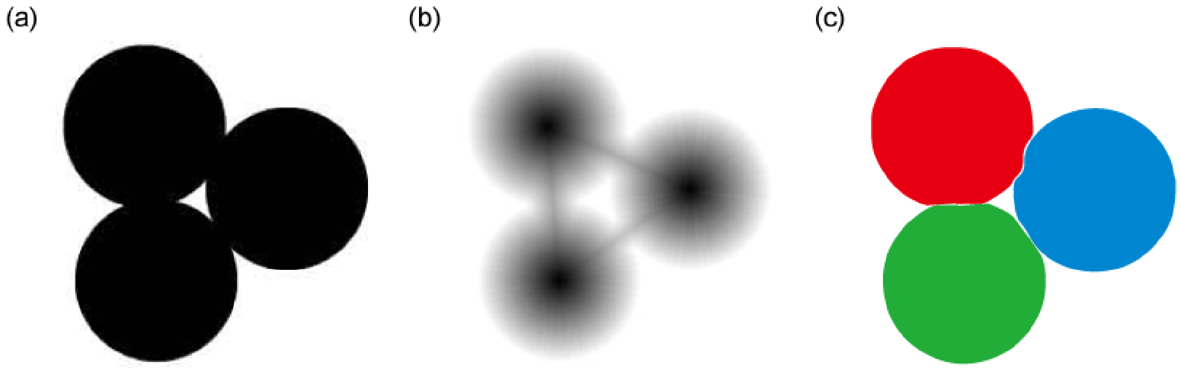

Figure C.2: (a) Original binary image. The black mask indicates bubbles, while the white pixels are the surrounding medium. (b) Distance map. Grayscale value of a pixel represents the distance from the nearest pixel of the surrounding medium. (c) Segmented bubbles after the watershed segmentation.

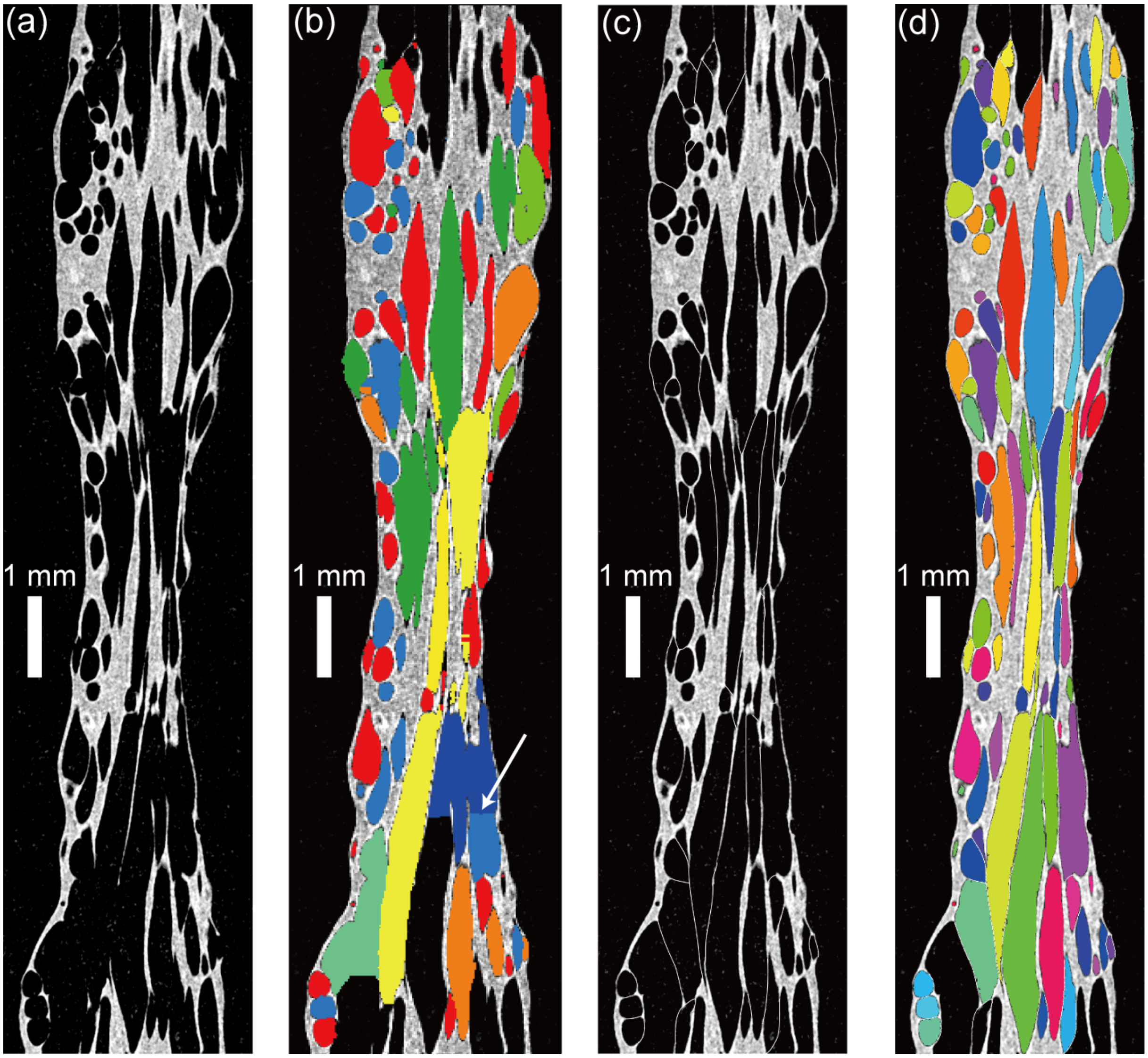

Figure C.3: Examples of bubble segmentation of sample T19010703. (a) Original grayscale image. (b) Separated bubbles after watershed segmentation. The watershed segmentation was performed in three dimensions. Adjacent bubbles with different colors indicate that the bubbles are recognized as different bubbles. (c) Glass walls traced manually by eye. (d) Colored bubbles of the image c. In image b and d, bubbles contacting the upper and lower boundaries are omitted.

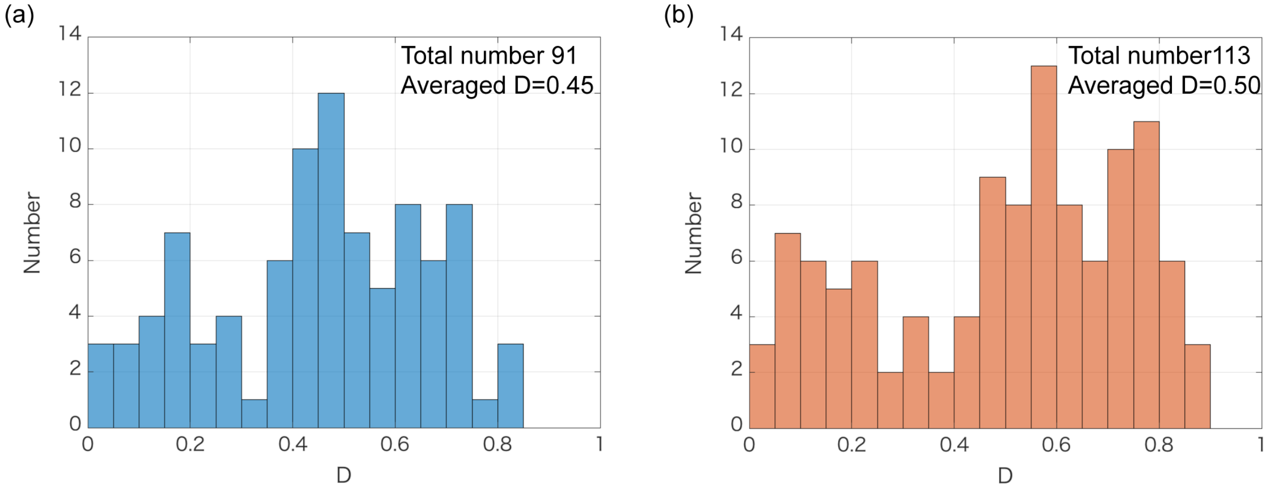

Figure C.4: The histogram of D. (a) The histogram based on the image after watershed segmentation (Fig. C.3b). (b) The histogram based on the image obtained by drawing glass walls manually (Fig. C.3d).

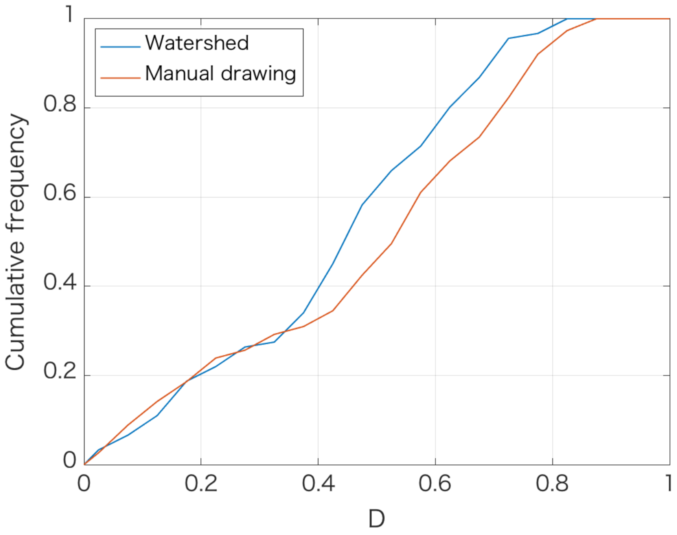

Figure C.5: The cumulative frequency distribution of the deformation degrees for the images after the watershed segmentation (blue line) and after the drawing glass walls manually (red line). The maximum difference of D between watershed segmentation and manual drawing is about 0.1 when the cumulative frequency reaches 0.6.

Appendix D

Conduit flow model

D.1 Derivation of the basic equations

First of all, we derive the dimensional equations of the viscous-heating model, and then simplify the equations. The following derivations of the basic equations are based on *Barmin et al.* (2004) and *Vedeneeva* (2007a).

D.1.1 Dimensional complete equations in the bubbly flow region

The basic equations before fragmentation are two-dimensional and axisymmetric. The complete equations describing the conduit flow is composed of the continuity equation, the momentum equations, and the energy equation. In the vector form, these equations are given by the following form (*Bird et al.*, 2007):

$$\frac{\partial \rho}{\partial t} + \mathrm{div}(\rho \boldsymbol{v}) = 0, \tag{D.1}$$

$$\frac{\partial (\rho \boldsymbol{v})}{\partial t} + \mathrm{div}(\rho \boldsymbol{v}\boldsymbol{v}) = -\nabla p + \mathrm{div}\ \boldsymbol{\tau} + \rho \boldsymbol{g}, \tag{D.2}$$

$$\frac{\partial (\rho e)}{\partial t} + \mathrm{div}(\rho e \boldsymbol{v}) = -p\ \mathrm{div}\ \boldsymbol{v} + (\boldsymbol{\tau} : \boldsymbol{L}) - \mathrm{div}(\kappa \nabla T). \tag{D.3}$$

Here, ρ is the density, $\boldsymbol{v}$ is the velocity vector, p is the pressure, $\boldsymbol{\tau}$ is the viscous stress tensor, $\boldsymbol{g}$ is the gravitational acceleration, e is the internal energy density, $\boldsymbol{L}$ is the velocity gradient tensor, κ is the thermal conductivity, and T is the temperature. The colon (:) represents the inner product of two second-order tensors.

The cylindrical coordinate is defined as (z, r, θ), where z is the elevation, r is the radial distance from the conduit center, and θ is the azimuth. The corresponding velocity components are defined by $\boldsymbol{v} = (u, w, 0)$, and those of the gravitational acceleration are by $\boldsymbol{g} = (-g, 0, 0)$ with $g > 0$. I will consider a steady-state two-dimensional axisymmetric magma flow in a cylindrical conduit. The flow is assumed to be steady ($\frac{\partial}{\partial t} = 0$)

and axisymmetric ($\frac{\partial}{\partial\theta}=0$). Then, Eqs. (D.1)-(D.3) are rewritten as

$$\frac{1}{r}\frac{\partial}{\partial r}\left(r\rho w\right)+\frac{\partial}{\partial z}\left(\rho u\right)=0, \tag{D.4}$$

$$\frac{1}{r}\frac{\partial}{\partial r}(r\rho w^2)+\frac{\partial}{\partial z}(\rho u w)=-\frac{\partial p}{\partial r}+\left[\frac{1}{r}\frac{\partial}{\partial r}(r\tau_{rr})+\frac{\partial \tau_{zr}}{\partial z}-\frac{\tau_{\theta\theta}}{r}\right], \tag{D.5}$$

$$\frac{1}{r}\frac{\partial}{\partial r}(r\rho u w)+\frac{\partial}{\partial z}(\rho u^2)=-\frac{\partial p}{\partial z}+\left[\frac{1}{r}\frac{\partial}{\partial r}(r\tau_{rz})+\frac{\partial \tau_{zz}}{\partial z}\right]-\rho g, \tag{D.6}$$

$$\begin{aligned}\frac{1}{r}\frac{\partial}{\partial r}\left(r\rho w e\right)+\frac{\partial}{\partial z}\left(\rho v e\right)=&-p\,\mathrm{div}\,\boldsymbol{v}+\tau_{zz}L_{zz}+\tau_{rr}L_{rr}+\tau_{\theta\theta}L_{\theta\theta}+\tau_{zr}L_{zr}\\ &+\tau_{rz}L_{rz}+\frac{1}{r}\frac{\partial}{\partial r}\left(r\kappa\frac{\partial T}{\partial r}\right)+\frac{\partial}{\partial z}\left(\kappa\frac{\partial T}{\partial z}\right).\end{aligned} \tag{D.7}$$

In the axisymmetric flow, the velocity gradient tensor can be written as

$$\boldsymbol{L}=\begin{pmatrix} L_{zz} & L_{zr} & 0\\ L_{rz} & L_{rr} & 0\\ 0 & 0 & L_{\theta\theta}\end{pmatrix}=\begin{pmatrix} \frac{\partial u}{\partial z} & \frac{\partial w}{\partial z} & 0\\ \frac{\partial u}{\partial r} & \frac{\partial w}{\partial r} & 0\\ 0 & 0 & \frac{w}{r}\end{pmatrix}. \tag{D.8}$$

The viscous stress tensor is also written as

$$\begin{aligned}\boldsymbol{\tau}\ &=\ \left(\chi-\frac{2}{3}\eta\right)(\mathrm{div}\ \boldsymbol{v})\boldsymbol{\delta}+\eta\left(\boldsymbol{L}+\boldsymbol{L}^{\top}\right)\\ &=\ \begin{pmatrix} \left(\chi-\frac{2}{3}\eta\right)\ \mathrm{div}\ \boldsymbol{v}+2\eta\frac{\partial u}{\partial z} & \eta\left(\frac{\partial u}{\partial r}+\frac{\partial w}{\partial z}\right) & 0\\ \eta\left(\frac{\partial u}{\partial r}+\frac{\partial w}{\partial z}\right) & \left(\chi-\frac{2}{3}\eta\right)\ \mathrm{div}\ \boldsymbol{v}+2\eta\frac{\partial w}{\partial r} & 0\\ 0 & 0 & \left(\chi-\frac{2}{3}\eta\right)\ \mathrm{div}\ \boldsymbol{v}+2\eta\frac{w}{r}\end{pmatrix},\end{aligned} \tag{D.9}$$

where χ is the dilatational viscosity, and δ is the unit tensor.

The divergence of the axisymmetric flow is given by

$$\mathrm{div}\ \boldsymbol{v}=\frac{1}{r}\frac{\partial}{\partial r}\left(rw\right)+\frac{\partial u}{\partial z}. \tag{D.10}$$

Using Eqs. (D.4)-(D.7), the basic equations of Eqs. (D.1)-(D.3) are re-written as

$$\frac{1}{r}\frac{\partial}{\partial r}(r\rho w)+\frac{\partial}{\partial z}(\rho u)=0, \tag{D.11}$$

$$\begin{aligned}\frac{1}{r}\frac{\partial}{\partial r}(r\rho uw)+\frac{\partial}{\partial z}(\rho u^2)=-\frac{\partial p}{\partial z}+\frac{1}{r}\frac{\partial}{\partial r}\left[r\eta\left(\frac{\partial u}{\partial r}+\frac{\partial w}{\partial z}\right)\right]&\\ +\frac{\partial}{\partial z}\left[\left(\chi-\frac{2}{3}\eta\right)\operatorname{div}\boldsymbol{v}+2\eta\frac{\partial u}{\partial z}\right]-\rho g,&\end{aligned} \tag{D.12}$$

$$\begin{aligned}\frac{1}{r}\frac{\partial}{\partial r}(r\rho w^2)+\frac{\partial}{\partial z}(\rho wu)=-\frac{\partial p}{\partial r}+\frac{\partial}{\partial r}\left[\left(\chi-\frac{2}{3}\eta\right)\operatorname{div}\boldsymbol{v}\right]+2\frac{1}{r}\frac{\partial}{\partial r}\left(r\eta\frac{\partial w}{\partial r}\right)-2\frac{1}{r^2}\eta w&\\ +\frac{\partial}{\partial z}\left[\eta\left(\frac{\partial u}{\partial r}+\frac{\partial w}{\partial z}\right)\right],&\end{aligned} \tag{D.13}$$

$$\begin{aligned}\frac{1}{r}\frac{\partial}{\partial r}(r\rho we)+\frac{\partial}{\partial z}(\rho ue)=-p\operatorname{div}\boldsymbol{v}+\left(\chi-\frac{2}{3}\eta\right)(\operatorname{div}\boldsymbol{v})^2&\\ +\eta\left[2\left(\frac{\partial w}{\partial r}\right)^2+2\frac{w^2}{r^2}+2\left(\frac{\partial u}{\partial z}\right)^2+\left(\frac{\partial u}{\partial r}+\frac{\partial w}{\partial z}\right)^2\right]&\\ +\frac{1}{r}\frac{\partial}{\partial r}\left(r\kappa\frac{\partial T}{\partial r}\right)+\frac{\partial}{\partial z}\left(\kappa\frac{\partial T}{\partial z}\right).&\end{aligned} \tag{D.14}$$

Density, Internal energy, and Viscosity

The magma density ρ satisfies the following relation:

$$\rho=(1-\phi)\rho_m+\phi\rho_g, \tag{D.15}$$

where ρ_m is the melt density, ρ_g is the density of the gas phase, and ϕ is the volume fraction of gas bubbles in magma.

The mass conservations of the gas component and the other melt components are individually,

$$\rho_m c\frac{1-\phi}{\rho}+\rho_g\frac{\phi}{\rho}=c_{max}, \tag{D.16}$$

$$\rho_m(1-c)\frac{1-\phi}{\rho}=1-c_{max}, \tag{D.17}$$

where c is the weight fraction of the gas dissolved in the melt and c_{max} is the maximum weight fraction of the gas dissolved in the melt when bubbles nucleated.

From Eqs. (D.16 and D.17), the magma density and the gas volume fraction can be written as

$$\frac{1}{\rho}=\frac{1-c_{max}}{1-c}\frac{1}{\rho_m}+\frac{c_{max}-c}{1-c}\frac{1}{\rho_g}, \tag{D.18}$$

$$\frac{1}{\phi}=1+\frac{1-c_{max}}{c_{max}-c}\frac{\rho_g}{\rho_m}, \tag{D.19}$$

Using $\alpha(p) = \frac{c_{max} - c}{1-c}$, Eq. (D.18) can be rewritten as

$$\frac{1}{\rho} = \frac{1-\alpha(p)}{\rho_m} + \frac{\alpha(p)}{\rho_g}. \tag{D.20}$$

The above equation implies that $\alpha(p)$ is the weight fraction of the gas phase in magma.

The melt phase of magma is assumed to be incompressible, while the gas phase follows the ideal gas law. I do not take account of the kinetics of bubble growth and the weight fraction c is assumed to be determined from the equilibrium solubility law for H_2O in magma (*Liu et al.*, 2005). These assumptions are represented by

$$\rho_m = \text{const}, \qquad \rho_g = \frac{p}{R_g T}, \qquad c = c(p) = \min(C_f\sqrt{p},\ c_{max}), \tag{D.21}$$

where R_g is the gas constant and C_f is the solubility coefficient.

The internal energy per unit volume is given in the form of

$$e = c_V T, \tag{D.22}$$

where c_V is the specific heat capacity. Considering that the temperature of the melt and gas phase is uniform, the internal energy of magma is given by

$$\rho e = \left[\rho_m(1-\phi)c_{Vm} + \rho_g \phi c_{Vg}\right] T, \tag{D.23}$$

where c_{Vm} and c_{Vg} are the specific heat capacity of the melt and gas phase, respectively. The substitution of Eq. (D.18) and (D.19) into Eq. (D.23) yields

$$e = \left(\frac{1-c_{max}}{1-c} c_{Vm} + \frac{c_{max}-c}{1-c} c_{Vg}\right) T. \tag{D.24}$$

The shear viscosity is from the empirical model of *Hess and Dingwell* (1996)

$$\begin{aligned} &\eta(c,\, T) = 10^{A(c,\, T)}, \\ &A(c,\, T) = 0.291 + 0.833\mathrm{ln}(c) - \frac{1304 + 2368\ln(c)}{T - (344.2 + 32.25\ln(c))}. \end{aligned} \tag{D.25}$$

Boundary condition

The conduit length L and its radius R are fixed. At the entrance of the conduit, the velocity profile of the flow is parabolic, and the temperature is uniform throughout the conduit section

$$z = 0: \quad w(r,0) = 0, \quad u(r,0) = 2u_{a0}\left(1 - \left(\frac{r}{R}\right)^2\right), \quad T(r,0) = T_0, \tag{D.26}$$

where u_{a0} is the flow velocity averaged by the conduit section at the entrance and, T_0 is the initial magma temperature. From the conservation of mass, u_{a0} can be written as a function of the mass discharge rate $Q_m = 2\pi \int_0^R \rho(r,z)u(r,z)rdr$:

$$u_{a0} = \frac{Q_m}{4\pi \int_0^R \rho(r,0)\left(1-\left(\frac{r}{R}\right)^2\right) rdr}. \tag{D.27}$$

The boundary conditions at the axis on the conduit are defined by the absence of fluxes

$$r = 0: \quad w(0,z) = 0, \quad \frac{\partial u}{\partial r}(0,z) = 0, \quad \frac{\partial p}{\partial r}(0,z) = 0, \quad \frac{\partial T}{\partial r}(0,z) = 0. \tag{D.28}$$

On the conduit wall, I assume a no-slip condition for the velocity and an isothermal condition for the temperature, that is

$$r = R: \quad w(R,z) = 0, \quad u(R,z) = 0, \quad T(R,z) = T_0. \tag{D.29}$$

D.1.2 Dimensional equations in the gas-particle region

After fragmentation, the flow is turbulent. I deal with it as a one dimensional flow, that is $\boldsymbol{v} = (u,0,0)$. Because the flow is mainly held by gas, I neglect the viscous resistance. I also assume that the temperature of the flow is equal to the initial magma temperature T_0 because the viscous-heating in the bubbly flow increases the temperature only in a very thin layer near the conduit walls and has only a minor contribution to the entire internal energy, which is shown in the result section. With these assumptions, the conservation equations (D.4)-(D.7) are simplified for the gas-particle region as

$$\pi R^2 \left(\rho_g \phi + \rho_m(1-\phi)\right) u = Q_m, \tag{D.30}$$

$$\frac{dp}{dz} = -\rho u \frac{du}{dz} - \rho g, \tag{D.31}$$

$$T = T_0. \tag{D.32}$$

The density and gas volume fraction are calculated from the same equations as the bubbly flow region (Eqs. D.18-D.21).

D.1.3 Dimensionless equations in the bubbly region

As a reference of dimensional values, following values are introduced

$$u_0 = 1\ [\mathrm{m/s}], \quad p_0 = \rho_m g L + p_{out}\ [\mathrm{Pa}], \quad \eta_0 = \eta(c(p_0,T_0),T_0)\ [\mathrm{Pa\cdot s}]. \tag{D.33}$$

where p_{out} is the pressure at the conduit outlet. Following *Barmin et al.* (2004), I set u_0 to a constant value in order to regard the non-dimensional mass discharge rate as a variable.

Hereafter, dimensional values are indicated by an overscript $\tilde{}$. Non-dimensional values, which have no subscripts, are obtained by the following equations:

$$
\begin{aligned}
&r = \frac{\tilde{r}}{\tilde{R}}, \quad z = \frac{\tilde{z}}{\tilde{R}}, \quad L = \frac{\tilde{L}}{\tilde{R}}, \quad \zeta = \frac{1}{L} \\
&w = \frac{\tilde{w}}{\tilde{u}_0}, \quad u = \frac{\tilde{u}}{\tilde{u}_0}, \quad u_{a0} = \frac{\tilde{u}_{a0}}{\tilde{u}_0}, \\
&\rho = \frac{\tilde{\rho}}{\tilde{\rho}_m}, \quad \rho_g = \frac{\tilde{\rho}_g}{\tilde{\rho}_m}, \quad Q_m = \frac{\tilde{Q}_m}{\tilde{\rho}_m \tilde{u}_0 \tilde{R}^2}, \\
&p = \frac{\tilde{p}}{\tilde{p}_0}, \quad p_{out} = \frac{\tilde{p}_{out}}{\tilde{p}_0}, \quad T = \frac{\tilde{T} - \tilde{T}_0}{\tilde{T}_0}, \\
&c_{Vg} = \frac{\tilde{c}_{Vg}}{\tilde{c}_{Vm}}, \quad e = \frac{\tilde{e}}{\tilde{c}_{Vm}\tilde{T}_0}, \\
&\eta = \frac{\tilde{\eta}}{\tilde{\eta}_0}, \quad \left(\chi - \frac{2}{3}\eta\right) = \frac{\left(\tilde{\chi} - \frac{2}{3}\tilde{\eta}\right)}{\tilde{\eta}_0}.
\end{aligned}
\tag{D.34}
$$

Keep in mind that the dimensional temperature is replaced by the magma temperature increment with respect to the initial temperature at the conduit inlet. Using Eq. (D.34), I rewrite equations Eqs. (D.11)-(D.29) in non-dimensional forms following the representation by *Vedeneeva* (2007b) but with some modification to present the physical meaning clearer.

$$\frac{1}{r}\frac{\partial}{\partial r}(r\rho w) + \frac{\partial}{\partial z}(\rho u) = 0, \tag{D.35}$$

$$\begin{aligned}\frac{1}{r}\frac{\partial}{\partial r}(r\rho u w) + \frac{\partial}{\partial z}(\rho u^2) = &-\frac{1}{2Eu^{-1}}\frac{\partial p}{\partial z} + \frac{1}{Re}\frac{1}{r}\frac{\partial}{\partial r}\left[r\eta\left(\frac{\partial u}{\partial r} + \frac{\partial w}{\partial z}\right)\right] \\ &+\frac{1}{Re}\frac{\partial}{\partial z}\left[\left(\chi - \frac{2}{3}\eta\right)\operatorname{div}\boldsymbol{v} + 2\eta\frac{\partial u}{\partial z}\right] - \frac{1}{Fr^2}\rho,\end{aligned} \tag{D.36}$$

$$\begin{aligned}\frac{1}{r}\frac{\partial}{\partial r}(r\rho w^2) + \frac{\partial}{\partial z}(\rho w u) = &-\frac{1}{2Eu^{-1}}\frac{\partial p}{\partial r} + \frac{1}{Re}\frac{\partial}{\partial r}\left[\left(\chi - \frac{2}{3}\eta\right)\operatorname{div}\boldsymbol{v}\right] + \frac{2}{Re}\frac{1}{r}\frac{\partial}{\partial r}\left(r\eta\frac{\partial w}{\partial r}\right) \\ &-\frac{2}{Re}\frac{1}{r^2}\eta w + \frac{1}{Re}\frac{\partial}{\partial z}\left[\eta\left(\frac{\partial u}{\partial r} + \frac{\partial w}{\partial z}\right)\right],\end{aligned} \tag{D.37}$$

$$\begin{aligned}\frac{1}{r}\frac{\partial}{\partial r}(r\rho w e) + \frac{\partial}{\partial z}(\rho u e) = &-\frac{Ec}{2Eu^{-1}}p\operatorname{div}\boldsymbol{v} + \frac{Ec}{Re}\left(\chi - \frac{2}{3}\eta\right)(\operatorname{div}\boldsymbol{v})^2 \\ &+\frac{Ec}{Re}\eta\left[2\left(\frac{\partial w}{\partial r}\right)^2 + 2\frac{w^2}{r^2} + 2\left(\frac{\partial u}{\partial z}\right)^2 + \left(\frac{\partial u}{\partial r} + \frac{\partial w}{\partial z}\right)^2\right] \\ &+\frac{1}{Pe}\frac{1}{r}\frac{\partial}{\partial r}\left(r\frac{\partial T}{\partial r}\right) + \frac{1}{Pe}\frac{\partial}{\partial z}\left(\frac{\partial T}{\partial z}\right),\end{aligned} \tag{D.38}$$

$$\operatorname{div}\boldsymbol{v} = \frac{1}{r}\frac{\partial}{\partial r}(rw) + \frac{\partial u}{\partial z}, \tag{D.39}$$

$$\frac{1}{\rho} = \frac{1 - c_{max}}{1 - c} + \frac{c_{max} - c}{1 - c}\frac{1}{\rho_g}, \quad \rho_g = \rho_{g0}\frac{p}{T + 1}, \tag{D.40}$$

$$\frac{1}{\phi} = 1 + \frac{1 - c_{max}}{c_{max} - c}\rho_g, \tag{D.41}$$

$$e = \psi(p)(T + 1), \quad \psi(p) = \frac{1 - c_{max}}{1 - c} + \frac{c_{max} - c}{1 - c}c_{Vg}, \tag{D.42}$$

$$c = c(p) = \min(c_0\sqrt{p}, c_{max}). \tag{D.43}$$

Non-dimensional constant values are defined by

$$\begin{aligned}&Re = \frac{\tilde{\rho}_m\tilde{u}_0\tilde{R}}{\tilde{\eta}_0}, \quad Fr = \frac{\tilde{u}_0}{\sqrt{\tilde{g}\tilde{R}}}, \quad Ec = \frac{\tilde{u}_0^2}{\tilde{c}_{Vm}\tilde{T}_0}, \quad Eu^{-1} = \frac{\tilde{\rho}_m\tilde{u}_0^2/2}{\tilde{p}_0}, \quad Pe = \frac{\tilde{\rho}_m\tilde{u}_0\tilde{R}\tilde{c}_{Vm}}{\tilde{\kappa}}, \\ &\rho_{g0} = \frac{\tilde{p}_0}{\tilde{\rho}_m\tilde{R}_g\tilde{T}_0}, \quad c_0 = \tilde{C}_f\sqrt{\tilde{p}_0}.\end{aligned} \tag{D.44}$$

Re is the ratio of the inertia force to the viscous force. Fr and Ec compare the kinetic energy with the gravitational potential energy and thermal energy, respectively. Eu^{-1} compares the dynamic pressure due to the fluid inertia to the pressure. In the flow below the fragmentation surface, not only Re but also Fr, Ec, and Eu^{-1} are considered to be very small. Therefore, I neglect the left-hand side of the momentum equations (Eqs. D.36 and D.37).

Boundary condition of Eqs. (D.26)-(D.29) are also non-dimensionalized

$$\begin{aligned}
z=0: &\quad w(r,0)=0, \quad u(r,0)=2u_{a0}\left(1-r^2\right), \quad T(r,0)=0, \quad u_{a0}=\frac{Q_m}{4\pi\int_0^1 \rho(r,0)\left(1-r^2\right) r dr}. \\
r=0: &\quad w(0,z)=0, \quad \frac{\partial u}{\partial r}(0,z)=0, \quad \frac{\partial p}{\partial r}(0,z)=0, \quad \frac{\partial T}{\partial r}(0,z)=0. \\
r=1: &\quad w(1,z)=0, \quad u(1,z)=0, \quad T(1,z)=0.
\end{aligned} \tag{D.45}$$

D.1.4 Simplification of the basic equations

Vedeneeva (2007a) and *Vedeneeva* (2007b) further simplified the basic equations of Eqs. (D.35)-(D.43) with the assumption that the conduit length is much greater than its radius ($\zeta = 1/L \ll 1$). This assumption is reasonable for typical explosive eruptions.

The length scale along the axis is rescaled as $z'' = \zeta z$ so that z'' has a scale of $O(1)$. As r and u are also in order $O(1)$, the mass conservation equation (Eq. D.35) requires that $w \sim O(\zeta)$. Then, I also rescale w as $w'' = w/\zeta$ with w'' having a scale of $O(1)$. The differential equations (D.35)-(D.43) are written as the following equations.

$$\frac{1}{r}\frac{\partial}{\partial r}\left(r\rho w''\right)+\frac{\partial}{\partial z''}\left(\rho u\right)=0, \tag{D.46}$$

$$\begin{aligned}
0=-\zeta\frac{1}{2Eu^{-1}}\frac{\partial p}{\partial z''}+&\underbrace{\frac{1}{Re}\frac{1}{r}\frac{\partial}{\partial r}\left(r\eta\frac{\partial u}{\partial r}\right)}_{F1} \\
&+\zeta^2\frac{1}{Re}\left[\frac{1}{r}\frac{\partial}{\partial r}\left(\frac{\partial w''}{\partial z''}\right)+\frac{\partial}{\partial z''}\left(\left(\chi-\frac{2}{3}\eta\right)\mathrm{div}''\,\boldsymbol{v}+2\eta\frac{\partial u}{\partial z''}\right)\right]-\frac{1}{Fr^2}\rho,
\end{aligned} \tag{D.47}$$

$$\begin{aligned}
0=-\frac{1}{2Eu^{-1}}\frac{\partial p}{\partial r}+\zeta&\underbrace{\frac{1}{Re}\left[\frac{\partial}{\partial r}(\left(\chi-\frac{2}{3}\eta\right)\mathrm{div}''\,\boldsymbol{v})+2\frac{1}{r}\frac{\partial}{\partial r}\left(r\eta\frac{\partial w''}{\partial r}\right)-2\frac{1}{r^2}\eta w''+\frac{\partial}{\partial z''}\left(\eta\frac{\partial u}{\partial r}\right)\right]}_{F2} \\
&+\zeta^3\frac{1}{Re}\frac{\partial}{\partial z''}\left(\eta\frac{\partial w''}{\partial z''}\right),
\end{aligned} \tag{D.48}$$

$$\begin{aligned}
\zeta\left[\frac{1}{r}\frac{\partial}{\partial r}(r\rho w''e)+\frac{\partial}{\partial z}(\rho ue)\right]=&-\zeta\frac{Ec}{2Eu^{-1}}p\,\mathrm{div}''\boldsymbol{v}+\frac{Ec}{Re}\eta\left(\frac{\partial u}{\partial r}\right)^2 \\
&+\zeta^2\frac{Ec}{Re}\left[\left(\chi-\frac{2}{3}\eta\right)(\mathrm{div}''\,\boldsymbol{v})^2+2\eta\left(\left(\frac{\partial w''}{\partial r}\right)^2+\frac{w''^2}{r^2}+\left(\frac{\partial u}{\partial z''}\right)^2+\frac{\partial u}{\partial r}\frac{\partial w''}{\partial z''}\right)\right] \\
&+\zeta^4\frac{Ec}{Re}\eta\left(\frac{\partial w''}{\partial z''}\right)^2+\frac{1}{Pe}\left[\frac{1}{r}\frac{\partial}{\partial r}\left(r\frac{\partial T}{\partial r}\right)+\zeta^2\frac{\partial}{\partial z''}\left(\frac{\partial T}{\partial z''}\right)\right],
\end{aligned} \tag{D.49}$$

$$\mathrm{div}''\,\boldsymbol{v}=\frac{1}{r}\frac{\partial}{\partial r}\left(rw''\right)+\frac{\partial u}{\partial z''}. \tag{D.50}$$

Small terms with higher orders of ζ in Eqs. (D.46)-(D.49) can be neglected. The rescaling guarantees that both F1 in Eq. (D.47) and F2 in Eq. (D.48) are in the same order of $O(Re^{-1})$, so that, *Vedeneeva* (2007a) got the following relationship.

$$\frac{\partial p}{\partial z''} / \frac{\partial p}{\partial r} \sim \frac{1}{\zeta^2}, \quad O(1/\zeta^2) \gg 1 \tag{D.51}$$

This means that the pressure change in the radial direction is negligible, that is, $p(r, z) \sim p(z)$. Previous theoretical studies also verified this approximation under the condition of a long conduit length and a low Reynolds number by a perturbation method (*Van Den Berg et al.*, 1993; *Venerus*, 2006).

Finally, I obtain the non-dimensional basic equations:

$$\frac{1}{r}\frac{\partial}{\partial r}(r\rho w) + \frac{\partial}{\partial z}(\rho u) = 0, \tag{D.52}$$

$$\frac{dp}{dz} = \frac{2Eu^{-1}}{Re}\frac{1}{r}\frac{\partial}{\partial r}\left(r\eta\frac{\partial u}{\partial r}\right) - \frac{2Eu^{-1}}{Fr^2}\rho, \quad p(r, z) = p(z), \tag{D.53}$$

$$\frac{1}{r}\frac{\partial}{\partial r}(r\rho we) + \frac{\partial}{\partial z}(\rho ue) = -\frac{Ec}{2Eu^{-1}}p\,\mathrm{div}\boldsymbol{v} + \frac{Ec}{Re}\eta\left(\frac{\partial u}{\partial r}\right)^2 + \frac{1}{Pe}\frac{1}{r}\frac{\partial}{\partial r}\left(r\frac{\partial T}{\partial r}\right), \tag{D.54}$$

$$\mathrm{div}\,\boldsymbol{v} = \frac{1}{r}\frac{\partial}{\partial r}(rw) + \frac{\partial u}{\partial z}. \tag{D.55}$$

D.1.5 Dimensionless equations in the gas-particle region

Using the non-dimensional values (Eq. D.34) and the mass conservation law $Q_m = \pi\rho u$, the continuity and momentum equations in the gas-particle region (D.30)-(D.32) can be written in the dimensionless forms:

$$u(p) = \frac{Q_m/\pi}{\rho_g(p)\phi(p) + (1 - \phi(p))}, \tag{D.56}$$

$$\frac{dp}{dz} = \frac{1}{f(p)}, \quad f(p) = -Fr^2\left(\frac{\pi}{Q_m}\frac{Eu}{2} + \frac{du}{dp}\right)u(p), \tag{D.57}$$

$$T = 0. \tag{D.58}$$

The density and gas volume ratio are calculated from Eqs. (D.40) and (D.41). The vertical change of p can be solved explicitly from Eq. (D.56).

D.2 Numerical method for solving the equations

D.2.1 Numerical method for solving the viscous-heating model

The numerical method for solving the basic equations is not explicitly written in *Barmin et al.* (2004) or *Vedeneeva et al.* (2005). The following method is based on the doctoral thesis of *Agur* (1983) and *Cox* (1973).

Computational grid

Non-uniform grid is used (Fig. D.1). The grid consists of $M+1 \times N+1$ points. The step size along the z-axis is defined as

$$\Delta z^n = z^{n+1} - z^n, \quad (1 \le n \le N). \tag{D.59}$$

The step size along the radial direction is defined as follow

$$\begin{aligned} \Delta r_m &= r_{m+1} - r_m, \quad (1 \le m \le M) && \text{(D.60)} \\ X_m &= \frac{\Delta r_{m+1}}{\Delta r_m}. \quad (1 \le m \le M-1) && \text{(D.61)} \end{aligned}$$

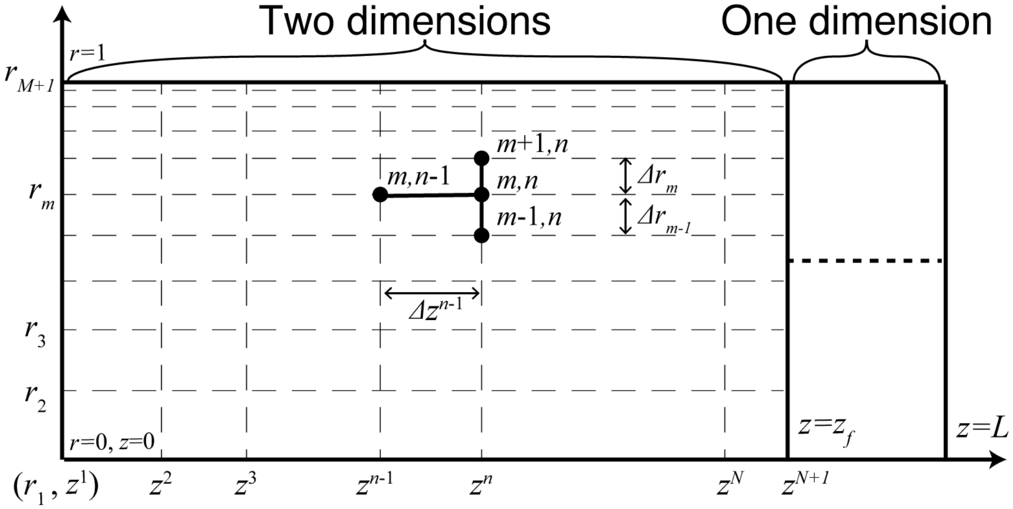

Figure D.1: Non-uniform grid.

Differential equations for the energy equation

Substituting the the continuity equation (Eq. D.52) into the left side of the energy equation (Eq. D.54), I obtain:

$$\begin{aligned} \rho w \frac{\partial e}{\partial r} + \rho u \frac{\partial e}{\partial z} &= -\frac{EcEu}{2} p \,\mathrm{div}\boldsymbol{v} + \frac{Ec}{Re} \eta \left(\frac{\partial u}{\partial r}\right)^2 + \frac{1}{Pe} \frac{1}{r} \frac{\partial}{\partial r} \left(r \frac{\partial T}{\partial r} \right) \\ &= -\frac{EcEu}{2} p \,\mathrm{div}\boldsymbol{v} + \frac{Ec}{Re} \eta \left(\frac{\partial u}{\partial r}\right)^2 + \frac{1}{Pe} \left(\frac{\partial^2 T}{\partial r^2}\right) + \frac{1}{Pe} \frac{1}{r} \left(\frac{\partial T}{\partial r}\right) \end{aligned} \tag{D.62}$$

When $r = 0$, $\frac{1}{r}\left(\frac{\partial T}{\partial r}\right)$ has the indeterminate form, $\frac{0}{0}$. By L'Hospital's rule, I obtain

$$\lim_{r \to 0} \frac{1}{r}\left(\frac{\partial T}{\partial r}\right) = \left(\frac{\partial^2 T}{\partial r^2}\right). \tag{D.63}$$

Similarly, when $r = 0$, the divergence of the velocity becomes

$$\operatorname{div} \boldsymbol{v} = \frac{1}{r}\frac{\partial}{\partial r}(rw) + \frac{\partial u}{\partial z} = 2\frac{\partial w}{\partial r} + \frac{\partial u}{\partial z} \tag{D.64}$$

Taking into the boundary condition (Eqs. D.45 and D.46), the energy equation becomes:

$$\rho u \frac{\partial e}{\partial z} = -\frac{EcEu}{2} p \operatorname{div}\boldsymbol{v} + \frac{2}{Pe}\left(\frac{\partial^2 T}{\partial r^2}\right), \quad \text{for } r = 0 \tag{D.65}$$

$$\rho w \frac{\partial e}{\partial r} + \rho u \frac{\partial e}{\partial z} = -\frac{EcEu}{2} p \operatorname{div}\boldsymbol{v} + \frac{Ec}{Re}\eta\left(\frac{\partial u}{\partial r}\right)^2 + \frac{1}{Pe}\left(\frac{\partial^2 T}{\partial r^2}\right) + \frac{1}{Pe}\frac{1}{r}\left(\frac{\partial T}{\partial r}\right), \quad \text{for } 0 < r < 1 \tag{D.66}$$

The following discretization is used for the energy equation:

$$\begin{aligned}
\left.\frac{\partial T}{\partial r}\right|_m^n &= \frac{1}{2X_{m-1}(1+X_{m-1})\Delta r_{m-1}}\left\{-X_{m-1}^2 T_{m-1}^n + (X_{m-1}^2 - 1)T_m^n + T_{m+1}^n\right\} \\
&+ \frac{1}{2X_{m-1}(1+X_{m-1})\Delta r_{m-1}}\left\{-X_{m-1}^2 T_{m-1}^{n-1} + (X_{m-1}^2 - 1)T_m^{n-1} + T_{m+1}^{n-1}\right\}, && \text{(D.67)} \\
\left.\frac{\partial^2 T}{\partial r^2}\right|_m^n &= \frac{1}{X_{m-1}(1+X_{m-1})(\Delta r_{m-1})^2}\left\{X_{m-1} T_{m-1}^n - (1+X_{m-1})T_m^n + T_{m+1}^n\right\} \\
&+ \frac{1}{X_{m-1}(1+X_{m-1})(\Delta r_{m-1})^2}\left\{X_{m-1} T_{m-1}^{n-1} - (1+X_{m-1})T_m^{n-1} + T_{m+1}^{n-1}\right\}, && \text{(D.68)} \\
\left.\frac{\partial u}{\partial r}\right|_m^n &= \frac{1}{2X_{m-1}(1+X_{m-1})\Delta r_{m-1}}\left\{-X_{m-1}^2 u_{m-1}^n + (X_{m-1}^2 - 1)u_m^n + u_{m+1}^n\right\} \\
&+ \frac{1}{2X_{m-1}(1+X_{m-1})\Delta r_{m-1}}\left\{-X_{m-1}^2 u_{m-1}^{n-1} + (X_{m-1}^2 - 1)u_m^{n-1} + u_{m+1}^{n-1}\right\}, && \text{(D.69)} \\
\left.\frac{\partial u}{\partial z}\right|_m^n &= \frac{u_m^n - u_m^{n-1}}{\Delta z^{n-1}}, && \text{(D.70)} \\
\left.\frac{\partial e}{\partial r}\right|_m^n &= \psi(p^n)\frac{\partial T}{\partial r}, && \text{(D.71)} \\
\left.\frac{\partial e}{\partial z}\right|_m^n &= \frac{\psi(p^n)(T_m^n + 1) - \psi(p^{n-1})(T_m^{n-1} + 1)}{\Delta z^{n-1}}. && \text{(D.72)}
\end{aligned}$$

Substituting Eqs. (D.67) - (D.72) into Eqs. (D.65) and (D.66), I obtain:

$$\rho_m^n u_m^n \frac{\psi(p^n)(T_m^n+1)-\psi(p^{n-1})(T_m^{n-1}+1)}{\Delta z^{n-1}} = -\frac{EuEc}{2}p^n \left[\frac{u_1^n-u_1^{n-1}}{\Delta z^{n-1}} + 2\frac{w_2^n-w_1^n}{\Delta r_1}\right] + \frac{2}{Pe}\left[\frac{T_0^n-2T_1^n+T_2^n}{2(\Delta r_1)^2} + \frac{T_0^{n-1}-2T_1^{n-1}+T_2^{n-1}}{2(\Delta r_1)^2}\right], \quad \text{for } r=0 \tag{D.73}$$

$$\begin{aligned}
&\rho_m^n w_m^n \psi(p^n)\left[\frac{1}{2X_{m-1}(1+X_{m-1})\Delta r_{m-1}}\left\{-X_{m-1}^2 T_{m-1}^n + (X_{m-1}^2-1)T_m^n + T_{m+1}^n\right\}\right.\\
&\qquad\left. + \frac{1}{2X_{m-1}(1+X_{m-1})\Delta r_{m-1}}\left\{-X_{m-1}^2 T_{m-1}^{n-1} + (X_{m-1}^2-1)T_m^{n-1} + T_{m+1}^{n-1}\right\}\right]\\
&\quad + \rho_m^n u_m^n \frac{\psi(p^n)(T_m^n+1)-\psi(p^{n-1})(T_m^{n-1}+1)}{\Delta z^{n-1}}\\
&= -\frac{EuEc}{2}p^n \,\mathrm{div}\boldsymbol{v}\big|_m^n + \frac{Ec}{Re}\eta_m^n \left(\left.\frac{\partial u}{\partial r}\right|_m^n\right)^2\\
&\quad + \frac{1}{Pe}\left[\frac{1}{X_{m-1}(1+X_{m-1})(\Delta r_{m-1})^2}\left\{X_{m-1}T_{m-1}^n - (1+X_{m-1})T_m^n + T_{m+1}^n\right\}\right.\\
&\quad\left. + \frac{1}{X_{m-1}(1+X_{m-1})(\Delta r_{m-1})^2}\left\{X_{m-1}T_{m-1}^{n-1} - (1+X_{m-1})T_m^{n-1} + T_{m+1}^{n-1}\right\}\right]\\
&\quad + \frac{1}{Pe}\frac{1}{r_m}\left[\frac{1}{2X_{m-1}(1+X_{m-1})\Delta r_{m-1}}\left\{-X_{m-1}^2 T_{m-1}^n + (X_{m-1}^2-1)T_m^n + T_{m+1}^n\right\}\right.\\
&\quad\left. + \frac{1}{2X_{m-1}(1+X_{m-1})\Delta r_{m-1}}\left\{-X_{m-1}^2 T_{m-1}^{n-1} + (X_{m-1}^2-1)T_m^{n-1} + T_{m+1}^{n-1}\right\}\right]\\
&\hspace{20em}\text{for } 0<r<1
\end{aligned} \tag{D.74}$$

We rearrange Eqs. (D.73) and (D.74):

$$\frac{(\Delta r_1)^2}{\Delta z^{n-1}}\rho_1^n u_1^n \left\{\psi(p^n)(T_1^n+1)-\psi(p^{n-1})(T_1^{n-1}+1)\right\} = -\frac{EuEc\,p^n(\Delta r_1)^2}{2}\left[\frac{u_1^n-u_1^{n-1}}{\Delta z^{n-1}}+2\frac{w_2^n-w_1^n}{\Delta r_1}\right]$$
$$+\frac{1}{Pe}\left[-2T_1^n+2T_2^n-2T_1^{n-1}+2T_2^{n-1}\right], \quad \text{for } r=0 \qquad \text{(D.75)}$$

$$\frac{\rho_m^n w_m^n \psi(p^n)\Delta r_{m-1}}{X_{m-1}(1+X_{m-1})}\left[-X_{m-1}^2T_{m-1}^n+(X_{m-1}^2-1)T_m^n+T_{m+1}^n-X_{m-1}^2T_{m-1}^{n-1}+(X_{m-1}^2-1)T_m^{n-1}+T_{m+1}^{n-1}\right]$$
$$+\frac{2(\Delta r_{m-1})^2\rho_m^n u_m^n}{\Delta z^{n-1}}\left[\psi(p^n)(T_m^n+1)-\psi(p^{n-1})(T_m^{n-1}+1)\right]$$
$$= -EuEc(\Delta r_{m-1})^2 p^n\,\mathrm{div}\boldsymbol{v}\big|_m^n + \frac{2(\Delta r_{m-1})^2Ec}{Re}\eta_m^n\left(\left.\frac{\partial u}{\partial r}\right|_m^n\right)^2$$
$$+\frac{1}{Pe}\frac{2\left[X_{m-1}T_{m-1}^n-(1+X_{m-1})T_m^n+T_{m+1}^n+X_{m-1}T_{m-1}^{n-1}-(1+X_{m-1})T_m^{n-1}+T_{m+1}^{n-1}\right]}{X_{m-1}(1+X_{m-1})}$$
$$+\frac{1}{Pe}\frac{\Delta r_{m-1}\left[-X_{m-1}^2T_{m-1}^n+(X_{m-1}^2-1)T_m^n+T_{m+1}^n-X_{m-1}^2T_{m-1}^{n-1}+(X_{m-1}^2-1)T_m^{n-1}+T_{m+1}^{n-1}\right]}{r_mX_{m-1}(1+X_{m-1})}$$
$$, \qquad \text{for } 0<r<1 \qquad \text{(D.76)}$$

Eqs. (D.75) and (D.76) can be reduced to the following forms:

$$B_1^n T_1^n + C_1^n T_2^n = H_1^n, \quad \text{for } r = 0$$

where

$$\begin{aligned}
B_1^n &= \frac{(\Delta r_1)^2}{\Delta z^{n-1}} \rho_1^n u_1^n \psi(p^n) + \frac{2}{Pe} \\
C_1^n &= -\frac{2}{Pe} \\
H_1^n &= -\frac{(\Delta r_1)^2}{\Delta z^{n-1}} \rho_1^n u_1^n \left\{ \psi(p^n) - \psi(p^{n-1})(T_1^{n-1} + 1) \right\} \\
&\quad - \frac{EuEc\, p^n (\Delta r_1)^2}{2} \left[\frac{u_1^n - u_1^{n-1}}{\Delta z^{n-1}} + 2\frac{w_2^n - w_1^n}{\Delta r_1} \right] + \frac{1}{Pe} \left[-2T_1^{n-1} + 2T_2^{n-1} \right]
\end{aligned} \tag{D.77}$$

$$A_m^n T_{m-1}^n + B_m^n T_m^n + C_m^n T_{m+1}^n = D_m^n T_{m-1}^{n-1} + E_m^n T_m^{n-1} + F_m^n T_{m+1}^{n-1} + G_m^n = H_m^n, \quad \text{for } r > 0$$

where

$$\begin{aligned}
A_m^n &= -a_m^n X_{m-1}^2 - b_m X_{m-1} + c_m X_{m-1}^2 \\
B_m^n &= a_m^n (X_{m-1}^2 - 1) + d_m^n \psi(p^n) + b_m (1 + X_{m-1}) - c_m (X_{m-1}^2 - 1) \\
C_m^n &= a_m^n - b_m - c_m \\
D_m^n &= a_m^n X_{m-1}^2 + b_m X_{m-1} - c_m X_{m-1}^2 \\
E_m^n &= -a_m^n (X_{m-1}^2 - 1) + d_m^n \psi(p^{n-1}) - b_m (1 + X_{m-1}) + c_m (X_{m-1}^2 - 1) \\
F_m^n &= -a_m^n + b_m + c_m \\
G_m &= \frac{2(\Delta r_{m-1})^2 Ec}{Re} \eta_m^n \left(\left. \frac{\partial u}{\partial r} \right|_m^n \right)^2 - EuEc(\Delta r_1)^2 p^n \,\mathrm{div}\boldsymbol{v}|_m^n - d_m^n \left\{ \psi(p^n) - \psi(p^{n-1}) \right\} \\
a_m^n &= \frac{\rho_m^n w_m^n \psi(p^n) \Delta r_{m-1}}{X_{m-1}(1 + X_{m-1})} \\
b_m &= \frac{1}{Pe} \frac{2}{X_{m-1}(1 + X_{m-1})} \\
c_m &= \frac{1}{Pe} \frac{\Delta r_{m-1}}{r_m X_{m-1}(1 + X_{m-1})} \\
d_m^n &= \frac{2(\Delta r_{m-1})^2 \rho_m^n u_m^n}{\Delta z^{n-1}}
\end{aligned} \tag{D.78}$$

The divergence of the velocity can be written as follows:

$$\begin{aligned}
\mathrm{div}\boldsymbol{v}|_m^n = \frac{w_m^n}{r_m} + \frac{1}{X_{m-1} \Delta r_{m-1} (1 + X_{m-1})} \left\{ -X_{m-1}^2 w_{m-1}^n + (X_{m-1}^2 - 1) w_m^n + w_{m+1}^n \right\} \\
+ \frac{u_m^n - u_m^{n-1}}{\Delta z^{n-1}}
\end{aligned} \tag{D.79}$$

Therefore, the basic equations can be reduced to a tridiagonal matrix

$$\begin{pmatrix} B_1^n & 2C_1^n & & & & & \\ A_2^n & B_2^n & C_2^n & & & & \\ & \ddots & \ddots & \ddots & & & \\ & & A_m^n & B_m^n & C_m^n & & \\ & & & \ddots & \ddots & \ddots & \\ & & & & A_{M-1}^n & B_{M-1}^n & C_{M-1}^n \\ & & & & & B_M^n & C_M^n \end{pmatrix} \begin{pmatrix} T_1^n \\ T_2^n \\ \vdots \\ T_m^n \\ \vdots \\ T_{M-1}^n \\ T_M^n \end{pmatrix} = \begin{pmatrix} H_1^n \\ H_2^n \\ \vdots \\ H_m^n \\ \vdots \\ H_{M-1}^n \\ H_M^n \end{pmatrix}. \tag{D.80}$$

This linear system of equations is solved implicitly.

Differential equations for the momentum equation

The integration of the momentum equation (Eq. D.53) with respect to r gives

$$\begin{aligned} \frac{1}{2}r^2\frac{dp}{dz} &= \frac{2}{EuRe}r\eta\frac{\partial u}{\partial r} - \frac{2}{EuFr^2}\int_0^r \rho r' dr' \\ \frac{\partial u}{\partial r} &= \frac{rEuRe}{4\eta}\frac{dp}{dz} + \frac{Re}{Fr^2}\frac{1}{r\eta}\int_0^r \rho r' dr. \end{aligned} \tag{D.81}$$

The above equation satisfies the boundary condition $\frac{\partial u(0,z)}{\partial r} = 0$. For simplicity, the second term of the right side is replaced by

$$I(r) = \frac{Re}{Fr^2}\frac{1}{r\eta}\int_0^r \rho r' dr'. \tag{D.82}$$

Using the no-slip condition ($u(1,z) = 0$), I obtain the vertical velocity profile

$$u = \frac{EuRe}{4}\frac{dp}{dz}\int_1^r \frac{r'}{\eta}dr' + \int_1^r I(r')dr'. \tag{D.83}$$

Since the vertical velocity is related to the mass discharge rate $Q_m = 2\pi\int_0^1 \rho u r dr$, the pressure gradient can be determined:

$$\frac{dp}{dz} = \frac{Q_m - 2\pi\int_0^1 \left(\rho r\int_1^r I(r')dr'\right)dr}{2\pi\int_0^1 \left(\rho r\frac{EuRe}{4}\int_1^r \frac{r'}{\eta}dr'\right)dr}. \tag{D.84}$$

The above equation requires the viscosity and density as a function of r.

Once I get the pressure gradient, I also obtain the vertical velocity from Eq. (D.83). The horizontal velocity is determined from the continuity equation (Eq. D.52) with the axis-symmetry conditon:

$$w = -\frac{1}{r\rho}\int_0^r r' \frac{\partial(\rho u)}{\partial z} dr'. \tag{D.85}$$

Computational procedure

The continuity, momentum, and energy equations are coupled by two velocities and temperature. Therefore, they cannot be solved separately. The coupled equations can be solved by the combination of the finite difference method and the iteration method. I outline the computational method as follows. Fig. D.2 illustrates the algorithm to solve the basic equations and boundary problems.

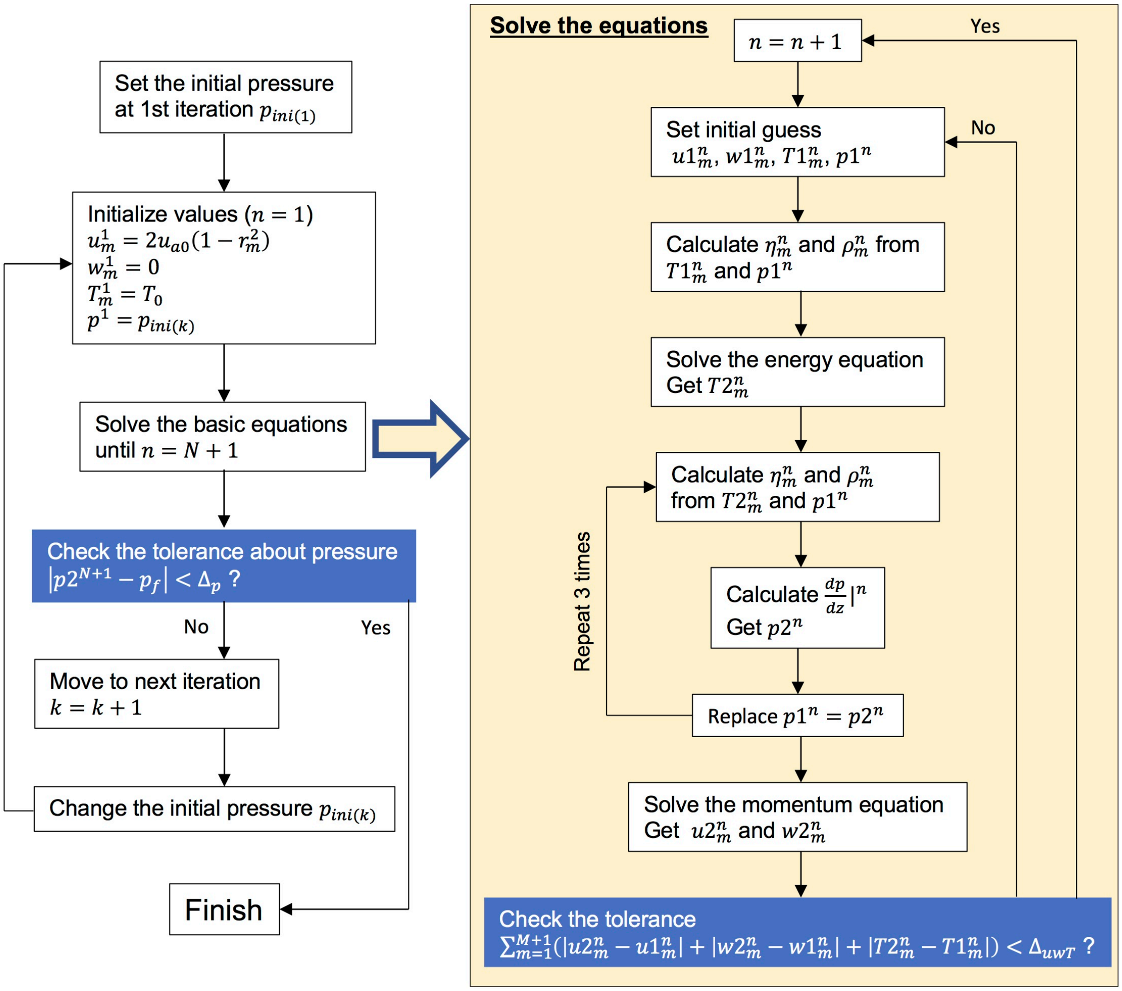

Figure D.2: Flowchart to solve the basic equations and boundary problems.

Notation

- $u1_m^n$, $w1_m^n$, $T1_m^n$, $p1^n$, $\left(\frac{dp}{dz}1\right)\Big|^n$ are the estimated u, w, T, p, $\frac{dp}{dz}$ at column n, respectively.
- $u2_m^n$, $w2_m^n$, $T2_m^n$, $p2^n$, $\left(\frac{dp}{dz}2\right)\Big|^n$ are the most recently calculated u, w, T, p, $\frac{dp}{dz}$ at column n, respectively.
- u_m^{n-1}, w_m^{n-1}, T_m^{n-1} are u, w, T at column n-1, respectively.
- $p_{ini\,(k)}$ is the initial pressure at the k-th iteration.

<u>Procedure</u>

1. I give the initial pressure $p_{ini\,(1)}$ arbitrarily.
2. The parabolic velocity profile and homogeneous temperature profile are assumed at the conduit entrance.

$$\begin{aligned} u_m^1 &= 2u_{a0}\left(1 - r_m^2\right) \\ w_m^1 &= 0, \qquad\qquad (m = 1, 2, \cdots, M+1) \\ T_m^1 &= T_0 \\ p^1 &= p_{ini\,(1)}. \end{aligned}$$

3. The initial values of the pressure, velocity, temperature in the first iteration at $n+1=2$ equal to the values at $n=1$.

$$\begin{aligned} u1_m^{n+1} &= u_m^n \\ w1_m^{n+1} &= w_m^n, \qquad\qquad (m = 1, 2, \cdots, M+1) \\ T1_m^{n+1} &= T_m^n \\ p1^{n+1} &= p^n. \end{aligned}$$

4. The strain rate $\frac{\partial u}{\partial z}\Big|_m^n$ and divergence $\mathrm{div}\,\boldsymbol{v}|_m^n$ at column n are calculated from $u1_m^n$ and $w1_m^n$. I also calculate the viscosity η_m^n and density ρ_m^n from $T1_m^n$ and $p1^n$.
5. Using $u1_m^n$, $w1_m^n$, $p1^n$, η_m^n, ρ_m^n, $\frac{\partial u}{\partial z}\Big|_m^n$, $\mathrm{div}\,\boldsymbol{v}|_m^n$, $T1_m^{n-1}$, I solve the energy equation of Eq. (D.80) implicitly, and then get $T2_m^n$.
6. Using $p1^n$ and $T2_m^n$, I calculate η_m^n and ρ_m^n at column n.
7. Using η_m^n and ρ_m^n, I calculate $\frac{dp}{dz}\Big|^n$ from Eq. (D.84), and then calculate the new pressure $p2^n$.
8. The new pressure is set to be used in the next iteration at column n.

$$p1^n = p2^n$$

9. I repeat steps 6-8 three times. After that, I calculate η_m^n and ρ_m^n from the latest $p2^n$.

10. Using η^n_m, ρ^n_m, $\left.\frac{dp}{dz}\right|^n$, I obtain $u2^n_m$ and $w2^n_m$ from Eqs. (D.83) and (D.85).

11. The estimated velocity and temperature are compared with the pre-estimation value. If the following tolerance condition is fulfilled, then proceed to step 14. Otherwise, continue to step 12.

$$\sum_{m=1}^{M+1} \left(|u2^n_m - u1^n_m| + |w2^n_m - w1^n_m| + |T2^n_m - T1^n_m| \right) < \Delta_{uwT}$$

    where Δ_{uwT} is the pre-determined positive small value.

12. The estimated velocity, temperature, and pressure are used in the next iteration at column n.

$$\begin{aligned} u1^n_m &= u2^n_m \\ w1^n_m &= w2^n_m, \qquad\qquad (m = 1, 2, \cdots, M+1) \\ \\ T1^n_m &= T2^n_m \\ p1^n &= p2^n \end{aligned}$$

13. I repeat steps 4-11 until the tolerance condition is fulfilled.

14. The estimated velocity, temperature, and pressure are used in the first iteration at column n+1.

$$\begin{aligned} u1^{n+1}_m &= u2^n_m \\ w1^{n+1}_m &= w2^n_m, \qquad\qquad (m = 1, 2, \cdots, M+1) \\ \\ T1^{n+1}_m &= T2^n_m \\ p1^{n+1} &= p2^n \end{aligned}$$

15. I repeat steps 4-14 until the column reached the fragmentation surface.

16. The estimated pressure at column $N+1$ is compared with the exit pressure. If the tolerance condition $\left|p2^{N+1} - p_f\right| < \Delta_p$ is fulfilled where p_f is the non-dimensional fragmentation pressure (Eq. 4.20), then the calculation finishes. Δ_p is the pre-determined positive small value. Otherwise, continue to step 17.

17. I change the initial $p_{ini\,(k)}$ to meet the tolerance condition. If $k = 1$, the next initial pressure is determined as follows

$$p_{ini\,(2)} = \begin{cases} p_{ini\,(1)} - \delta_p, & (\text{when} \quad p2^{N+1}_{(1)} > p_f) \\ p_{ini1\,(1)} + \delta_p, & (\text{when} \quad p2^{N+1}_{(1)} < p_f) \end{cases}$$

where δ_p is the pre-determined small value. If $k \geq 2$, the next initial pressure is determined by the Newton-iteration method.

$$p_{ini\,(k+1)} = p_{ini\,(k)} + \left(p_f - p2^{N+1}_{(k)}\right) \frac{p_{ini\,(k)} - p_{ini\,(k-1)}}{p2^{N+1}_{(k)} - p2^{N+1}_{(k-1)}}$$

where $p2^{N+1}_{(k)}$ is the estimated exit pressure at the k-th iteration and $p_{ini\,(k)}$ is the initial pressure at the k-the iteration.

Step Size and Tolerance

Because the derivatives are sensitive to step size, small step sizes are used where the velocity profile changes dramatically. For the radial direction, I used the following geometric series:

$$r_m = \Delta r_1 Y^{m-1} \qquad (m = 1, 2, \cdots, M+1) \tag{D.86}$$

where Δr_1 is the first term of the series and Y is the common ratio. The common ratio is determined by the length ($R = 1$), the step number M, and the first term Δr_1. For the simulation of the Tupo plinian event, I set the step numbers and the first term as $M = 1000$, $N = 10000$, $\Delta r_1 = 0.01$. The horizontal step size is small just above the conduit inlet (Table D.1).

Table D.1: Vertical step size

Range of z	Δz
$0 - 0.1$	$\frac{1}{30000}$
$0.1 - 1$	$\frac{9}{20000}$

The tolerances for the iteration are defined as follows:

$$\Delta_{uwT} = 0.001, \qquad \Delta_p = 0.001, \qquad \delta_p = 0.005. \tag{D.87}$$

D.2.2 Numerical method for solving the Newtonian isothermal model

Because the density and viscosity do not depend on the radial position, I can obtain the analytical solution of Eq. (D.84):

$$\frac{dp}{dz} = -\frac{16Fr^2\eta Q_m + 2\pi\rho^2 Re}{\pi\rho EuReFr^2}. \tag{D.88}$$

Substituting Eq. (D.88) into Eq. (D.83), I obtain the vertical velocity

$$u = \frac{2Q_m}{\pi\rho}\left(1 - r^2\right) \tag{D.89}$$

Eq. (D.89) indicates that the profile of the vertical velocity is parabolic. The vertical velocity also shows $\frac{\partial \rho u}{\partial z} = 0$. Thus, I get $w = 0$ from Eq. (D.85).

D.2.3 Numerical method for solving the shear-thinning model due to bubble deformation

The pressure gradient can be obtained by the same way as the constant viscosity from Eq. (D.84). In the shear-thinning case, it is not possible to obtain an explicit solution of u, because viscosity is not uniform along the radius. The integration of the momentum equation (Eq. D.53) with respect to r gives

$$\frac{1}{2} r^2 \frac{dp}{dz} = \frac{2}{EuRe} r \eta_b \frac{\partial u}{\partial r} - \frac{\rho r^2}{EuFr^2}. \tag{D.90}$$

Keep in mind that the viscosity η is replaced by the bulk viscosity η_b. Substituting the viscosity model of Eqs. (4.22) - (4.25), I obtain

$$\frac{1}{2} r^2 \frac{dp}{dz} = \frac{2}{EuRe} r \eta \left(\eta_{r,\infty} + \frac{\eta_{r,0} - \eta_{r,\infty}}{1 + \left(\frac{6}{5} \frac{R_b \frac{\partial u}{\partial r} \eta}{\Gamma} \right)^2} \right) \frac{\partial u}{\partial r} - \frac{\rho r^2}{EuFr^2}. \tag{D.91}$$

For a given $\frac{dp}{dz}$ and ρ, I can find the radial change of the vertical velocity $\frac{\partial u}{\partial r}$ from Eq. (D.91) by the Newton's method. Once I get $\frac{\partial u}{\partial r}$, the vertical velocity can be obtained with the no-slip boundary condition.

$$u = - \int_1^0 \frac{\partial u}{\partial r} dr. \tag{D.92}$$

The horizontal velocity is also given by Eq. (D.85).

Appendix E

The conduit flow model combining the viscous-heating model and the shear-thinning model due to bubble deformation

As described in section 4.6.2, the shear-thinning effect due to bubble elongation is a possible mechanism that reduces the very large temperature rise around the conduit walls. In this appendix, I show the simulation result of the viscous-heating model with the shear-thinning effect due to bubble deformation. Unfortunately, it is unable to couple the viscous-heating model (Eqs. 4.1-4.5) with the viscosity model by *Llewellin et al.* (2002b) (Eqs. 4.22-4.25) because the calculation procedure is too complex to converge. A more sophisticated computational procedure is required to converge the calculation.

In order to make the computation tractable, I assume high Capillary numbers ($Ca \gg 1$) across and along the conduit. Instead of using the viscosity model by *Llewellin et al.* (2002b), I use $\eta_{r,\infty}$ which is the asymptotic relative viscosity at high Ca (Eq. 4.25). Strictly speaking, the above assumption of high Ca throughout the conduit is incorrect, because bubbles at the conduit center may be nearly spherical after the velocity profile becomes a parabolic shape. However, this assumption is reasonable for evaluating its effect on the magma temperature around the conduit walls because the region close to the conduit walls has high Ca.

Fig. E.1 shows the simulation results of the viscous-heating model with the shear-thinning effect due to bubble deformation. The magma temperature around the conduit walls reaches about 2300 $^{\circ}$C at the fragmentation surface, which is 1000 $^{\circ}$C lower than the same temperature of the viscous-heating model without the shear-thinning effect (Fig. 4.9). In spite of the shear-thinning effect due to bubble elongation, the profiles of vertical velocity and pressure are almost the same between the two modes (Figs. 4.8 and E.1), because the profile of the melt viscosity in the viscous-heating model is similar to that of the bulk viscosity in the model without the shear-thinning effect (Figs. 4.9c and E.1d). In this result, the reduction of the bulk viscosity caused by bubble elongation has partly compensated with the effect of viscous-heating.

Fig. E.1 indicates that the shear-tinning effect due to bubble elongation has a potential to suppress the temperature rise around the conduit walls. Further study requires the viscosity model in an arbitrary shear field.

The current viscosity models, such as Eqs. (4.22)-(4.25) are based on bubble deformation in simple shear field. This shear filed is reasonable for the conduit fluid with a parabolic velocity profile. However, when the conduit flow becomes a plug flow, most of the flow is occupied by pure shear as well as simple shear. Bulk viscosity model should be extended to an arbitrary shear field.

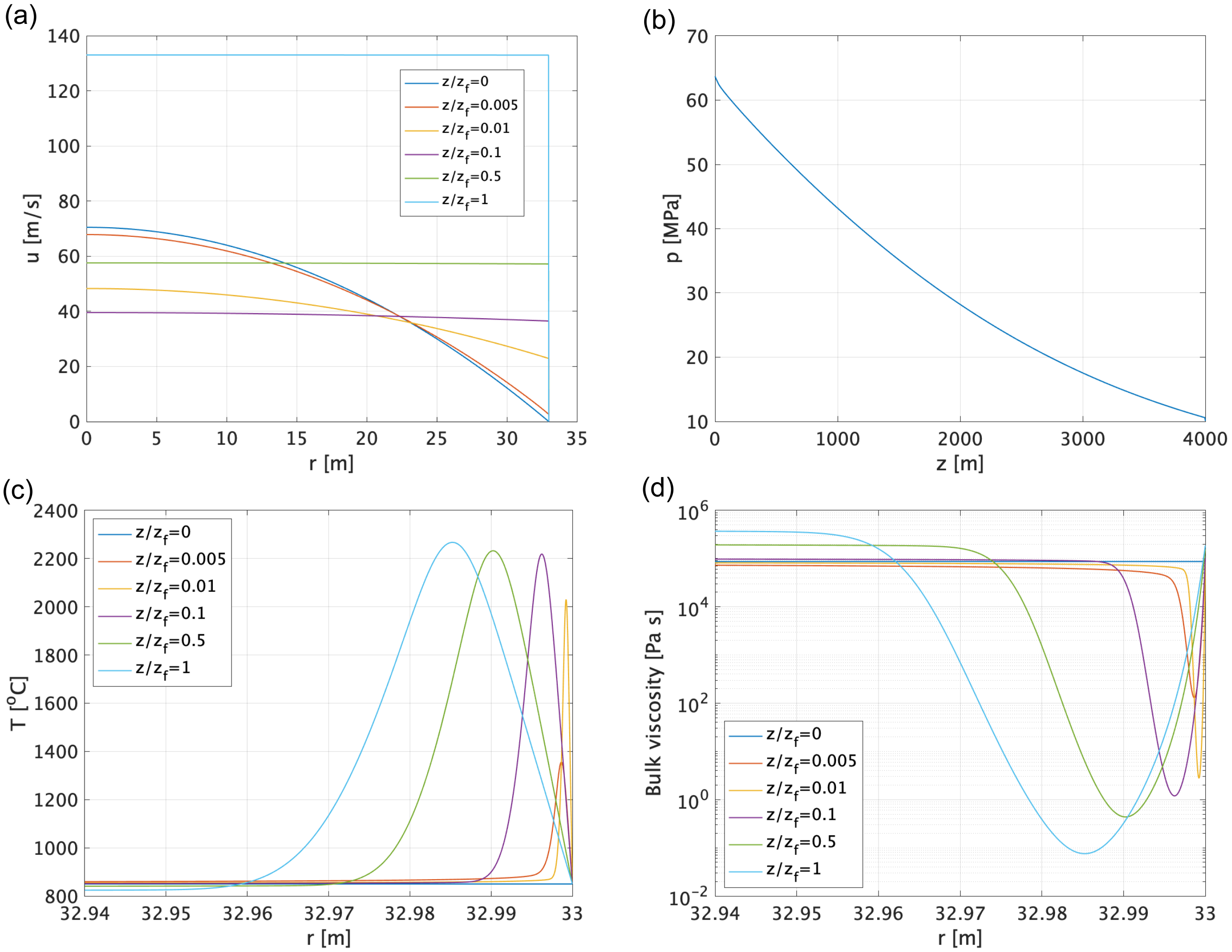

Figure E.1: The calculation result of the viscous-heating model with the shear-thinning effect due to bubble deformation. (a) Vertical velocity distribution across the conduit at $z/z_f = 0, 0.005, 0.001, 0.1, 0.5, 1$. The fragmentation surface z_f is 3994 m. (b) Pressure profile along with the conduit axis. (c) Temperature around the conduit walls. (d) Bulk viscosity around the conduit walls.

Appendix F

Image processing of pumice

Three-dimensional analyses were performed by using an open-source software called Fiji which is a distribution of the popular software ImageJ (*Schindelin et al.*, 2012). We first cut a cuboid from the volume. Image sizes range from $483 \times 732 \times 1299$ voxels to $736 \times 984 \times 1568$ voxels, depending on the sample. Subsequently, we applied the 3D median filter to reduce noise in the images by replacing each voxel with the median of the neighboring voxel values. Since the watershed process described later is sensitive to low-amplitude noise, we adjust the brightness and contrast window to suppress all minima whose depth is less than a specified cut-off level. Binarization, the process by which a grayscale image is converted into a binary image, was done by Otsu's method which determines the threshold of brightness automatically (*Otsu*, 1979). To separate impinging but not coalescing bubbles, we applied the opening operation which is defined as the several cycles of volume erosion and dilation.

Before measuring bubble shapes, we first needed to rebuild some bubble walls in order to rebuild very thin bubble walls which disappeared during the binarization process. The watershed used for solidified foam (appendix B) is suitable for ideal elliptical bubbles, but it fails to separate intricately distorted bubbles like bubbles in pumice. To overcome this problem, we used an open-source plugin called Marker-controlled Watershed (*Legland et al.*, 2016), which is based on the marker-controlled watershed algorithm (*Meyer and Beucher*, 1990).

Fig. F.1 shows the schematic image of the marker-controlled watershed. For the simplicity, I here explain the watershed algorithm in one dimension. The basic idea of the watershed consists of considering the input grayscale images as a topographic surface and placing a water source in each marker point (Fig. F.1a). The water is flooded from the sources, and dams are made at the boundaries where the different water sources meet (Fig. F.1b). This boundary corresponds to the missing bubble wall which divides adjacent bubbles. Flooding continues until the water covers the entire mask.

The marker-controlled watershed needs three images to run: (1) input grayscale which is used to calculate the elevation of the topographic field, (2) mask image (binary image) which is used to define the water level, (3) marker image (binary image) which is used to define the water sources (Fig. F.2). In this thesis, I used the gradient magnitude of the original image as the input grayscale image and used the binarized image as the mask image. The choice of the marker image is one of the essential parts of the marker-controlled watershed. If I set many markers, the watershed algorithm results in over-segmented bubbles, but otherwise results in no-segmented bubbles. In order to separate bubble and rebuild thin walls correctly, the marker image should contain the small seeds for small bubbles while separating the large seeds for large bubbles. The marker image is usually defined by the local minima of the input grayscale image, which is the connected regions of voxels with the same value whose neighboring voxels have greater than that of the region. In our study, local minima succeeded in the identification of small seeds, but failed to separate large seeds. To segment the large seeds, I applied the opening operation to the large bubbles having 10000 or more voxels. The marker image after the opening operation is shown in Fig. F.2c. Using the input grayscale, mask, and marker images, I obtained the segmented bubbles divided by the rebuilt bubble walls (Fig. F.2e).

The watershed operation introduced some over-segmented bubbles, especially with a small volume, due to the low-resolution of the X-ray CT. In chapter 5, I report analytical results for bubbles with > 100 voxels. Bubbles contacted with the borders were also removed automatically. The bubble shape was obtained by fitting a 3D ellipsoid to the volume. All the bubbles were approximated as triaxial ellipsoids, wherein three principle axes pass through the center of gravity of the bubble.

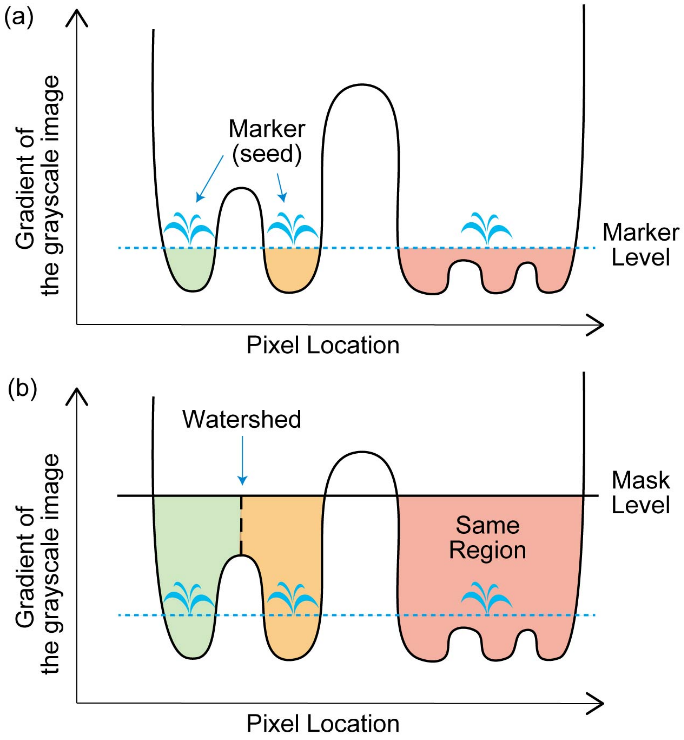

Figure F.1: Schematic image of the marker-controlled watershed. For the simplicity, I explain the watershed algorithm in one dimension. The topographic image before flooding (a) and after flooding (b).

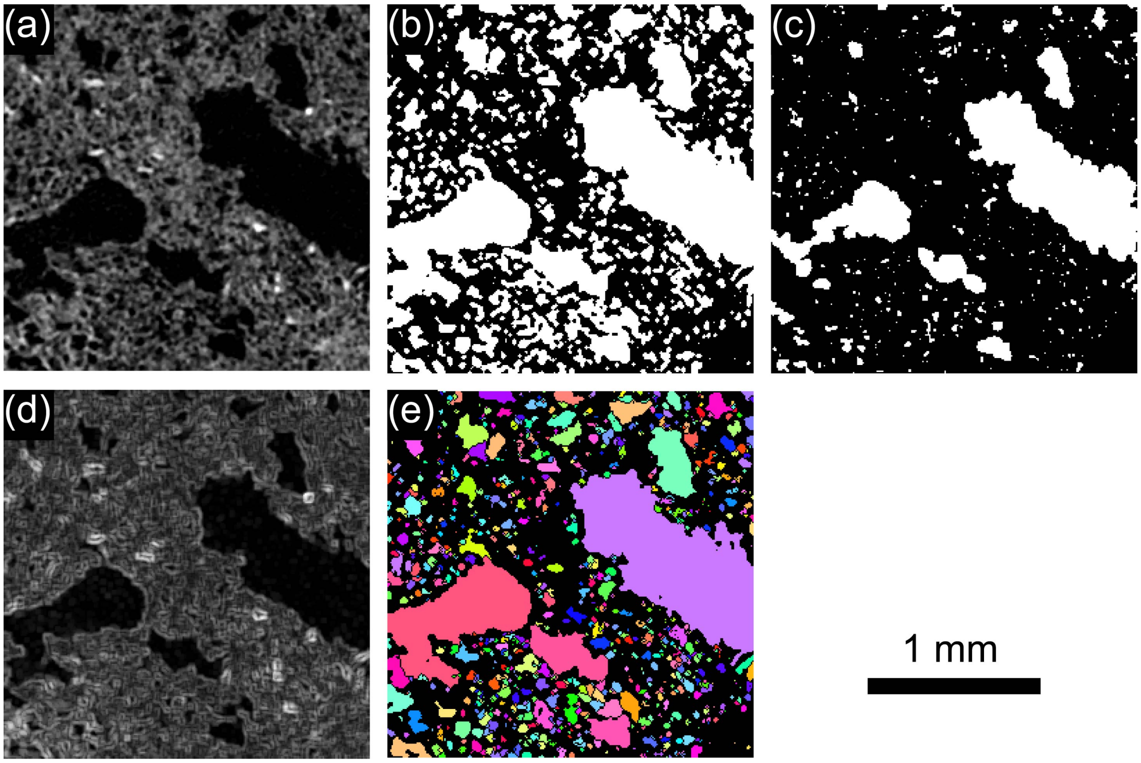

Figure F.2: Representative images used for the marker-controlled watershed algorithm. (a) Original image. (b) Mask image. (c) Marker image. (d) Gradient image of the original image. (e) Result of the watershed algorithm. Thin bubble walls are rebuilt. Different colors among neighboring bubbles indicate the segmented bubbles.

Appendix G

Numerical procedure of shape relaxation in an eruptive column

The numerical procedure is basically based on *Hort and Gardner* (2000) who modeled the cooling of a pumice clast within an eruption column. First, we obtain the ambient temperature of a pumice clast in the eruption column, using a steady state eruption column model, Plumeria *Mastin* (2007). Second, we solve thermal conduction in a pumice clast and get the temporal profiles of temperature and viscosity. Finally, we calculate the shape relaxation of a bubble with the MJT model.

G.1 One-dimensional eruption column model

We used a steady one-dimensional eruption column model called as Plumeria (*Mastin*, 2007). This model assumes the plume as a series of control volumes. In each control volume, mass, momentum, and energy are conserved by equating the vertical gradient of their properties to the lateral inputs from the ambient atmosphere. Following the formulation given by *Woods* (1988), *Mastin* (2007) divided the momentum conservation into two regions: a momentum-dominated gas-thrust region above the vent and an overlying buoyancy-dominated convective region. The basic equations are given by the following equations:

Mass conservation for the gas-thrust region

$$\frac{d(\pi r^2 \rho u)}{dz} = 2\pi r \epsilon u \sqrt{\rho \rho^{amb}}, \tag{G.1}$$

Mass conservation for the convective region

$$\frac{d(\pi r^2 \rho u)}{dz} = 2\pi r \rho^{amb} \epsilon u, \tag{G.2}$$

Momentum conservation

$$\frac{d(\pi r^2 \rho u^2)}{dz} = \pi r^2 \left(\rho^{amb} - \rho\right) g, \tag{G.3}$$

Energy conservation

$$\frac{d}{dz}\left[\pi r^2 \rho u \left(\frac{u^2}{2} + gz + h\right)\right] = \left(gz + h^{amb}\right) \frac{d\left(\pi r^2 \rho u\right)}{dz}, \tag{G.4}$$

where r is the plume radius, u is the plume velocity, z is the vertical coordinate upward; ρ and ρ^{amb} are the densities of the plume and the ambient atmosphere, ϵ is the entrainment factor, g is the gravitational acceleration, and h and h^{amb} are the enthalpies per unit mass of the plume and of the ambient atmosphere, respectively. All parameters, such as velocity and temperature, are averaged horizontally inside the column. Gas and material are assumed to be in thermal equilibrium, and all components move up confluently. In the convective region, horizontal entrainment velocity is calculated from ϵu, with $\epsilon = 0.09$. In the gas-thrust region, the entrainment factor is adjusted by a factor $\sqrt{\rho/\rho^{amb}}$ to account for the density differences between the plume and the ambient atmosphere. In the equations, the plume temperature T_p does not appear explicitly, but it is related to the enthalpy $h = C_p T_p$, where C_p is the bulk specific heat.

The input parameters for Plumeria are determined to simulate the eruption column of the Taupo plinian eruption. The parameters are summarized in Table. G.1.

Table G.1: Parameters for the one-dimensional eruption column model

Notation	Parameter	Value
T_0^{amb}	Air temperature at the vent	15 °C [a]
dT/dz	Thermal lapse rate in troposphere	-6.5 K/km [a]
z_0	Vent elevation	0 m
z^{trop}	Tropopause elevation	11 km [a]
H^{trop}	Tropopause thickness	9 km [a]
(dT/dz)	Thermal lapse rate in stratosphere	1.0 K/km [a]
r_0	Initial column diameter	432 m [b]
u_0	Initial plume velocity	306 m/s [c]
T_m	Initial plume temperature	850 °C [d]
n_0	Initial mass fraction gas in magma	0.0344 [c]
r_h	Relative humidity	0
Q_m	Mass discharge rate	2.5×10^8 kg/s [e]

[a] International standard atmosphere

[b] Initial column diameter is determined from u_0, n_0, T_m, and Q_m.

[c] Parameters from *Michaud-Dubuy et al.* (2018)

[d] Initial plume temperature from *Dunbar et al.* (1989b)

[e] Mass discharge rate from *Wilson* (1985)

G.2 Temporal position of a pumice clast

Using the Plumeria, I can obtain the temporal data of the averaged temperature T and velocity u in the plume. One of the important assumption of the eruption model is that every component moves up confluently. The velocity difference between gas and particles are assumed to be ignored. This assumption is reasonable for small particles whose terminal velocities are much less than the plume velocity. Large particles, which experience a bigger gravitational acceleration than smaller particles, may not move up confluently. However, the simulation by *Hort and Gardner* (2000) showed that the effect of differential movement on cooling can be neglected and may only be important for the rinds of large pumices. In this study, I focus on the shape relaxation of a bubble located on the pumice center, and therefore, I assume that pumice clasts move up confluently. The temporal position of a pumice clasts is calculated from

$$t(z) = \int_0^z \frac{1}{u(z)} dz. \tag{G.5}$$

G.3 Thermal conduction in pumice

Once I obtain the temporal data of the plume temperature, I can solve thermal conduction within a pumice clast. I assume that a spherical pumice is cooled only by conduction. Equation of heat conduction is given by

$$\frac{\partial T}{\partial t} = \kappa \frac{1}{r^2} \frac{\partial}{\partial r} \left(r^2 \frac{\partial}{\partial r} T \right), \tag{G.6}$$

where T is the temperature inside the pumice and κ is the thermal diffusivity. The initial and boundary conditions are given by

$$\begin{aligned} T(r,\ 0) &= T_m, && \text{(G.7)} \\ \left.\frac{\partial T}{\partial r}\right|_{r=0} &= 0, && \text{(G.8)} \\ q|_{r=R_C} &= h_a \left(T(R_C, t) - T_p(z) \right), && \text{(G.9)} \end{aligned}$$

where T_m is the initial plume temperature, R_C is the radius of the pumice clast, q is the heat flux, $\mathrm{W/m^2}$, h_a is the heat transfer coefficient, and $T_p(z)$ is the plume temperature. The heat flux q is also related to the temperature gradient at the pumice surface by the following equation $q = k \left.\frac{\partial T}{\partial r}\right|_{r=R_C}$ where k is the thermal conductivity. The above modeling (Eqs. G.6-G.9) has been used to calculate the cooling history of a pumice clast during fallout (*Thomas and Sparks*, 1992) and during an eruption column (*Hort and Gardner*, 2000). I assumed that the thermal diffusivity is constant during cooling. The parameters for thermal conduction are summarized in Table. G.2. The equation for thermal conduction (Eq. G.6) was solved with an implicit scheme.

Table G.2: Parameters for thermal conduction

Notation	Parameter	Value
h_a	Heat transfer coefficient	$340\ \mathrm{W/(m^2K)}$ [a]
κ	Thermal diffusivity	$3 \times 10^{-7}\ \mathrm{m^2/s}$ [b]
k	Thermal conductivity	$0.2\ \mathrm{W/m/K}$ [b]

[a] from *Hort and Gardner* (2000)

[b] from *Bagdassarov and Dingwell* (1994)

G.4 Shape relaxation

The temporal change of the viscosity inside the pumice clast can be calculated from the temporal data of temperature. Here, I calculate the viscosity change from the empirical viscosity model proposed by *Hess and Dingwell* (1996). During cooling, dissolved water content is assumed to be constant ($1.5\ \mathrm{wt.\%}$).

Finally, I calculate the shape relaxation of a deformed bubble within solidifying pumice, using the bubble deformation model (MJT model). The initial bubble has the bubble deformation degree of 0.667, which corresponds to the aspect ratio of $5 : 1$. The surface tension is assumed to be constant $0.3\ \mathrm{N/m}$. The bubble radius is set to $0.15\ \mathrm{mm}$ which is the same as the lower limit of analyzed bubbles in section 5.

Bibliography

Acrivos, A., and T. S. Lo (1978), Deformation and breakup of a single slender drop in an extensional flow, *Journal of Fluid Mechanics*, *86*(04), 641–672, doi:10.1017/S0022112078001329.

Acrivos, A. Lo, T. (1980), Extensional flow of dilute polymer solutions, *97*(1978), 666–671.

Agur, E. E. (1983), Heat transport in polymer melt flows, Ph.D. thesis, McMaster University, Hamilton, Ontario, L8S 4L7 Canada.

Aki, K., and P. G. Richards (2002), *Quantitative seismology*, University Science Books.

Alidibirov, M. A. (1994), A model for viscous magma fragmentation during volcanic blasts, *Bulletin of Volcanology*, *56*(6-7), 459–465, doi:10.1007/BF00302827.

Amoruso, A., and L. Crescentini (2009), Shape and volume change of pressurized ellipsoidal cavities from deformation and seismic data, *Journal of Geophysical Research*, *114*(B2), B02,210, doi:10.1029/2008JB005946.

Bacon, C. R. (1983), Eruptive history of Mount Mazama and Crater Lake Caldera, Cascade Range, U.S.A., *Journal of Volcanology and Geothermal Research*, *18*(1-4), 57–115, doi:10.1016/0377-0273(83)90004-5.

Bagdassarov, N., and D. Dingwell (1994), Thermal properties of vesicular rhyolite, *Journal of Volcanology and Geothermal Research*, *60*, 179–191.

Bagdassarov, N. S., a. M. Dorfman, and D. B. Dingwell (2000), Effect of alkalis, phosporus, and water on the surface tension of haplogranite melt, *American Mineralogist*, *85*, 33–40, doi:10.2138/am-2000-0105.

Barmin, A. A., E. A. Vedeneeva, and O. E. Melnik (2004), Effect of viscous dissipation on nonisothermal high-viscosity magma flow in a volcanic conduit, *Fluid Dynamics*, *39*(6), 863–873, doi:10.1007/s10697-004-0003-2.

Batchelor, G. K. G. K. (1967), *An introduction to fluid dynamics*, 615 pp., Cambridge University Press.

Bilby, B. A., J. D. Eshelby, and A. K. Kundu (1975), The change of shape of a viscous ellipsoidal region embedded in a slowly deforming matrix having a different viscosity, *Tectonophysics*, *28*(4), 265–274, doi:10.1016/0040-1951(75)90041-4.

Bird, R. B., W. E. Stewart, and E. N. Lightfoot (2007), *Transport phenomena*, 905 pp., J. Wiley.

Bouvet de Maisonneuve, C., O. Bachmann, and A. Burgisser (2009), Characterization of juvenile pyroclasts from the Kos Plateau Tuff (Aegean Arc): Insights into the eruptive dynamics of a large rhyolitic eruption, *Bulletin of Volcanology*, *71*(6), 643–658, doi:10.1007/s00445-008-0250-x.

Bradley, D., and G. Roth (2007), Adaptive Thresholding using the Integral Image, *Journal of Graphics Tools*, *12*(2), 13–21, doi:10.1080/2151237X.2007.10129236.

Budiansky, B., J. Hutchinson, and S. Slutsky (1982), Void Growth and Collapse in Viscous Solids, in *Mechanics of Solids*, pp. 13–45, Elsevier, doi:10.1016/b978-0-08-025443-2.50009-4.

Campagnola, S., C. Romano, L. G. Mastin, and A. Vona (2016), Confort 15 model of conduit dynamics: applications to Pantelleria Green Tuff and Etna 122 BC eruptions, *Contributions to Mineralogy and Petrology*, *171*(6), 1–25, doi:10.1007/s00410-016-1265-5.

Carey, S., and H. Sigurdsson (1989), The intensity of plinian eruptions, *Bulletin of Volcanology*, *51*(1), 28–40, doi:10.1007/BF01086759.

Caricchi, L., A. Pommier, M. Pistone, J. Castro, A. Burgisser, and D. Perugini (2011), Strain-induced magma degassing: Insights from simple-shear experiments on bubble bearing melts, *Bulletin of Volcanology*, *73*(9), 1245–1257, doi:10.1007/s00445-011-0471-2.

Caserta, S., S. Reynaud, M. Simeone, and S. Guido (2007), Drop deformation in sheared polymer blends, *Journal of Rheology*, *51*(4), 761–774, doi:10.1122/1.2723148.

Cole, J. W., S. J. Brown, R. M. Burt, S. W. Beresford, and C. J. Wilson (1998), Lithic types in ignimbrites as a guide to the evolution of a caldera complex, Taupo volcanic centre, New Zealand, *Journal of Volcanology and Geothermal Research*, *80*(3-4), 217–237, doi:10.1016/S0377-0273(97)00045-0.

Colucci, S., P. Papale, and C. P. Montagna (2017), Non-Newtonian flow of bubbly magma in volcanic conduits, *Journal of Geophysical Research: Solid Earth*, *122*(3), 1789–1804, doi:10.1002/2016JB013383.

Cordonnier, B., S. M. Schmalholz, K. Hess, and D. B. Dingwell (2012), Viscous heating in silicate melts : An experimental and numerical comparison, *117*(September 2010), 1–13, doi:10.1029/2010JB007982.

Costa, A., and G. Macedonio (2002), Nonlinear phenomena in fluids with temperature-dependent viscosity: An hysteresis model for magma flow in conduits, *Geophysical Research Letters*, *29*(10), 40–1–40–4, doi:10.1029/2001gl014493.

Costa, A., and G. Macedonio (2005), Viscous heating effects in fluids with temperature-dependent viscosity: triggering of secondary flows, *540*, 21–38, doi:10.1017/S0022112005006075.

Costa, A., O. Melnik, and E. Vedeneeva (2007), Thermal effects during magma ascent in conduits, *Journal of Geophysical Research: Solid Earth*, *112*(12), 1–16, doi:10.1029/2007JB004985.

Coward, M. P. (1980), The analysis of flow profiles in a basaltic dyke using strained vesicles, *Journal of the Geological Society*, *137*(5), 605–615, doi:10.1144/gsjgs.137.5.0605.

Cox, H. W. (1973), Shear heating of polymer melts in die flows, Ph.D. thesis, University of Minnesota Minneapolis, Minnesota.

Cross, M. M. (1965), Rheology of non-Newtonian fluids: A new flow equation for pseudoplastic systems, *Journal of Colloid Science*, *20*(5), 417–437, doi:10.1016/0095-8522(65)90022-X.

Davis, P. M. (1986), Surface deformation due to inflation of an arbitrarily oriented triaxial ellipsoidal cavity in an elastic half-space, with reference to Kilauea volcano, Hawaii, *Journal of Geophysical Research: Solid Earth*, *91*(B7), 7429–7438, doi:10.1029/JB091iB07p07429.

Degruyter, W., O. Bachmann, and A. Burgisser (2010a), Controls on magma permeability in the volcanic conduit during the climactic phase of the Kos Plateau Tuff eruption (Aegean Arc), *Bulletin of Volcanology*, *72*(1), 63–74, doi:10.1007/s00445-009-0302-x.

Degruyter, W., A. Burgisser, O. Bachmann, and O. Malaspinas (2010b), Synchrotron X-ray microtomography and lattice Boltzmann simulations of gas flow through volcanic pumices, *Geosphere*, *6*(5), 470–481, doi:10.1130/GES00555.1.

Delaby, I., B. Ernst, Y. Germain, and R. Muller (1994), Droplet deformation in polymer blends during uniaxial elongational flow: Influence of viscosity ratio for large capillary numbers, *Journal of Rheology*, *38*(6), 1705–1720, doi:10.1122/1.550568.

Dingwell, D., Y. Lavallée, K. U. Hess, A. Flaws, J. Marti, A. R. L. Nichols, H. A. Gilg, and B. Schillinger (2016), Eruptive shearing of tube pumice: pure and simple, *Solid Earth*, *7*(5), 1383–1393, doi:10.5194/sed-7-3053-2015.

Dingwell, D. B. (1996), Volcanic Dilemma : Flow or Blow ?, *Science*, *273*(August), 1054–1055, doi:10.1126/science.273.5278.1054.

Dunbar, N. W., and P. R. Kyle (1993), Lack of volatile gradient in the Taupo plinian-ignimbrite transition: evidence from melt inclusion analysis, *American Mineralogist*, *78*(5-6), 612–618.

Dunbar, N. W., R. L. Hervig, and P. R. Kyle (1989a), Determination of pre-eruptive H2O, F and Cl contents of silicic magmas using melt inclusions: Examples from Taupo volcanic center, New Zealand, *Bulletin of Volcanology*, *51*(3), 177–184, doi:10.1007/BF01067954.

Dunbar, N. W., P. R. Kyle, and C. J. Wilson (1989b), Evidence for limited zonation in silicic magma systems, Taupo Volcanic Zone, New Zealand, *Geology*, *17*(3), 234–236, doi:10.1130/0091-7613(1989)017<0234:EFLZIS>2.3.CO;2.

Eshelby, J. D. (1957), The Determination of the Elastic Field of an Ellipsoidal Inclusion, and Related Problems, *Proceedings of the Royal Society of London A: Mathematical, Physical and Engineering Sciences*, *241*(1226).

Flinn, D. (1962), On folding during three-dimensional progressive deformation, doi:10.1144/gsjgs.118.1.0385.

Frankel, N. A., and A. Acrivos (1970), The constitutive equation for a dilute emulsion, *Journal of Fluid Mechanics*, *44*(01), 65–78, doi:10.1017/S0022112070001696.

Gaonac'h, H., J. Stix, and S. Lovejoy (1996), Scaling effects on vesicle shape, size and heterogeneity of lavas from Mount Etna, *Journal of Volcanology and Geothermal Research*, *74*(1-2), 131–153, doi:10.1016/S0377-0273(96)00045-5.

Geshi, N., and Y. Miyabuchi (2016), Conduit enlargement during the precursory Plinian eruption of Aira Caldera, Japan, *Bulletin of Volcanology*, *78*(9), doi:10.1007/s00445-016-1057-9.

Giachetti, T., A. Burgisser, L. Arbaret, T. H. Druitt, and K. Kelfoun (2011), Quantitative textural analysis of Vulcanian pyroclasts (Montserrat) using multi-scale X-ray computed microtomography: Comparison with results from 2D image analysis, *Bulletin of Volcanology*, *73*(9), 1295–1309, doi:10.1007/s00445-011-0472-1.

Gurioli, L., A. J. L. Harris, B. F. Houghton, M. Polacci, and M. Ripepe (2008), Textural and geophysical characterization of explosive basaltic activity at Villarrica volcano, *Journal of Geophysical Research*, *113*(January), 1–16, doi:10.1029/2007JB005328.

Hale, A. J., and H. B. Mühlhaus (2007), Modelling shear bands in a volcanic conduit: Implications for over-pressures and extrusion-rates, *Earth and Planetary Science Letters*, *263*(1-2), 74–87, doi:10.1016/j.epsl.2007.08.026.

Hess, K., and D. Dingwell (1996), Viscosities of hydrous leucogranitic melts : A non-Arrhenian on the nature and efficiency of magmatic processes . As pendence (H20 concentration in weight percent) for each, *American Mineralogist*, *81*, 1297–1300, doi:10.1016/0016-7037(82)90381-7.

Hess, K. U., B. Cordonnier, Y. Lavallée, and D. B. Dingwell (2008), Viscous heating in rhyolite: An in situ experimental determination, *Earth and Planetary Science Letters*, *275*(1-2), 121–126, doi:10.1016/j.epsl.2008.08.014.

Hinch, E. J., and A. Acrivos (1980), Long slender drops in a simple shear flow, *Journal of Fluid Mechanics*, *98*(02), 305–328, doi:10.1017/S0022112080000171.

Hort, M., and J. Gardner (2000), Constraints on cooling and degassing of pumice during Plinian volcanic eruptions based on model calculations, *Journal of Geophysical Research: Solid Earth*, *105*(B11), 25,981–26,001, doi:10.1029/2000jb900186.

Houghton, B. F., and C. J. N. Wilson (1989), A vesicularity index for pyroclastic deposits, *Bulletin of Volcanology*, *51*(6), 451–462, doi:10.1007/BF01078811.

Houghton, B. F., B. J. Hobden, K. V. Cashman, C. J. Wilson, and R. T. Smith (2003), Large-scale interaction of lake water and rhyolitic magma during the 1.8 ka Taupo eruption, New Zealand, *Geophysical Monograph Series*, *140*(Figure 1), 97–109, doi:10.1029/140GM06.

Houghton, B. F., R. J. Carey, K. V. Cashman, C. J. Wilson, B. J. Hobden, and J. E. Hammer (2010), Diverse patterns of ascent, degassing, and eruption of rhyolite magma during the 1.8ka Taupo eruption, New Zealand: Evidence from clast vesicularity, *Journal of Volcanology and Geothermal Research*, *195*(1), 31–47, doi:10.1016/j.jvolgeores.2010.06.002.

Houghton, B. F., R. J. Carey, and M. D. Rosenberg (2014), The 1800a Taupo eruption: "Ill wind" blows the ultraplinian type event down to Plinian, *Geology*, *42*(5), 459–461, doi:10.1130/G35400.1.

Huber, C., Y. Su, C. T. Nguyen, a. Parmigiani, H. M. Gonnermann, and J. Dufek (2013), Journal of Geophysical Research : Solid Earth A new bubble dynamics model to study bubble growth , deformation , and coalescence, pp. 1–24, doi:10.1002/2013JB010419.Received.

Jackson, N. E., and C. L. Tucker (2003), A model for large deformation of an ellipsoidal droplet with interfacial tension, *Journal of Rheology*, *47*(3), 659–682, doi:10.1122/1.1562152.

Kaminski, É., and C. Jaupart (1997), Expansion and quenching of vesicular magma fragments in Plinian eruptions, *Journal of Geophysical Research: Solid Earth*, *102*(B6), 12,187–12,203, doi:10.1029/97jb00622.

Khakhar, D., and J. Ottino (1986), Deformation and breakup of slender drops in linear flows, *Journal of Fluid Mechanics*, *166*(1986), doi:10.1017/S0022112086000149.

Kieffer, S. W. (1977), Sound speed in liquid-gas mixtures: Water-air and water-steam, *Journal of Geophysical Research*, *82*(20), 2895–2904, doi:10.1029/JB082i020p02895.

Klug, C., and K. V. Cashman (1994), Vesiculation of May 18, 1980, Mount St. Helens magma, *Geology*, *22*(5), 468–472, doi:10.1130/0091-7613(1994)022<0468:VOMMSH>2.3.CO.

Klug, C., K. Cashman, and C. Bacon (2002), Structure and physical characteristics of pumice from the climactic eruption of Mount Mazama (Crater Lake), Oregon, *Bulletin of Volcanology*, *64*(7), 486–501, doi:10.1007/s00445-002-0230-5.

Laumonier, M., L. Arbaret, A. Burgisser, and R. Champallier (2011), Porosity redistribution enhanced by strain localization in crystal-rich magmas, *Geology*, *39*(8), 715–718, doi:10.1130/G31803.1.

Legland, D., I. Arganda-carreras, P. Andrey, U. R. Biopolymers, and I. J.-p. Bourgin (2016), MorphoLibJ : integrated library and plugins for mathematical morphology with ImageJ, *32*(July), 3532–3534, doi:10.1093/bioinformatics/btw413.

Legros, F., K. Kelfoun, and J. Martí (2000), The influence of conduit geometry on the dynamics of caldera-forming eruptions, *Earth and Planetary Science Letters*, *179*(1), 53–61, doi:10.1016/S0012-821X(00)00109-6.

Lensky, N. G., O. Navon, and V. Lyakhovsky (2004), Bubble growth during decompression of magma: Experimental and theoretical investigation, *Journal of Volcanology and Geothermal Research*, *129*(1-3), 7–22, doi:10.1016/S0377-0273(03)00229-4.

Lipshitz, S. D., and C. W. Macosko (1976), Rheological Changes During a Urethane Network Polymerization, *Polymer Engineering & Science*, *16*(12), 803–810.

Liu, Y., Y. Zhang, and H. Behrens (2005), Solubility of H2O in rhyolitic melts at low pressures and a new empirical model for mixed H2O-CO2 solubility in rhyolitic melts, *Journal of Volcanology and Geothermal Research*, *143*(1-3), 219–235, doi:10.1016/j.jvolgeores.2004.09.019.

Llewellin, E. W., H. M. Mader, and S. D. R. Wilson (2002a), The constitutive equation and flow dynamics of bubbly magmas, *Geophysical research letters.*, *29*(24), 2170, doi:10.1029/2002GL015697.

Llewellin, E. W., H. M. Mader, and S. D. R. Wilson (2002b), The rheology of a bubbly liquid, *Proceedings of the Royal Society A: Mathematical, Physical and Engineering Sciences*, *458*(2020), 987–1016, doi:10.1098/rspa.2001.0924.

Loewenberg, M. (1998), Numerical Simulation of Concentrated Emulsion Flows, *Journal of fluids engineering*, *120*(4), 824–832.

Mader, H. M., E. W. Llewellin, and S. P. Mueller (2013), The rheology of two-phase magmas: A review and analysis, *Journal of Volcanology and Geothermal Research*, *257*, 135–158, doi:10.1016/j.jvolgeores.2013.02.014.

Manga, M., and M. Loewenberg (2001), Viscosity of magmas containing highly deformable bubbles, *Journal of Volcanology and Geothermal Research*, *105*(1-2), 19–24, doi:10.1016/S0377-0273(00)00239-0.

Manga, M., J. Castro, K. V. Cashman, and M. Loewenberg (1998), Rheology of bubble-bearing magmas, *Journal of Volcanology and Geothermal Research*, *87*(1-4), 15–28, doi:10.1016/S0377-0273(98)00091-2.

Mangan, M., and T. Sisson (2000), Delayed, disequilibrium degassing in rhyolite magma: Decompression experiments and implications for explosive volcanism, *Earth and Planetary Science Letters*, *183*(3-4), 441–455, doi:10.1016/S0012-821X(00)00299-5.

Mangan, M., L. Mastin, and T. Sisson (2004), Gas evolution in eruptive conduits: Combining insights from high temperature and pressure decompression experiments with steady-state flow modeling, *Journal of Volcanology and Geothermal Research*, *129*(1-3), 23–36, doi:10.1016/S0377-0273(03)00230-0.

Martel, C., D. B. Dingwell, O. Spieler, M. Pichavant, and M. Wilke (2000), Fragmentation of foamed silicate melts: an experimental study, *Earth and Planetary Science Letters*, *178*, 47–58.

Marti, J., C. Soriano, and D. B. Dingwell (1999), Tube pumices as strain markers of the ductile-brittle transition during magma fragmentation, *Nature*, *402*(6762), 650–653, doi:10.1038/45219.

Mastin, L. G. (2002), Insights into volcanic conduit flow from an open-source numerical model, *Geochemistry, Geophysics, Geosystems*, *3*(7), 1–18, doi:10.1029/2001gc000192.

Mastin, L. G. (2005), The controlling effect of viscous dissipation on magma flow in silicic conduits, *Journal of Volcanology and Geothermal Research*, *143*(1-3), 17–28, doi:10.1016/j.jvolgeores.2004.09.008.

Mastin, L. G. (2007), A user-friendly one-dimensional model for wet volcanic plumes, *Geochemistry, Geophysics, Geosystems*, *8*(3), 1–24, doi:10.1029/2006GC001455.

Mastin, L. G., and M. S. Ghiorso (2000), A Numerical Program for Steady-State Flow of Magma-Gas Mixtures Through Vertical Eruptive Conduits.

Matsumoto, K., and M. Nakamura (2017), Syn-eruptive breakdown of pyrrhotite: a record of magma fragmentation, air entrainment, and oxidation, *Contributions to Mineralogy and Petrology*, *172*(10), 1–19, doi:10.1007/s00410-017-1403-8.

Meyer, F., and S. Beucher (1990), Morphological segmentation, *Journal of Visual Communication and Image Representation*, *1*(1), 21–46, doi:10.1016/1047-3203(90)90014-M.

Michaud-Dubuy, A., G. Carazzo, E. Kaminski, and F. Girault (2018), A revisit of the role of gas entrapment on the stability conditions of explosive volcanic columns, *Journal of Volcanology and Geothermal Research*, *357*, 349–361, doi:10.1016/j.jvolgeores.2018.05.005.

Minale, M. (2010), Models for the deformation of a single ellipsoidal drop: A review, *Rheologica Acta*, *49*(8), 789–806, doi:10.1007/s00397-010-0442-0.

Mitchell, S., et al. (2018), The interplay among clast size, vesicularity, postfragmentation expansion, and clast breakage: An example from the 1.8 ka Taupo eruption, in *Field Volcanology: A Tribute to the Distinguished Career of Don Swanson*, p. 538, Geological Society of America, doi:10.1130/2018.2538(17).

Mitchell, S. J., et al. (2019), Submarine giant pumice: a window into the shallow conduit dynamics of a recent silicic eruption, *Bulletin of Volcanology*, *81*(7), doi:10.1007/s00445-019-1298-5.

Mizuno, N., M. Ichihara, and N. Kame (2015), Moment tensors associated with the expansion and movement of fluid in ellipsoidal cavities, *Journal of Geophysical Research: Solid Earth*, *120*(9), 6058–6070, doi:10.1002/2015JB012084.

Moitra, P., H. M. Gonnermann, B. F. Houghton, and T. Giachetti (2013), Relating vesicle shapes in pyroclasts to eruption styles, *Bulletin of Volcanology*, *75*(2), doi:10.1007/s00445-013-0691-8.

Moitra, P., H. M. Gonnermann, B. F. Houghton, and C. S. Tiwary (2018), Fragmentation and Plinian eruption of crystallizing basaltic magma, *Earth and Planetary Science Letters*, *500*, 97–104, doi:10.1016/j.epsl.2018.08.003.

Mondy, L., et al. (2014), Experiments to Populate and Validate a Processing Model for Polyurethane Foam : BKC 44306 PMDI-10, *SAND2014-3292, Sandia National Laboratories*, (March).

Mondy, L. A., R. R. Rao, M. C. Celina, A. Quintana, B. Shelden, N. B. Wyatt, and E. M. Russick (2013), Experiments to estimate polyurethane foam reaction kinetics, *Proceedings of the Polymer Processing Society 29th Annual Meeting*, pp. 15–20.

Neff, R. A., C. W. Macosko, and W. A. Se (1996), Simultaneous measurement of viscoelastic changes and cell opening during processing of flexible polyurethane foam, *Rheologica Acta*, *666*, 656–666.

Okumura, S., M. Nakamura, A. Tsuchiyama, T. Nakano, and K. Uesugi (2008), Evolution of bubble microstructure in sheared rhyolite: Formation of a channel-like bubble network, *Journal of Geophysical Research: Solid Earth*, *113*(7), 1–18, doi:10.1029/2007JB005362.

Okumura, S., M. Nakamura, S. Takeuchi, A. Tsuchiyama, T. Nakano, and K. Uesugi (2009), Magma deformation may induce non-explosive volcanism via degassing through bubble networks, *Earth and Planetary Science Letters*, *281*(3-4), 267–274, doi:10.1016/j.epsl.2009.02.036.

Okumura, S., M. Nakamura, K. Uesugi, T. Nakano, and T. Fujioka (2013), Coupled effect of magma degassing and rheology on silicic volcanism, *Earth and Planetary Science Letters*, *362*, 163–170, doi:10.1016/j.epsl.2012.11.056.

Otsu, N. (1979), A Threshold Selection Method from Gray-Level Histograms, *IEEE Transactions on Systems, Man, and Cybernetics*, *9*(1), 62–66, doi:10.1109/TSMC.1979.4310076.

Pal, R. (2003), Rheological behavior of bubble-bearing magmas, *Earth and Planetary Science Letters*, *207*(1-4), 165–179, doi:10.1016/S0012-821X(02)01104-4.

Palladino, D. M., S. Simei, and K. Kyriakopoulos (2008), On magma fragmentation by conduit shear stress: Evidence from the Kos Plateau Tuff, Aegean Volcanic Arc, *Journal of Volcanology and Geothermal Research*, *178*(4), 807–817, doi:10.1016/j.jvolgeores.2008.09.011.

Papale, P. (1999), Strain-induced magma fragmentation in explosive eruptions, *Nature*, *397*(February), 425–428, doi:10.1038/17109.

Pearson, J. R. (1977), Variable-viscosity flows in channels with high heat generation, *Journal of Fluid Mechanics*, *83*(1), 191–206, doi:10.1017/S0022112077001141.

Phillips, J. C., S. J. Lane, A. M. Lejeune, and M. Hilton (1995), Gum rosin-acetone system as an analogue to the degassing behaviour of hydrated magmas, *Bulletin of Volcanology*, *57*(4), 263–268, doi:10.1007/BF00265425.

Pistone, M., L. Caricchi, P. Ulmer, L. Burlini, P. Ardia, E. Reusser, F. Marone, and L. Arbaret (2012), Deformation experiments of bubble- and crystal-bearing magmas: Rheological and microstructural analysis, *Journal of Geophysical Research: Solid Earth*, *117*(5), doi:10.1029/2011JB008986.

Pistone, M., L. Caricchi, P. Ulmer, E. Reusser, and P. Ardia (2013), Rheology of volatile-bearing crystal mushes: Mobilization vs. viscous death, *Chemical Geology*, *345*, 16–39, doi:10.1016/j.chemgeo.2013.02.007.

Polacci, M., K. V. Cashman, and J. P. Kauahikaua (1999), Textural characterization of the pahoehoe-'a'a transition in Hawaiian basalt, *Bulletin of Volcanology*, *60*(8), 595–609, doi:10.1007/s004450050254.

Polacci, M., P. Papale, and M. Rosi (2001), Textural heterogeneities in pumices from the climactic eruption of Mount Pinatubo, 15 June 1991, and implications for magma ascent dynamics, *Bulletin of Volcanology*, *63*(2-3), 83–97, doi:10.1007/s004450000123.

Polacci, M., L. Pioli, and M. Rosi (2003), The Plinian phase of the Campanian Ignimbrite eruption (phlegrean fields, Italy): Evidence from density measurements and textural characterization of pumice, *Bulletin of Volcanology*, *65*(6), 418–432, doi:10.1007/s00445-002-0268-4.

Polacci, M., D. R. Baker, L. Mancini, S. Favretto, and R. J. Hill (2009), Vesiculation in magmas from Stromboli and implications for normal Strombolian activity and paroxysmal explosions in basaltic systems, *Journal of Geophysical Research: Solid Earth*, *114*(1), 1–14, doi:10.1029/2008JB005672.

Prousevitch, A. A., D. L. Sahagian, and A. T. Anderson (1993), Dynamics of diffusive bubble growth in magmas: isothermal case, *Journal of Geophysical Research*, *98*(B12), doi:10.1029/93jb02027.

Proussevitch, A., and D. Sahagian (2005), Bubbledrive-1: A numerical model of volcanic eruption mechanisms driven by disequilibrium magma degassing, *Journal of Volcanology and Geothermal Research*, *143*(1-3), 89–111, doi:10.1016/j.jvolgeores.2004.09.012.

Proussevitch, A. A., and D. L. Sahagian (1996), Dynamics of coupled diffusive and decompressive bubble growth in magmatic systems, *Journal of Geophysical Research: Solid Earth*, *101*(B8), 17,447–17,455, doi:10.1029/96jb01342.

Prud'homme, R. K., and R. B. Bird (1978), The dilatational properties of suspensions of gas bubbles in incompressible newtonian and non-newtonian fluids, *Journal of Non-Newtonian Fluid Mechanics*, *3*(3), 261–279, doi:10.1016/0377-0257(78)87004-9.

Rosi, M., L. Vezzoli, A. Castelmenzano, and G. Grieco (1999), Plinian pumice fall deposit of the Campanian Ignimbrite eruption (Phlegraean Fields, Italy), *Journal of Volcanology and Geothermal Research*, *91*(2-4), 179–198, doi:10.1016/S0377-0273(99)00035-9.

Rosi, M., P. Landi, M. Polacci, A. Di Muro, and D. Zandomeneghi (2004), Role of conduit shear on ascent of the crystal-rich magma feeding the 800-year-B.P. Plinian eruption of Quilotoa Volcano (Ecuador), *Bulletin of Volcanology*, *66*(4), 307–321, doi:10.1007/s00445-003-0312-z.

Rust, A. C., and K. V. Cashman (2007), Multiple origins of obsidian pyroclasts and implications for changes in the dynamics of the 1300 B.P. eruption of Newberry Volcano, USA, *Bulletin of Volcanology*, *69*(8), 825–845, doi:10.1007/s00445-006-0111-4.

Rust, A. C., and M. Manga (2002), Bubble shapes and orientations in low Re simple shear flow, *Journal of colloid and interface science*, *249*(2), 476–480, doi:10.1006/jcis.2002.8292.

Rust, A. C., M. Manga, and K. V. Cashman (2003), Determining flow type, shear rate and shear stress in magmas from bubble shapes and orientations, *Journal of Volcanology and Geothermal Research*, *122*(1-2), 111–132, doi:10.1016/S0377-0273(02)00487-0.

Sarkar, K., and W. R. Schowalter (2001), Deformation of a two-dimensional viscous drop in time-periodic extensional flows: analytical treatment, *J. Fluid Mech.*, *436*(2001), 207–230, doi:10.1017/S0022112001004013.

Schindelin, J., et al. (2012), Fiji: An open-source platform for biological-image analysis, *Nature Methods*, *9*(7), 676–682, doi:10.1038/nmeth.2019.

Shea, T., B. F. Houghton, L. Gurioli, K. V. Cashman, J. E. Hammer, and B. J. Hobden (2010), Textural studies of vesicles in volcanic rocks: An integrated methodology, *Journal of Volcanology and Geothermal Research*, *190*(3-4), 271–289, doi:10.1016/j.jvolgeores.2009.12.003.

Shields, J. K., H. M. Mader, M. Pistone, L. Caricchi, D. Floess, and B. Putlitz (2014), Strain-induced outgassing of three-phase magmas during simple shear, *Journal of Geophysical Research B: Solid Earth*, *119*(9), 6936–6957, doi:10.1002/2014JB011111.

Smith, R. T., and B. F. Houghton (1995), Vent migration and changing eruptive style during the 1800a Taupo eruption: new evidence from the Hatepe and Rotongaio phreatoplinian ashes, *Bulletin of Volcanology*, *57*(6), 432–439, doi:10.1007/BF00300987.

Sparks, R. S. (1978), The dynamics of bubble formation and growth in magmas: A review and analysis, *Journal of Volcanology and Geothermal Research*, *3*(1-2), 1–37, doi:10.1016/0377-0273(78)90002-1.

Taddeucci, J., and K. H. Wohletz (2001), Temporal evolution of the Minoan eruption (Santorini , Greece), as recorded by its Plinian fall deposit and interlayered ash fow beds, *Journal of Volcanology and Geothermal Research*, *109*, 299–317.

Tait, S., R. Thomas, J. Gardner, and C. Jaupart (1998), Constraints on cooling rates and permeabilities of pumice in an explosive eruption jet from colour and magnetic mineralogy, *Journal of Volcanology and Geothermal Research*, *86*(1-4), 79–91, doi:10.1016/S0377-0273(98)00075-4.

Takeda, S., M. Ohashi, O. Kuwano, M. Kameda, and M. Ichihara (2019), Rheological tests of polyurethane foam undergoing vesiculation-deformation solidification as a magma analogue, *Journal of Volcanology and Geothermal Research*, *submitted*.

Taya, M., and E. D. Seidel (1981), Void growth in a viscous metal, *International Journal of Engineering Science*, *19*(8), 1083–1094, doi:10.1016/0020-7225(81)90099-9.

Taylor, G. I. (1934), The Formation of Emulsions in Definable Fields of Flow, *Proceedings of the Royal Society of London A: Mathematical, Physical and Engineering Sciences*, *146*(858), 501–523.

Thielicke, W., and E. J. Stamhuis (2014), PIVlab âĂŞ Towards User-friendly, Affordable and Accurate Digital Particle Image Velocimetry in MATLAB, *Journal of Open Research Software*, *2*, 1–10, doi:10.5334/jors.bl.

Thomas, N., C. Jaupart, and S. Vergniolle (1994), On the vesicularity of pumice, *Journal of Geophysical Research*, *99*(B8), doi:10.1029/94jb00650.

Thomas, R. M., and R. S. Sparks (1992), Cooling of tephra during fallout from eruption columns, *Bulletin of Volcanology*, *54*(7), 542–553, doi:10.1007/BF00569939.

Toramaru, A. (1988), Formation of propagation pattern in two-phase flow systems with application to volcanic eruption, *Geophys. J.*, *95*, 613–623, doi:10.1111/j.1365-246X.1988.tb06707.x.

Toramaru, A. (1995), Numerical study of nucleation and growth of bubbles in viscous magmas, *Journal of Geophysical Research: Solid Earth*, *100*(B2), 1913–1931, doi:10.1029/94JB02775.

Toramaru, A. (2006), BND (bubble number density) decompression rate meter for explosive volcanic eruptions, *Journal of Volcanology and Geothermal Research*, *154*, 303–316, doi:10.1016/j.jvolgeores.2006.03.027.

Van Den Berg, H. R., C. A. Ten Seldam, and P. S. Van Der Gulik (1993), Compressible Laminar Flow in a Capillary, *Journal of Fluid Mechanics*, *246*, 1–20, doi:10.1017/S0022112093000011.

Vedeneeva, E. A. (2007a), ДВУМЕРНЫЕ МОДЕЛИТЕЧЕНИЯ МАГМЫ В КАНАЛЕ ВУЛКАНА С УЧЕТОМСЖИМАЕМОСТИ И ТЕНЛОВЫХ ЭФФЕКТОВ, Ph.D. thesis, Moscow State University, Moscow, Russia.

Vedeneeva, E. A. (2007b), Two-dimensional models of magma flows in a volcanic conduit taking the magma compressibility and thermal effects into account, *Fluid Dynamics*, *42*(4), 528–539, doi:10.1007/s10697-007-0056-0.

Vedeneeva, E. A., O. E. Melnik, A. A. Barmin, and R. S. J. Sparks (2005), Viscous dissipation in explosive volcanic flows, *Geophysical Research Letters*, *32*(5), 1–5, doi:10.1029/2004GL020954.

Venerus, D. C. (2006), Laminar capillary flow of compressible viscous fluids, *Journal of Fluid Mechanics*, *555*, 59–80, doi:10.1017/S0022112006008755.

Walker, G. (1980), The Taupo pumice: Product of the most powerful known (ultraplinian) eruption?, *Journal of Volcanology and Geothermal Research*, *8*(1), 69–94, doi:10.1016/0377-0273(80)90008-6.

Walker, G. P. (1981), Characteristics of two phreatoplinian ashes, and their water-flushed origin, *Journal of Volcanology and Geothermal Research*, *9*(4), 395–407, doi:10.1016/0377-0273(81)90046-9.

Walker, G. P., R. F. Heming, and C. J. Wilson (1980), Low-aspect ratio ignimbrites [9], doi:10.1038/283286a0.

Wetzel, E. D., and C. L. Tucker (2001), Droplet deformation in dispersions with unequal viscosities and zero interfacial tension, *Journal of Fluid Mechanics*, *426*(1934), 199–228, doi:10.1017/S0022112000002275.

Wilson, C. J. (1993), Stratigraphy, chronology, styles and dynamics of late Quaternary eruptions from Taupo volcano, New Zealand, *Philosophical Transactions of the Royal Society of London. Series A: Physical and Engineering Sciences*, *343*(1668), 205–306, doi:10.1098/rsta.1993.0050.

Wilson, C. J. (2001), *The 26.5 ka Oruanui eruption, New Zealand: An introduction and overview*, vol. 112, 133–174 pp., doi:10.1016/S0377-0273(01)00239-6.

Wilson, C. J. N. (1985), The Taupo Eruption, New Zealand II. The Taupo Ignimbrite, *Philosophical Transactions of the Royal Society A: Mathematical, Physical and Engineering Sciences*, *314*(1529), 229–310, doi:10.1098/rsta.1985.0020.

Wilson, C. J. N., and G. P. L. Walker (1985), The Taupo Eruption, New Zealand I. General Aspects, *Philosophical Transactions of the Royal Society A: Mathematical, Physical and Engineering Sciences*, *314*(1529), 199–228, doi:10.1098/rsta.1985.0019.

Wilson, L., R. S. J. Sparks, and G. P. L. Walker (1980), Explosive volcanic eruptions – IV. The control of magma properties and conduit geometry on eruption column behaviour, *Geophysical Journal International*, *63*(1), 117–148, doi:10.1111/j.1365-246X.1980.tb02613.x.

Woods, A. W. (1988), The fluid dynamics and thermodynamics of eruption columns, *Bulletin of Volcanology*, *50*(3), 169–193, doi:10.1007/BF01079681.

Wright, H. M. N., J. J. Roberts, and K. V. Cashman (2006), Permeability of anisotropic tube pumice: Model calculations and measurements, *Geophysical Research Letters*, *33*(17), 2–7, doi:10.1029/2006GL027224.

Wright, H. M. N., K. V. Cashman, E. H. Gottesfeld, and J. J. Roberts (2009), Pore structure of volcanic clasts: Measurements of permeability and electrical conductivity, *Earth and Planetary Science Letters*, *280*(1-4), 93–104, doi:10.1016/j.epsl.2009.01.023.

Zhang, Y. (1999), A criterion for the fragmentation of bubbly magma based on brittle failure theory, *Nature*, *402*(6762), 648–650, doi:10.1038/45210.

Zhang, Y., and H. Behrens (2000), H2O diffusion in rhyolitic melts and glasses, *Chemical Geology*, *169*(1-2), 243–262, doi:10.1016/S0009-2541(99)00231-4.